Unconventional Superconductivity in Cuprates, Cobaltates and Graphene: What is Universal and what is Material-Dependent in strongly versus weakly Correlated Materials?

Dissertation zur Erlangung des naturwissenschaftlichen Doktorgrades
der Julius-Maximilians-Universität Würzburg

vorgelegt von

Maximilian Ludwig Kiesel
aus Bad Kissingen

Würzburg, November 2012

Eingereicht am: 08.11.2012
bei der Fakultät für Physik und Astronomie

1. Gutachter: Prof. Dr. Werner Hanke
2. Gutachter: Prof. Dr. Carsten Honerkamp
der Dissertation

Vorsitzende(r): Prof. Dr. Björn Trauzettel
1. Prüfer: Prof. Dr. Fakher Assaad
2. Prüfer: Prof. Dr. Carsten Honerkamp
3. Prüfer: Prof. Dr. Hartmut Buhmann
im Promotionskolloquium

Tag des Promotionskolloquiums: 08.02.2013

Doktorurkunde ausgehändigt am: TBA

Zusammenfassung

Eine allgemeingültige Theorie für alle unterschiedlichen Arten von unkonventionellen Supraleitern ist immer noch eine der ungelösten Kernfragen der Festkörperphysik. Momentan ist es nicht einmal bewiesen, dass es überhaupt einen gemeinsamen grundlegenden Mechanismus gibt, sondern es müssen vielleicht mehrere verschiedene Ursachen für unkonventionelle Supraleitung berücksichtigt werden. Der Einfluss der Elektron-Phonon-Wechselwirkung ist dabei noch nicht abschließend geklärt.

In dieser Dissertation wird ein rein elektronischer Paarungsmechanismus untersucht, in welchem die Paarung durch Spin-Fluktuationen vermittelt wird, was nach dem aktuellen Stand der Forschung auf dem Gebiet der unkonventionellen Supraleiter am wahrscheinlichsten ist. Der Schwerpunkt liegt dabei auf der Bestimmung von Material-unabhängigen Eigenschaften der supraleitenden Phase. Diese können durch eine Auswahl sehr unterschiedlicher Systeme herausgearbeitet werden. Eine Untersuchung der Phasendiagramme gibt außerdem Auskunft darüber, welche konkurrierenden Quantenfluktuationen den supraleitenden Zustand abschwächen oder verstärken.

Für diese Analyse von sehr unterschiedlichen supraleitenden Materialien ist der Einsatz einer einzelnen numerischen Lösungsmethode unzureichend. Für diese Dissertation ist dies aber kein Nachteil, sondern vielmehr ein großer Vorteil, da der Einsatz verschiedener Techniken die Abhängigkeit der Ergebnisse von der verwendeten Numerik reduziert und dadurch der grundlegende Mechanismus besser untersucht werden kann.

Im speziellen werden in dieser Dissertation die Kuprate mit der Variationellen Clusternäherung ausgewertet, weil die Elektronen hier eine starke Wechselwirkung untereinander besitzen. Besonders die Frage eines möglichen “Klebstoffs” für die Cooper-Paare wird ausführlich diskutiert, auch mit einer Unterscheidung in retardierte und nicht-retardierte Beträge. Den Kupraten werden das Kobaltat $\mathsf{Na}_x\mathsf{CoO}_2$ (NaCoO) sowie Graphen gegenübergestellt. Diese Materialien sind jedoch schwach korrelierte Systeme, so dass hier die Funkionelle Renormierungsgruppe als numerisches Grundgerüst dient. Die Ergebnisse sind reichhaltige Phasendiagramme mit vielen verschiedenen langreichweitigen Ordnungen, wie zum Beispiel d+id-wellenartige Supraleitung. Diese bricht die Zeitumkehr-Symmetrie und besitzt eine vollständige Bandlücke, welche im Falle von NaCoO jedoch eine stark Dotierungs-abhängige Anisotropie aufweist. Als letztes wird das Kagome-Gitter allgemein diskutiert, ohne ein konkretes Material zu beschreiben. Hier hat eine destruktive Interferenz zwischen den Elektronen auf verschiedenen Untergittern drastische Auswirkungen auf die Instabilitäten der Fermi-Fläche, so dass die übliche Spin-Dichte-Welle und die damit verbundene d+id-wellenartige Supraleitung unterdrückt werden. Dadurch treten ungewöhnliche Spin- und Ladungsdichte-Ordnungen sowie eine nematische Pomeranchuck Instabilität hervor.

Zusammengefasst bietet diese Dissertation einen Einblick in unterschiedliche Materialklassen von unkonventionellen Supraleitern. Dadurch wird es möglich, die Material-spezifischen Eigenschaften von den universellen zu trennen.

Die Ergebnisse wurden in Refs. [1–5] veröffentlicht.

Abstract

A general theory for all classes of unconventional superconductors is still one of the unsolved key issues in condensed-matter physics. Actually, it is not yet fully settled if there is a common underlying pairing mechanism. Instead, it might be possible that several distinct sources for unconventional (not phonon-mediated) superconductivity have to be considered, or an electron-phonon interaction is not negligible.

The focus of this thesis is on the most probable mechanism for the formation of Cooper pairs in unconventional superconductors, namely a strictly electronic one where spin fluctuations are the mediators. Studying different superconductors in this thesis, the emphasis is put on material-independent features of the pairing mechanism. In addition, the investigation of the phase diagrams enables a view on the "vicinity" of superconductivity. Thus, it is possible to clarify which competing quantum fluctuations enhance or weaken the propensity for a superconducting state.

The broad range of superconducting materials requires the use of more than one numerical technique to study an appropriate microscopic description. This is not a problem but a big advantage because this facilitates the approach-independent description of common underlying physics.

For this evaluation, the strongly correlated cuprates are simulated with the variational cluster approach. Especially the question of a "pairing glue" is taken into consideration. Furthermore, it is possible to distinguish between retarded and non-retarded contributions to the gap function. The cuprates are confronted with the cobaltate $\mathsf{Na}_x\mathsf{CoO}_2$ (NaCoO) and graphene. These weakly correlated materials are investigated with the functional renormalization group (fRG) and reveal a comprehensive phase diagram, including a d+id-wave superconductivity, which breaks time-reversal symmetry. The corresponding gap function is nodeless, but for NaCoO, it features a doping-dependent anisotropy. In addition, some general considerations on the kagome lattice are completing the discussion, where a "sublattice interference" dramatically affects the Fermi-surface instabilities, suppressing the usual spin-density wave and d+id-wave superconductivity. Thereby, some different fascinating charge and bond orders as well as a nematic are observable.

In short, this thesis provides an insight to distinct classes of unconventional superconductors with appropriate simulation techniques. This facilitates to separate the material specific properties from the universal ones.

The results of this thesis are published in Refs. [1–5].

Contents

1

Challenges in Unconventional Superconductivity

Until the discovery of cuprate superconductors, the underlying physics of superconductivity had been considered as clarified: In the 1950s, *L.N. Cooper* identified the charge carriers of the superconducting current as a pair of two electrons with opposite momentum and spin, subsequently called Cooper pairs [6]. Together with *J. Bardeen* and *J.R. Schrieffer*, he suggested that these pairs are formed due to an attractive force induced by phonons, i.e. vibrations of the ionic lattice (BCS theory, Ref. [7]).

High-T_c Superconductivity in Cuprates

However, in 1986, *J.G. Bednorz* and *K.A. Müller* discovered superconductivity in the exotic compound $\mathrm{La}_{2-x}\mathrm{Ba}_x\mathrm{CuO}_4$ [8]. That was an exciting observation because $\mathrm{La}_{2-x}\mathrm{Ba}_x\mathrm{CuO}_4$ is not a metal and its transition temperature is $T_c \approx 30\mathrm{K}$, nearly 10° higher than the old record has been (Fig. 1.1). Indeed, the transition temperatures of superconductors in this new class are so high that they can *not* be explained by the phonon-mediated pairing of electrons to Cooper pairs. Therefore, they were labeled as "unconventional" superconductors. In the following years, other cuprates with transition temperatures over 100K were discovered [9].

The cuprates typically consist of two-dimensional CuO-layers, separated by layers containing transition metals like lanthanum, barium and strontium. The coupling between the CuO-layers is very weak compared to the coupling within these layers. Furthermore, the superconducting current flows only parallel to these layers, while the other constituents stabilize the lattice structure but do not contribute to bands near the Fermi surface (FS). Hence, in a good approximation, cuprates can be described by two-dimensional lattice models. During the last 25 years, a large variety of experiments were performed on cuprates, e.g. angle-resolved photoemission spectroscopy (ARPES) [11,12], Raman spectroscopy [13,14], SQUID interferometry [15] and neutron scattering [16]. Thus, the physical properties of cuprates are well examined. A generic phase diagram is plotted in Fig. 1.2, including the insulating state in the undoped parent compound, which is a common feature of all cuprate superconductors [17]. Only with electron or hole doping and a sufficiently low temperature, a phase transition to a

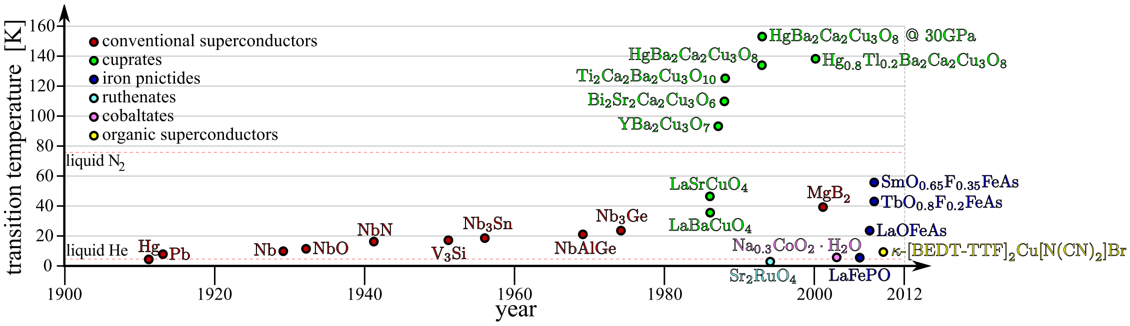

Figure 1.1: Timeline of the records for transition temperatures in various superconducting material classes [10].

superconducting state takes place. Here, the intermediate layers play an important role as electron donators or acceptors. The band structure of the cuprates, which is measurable via ARPES, reveals that only one band intersects the FS, which is dominated by the $d_{x^2-y^2}$-orbitals of the copper atoms. Hence, in a first approximation, it is possible to create an effective one-band model which neglects all other bands but reproduces the "correct" FS detected by ARPES. In contrast to the conventional superconductors with their constant (s-wave) gap, all cuprates have a non-uniform, i.e. strongly $\vec{k}$-dependent, gap at the Fermi energy, which even features "nodes" [18].

In detail, the undoped parent compounds are insulators, featuring an antiferromagnetic spin order. This Néel state robustly persists if the number of electrons per unit cell is increased [19], so superconductivity appears only in a narrow doping regime. On the other side, if the compound is hole doped, the antiferromagnetic configuration becomes soon less stable and, hence, superconductivity dominates over a wider doping regime. This asymmetry between electron and hole doping is an outstanding feature of the generic phase diagram (Fig. 1.2). In general, the electron-doped compounds are less investigated but gained some additional interest over the recent years [20, 21]. Another distinctive phenomenon appears for both hole and electron doping below a critical temperature T^*, where the spectral weight at the FS is drastically decreased. This reduction is momentum-dependent, leaving parts of the FS around the diagonal of the Brillouin zone ungapped. These "Fermi arcs" appear in the underdoped cuprates below T^* but above T_c. Here, due to the high temperature, the pairing field creates only non-coherent phase fluctuations, opening a partial gap without a superconducting current [22, 23]. But there is still an ongoing discussion whether this "pseudogap" phase is a precursor of the superconducting phase [24] or a complete new electronic phase [25, 26].

Although the classical BCS theory with its phonon-mediated pairing fails to describe the superconductivity in cuprates, the replacement of ^{16}O by ^{18}O in $YBa_2Cu_2O_{7-\delta}$ clearly decreases T_c in the underdoped regime, while this effect is minimal at optimal doping. [17, 31, 32], However, there are some proposals how a non-phononic but electronic formalism can explain this "isotope effect" [33, 34].

Since the discovery of iron-based superconductors by *Y. Kamihara et al.* in 2006 [35], the focus of condensed-matter physicists has somewhat moved away from the cuprates, although many open questions remain.

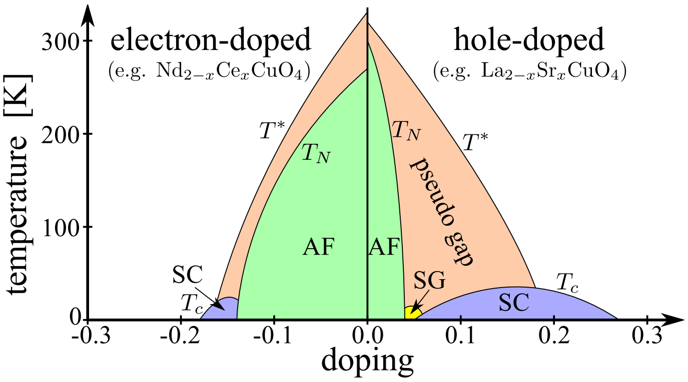

Figure 1.2: Generic phase diagram for cuprate superconductors, adopted from phase diagrams in Refs. [12, 21]. The basic compounds are antiferromagnetic Mott insulators [17]. For both electron- and hole-doped materials, the antiferromagnetic phase (AF) remains stable up to a critical doping, where superconductivity (SC) appears. There is an asymmetry between electron and hole doping, with a spin-glass phase (SG) only appearing in the latter case. The Néel temperature T_N indicates the phase transition to the antiferromagnetic phase, while T_c is the critical temperature for superconductivity. Below a temperature T^*, the Fermi surface (FS) remains ungapped only in parts around the diagonals of the Brillouin zone. This effect is similar to the SC phase, but without the SC current. Hence, this phase is called “pseudogap” and may be discussed as a precursor to the superconducting gap [27–30].

Novel Superconductors

In recent years, superconductivity has been discovered in many classes of materials, e.g. the iron pnictides [35, 36], the cobaltates [37] and organic structures [38]. Also, spin-triplet superconductivity has been measured in ruthenates [39] and predicted to appear in doped graphene [40]. These very different systems have in common that their superconductivity is considered as not phonon mediated. Hence, they are all labeled unconventional superconductors, but a common underlying mechanism is still missing.

From the pool of novel superconductors, the iron pnictides have gained the most attention over the last few years (for a review, see Ref. [41]). In contrast to the undoped cuprates, the undoped pnictides are metals. However, their resistivity is very high, so their classification in bad metals (weakly correlated) or bad insulators (strongly correlated) is not obvious, but the former assumption is established [41]. In the undoped parent compounds, most iron pnictides feature a stripe spin-density wave below $T_N \approx 150$K, succeeding to (or even coinciding with) a structural phase transition [42]. The states in the proximity of the Fermi energy are dominated by all 5 Fe_d-orbitals [43, 44], resulting in four (e.g. LaOFeP) or five (e.g. LaOFeAs) pockets [45, 46], so the FS is much more complicated than the cuprates one. Within the superconducting phase, the FS is completely gapped, and the gap function changes sign only between the pockets ($s^{\pm}$-wave type) [47]. Recently, also a time-reversal symmetry-breaking state with s+id-wave pairing symmetry has been proposed [48].

Another candidate for a chiral, i.e. parity and time-reversal symmetry-breaking, superconducting state is graphene [2]. The most exciting feature of graphene is its two-dimensional nature because, until the discovery of graphene [49, 50], two-dimensional crystals had been classified as unstable [51, 52]. For graphene, the evasion from this conflict is the forming of ripples to avoid a strict two-dimensionality [53, 54]. Graphene features very interesting properties like an FS consisting of only six points, called Dirac points, at half filling. Furthermore, the low-energy excitations have a linear dispersion (“Dirac cones”) and are similar to the massless Fermions in quantum electrodynamics (QED) but with much smaller velocity [55,56]. Due to this resemblance, the electrons around the Fermi level got the attribute “relativistic”. A detailed review of graphene’s electronic properties is given by *A.H. Castro Neto et al.* in Ref. [57]. Up to now, superconductivity has not yet been detected in graphene yet.

Furthermore, if the cobaltate $\mathsf{Na}_{0.3}\mathsf{CoO}_2$ is immersed with water, a superconducting phase can be measured [58]. The intercalation with water is volatile, so experiments are complicated. As a result, there is an evidence for a singlet pairing state [59], which is fully gapped by symmetry (s-wave or d+id-wave type). However, also an anisotropic superconducting gap function with nodes was reported [60, 61]. A solution for this contradiction is still in discussion.

A common feature of these unconventional superconductors are their two-dimensional layers, where Cooper pairs are formed. Also, the proximity to a magnetic instability is conspicuous and, consequently, the evaluation of competing phases is necessary.

Many-Body Physics

The interplay between the kinetic energy of electrons and their Coulomb interaction plays a crucial role in condensed-matter physics but is difficult to resolve. In general, it is impossible to solve both kinetic motion and interaction analytically for an arbitrary system of electrons in an ionic lattice, so perturbation theory is used. One ansatz is to solve only the kinetic part and, afterwards, introduce the interaction as a perturbation. This general approximation is reasonable for systems with weakly correlated electrons. The numerical implementation of the functional renormalization group used in this thesis (fRG, see Sec. 2.6 for details) is based on this idea. In contrast, the approach for strongly correlated electrons includes the full interaction but a limited electron motion. Thereafter, the full kinetic motion is restored as a perturbation. A realization of this concept is the variational cluster approach (VCA, see Sec. 2.4 for details). To decide which approximation is appropriate, the bandwidth of the electronic band structure around the Fermi level (as a degree of kinetic energy) is compared to the effective - i.e. screened - Coulomb interaction. As a rough estimate, if the bandwidth is larger, it is a system with weak coupling, but if the interaction is larger, the system is strongly correlated.

There are a plethora of methods to investigate condensed-matter physics on a theoretical level, including both analytical and numerical methods. All have advantages and disadvantages, hence the choice of the method is crucial. Additionally, new concepts and approaches are developed year after year.

After the formulation of the functional renormalization-group (fRG, presented in Sec. 2.6), it was natural to test this new technique with the one-band Hubbard model for the cuprates. *C. Honerkamp et al.* published results in Ref. [62]. Here, a simple g-ology model was used to set the starting value for the fRG-flow (see App. A.1 for details). The result was a phase diagram including three regimes with spin-density wave (low hole doping), insulating spin liquid (intermediate doping) and d-wave superconductivity (high doping). This doping dependence was explained with the decreasing condition of nesting at the FS. But (undoped) cuprates are Mott insulators [17], thus the interaction between the electrons is not negligible. In contrast, the fRG is appropriate in the weak-coupling scenario of the Fermi liquid. Only for strongly overdoped cuprates, the screening of the interaction is sufficient to apply the approximation of a Fermi liquid [63]. Alternatively, in the infinite coupling limit at half filling, the spin physics are available through the pseudofermion functional renormalization group (PFFRG) [64, 65].

This leads to the conclusion that the cuprates are a nice technical test scenario for the fRG but not the optimal field of application. In this thesis, both cuprates and fRG are discussed but not in combination with each other.

For the cuprates, a strong-coupling approximation is needed to handle this strongly correlated material. The VCA is a well recognized cluster technique that provides a route to Mott physics. In addition to a simple one-band model, which includes only the $d_{x^2-y^2}$-orbital of the copper atoms, a more intricate three-band model is considered. Here, the p_x- and p_y-orbitals of oxygen constituents are added. These additional bands change the undoped compound from a Mott insulator to a charge-transfer insulator. The effects of this transformation are discussed under the aspect of a common "pairing glue". On the other hand, the fRG works fine for weakly correlated systems. Hence, it is a suitable technique for cobaltates and graphene because in these systems, the electron-electron interaction is relatively small.

A General Theory for High-T_c Superconductivity?

Although the record for a measured transition temperature with 138K in $\mathrm{Hg_{0.8}Tl_{0.2}Ba_2Ca_2Cu_3O_x}$ [66] for ambient pressure and 155K in $\mathrm{HgBa_2Ca_2Cu_3O_x}$ [9] for high pressure has been holding for nearly 20 years, high-T_c superconductivity is still one of the key issues in condensed-matter physics. Even 25 years after the discovery of cuprate high-T_c superconductors, a complete theory is still missing [67]. It is accepted that the superconducting current is carried by Cooper pairs, but the high transition temperatures preclude a strictly phonon-mediated pairing. Consequently, another mechanism is needed to form Cooper pairs in high-T_c superconductors. With the iron pnictides, the cobaltates, the ruthenates and some organic structures, the field of materials with unconventional superconducting phases has been further increased in recent years, which do not feature a phonon-mediated pairing mechanism. However, a common underlying mechanism is still unknown.

The important task is to determine which properties of these different classes are material specific and which ones are generic for unconventional superconductors. For example, a spin-fluctuation mediated pairing is proposed to be the common underlying mechanism (for a review on this topic, see Ref. [68]). With more information about the pairing mechanism, it may be possible to define the optimal requirements for superconducting materials. After this, the experimental physicists have to create samples which fulfill the requirements as good as possible. This route might lead to increased transition temperatures in each class of materials and perhaps to a new overall record. If the mechanism of unconventional superconductivity is revealed, the search for new high-T_c superconducting compounds can be focused. Even more, the question about the Holy Grail of condensed-matter physics can be answered: “Do room-temperature superconductors exist?”

The purpose and key issue of this thesis is the research on an electronic pairing mechanism:

The formation of Cooper pairs is mediated by the electron-electron Coulomb interaction on a static background lattice. By the selection of very different material classes (cuprates, cobaltates, graphene and a generic kagome lattice) and the simulation with appropriate techniques (VCA and fRG), the material specific properties can be separated from the universal ones.

Structure of this Thesis

This thesis is organized as follows:

In **Chap. 2**, the theoretical background is given to understand the concepts of this thesis. This includes an introduction to the implementation of the second quantization in lattice systems in Secs. 2.1-2.3. After this, the framework is built for the two major techniques within this thesis, namely the **variational cluster approximation** (VCA) in Sec. 2.4 and the **functional renormalization group** (fRG) in Sec. 2.6. In between these blocks, in Sec. 2.5, the analytical renormalization group (aRG) is introduced, which is a simplified version of the fRG, restricted to superconducting instabilities at infinitesimal couplings.

After the theoretical part, the VCA is applied to the **cuprate high-$\mathbf{T_c}$ superconductors**, which are strongly correlated systems (**Chap. 3**). Here, the topic is the **“pairing glue”** of the Cooper pairs. In a detailed discussion, the three-band model (doped charge-transfer insulator) is opposed to the simplified one-band model (doped Mott insulator). The similarities and differences of these two models are emphasized. Also, the one-band model is challenged as a justified simplification.

The **cobaltate $\mathbf{Na_xCoO_2 \cdot yH_2O}$** (NaCoO) is investigated with the fRG in **Chap. 4**. It features an effective triangular lattice with three hybridized orbitals per site. The phase diagram reveals (triplet) f-wave superconductivity as well as a **chiral d+id-wave superconductivity** in competition with a spin-density wave order. This strong competition creates an **anisotropy** of the d+id-wave form factors. Consequently, the effects on the gap function are striking.

In **Chap. 5**, the fRG is applied to **graphene**, the two-dimensional derivate of carbon. Recently, graphene was doped away from half filling to a van Hove singularity, where a **spin-density order** and **chiral d+id-wave superconductivity** are competing. The winner of this competition is still in discussion because it depends on the parameters for long-range hoppings as well as the screening of the Coulomb potential.

The last topic is the **kagome lattice**. Here, no real physical material is simulated, but a more generic discussion is given about the competing orders in this particular lattice. Beginning in **Chap. 6**, the kagome lattice is investigated with aRG. This simple method regards only the spin-singlet superconductivity, but this is sufficient to show the **non-intuitive effects of sublattice interference**.

This consideration is repeated with the more elaborate fRG in **Chap. 7**, where all competing orders are considered. The result is that the kagome lattice shows an unexpected behavior not only in the superconducting channel, but also some **exotic long-range orders** appear.

This thesis closes with an overview and outlook in **Chap. 8**.

2

Models and Methodology

In this chapter, I focus on the route to the two major techniques which are used within this thesis, namely the **variational cluster approach (VCA)** and the **functional renormalization group (fRG)**.

For the basic concepts of many-particle physics, I recommend some common textbooks [69–79]. Especially the chapters about Green's functions, perturbation theory, functional-integral formalism and Feynman diagrams are advisable.

At the beginning, I introduce the tight-binding Hubbard model as prototype of interacting models in a lattice. Subsequently, some basic two-dimensional lattice structures are presented which set the base for the condensed-matter physics described in the next chapters. I also explain the symmetry groups of these lattices and their analytical form factors. The VCA is explicitly deduced in Sec. 2.4. After this, I give a short introduction to the analytical renormalization group (aRG), which is the infinitesimal-coupling limit of the fRG, presented in Sec. 2.6.

Together, these tools provide a comprehensive gateway to both the strong- and weak-coupling limits of many-body physics.

2.1 Hubbard Model

A very simple model for the interplay between kinetic energy and Coulomb interaction, which was introduced by *J. Hubbard* in 1963 [80], features electrons which are strongly located at an atomic core but are allowed to "tunnel" instantaneously to a nearest-neighbor core, commonly referred as hopping between lattice sites. A straightforward simplification is to concentrate on electronic bands at or near the Fermi surface (FS) because these bands will dominate the electronic features at low temperatures.

The tight-binding model in its simplest version includes only one orbital per site. Its Hamiltonian reeds

$$\hat{H} = \underbrace{-t\sum_{\langle i,j\rangle}\sum_{\sigma}\left(\hat{c}^{\dagger}_{i\sigma}\hat{c}_{j\sigma}+\text{H.c.}\right)}_{\text{kinetic energy}}\underbrace{+U\sum_{i}\hat{n}_{i\uparrow}\hat{n}_{i\downarrow}}_{\text{interaction}}\underbrace{-\mu\sum_{i}\left(\hat{n}_{i\uparrow}+\hat{n}_{i\downarrow}\right)}_{\text{filling}}\ . \tag{2.1}$$

Here, $\hat{c}_{i\sigma}^{\dagger}$ creates an electron with spin σ at site i. The occupation number is $\hat{n}_{i\sigma} = \hat{c}_{i\sigma}^{\dagger}\hat{c}_{i\sigma}$, and the chemical potential μ is the amount of energy needed to remove a single electron from the system. At $T = 0\text{K}$, it is identical to the Fermi energy. Hence, the filling of the system is depending on the chemical potential with $n = -\frac{\partial\Omega}{\partial\mu}$, where Ω is the grand potential. In this thesis, I use the notation for the filling n as number of occupied states divided by all possible states. This ensures that half filling is always at $n = 0.5$, independently of the number of included bands or considered spins. For $\mu = \frac{U}{2}$, a bipartite lattice features one electron per unit cell, hence the system is half filled. Moreover, the parameter t represents the hopping and thereby the kinetic energy. It corresponds to the overlap integral between atomic orbitals at adjacent sites. The hopping is restricted to nearest neighbors, abbreviated by $\langle i, j\rangle$, thus hoppings to next-nearest neighbors and larger distances are neglected. This is justified by the exponential decline of overlap integrals with increasing distance. The symbol H.c. indicates the Hermitian conjugate of the previous operator. In Eq. 2.1, this corresponds to a back-hopping of particles. Finally, the on-site Coulomb interaction is represented by the parameter U. The reduction to a strictly local interaction is reasonable for a strong screening because the long-range Coulomb potential decreases with $\sim \frac{\mathrm{e}^{-Kr}}{r}$, i.e. the Yukawa potential. Furthermore, possible screening-induced bandwidth corrections [81] are negligible for a first approximation.

For $U \to 0$, the Hamiltonian represents a free system and can be transformed to momentum space by a Fourier transform. This yields the energy dispersion, depending on the background lattice. Some basic types of two-dimensional lattices are presented in the next section, including their energy dispersion. With increasing U, the model is in the weak-coupling ($\frac{U}{t} < 1$), intermediate-coupling ($\frac{U}{t} \approx 1$) or strong-coupling ($\frac{U}{t} > 1$) regime, respectively. A special case is $U \to \infty$, where double occupied sites are extremely energetically unfavorable and hence avoided. At half filling, every site is populated with exactly one electron and, consequently, only virtual hopping processes are possible. This limit is called Heisenberg model, featuring a new magnetic interaction scale $J \sim \frac{t^2}{U}$.

The basic Hubbard model has to be expanded if a more accurate description of a material is needed. These expansions may include long-range hoppings, long-range Coulomb interactions, multiorbital models or spin operators. Thus, one must have in mind that a simple model reduces the analytical or numerical effort needed for solving, but it can be an oversimplification which does not include all relevant physics. For example, in Chap. 3, I will discuss whether a three-band model is needed for high-T_c cuprates or a one-band model is already sufficient.

2.2 Two-dimensional Lattices

In a first approximation, the background ions are neglected because the most physical properties of a condensed-matter system are founded on electronic processes. The charge neutrality is fulfilled by a uniformly distributed positive background. For this picture, the atomic cores are smeared over the whole space. This “jellium” model includes quantum fluctuations within the electron-electron coupling but fails if the electron-ion interaction is not negligible, so it is the perfect model for metals. For further details, see Ref. [76].

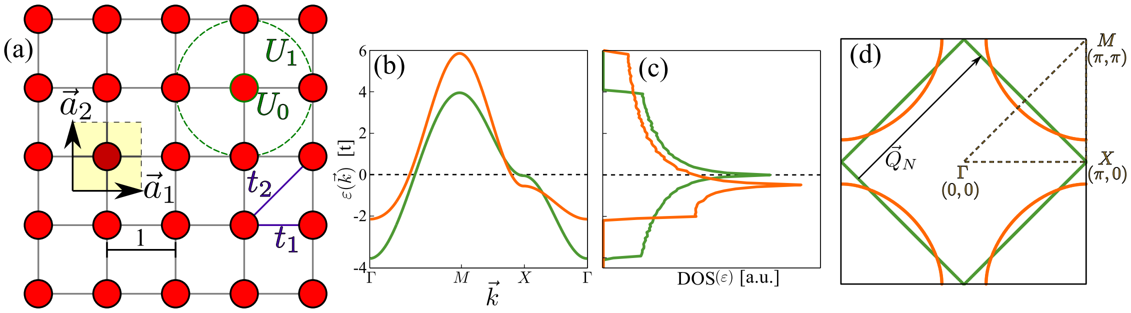

Figure 2.1: **(a)** The quadratic lattice with one site per unit cell. **(b)** Band dispersion for $t_1 = 1.0$, $\mu = 0.0$ (green) and $t_1 = 1.0$, $t_2 = -0.3$, $\mu = -0.7$ (orange) between the high symmetry points $\Gamma M X \Gamma$. **(c)** The corresponding density of states (DOS), with a van Hove singularity (VHS) for each setting. **(d)** The resulting Fermi surface (FS) in the Brillouin zone contains either a hole pocket around the Γ-point or an electron pocket around the M-point, respectively. For the first setting, the FS has a perfect nesting with $\vec{Q} = (\pi, \pi)$.

If the ionic background becomes crucial, the crystal structure of the condensed matter has to be included in the theory framework. Certainly, real life matter is three-dimensional, but a complete handling of all degrees of freedom may burst the analytical and numerical effort. The reduction to two dimensions might be reasonable in the following cases:

- The focus is on surface structures, e.g. Au on Ge(111) [82] or the Sn-induced surface reconstruction on Si(111) [83].
- The crystal structure is anisotropic, so the essential physics act within two-dimensional layers, e.g. the high-T_c cuprates [84] and the (1111) class of the iron pnictides [85].
- The topic is graphene, the alone real two-dimensional stuff known up to date [53, 54].

Here, I will present the most commonly used two-dimensional lattice structures.

Quadratic Lattice

The simplest two-dimensional lattice includes a quadratic structure and is obtained if a primitive, body-centered or face-centered cubic is cut in the (100) direction. Despite its plainness, it is useful to discuss the generic features like the dispersion relation. Concerning this, the kinetic part of the Hamiltonian in Eq. 2.1 has to be Fourier transformed to momentum space. Then, the creation operator and its adjoint annihilation operator read

$$\begin{aligned} \hat{c}^\dagger_{i\sigma} &= \frac{1}{\sqrt{N}} \sum_{\vec{k}} \hat{c}^\dagger_{\vec{k}\sigma} \cdot \mathrm{e}^{-\mathrm{i}\vec{k}\vec{r}_i} \\ \hat{c}_{i\sigma} &= \left(\hat{c}^\dagger_{i\sigma}\right)^\dagger = \left(\frac{1}{\sqrt{N}} \sum_{\vec{k}} \hat{c}^\dagger_{\vec{k}\sigma} \cdot \mathrm{e}^{-\mathrm{i}\vec{k}\vec{r}_i}\right)^\dagger = \frac{1}{\sqrt{N}} \sum_{\vec{k}} \hat{c}_{\vec{k}\sigma} \cdot \mathrm{e}^{+\mathrm{i}\vec{k}\vec{r}_i}\,. \end{aligned} \tag{2.2}$$

Applying these transformations to the hopping part of the Hamiltonian in Eq. 2.1 and using some algebra,

$$
\begin{aligned}
\hat{H}_0 &= -t \sum_{\langle i,j\rangle} \sum_{\sigma} \hat{c}^{\dagger}_{i\sigma} \hat{c}_{j\sigma} \\
&= -t \frac{1}{N} \sum_{\langle i,j\rangle} \sum_{\sigma} \sum_{\vec{k}} \sum_{\vec{l}} \hat{c}^{\dagger}_{\vec{k}\sigma} \mathrm{e}^{-\mathrm{i}\vec{k}\vec{r}_i} \cdot \hat{c}_{\vec{l}\sigma} \mathrm{e}^{+\mathrm{i}\vec{l}\vec{r}_j} \\
&= -t \frac{1}{N} \sum_{\sigma} \sum_{i} \sum_{\mathcal{N}} \sum_{\vec{k}} \sum_{\vec{l}} \mathrm{e}^{-\mathrm{i}\vec{k}\vec{r}_i + \mathrm{i}\vec{l}(\vec{r}_i + \vec{r}_{\mathcal{N}})} \hat{c}^{\dagger}_{\vec{k}\sigma} \hat{c}_{\vec{l}\sigma} \\
&= -t \sum_{\sigma} \sum_{\mathcal{N}} \sum_{\vec{k}} \sum_{\vec{l}} \underbrace{\frac{1}{N} \sum_{i} \mathrm{e}^{-\mathrm{i}(\vec{k}-\vec{l})\vec{r}_i}}_{\delta_{\vec{k}\vec{l}}} \mathrm{e}^{+\mathrm{i}\vec{l}\vec{r}_{\mathcal{N}}} \hat{c}^{\dagger}_{\vec{k}\sigma} \hat{c}_{\vec{l}\sigma} \\
&= \sum_{\sigma} \sum_{\vec{k}} \hat{c}^{\dagger}_{\vec{k}\sigma} \hat{c}_{\vec{k}\sigma} \underbrace{\left(-t \sum_{\mathcal{N}} \mathrm{e}^{+\mathrm{i}\vec{k}\vec{r}_{\mathcal{N}}} \right)}_{\varepsilon(\vec{k})} \\
&= \sum_{\sigma} \sum_{\vec{k}} \varepsilon\left(\vec{k}\right) \hat{c}^{\dagger}_{\vec{k}\sigma} \hat{c}_{\vec{k}\sigma}
\end{aligned}
\tag{2.3}
$$

the creation and annihilation operators become diagonal in $\vec{k}$ with a prefactor $\varepsilon\left(\vec{k}\right)$, called energy dispersion. The sum over nearest-neighbor connections $\sum\limits_{\langle i,j\rangle}$ was transformed to a double sum over all sites and their nearest-neighbor sites $\sum\limits_{i}\sum\limits_{\mathcal{N}}$. The lattice structure is reflected in the relative position of the nearest neighbors, so this has to be adapted for each lattice. For example, the quadratic lattice with lattice constant $a = 1$ features four nearest neighbors at

$$
\vec{r}_{\mathcal{N}} = \left\{ \begin{pmatrix} 1 \\ 0 \end{pmatrix}, \begin{pmatrix} -1 \\ 0 \end{pmatrix}, \begin{pmatrix} 0 \\ 1 \end{pmatrix}, \begin{pmatrix} 0 \\ -1 \end{pmatrix} \right\} . \tag{2.4}
$$

This yields

$$
\begin{aligned}
\varepsilon\left(\vec{k}\right) &= -t \sum_{\mathcal{N}} \mathrm{e}^{+\mathrm{i}\vec{k}\vec{r}_{\mathcal{N}}} = -t \left(\mathrm{e}^{+\mathrm{i}k_x} + \mathrm{e}^{-\mathrm{i}k_x} + \mathrm{e}^{+\mathrm{i}k_y} + \mathrm{e}^{-\mathrm{i}k_y} \right) \\
&= -2t \left(\cos\left(k_x\right) + \cos\left(k_y\right) \right) .
\end{aligned}
\tag{2.5}
$$

The hopping to next-nearest neighbors can be analogously transformed, so the energy dispersion for the quadratic lattice is extended to

$$
\varepsilon\left(\vec{k}\right) = -2t_1 \left(\cos\left(k_x\right) + \cos\left(k_y\right) \right) - 4t_2 \left(\cos\left(k_x\right) \cos\left(k_y\right) \right) - \mu , \tag{2.6}
$$

where t_1 and t_2 are the hopping integrals to the nearest neighbors and next-nearest neighbors, respectively. The structure of the quadratic lattice is plotted in Fig. 2.1a, including notations for hopping-matrix elements and ranges of the Coulomb interaction.

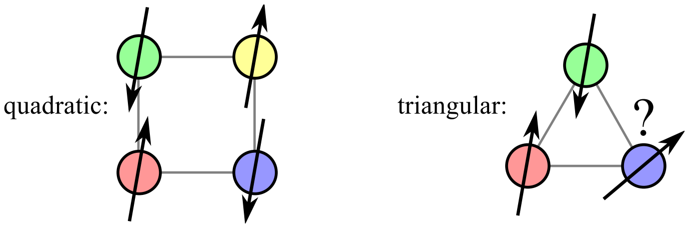

Figure 2.2: A simple depiction for the geometric spin frustration in the triangular lattice: At half filling and a sufficiently large Coulomb repulsion, each site is occupied with exactly one electron. If the exchange interaction is negligible, an energetically favorable state features electrons with antiparallel spins on neighboring sites because this configuration allows virtual hopping processes. For simplicity, the spin of the electrons is mapped to “up” or “down”, respectively. This task is very easy to solve for the quadratic lattice but impossible for the triangular one because, if the first two electrons are set (here on the red and green sites), the third one is a problem.

It features only one site per unit cell. The energy dispersion (Eq. 2.6) is plotted in Fig. 2.1b for a simple setting with $t_1 = 1.0$ and $\mu = 0.0$ (green line). If an additional next-nearest-neighbor hopping is included ($t_1 = 1.0$, $t_2 = -0.3$, $\mu = -0.7$; orange line), the result features a broken particle-hole symmetry. Here, the particle fillings are $n = 0.5$ and $n = 0.48$, respectively. The corresponding DOS are presented in Fig. 2.1c, where a clear van Hove singularity (VHS) is visible for each setting. Finally, the FSs of these two settings are compared in Fig. 2.1d. Without the next-nearest-neighbor hopping, the FS (green line in Fig. 2.1d) features parallel parts, connected by a nesting vector $\vec{Q}_N = (\pi,\pi)$. For particle excitations with this momentum transfer, there is a huge phase space for possible processes. This has a significant effect on collective particle modes with a non-zero ordering vector, e.g. the charge- and spin-density waves.

I will use this very simple model for the Cu-sites of cuprate superconductors in Chap. 3. There, I will also expand this model to three sites per unit cell, including the additional degrees of freedom of the O-sites. While the one-band model is a Mott insulator at half filling, the three-band model is a charge-transfer insulator at the corresponding filling. By doping these compounds in a $T = 0$K calculation, both become superconductors, but reveal discrepancies in the high-energy excitations.

Triangular Lattice

Another simple arrangement of sites is the triangular lattice. This structure appears, for example, if a basic cubic crystal is cut in the (111) direction or the body-centered cubic crystal in the (110) direction.

In the quadratic lattice, the antiferromagnetic order of electrons is well-known [86]. There, the free energy of a system is minimized if two electrons have antiparallel spins on neighboring sites because this configuration allows virtual hopping processes. Thus, they will arrange themselves in a checkerboard pattern. In opposite, in the triangular lattice, if two neighboring sites are fixed, they have a third neighbor in common which either violates the optimal link to the first or to the second site (Fig. 2.2). Thus, the lattice is in a geometric *spin frustration*, and the antiferromagnetic order is suppressed. The system

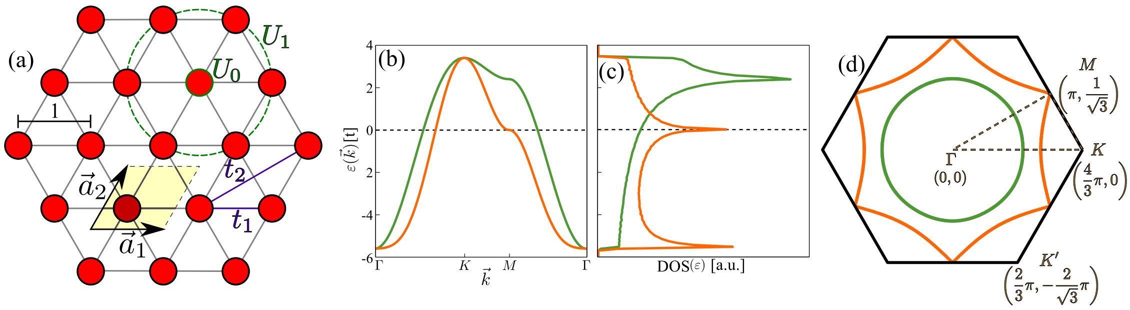

Figure 2.3: **(a)** The triangular lattice with one site per unit cell. **(b)** Band dispersion for $t_1 = 1.0$, $\mu = -0.4$ (green) and $t_1 = 1.0$, $t_2 = -0.3$, $\mu = 1.4$ (orange) between the high symmetry points $\Gamma K M \Gamma$. **(c)** The corresponding DOS. While $t_2 = 0$ has one VHS, for $t_2 > 0$ the weight is redistributed to a second singularity at the bottom of the band. **(d)** The resulting FS in the Brillouin zone (BZ) contains one hole pocket around the Γ-point for the first setting. The second parameter set is chosen to hit the Fermi energy at the VHS. At this limit, the FS undergoes a topological transition from one hole to two electron pockets.

has to form another magnetic order, e.g. a 120° Néel order [87]. Analogously to Eq. 2.6, The energy dispersion reads

$$\begin{aligned}\varepsilon(\vec{k}) = &-2t_1\left(\cos(k_x) + 2\cos\left(\frac{1}{2}k_x\right)\cos\left(\frac{\sqrt{3}}{2}k_y\right)\right)\\ &-2t_2\left(\cos\left(\sqrt{3}k_y\right) + 2\cos\left(\frac{3}{2}k_x\right)\cos\left(\frac{\sqrt{3}}{2}k_y\right)\right)\end{aligned} \tag{2.7}$$

The triangular lattice with hopping elements and interaction ranges is plotted in Fig. 2.3a. The unit cell contains one site and has the form of a parallelogram. For $t_1 = 0$ and $\mu = -0.4$, the energy dispersion is plotted with a green line in Fig. 2.3b. There is one VHS in the DOS (Fig. 2.3c). The filling is $n = 0.35$. If an additional next-nearest-neighbor hopping is implemented ($t_1 = 1.0$, $t_2 = -0.3$, $\mu = 1.4$, $n = 0.65$; orange line), the singularity is considerably weakened. Its weight is redistributed to a second singularity, which occurs because the bottom end of the band becomes vary flat. For $\mu < \mu_{crit} = 2t_1 + 3t_2$, the FS has a hole pocket around the Γ-point. In contrast, for $\mu > \mu_{crit}$, it contains two electron pockets, centered around the K- and K'-point. At $\mu = \mu_{crit}$, these pockets get in contact, marking a topological transition in the FS.

Within this thesis, an effective three-band model with three hybridized ions per unit cell in a triangular superlattice is used to simulate the cobaltate NaCoO (Chap. 4).

Honeycomb Lattice

Motivated by the first separation of graphene by *K.S. Novoselov et al.* in 2005 [49, 50], the honeycomb structure has gained a renaissance of attention. 60 years after the first evaluation of the band structure [88], it was possible to measure the unique properties of graphene, i.e. a two-dimensional allotrope of carbon, organized in a honeycomb-like lattice structure. At half filling, the FS of graphene is reduced to six Dirac points (see blue circles in Fig. 2.4). But in this thesis, the focus is on fillings around to the VHS.

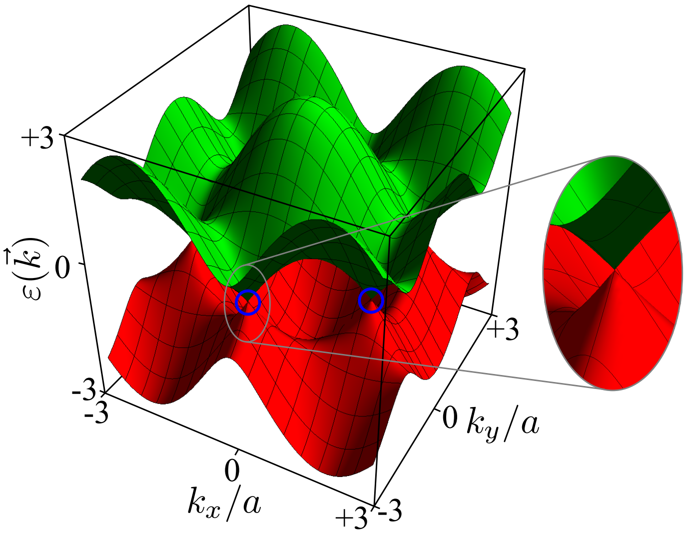

Figure 2.4: A calculated three-dimensional representation of the energy dispersion with $t_1 = 1$. The upper band is green colored, the lower one red. The blue circles mark two of six contact points of the Dirac cones, the others are not visible.

Here, the very high DOS combined with a very good nesting condition of the FS results in strong interaction effects, although the scale of the interaction is small compared to the bandwidth [89, 90].

The honeycomb lattice consists of two sites per unit cell, resulting in a two-band energy dispersion

$$\begin{aligned}\varepsilon(\vec{k}) = \pm t_1 & \sqrt{3 + 2\cos\left(\sqrt{3}k_x a\right) + 4\cos\left(\frac{\sqrt{3}}{2}k_x a\right)\cos\left(\frac{3}{2}k_y a\right)} \\ & + t_2\left(2\cos\left(\sqrt{3}k_x a\right) + 4\cos\left(\frac{\sqrt{3}}{2}k_x a\right)\cos\left(\frac{3}{2}k_y a\right)\right) \\ & \pm t_3\sqrt{3 + 2\cos\left(2\sqrt{3}k_x a\right) + 4\cos\left(\sqrt{3}k_x a\right)\cos\left(3k_y a\right)}\,,\end{aligned} \tag{2.8}$$

with the "+" before the first and third addend for the upper band and the "−" for the lower band, respectively. The hoppings $\{t_1, t_2, t_3\}$ correspond to diverse neighbor distances, as shown in Fig. 2.5a. The DOS has two singularities, which coincide with a perfect nesting of the FS, as long as t_3 and higher order hoppings are set to zero. The chemical potential to hit this concurrence is $\mu = \pm t_1 + 2t_2$. In Figs. 2.5b-d, the band dispersion, the DOS and the FS is plotted for two distinctive settings. For the first one (green), alone $t_1 = 1$ is included. To represent a longer ranged hopping, the second set (orange) provides $t_1 = 1, t_2 = -0.1, t_3 = 0.01$. The chemical potential is set to $\mu = 0.8$ and $\mu = 1.4$, resulting in fillings with $n = 0.57$ and $n = 0.75$, respectively. The sublattice contributions to the band dispersion are complex and vary around the BZ (the definition of sublattice contributions is explained in detail for the kagome lattice in Sec. 2.2), but the absolute values of these sublattice weights around the orange pocket in Fig. 2.5d are constant, with

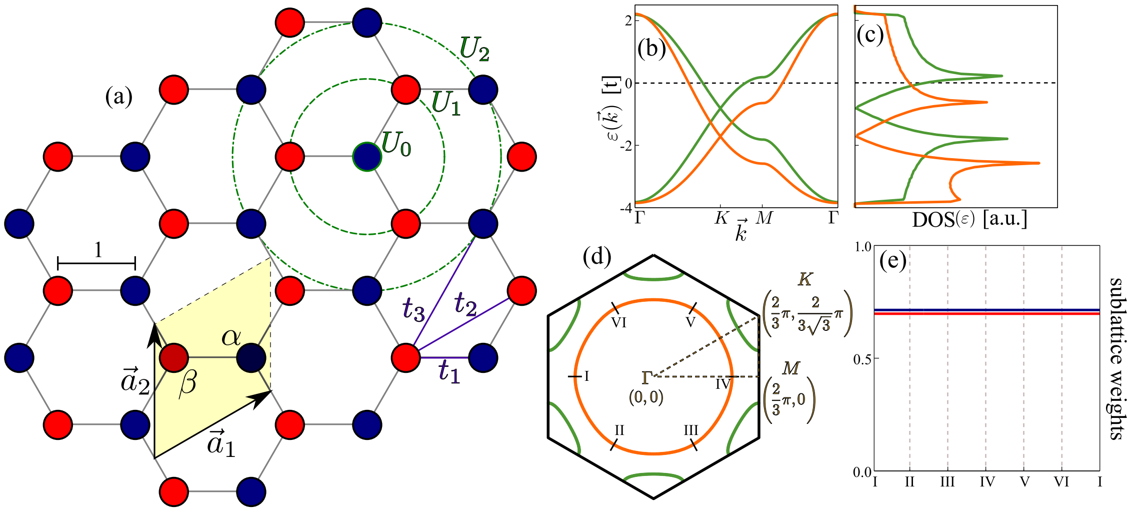

Figure 2.5: **(a)** The honeycomb lattice with two sites per unit cell. **(b)** Band dispersion for $t_1 = 1.0$, $\mu = 0.8$ (green) and $t_1 = 1.0$, $t_2 = -0.1$, $t_3 = 0.01$, $\mu = 1.4$ (orange) between the high symmetry points $\Gamma K M \Gamma$. **(c)** The corresponding DOS, with two van Hove singularities for each setting. **(d)** The resulting FS in the BZ contains either one hole pocket around the Γ-point or two electron pockets around the K- and K'-point, respectively. The sublattice contributions to the hole pocket (orange) are plotted in **(e)**. These contributions are complex, so the absolute value is depicted, which is constant. The complex phases differ within the BZ but have only a minimal influence on the results.

both sublattices contributing equally to the FS (Fig. 2.5e). Indeed, the complex phase factors are $\vec{k}$-dependent, but that feature had no effect on my calculations.

For both analytical RG (Sec. 2.5) and functional RG (Sec. 2.6), the interaction has to be transformed to momentum space. The explicit calculation will be done for the more complicated kagome lattice in Sec. 2.2. After a Fourier transform, the interaction in the honeycomb lattice reads

$$\begin{aligned}
V(\vec{k}_1,\vec{k}_2,\vec{k}_3) = U_0 \sum_{mn} & u^*_{mn}(\vec{k}_1)\, u^*_{mn}(\vec{k}_2)\, u_{mn}(\vec{k}_3)\, u_{mn}(\vec{k}_1+\vec{k}_2-\vec{k}_3) \\
& + \frac{U_1}{2} \sum_n \left(e^{i\frac{q_x}{2}+i\sqrt{3}\frac{q_y}{2}} + e^{i\frac{q_x}{2}-i\sqrt{3}\frac{q_y}{2}} + e^{-iq_x} \right) \\
& \qquad \times u^*_{\alpha n}(\vec{k}_1)\, u^*_{\beta n}(\vec{k}_2)\, u_{\alpha n}(\vec{k}_3)\, u_{\beta n}(\vec{k}_1+\vec{k}_2-\vec{k}_3) \\
& + \frac{U_1}{2} \sum_n \left(e^{-i\frac{q_x}{2}-i\sqrt{3}\frac{q_y}{2}} + e^{-i\frac{q_x}{2}+i\sqrt{3}\frac{q_y}{2}} + e^{iq_x} \right) \\
& \qquad \times u^*_{\beta n}(\vec{k}_1)\, u^*_{\alpha n}(\vec{k}_2)\, u_{\beta n}(\vec{k}_3)\, u_{\alpha n}(\vec{k}_1+\vec{k}_2-\vec{k}_3) \\
& + U_2 \left(\cos\left(3\frac{q_x}{2} - \sqrt{3}\frac{q_y}{2}\right) + \cos\left(\sqrt{3}q_y\right) + \cos\left(3\frac{q_x}{2} + \sqrt{3}\frac{q_y}{2}\right) \right) \\
& \qquad \times \sum_{mn} u^*_{mn}(\vec{k}_1)\, u^*_{mn}(\vec{k}_2)\, u_{mn}(\vec{k}_3)\, u_{mn}(\vec{k}_1+\vec{k}_2-\vec{k}_3)
\end{aligned} \tag{2.9}$$

with $q_x := k_{1,x} - k_{3,x}$, $q_y := k_{1,y} - k_{3,y}$ and the Bogoliubov-transform matrix element $u_{mn}(\vec{k})$ for sublattice m and band n at vector $\vec{k}$.

The honeycomb lattice will be the basis for the fRG calculations on graphene in Chap. 5.

Kagome Lattice

Another two-dimensional lattice considered within this thesis is the kagome lattice, which features three sites per unit cell, and it is possible to decompose it into three regular triangular sublattices. This unusual structure is realized in some exotic compounds, e.g. $\mathrm{ZnCu_3}(OH)_6\mathrm{Cl_2}$ (herbertsmithite) [91], $\mathrm{SrCr}_{8-x}\mathrm{Ga}_{4+x}\mathrm{O}_{19}$ [92], $\mathrm{Pr_3Ga_5SiO_{14}}$ (langasite) [93] and $\mathrm{BaNi_3(OH)_2(VO_4)_2}$ (vesignieite) [94]. In this thesis, the considerations are not adjusted to a special material but a general discussion about the influence of this extraordinary lattice structure to many-body physics.

The kagome lattice features a triangular superlattice where each unit cell contains three sites in a triangular arrangement (Fig. 2.6a). The nearest and next-nearest neighbors are sites from a different sublattice, while the 3rd-nearest neighbors are sites from the same sublattice again. The Hamiltonian reads

$$\hat{H} = t\sum_{\langle i,j\rangle}\sum_{\sigma}\left(\hat{c}^{\dagger}_{i\sigma}\hat{c}_{j\sigma} + \mathrm{H.c.}\right) + U_0\sum_{i}\hat{n}_{i\uparrow}\hat{n}_{i\downarrow} + \frac{U_x}{2}\sum_{[i,j]}\sum_{\sigma,\nu}\hat{n}_{i\sigma}\hat{n}_{j\nu} + \mu\sum_{i}\sum_{\sigma}\hat{n}_{i\sigma}, \tag{2.10}$$

where $\hat{n}_{i\sigma} = \hat{c}^{\dagger}_{i\sigma}\hat{c}_{i\sigma}$, and $\hat{c}^{\dagger}_{i\sigma}$ denotes the electron creation operator of spin $\sigma = \{\uparrow,\downarrow\}$ at site i. The hopping is restricted to nearest neighbors, indicated by $\langle i,j\rangle$. The local interaction is U_0, while the long-range interaction U_x is implemented for U_1, U_2 and U_3 as an interaction between nearest neighbors, next-nearest neighbors or 3rd-nearest neighbors, respectively. U_1 and U_2 connect different sublattices, while U_3 connects sites of the same sublattice. To obtain the band structure of the non-interacting system, the free part of the Hamiltonian has to be transformed to momentum space. Consequently, the lattice is divided in (translational invariant) unit cells, each containing three sites. This results in a triangular superlattice with three sublattices. The new creation operator has indices for (super)site, sublattice and spin:

$$\hat{c}^{\dagger}_{\underbrace{i}_{\text{site}}\underbrace{m}_{\text{sublattice}}\underbrace{\sigma}_{\text{spin}}} = \frac{1}{\sqrt{N}}\sum_{\vec{k}}\sum_{n}u^{*}_{mn}(\vec{k})\;\hat{c}^{\dagger}_{\underbrace{\vec{k}}_{\text{momentum}}\underbrace{n}_{\text{band}}\underbrace{\sigma}_{\text{spin}}}\mathrm{e}^{-\mathrm{i}\vec{k}(\vec{R}_i+\vec{r}_m)}. \tag{2.11}$$

After the Fourier transform, the new creation operator has indices for momentum, band

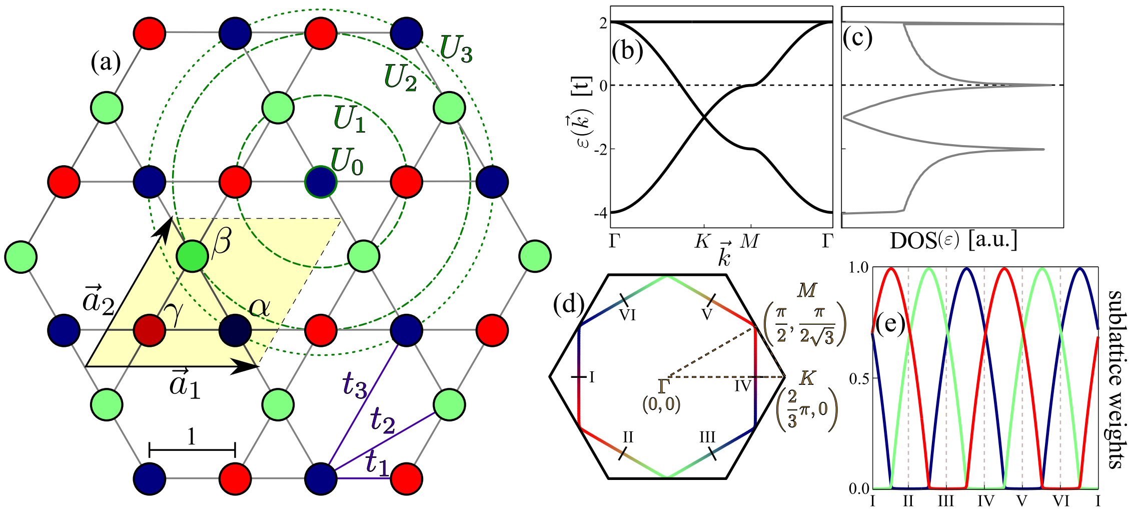

Figure 2.6: **(a)** The kagome lattice with three sites (α,β,γ) per unit cell. Each sublattice (indicated by blue/green/red circles) has a triangular structure. The nearest and next-nearest neighbors are from a distinct sublattice. **(b)** Band dispersion for $t_1 = 1.0$, $\mu = -0.2$ between the high symmetry points $\Gamma KM\Gamma$. The third completely flat band is striking. **(c)** The corresponding DOS, with two van Hove singularities and an additional singularity induced by the flat band. **(d)** The resulting FS in the BZ. Here, the colors encode the sublattice contributions. **(e)** Sublattice weights of the three sublattices at the FS.

and spin. The transformation of the non-interacting Hamiltonian follows

$$\begin{aligned}
\hat{H}_0 &= \sum_{i,j}\sum_{a,b}\sum_{\sigma} \tilde{t}_{iajb}\hat{c}^{\dagger}_{ia\sigma}\hat{c}_{jb\sigma} \\
&= \sum_{i,j}\sum_{\sigma} \begin{pmatrix} \hat{c}^{\dagger}_{i\alpha\sigma} & \hat{c}^{\dagger}_{i\beta\sigma} & \hat{c}^{\dagger}_{i\gamma\sigma} \end{pmatrix} \begin{pmatrix} \tilde{t}_{i\alpha j\alpha} & \tilde{t}_{i\alpha j\beta} & \tilde{t}_{i\alpha j\gamma} \\ \tilde{t}_{i\beta j\alpha} & \tilde{t}_{i\beta j\beta} & \tilde{t}_{i\beta j\gamma} \\ \tilde{t}_{i\gamma j\alpha} & \tilde{t}_{i\gamma j\beta} & \tilde{t}_{i\gamma j\gamma} \end{pmatrix} \begin{pmatrix} \hat{c}_{j\alpha\sigma} \\ \hat{c}_{j\beta\sigma} \\ \hat{c}_{j\gamma\sigma} \end{pmatrix} \\
&= \sum_{i,j}\sum_{\sigma} \underbrace{\begin{pmatrix} \hat{c}^{\dagger}_{i\alpha\sigma} & \hat{c}^{\dagger}_{i\beta\sigma} & \hat{c}^{\dagger}_{i\gamma\sigma} \end{pmatrix}\mathbf{U}}_{:=\frac{1}{\sqrt{N}}\sum_{\vec{k}}\begin{pmatrix} \hat{c}^{\dagger}_{\vec{k}1\sigma} & \hat{c}^{\dagger}_{\vec{k}2\sigma} & \hat{c}^{\dagger}_{\vec{k}3\sigma} \end{pmatrix}\mathrm{e}^{\mathrm{i}\vec{k}\vec{r}_i}} \begin{pmatrix} \varepsilon_1 & 0 & 0 \\ 0 & \varepsilon_2 & 0 \\ 0 & 0 & \varepsilon_3 \end{pmatrix} \mathbf{U}^T \begin{pmatrix} \hat{c}_{j\alpha\sigma} \\ \hat{c}_{j\beta\sigma} \\ \hat{c}_{j\gamma\sigma} \end{pmatrix} \\
&= \sum_{\vec{k}}\sum_{\sigma} \begin{pmatrix} \hat{c}^{\dagger}_{\vec{k}1\sigma} & \hat{c}^{\dagger}_{\vec{k}2\sigma} & \hat{c}^{\dagger}_{\vec{k}3\sigma} \end{pmatrix} \begin{pmatrix} \varepsilon_1(\vec{k}) & 0 & 0 \\ 0 & \varepsilon_2(\vec{k}) & 0 \\ 0 & 0 & \varepsilon_3(\vec{k}) \end{pmatrix} \begin{pmatrix} \hat{c}_{\vec{k}1\sigma} \\ \hat{c}_{\vec{k}2\sigma} \\ \hat{c}_{\vec{k}3\sigma} \end{pmatrix} \\
&= \sum_{\vec{k}}\sum_{\sigma}\sum_{n} \varepsilon_n(\vec{k})\, \hat{c}^{\dagger}_{\vec{k}n\sigma}\hat{c}_{\vec{k}n\sigma}
\end{aligned} \tag{2.12}$$

The matrix $\mathbf{U}$ performs a Bogoliubov transform from a sublattice representation to a band representation, with $\vec{k}$-dependent matrix elements $u_{mn}(\vec{k})$. The overlap integral $\tilde{t}_{iajb}$ represents a hopping from sublattice b on site j to sublattice a on site i. After the Fourier transform, the hopping is diagonal in the band operators, resulting in the one-particle energy dispersion of the free system $\varepsilon_n(\vec{k})$. For an alone nearest-neighbor hopping t_1,

$\varepsilon_n(\vec{k})$ can be calculated analytically:

$$\begin{aligned}
\varepsilon_1(\vec{k}) &= -t_1 - t_1\sqrt{3+2\cos(2k_x)+2\cos\left(k_x+\sqrt{3}k_y\right)+2\cos\left(k_x-\sqrt{3}k_y\right)} \\
\varepsilon_2(\vec{k}) &= -t_1 + t_1\sqrt{3+2\cos(2k_x)+2\cos\left(k_x+\sqrt{3}k_y\right)+2\cos\left(k_x-\sqrt{3}k_y\right)} \\
\varepsilon_3(\vec{k}) &= 2t_1
\end{aligned} \tag{2.13}$$

The third band is totally flat with not $\vec{k}$ dependence. This is also conspicuous in the plot of the dispersion relation (Fig. 2.6b). For next-nearest-neighbor hopping and higher orders, $\varepsilon_n(\vec{k})$ is more complicated. In addition, only for a kagome Hubbard model with pure next-nearest-neighbor hopping, the VHS in the DOS (Fig. 2.6c) and the perfect nesting condition (Fig. 2.6d) coincide at the same particle filling.

Subsequently, the interaction part of the Hamiltonian has to be transformed to momentum space. For Example, the nearest-neighbor Coulomb interaction can be transformed by

$$\begin{aligned}
\hat{H}_{U_1} &= \frac{U_1}{2}\sum_i\sum_s\sum_{\langle m,n\rangle}\sum_{\sigma,\nu}\hat{c}^\dagger_{im\sigma}\hat{c}^\dagger_{in\nu}\hat{c}_{im\sigma}\hat{c}_{in\nu} \\
&= \frac{U_1}{2}\frac{1}{N}\sum_i\sum_s\sum_{\langle m,n\rangle}\sum_{\sigma,\nu}\sum_{\vec{k}_1}u^*_{ms}(\vec{k}_1)\ \hat{c}^\dagger_{\vec{k}_1\sigma}\mathrm{e}^{-\mathrm{i}\vec{k}_1(\vec{R}_i+\vec{r}_m)}\sum_{\vec{k}_2}u^*_{ns}(\vec{k}_2)\ \hat{c}^\dagger_{\vec{k}_2\nu}\mathrm{e}^{-\mathrm{i}\vec{k}_2(\vec{R}_i+\vec{r}_n)} \\
&\qquad\times\sum_{\vec{k}_3}u_{ms}(\vec{k}_3)\ \hat{c}_{\vec{k}_3\sigma}\mathrm{e}^{+\mathrm{i}\vec{k}_3(\vec{R}_i+\vec{r}_m)}\sum_{\vec{k}_4}u_{ns}(\vec{k}_4)\ \hat{c}_{\vec{k}_4\nu}\mathrm{e}^{+\mathrm{i}\vec{k}_4(\vec{R}_i+\vec{r}_n)} \\
&= \frac{U_1}{2}\sum_{\sigma,\nu}\sum_{ms}\sum_{\mathcal{N}}\sum_{\substack{\vec{k}_1\vec{k}_2\\ \vec{k}_3\vec{k}_4}}\underbrace{\frac{1}{N}\sum_i\mathrm{e}^{\mathrm{i}\vec{R}_i(\vec{k}_3+\vec{k}_4-\vec{k}_1-\vec{k}_2)}}_{\delta_{\vec{k}_1+\vec{k}_2,\vec{k}_3+\vec{k}_4}}u^*_{ms}(\vec{k}_1)\ u^*_{\mathcal{N}s}(\vec{k}_2)\ u_{ms}(\vec{k}_3)\ u_{\mathcal{N}s}(\vec{k}_4) \\
&\qquad\times\mathrm{e}^{\mathrm{i}\vec{R}_m(\vec{k}_3-\vec{k}_1)}\mathrm{e}^{\mathrm{i}(\vec{R}_m+\vec{R}_{\mathcal{N}})(\vec{k}_4-\vec{k}_2)}\hat{c}^\dagger_{\vec{k}_1\sigma}\hat{c}^\dagger_{\vec{k}_2\nu}\hat{c}_{\vec{k}_3\sigma}\hat{c}_{\vec{k}_4\nu} \\
&= \frac{U_1}{2}\sum_{\sigma,\nu}\sum_{ms}\sum_{\mathcal{N}}\sum_{\substack{\vec{k}_1\vec{k}_2\\ \vec{k}_3}}u^*_{ms}(\vec{k}_1)\ u^*_{\mathcal{N}s}(\vec{k}_2)\ u_{ms}(\vec{k}_3)\ u_{\mathcal{N}s}(\vec{k}_1+\vec{k}_2-\vec{k}_3) \\
&\qquad\times\underbrace{\mathrm{e}^{\mathrm{i}\vec{R}_m(\vec{k}_1+\vec{k}_2-\vec{k}_3-(\vec{k}_1+\vec{k}_2-\vec{k}_3))}}_{1}\ \underbrace{\mathrm{e}^{\mathrm{i}\vec{R}_{\mathcal{N}}(\vec{k}_1+\vec{k}_2-\vec{k}_3-\vec{k}_2)}}_{\mathrm{e}^{\mathrm{i}\vec{R}_{\mathcal{N}}(\vec{k}_1-\vec{k}_3)}:=F_{m,\mathcal{N}}(\vec{k}_1-\vec{k}_3)}\ \hat{c}^\dagger_{\vec{k}_1\sigma}\hat{c}^\dagger_{\vec{k}_2\nu}\hat{c}_{\vec{k}_3\sigma}\hat{c}_{\vec{k}_1+\vec{k}_2-\vec{k}_3\nu} \\
&= \frac{U_1}{2}\sum_{\sigma,\nu}\sum_{ms}\sum_{\mathcal{N}}\sum_{\substack{\vec{k}_1\vec{k}_2\\ \vec{k}_3}}F_{m,\mathcal{N}}(\vec{k}_1-\vec{k}_3)\ u^*_{ms}(\vec{k}_1)\ u^*_{\mathcal{N}s}(\vec{k}_2)\ u_{ms}(\vec{k}_3)\ u_{\mathcal{N}s}(\vec{k}_1+\vec{k}_2-\vec{k}_3) \\
&\qquad\times\hat{c}^\dagger_{\vec{k}_1\sigma}\hat{c}^\dagger_{\vec{k}_2\nu}\hat{c}_{\vec{k}_3\sigma}\hat{c}_{\vec{k}_1+\vec{k}_2-\vec{k}_3\nu}
\end{aligned} \tag{2.14}$$

with

$$\sum_{\langle m,n\rangle}\vec{r}_n = \sum_m\sum_{\mathcal{N}}\vec{r}_m+\vec{r}_{\mathcal{N}} \tag{2.15}$$

and $\mathcal{N}$ indicating nearest neighbors. The long-range prefactor $F_{m,\mathcal{N}}(\vec{k}_1 - \vec{k}_3)$ depends on the sublattice and the nearest neighbors to this:

sublattice	nearest-neighbor sublattice	$\vec{R}_{\mathcal{N}}$	prefactor
α	β	$\left\{\frac{1}{2}\begin{pmatrix}-1\\ \sqrt{3}\end{pmatrix}, \frac{1}{2}\begin{pmatrix}1\\ -\sqrt{3}\end{pmatrix}\right\}$	$\cos\left(\frac{q_x}{2} - \sqrt{3}\frac{q_y}{2}\right)$
α	γ	$\left\{\begin{pmatrix}1\\ 0\end{pmatrix}, \begin{pmatrix}-1\\ 0\end{pmatrix}\right\}$	$\cos\left(q_x\right)$
β	α	$\left\{\frac{1}{2}\begin{pmatrix}-1\\ \sqrt{3}\end{pmatrix}, \frac{1}{2}\begin{pmatrix}1\\ -\sqrt{3}\end{pmatrix}\right\}$	$\cos\left(\frac{q_x}{2} - \sqrt{3}\frac{q_y}{2}\right)$
β	γ	$\left\{\frac{1}{2}\begin{pmatrix}1\\ \sqrt{3}\end{pmatrix}, \frac{1}{2}\begin{pmatrix}-1\\ -\sqrt{3}\end{pmatrix}\right\}$	$\cos\left(\frac{q_x}{2} + \sqrt{3}\frac{q_y}{2}\right)$
γ	α	$\left\{\begin{pmatrix}1\\ 0\end{pmatrix}, \begin{pmatrix}-1\\ 0\end{pmatrix}\right\}$	$\cos\left(q_x\right)$
γ	β	$\left\{\frac{1}{2}\begin{pmatrix}1\\ \sqrt{3}\end{pmatrix}, \frac{1}{2}\begin{pmatrix}-1\\ -\sqrt{3}\end{pmatrix}\right\}$	$\cos\left(\frac{q_x}{2} + \sqrt{3}\frac{q_y}{2}\right)$

with $q_x := k_{1x} - k_{3x}$ and $q_y := k_{1y} - k_{3y}$. This transformation is analogous for U_2 and U_3.

The full interaction up to 3rd-nearest neighbors reads

$$\begin{aligned}
V(\vec{k}_1,\vec{k}_2,\vec{k}_3) = U_0 \sum_{ms} & u^*_{ms}(\vec{k}_1)\, u^*_{ms}(\vec{k}_2)\, u_{ms}(\vec{k}_3)\, u_{ms}(\vec{k}_1+\vec{k}_2-\vec{k}_3) \\
& + U_1 \cos\left(\frac{q_x}{2} - \sqrt{3}\frac{q_y}{2}\right) \sum_s \Big(u^*_{\alpha s}(\vec{k}_1)\, u^*_{\beta s}(\vec{k}_2)\, u_{\alpha s}(\vec{k}_3)\, u_{\beta s}(\vec{k}_1+\vec{k}_2-\vec{k}_3) \\
& \qquad\qquad + u^*_{\beta s}(\vec{k}_1)\, u^*_{\alpha s}(\vec{k}_2)\, u_{\beta s}(\vec{k}_3)\, u_{\alpha s}(\vec{k}_1+\vec{k}_2-\vec{k}_3) \Big) \\
& + U_1 \cos(q_x) \sum_s \Big(u^*_{\alpha s}(\vec{k}_1)\, u^*_{\gamma s}(\vec{k}_2)\, u_{\alpha s}(\vec{k}_3)\, u_{\gamma s}(\vec{k}_1+\vec{k}_2-\vec{k}_3) \\
& \qquad\qquad + u^*_{\gamma s}(\vec{k}_1)\, u^*_{\alpha s}(\vec{k}_2)\, u_{\gamma s}(\vec{k}_3)\, u_{\alpha s}(\vec{k}_1+\vec{k}_2-\vec{k}_3) \Big) \\
& + U_1 \cos\left(\frac{q_x}{2} + \sqrt{3}\frac{q_y}{2}\right) \sum_s \Big(u^*_{\beta s}(\vec{k}_1)\, u^*_{\gamma s}(\vec{k}_2)\, u_{\beta s}(\vec{k}_3)\, u_{\gamma s}(\vec{k}_1+\vec{k}_2-\vec{k}_3) \\
& \qquad\qquad + u^*_{\gamma s}(\vec{k}_1)\, u^*_{\beta s}(\vec{k}_2)\, u_{\gamma s}(\vec{k}_3)\, u_{\beta s}(\vec{k}_1+\vec{k}_2-\vec{k}_3) \Big) \\
& + U_2 \cos\left(3\frac{q_x}{2} + \sqrt{3}\frac{q_y}{2}\right) \sum_s \Big(u^*_{\alpha s}(\vec{k}_1)\, u^*_{\beta s}(\vec{k}_2)\, u_{\alpha s}(\vec{k}_3)\, u_{\beta s}(\vec{k}_1+\vec{k}_2-\vec{k}_3) \\
& \qquad\qquad + u^*_{\beta s}(\vec{k}_1)\, u^*_{\alpha s}(\vec{k}_2)\, u_{\beta s}(\vec{k}_3)\, u_{\alpha s}(\vec{k}_1+\vec{k}_2-\vec{k}_3) \Big) \\
& + U_2 \cos\left(\sqrt{3} q_y\right) \sum_s \Big(u^*_{\alpha s}(\vec{k}_1)\, u^*_{\gamma s}(\vec{k}_2)\, u_{\alpha s}(\vec{k}_3)\, u_{\gamma s}(\vec{k}_1+\vec{k}_2-\vec{k}_3) \\
& \qquad\qquad + u^*_{\gamma s}(\vec{k}_1)\, u^*_{\alpha s}(\vec{k}_2)\, u_{\gamma s}(\vec{k}_3)\, u_{\alpha s}(\vec{k}_1+\vec{k}_2-\vec{k}_3) \Big) \\
& + U_2 \cos\left(3\frac{q_x}{2} - \sqrt{3}\frac{q_y}{2}\right) \sum_s \Big(u^*_{\beta s}(\vec{k}_1)\, u^*_{\gamma s}(\vec{k}_2)\, u_{\beta s}(\vec{k}_3)\, u_{\gamma s}(\vec{k}_1+\vec{k}_2-\vec{k}_3) \\
& \qquad\qquad + u^*_{\gamma s}(\vec{k}_1)\, u^*_{\beta s}(\vec{k}_2)\, u_{\gamma s}(\vec{k}_3)\, u_{\beta s}(\vec{k}_1+\vec{k}_2-\vec{k}_3) \Big) \\
& + U_3 \left(\cos\left(q_x - \sqrt{3} q_y\right) + \cos(2q_x) + \cos\left(q_x + \sqrt{3} q_y\right) \right) \\
& \qquad \times \sum_{ms} u^*_{ms}(\vec{k}_1)\, u^*_{ms}(\vec{k}_2)\, u_{ms}(\vec{k}_3)\, u_{ms}(\vec{k}_1+\vec{k}_2-\vec{k}_3)
\end{aligned} \tag{2.16}$$

with the abbreviation $q_x := k_{1,x} - k_{3,x}$, $q_y := k_{1,y} - k_{3,y}$.

The kagome lattice will be investigated on a general level with analytical RG in Chap. 6 and functional RG in Chap. 7. In particular, the $\vec{k}$-dependent matrix elements $u_{mn}(\vec{k})$ create non-trivial contributions of the sublattices to the FS, which heavily influences the nesting condition. This "sublattice interference" opens a route to new and exotic long-range orders.

2.3 Symmetry Group Representations

The lattices presented in the latter sections can be categorized by their symmetries. This enables the use of common features and general simplifications.

The quadratic lattice is invariant under 90°-rotations and features four reflection axis (Fig. 2.1a). These properties are classified as C_4 symmetry. Furthermore, the triangular

(a)

type	E	C_2	$2C_3$	$2C_6$	$3\sigma_v$	$3\sigma_d$	form
A_1	$+1$	$+1$	$+1$	$+1$	$+1$	$+1$	$s^{\pm}$
A_2	$+1$	$+1$	$+1$	$+1$	-1	-1	
B_1	$+1$	-1	$+1$	-1	$+1$	-1	f
B_2	$+1$	-1	$+1$	-1	-1	$+1$	f'
E_1	$+2$	-2	-1	$+1$	0	0	p_x, p_y
E_2	$+2$	$+2$	-1	-1	0	0	$d_{x^2-y^2}, d_{xy}$

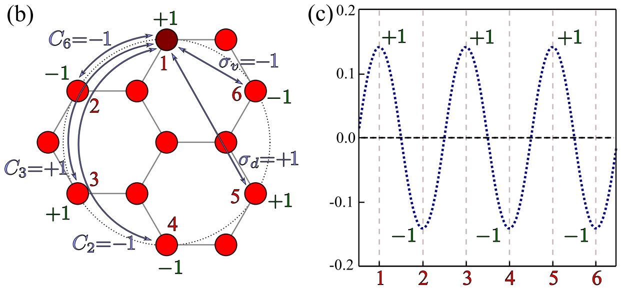

Figure 2.7: **(a)** Symmetry group table for C_{6v}: Here, E are the number of elements and C_2 is the trace of a 180° rotation matrix. Accordingly, C_3 and C_6 are for 120° and 60° rotations, respectively. σ_v and σ_d define reflections at distinct lattice axis. The resulting form factors in the BZ are plotted in Fig. 2.8. **(b)** Construction of the B_2 form factor between next-nearest neighbors in the honeycomb lattice. The sign at site 1 is fixed, so the symmetry transformations define the signs on the other five sites. **(c)** Harmonical function (f-wave in Eq. 2.19) which obeys to the signs on sites 1 to 6 defined in **(b)**.

lattice (Fig. 2.3a) features a symmetry under rotations by 60°. It is also invariant under reflections at a plane which includes the axis of rotation. The other symmetry axis are covered by rotations of the vertical one. Together, these symmetries define the C_{6v} group. The honeycomb and kagome lattices (Fig. 2.5a and Fig. 2.6a) are also elements of this group. There, the center of rotation is the middle of the hexagonal structures.

The categorization into symmetry groups enables the definition of harmonical functions which belong to the same group. For example, the C_{6v} group includes the representations plotted in Fig. 2.7a. The group members E_1 and E_2 consist of two elements, which are orthogonal, so any linear combination of these two elements fulfills the requirements of the symmetry. The construction of the f-wave form factor, i.e. a B_2-type group element, is presented in Fig. 2.7b,c.

It is possible to construct a harmonical function which fit to the point group representations. For next-nearest neighbors in the triangular lattice, the corresponding bonds have to be transformed to momentum space [95]. Then, the superposition reads

$$\begin{aligned}\Delta_s(\vec{k}) &= \cos(k_x) + e^{i\theta}\cos\left(\frac{k_x}{2} + \sqrt{3}\frac{k_y}{2}\right) + e^{i\phi}\cos\left(\frac{k_x}{2} - \sqrt{3}\frac{k_y}{2}\right) \\ \Delta_t(\vec{k}) &= \sin(k_x) - e^{i\theta}\sin\left(\frac{k_x}{2} + \sqrt{3}\frac{k_y}{2}\right) - e^{i\phi}\sin\left(\frac{k_x}{2} - \sqrt{3}\frac{k_y}{2}\right)\end{aligned} \tag{2.17}$$

for the singlet and triplet channel, respectively. The phases θ and ϕ have to fit in the C_{6v}

symmetry. For example, the singlet channel with $\theta = \frac{2\pi}{3}$ and $\phi = -\frac{2\pi}{3}$ yields

$$\begin{aligned}
\Delta_{d+\mathrm{i}d}(\vec{k}) &= \cos(k_x) + \mathrm{e}^{\mathrm{i}\frac{2\pi}{3}} \cos\left(\frac{k_x}{2} + \sqrt{3}\frac{k_y}{2}\right) + \mathrm{e}^{-\mathrm{i}\frac{2\pi}{3}} \cos\left(\frac{k_x}{2} - \sqrt{3}\frac{k_y}{2}\right) \\
&= \cos(k_x) + (\cos\left(\frac{2\pi}{3}\right) + \mathrm{i}\sin\left(\frac{2\pi}{3}\right)) \cos\left(\frac{k_x}{2} + \sqrt{3}\frac{k_y}{2}\right) \\
&\quad + (\cos\left(-\frac{2\pi}{3}\right) + \mathrm{i}\sin\left(-\frac{2\pi}{3}\right)) \cos\left(\frac{k_x}{2} - \sqrt{3}\frac{k_y}{2}\right) \\
&= \cos(k_x) - \frac{1}{2}\cos\left(\frac{k_x}{2} + \sqrt{3}\frac{k_y}{2}\right) + \mathrm{i}\frac{\sqrt{3}}{2}\cos\left(\frac{k_x}{2} + \sqrt{3}\frac{k_y}{2}\right) \\
&\quad - \frac{1}{2}\cos\left(\frac{k_x}{2} - \sqrt{3}\frac{k_y}{2}\right) - \mathrm{i}\frac{\sqrt{3}}{2}\cos\left(\frac{k_x}{2} - \sqrt{3}\frac{k_y}{2}\right) \\
&= \cos(k_x) - \cos\left(\frac{k_x}{2}\right)\cos\left(\sqrt{3}\frac{k_y}{2}\right) + \mathrm{i}\frac{\sqrt{3}}{2}\sin\left(\frac{k_x}{2}\right)\sin\left(\sqrt{3}\frac{k_y}{2}\right) ,
\end{aligned} \tag{2.18}$$

which is labeled as a $d+\mathrm{i}d$-wave symmetry. For $\theta = 0$ and $\phi = 0$, the result is an $s^{\pm}$-wave. In the triplet channel, the symmetries are $p+\mathrm{i}p$-wave (for $\theta = \frac{2\pi}{3}$ and $\phi = -\frac{2\pi}{3}$) and f-wave (for $\theta = 0$ and $\phi = 0$). The final form factors are

$$\begin{aligned}
s^{\pm}: &\quad \cos(k_x) + 2\cos\left(\frac{k_x}{2}\right)\cos\left(\sqrt{3}\frac{k_y}{2}\right) \\
p_x + \mathrm{i}p_y: &\quad \left[\sin(k_x) + \sin\left(\frac{k_x}{2}\right)\cos\left(\sqrt{3}\frac{k_y}{2}\right)\right] + \mathrm{i}\left[\sqrt{3}\cos\left(\frac{k_x}{2}\right)\sin\left(\sqrt{3}\frac{k_y}{2}\right)\right] \\
d_{x^2-y^2} + \mathrm{i}d_{xy}: &\quad \left[\cos(k_x) - \cos\left(\frac{k_x}{2}\right)\cos\left(\sqrt{3}\frac{k_y}{2}\right)\right] + \mathrm{i}\left[\sqrt{3}\sin\left(\frac{k_x}{2}\right)\sin\left(\sqrt{3}\frac{k_y}{2}\right)\right] \\
f: &\quad \sin(k_x) - 2\sin\left(\frac{k_x}{2}\right)\cos\left(\sqrt{3}\frac{k_y}{2}\right) .
\end{aligned} \tag{2.19}$$

These form factors have to be adapted for correlations beyond next-nearest neighbors or other lattices, but the results are similar. For illustration, the form factors of Eq. 2.19 are plotted in Fig. 2.8.

The symmetry and the resulting form factors of long-range orders are crucial for condensed-matter physics. For example, the d-wave form factor of the cuprate superconductivity features nodes, which can be detected experimentally [17]. Often, symmetries are available from experimental data and permit an elementary test for theoretical models.

2.4 Variational Cluster Approach

The numerical effort to solve a model physically correct and complete dramatically increases if additional degrees of freedom are included. For a two-dimensional layer in a crystal, the critical parameter is the number of lattice sites and relevant orbitals.

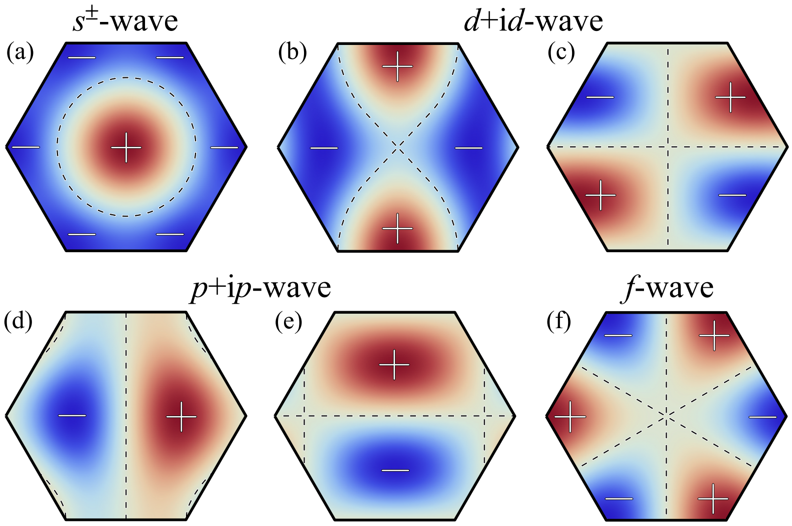

Figure 2.8: Nearest-neighbor form factors within the Brillouin zone of the triangular lattice. The analytical expressions are presented in Eq. 2.19.

Although the computational power is still exponentially growing (*Moore's law* [96]), the exact diagonalization reaches its limits at only a few lattice sites.

A first ansatz is a strong-coupling perturbation theory for Hubbard models, which already shows features like the Mott transition [97]. One possibility to get access to larger systems is to tile up the complete lattice into small clusters. These are exactly calculated, and, thereafter, the results are projected to the complete lattice. This class of approximations is called embedded cluster techniques [98]. In one ansatz, the hoppings between the clusters are regarded as a perturbation to the reference clusters, namely in the cluster perturbation theory (CPT) [99, 100]. The subsequent step is to add a self-consistency principle to get the "best" reference system out of a test space (self-energy-functional theory (SFA) [101]). If this concept is combined with clusters, one yields the variational cluster approach (VCA). The advantage of this method is an exact treatment of the reference cluster combined with a self-consist variational principle for the extrapolation to the infinite lattice. I will use the VCA for the simulation of high-T_c cuprates in Chap. 3. Certainly, there exist many other approximations for strongly correlated electron systems. An overview of dynamical variational principles is given in Refs. [102–104].

The use of the VCA is well justified by the successful application on various fields: Beginning with calculations on cuprates, the spectral function [105] as well as the ground-state phase diagram [106] was investigated. Then, a closer look was taken on the pseudogap phase [107] and two distinct temperature scales [25] were reported. Moreover, it was successfully applied to layered organic conductors [108] and also some more general features like a charge ordering are accessible [109]. In recent publications, the VCA was adopted to the single-impurity Anderson model [110] and topological insulators [111]. In addition, a time-reversal symmetry-breaking phase was studied in the Hubbard model [112].

In this thesis, the formalism for two-particle excitations [113] is extended to the three-band model [114]. Furthermore, the gap function of Ref. [115] is implemented for both the one-band and three-band Hubbard model. All together, this gives insight to the pairing dynamics in terms of a "pairing glue" for superconductivity. The results are presented in Chap. 3.

2.4.1 Self-Energy-Functional Approach

One goal of theoretical physics is to create a model that reproduces and explains results obtained by experiments. There, a sample is scanned for one-particle (e.g. photoemission spectroscopy), two-particle (e.g. magnetic susceptibility) or collective excitations with multiple particles (e.g. phonons). But, at the beginning, one has to determine the ground state.

M. Potthoff has proved [101] that the grand potential Ω, one of the fundamental thermodynamical quantities in statistical mechanics, can be expressed as a functional of the self-energy of the system. Furthermore, the stationary points of this functional determine the thermodynamically consistent approximations in a grand canonical ensemble. This principle is called self-energy-functional approach (SFA). A detailed review is given by *M. Potthoff* himself in Ref. [116].

The starting point is an arbitrary Hamiltonian for a system of electrons in an infinite lattice. It can be divided in one-particle and two-particle operators

$$\hat{H} = \underbrace{\hat{H}_0(\mathbf{t})}_{1\mathrm{p}} + \underbrace{\hat{H}_I(\mathbf{U})}_{2\mathrm{p}} , \tag{2.20}$$

where **t** and **U** represent sets of parameters. In general, the elementary excitations of a system are described by Green's functions. For fermionic systems, it is defined in the Matsubara formalism

$$\begin{aligned} G_{\alpha\beta}(i\omega) &= \ll \hat{A}_\alpha ; \hat{B}_\beta \gg_{i\omega} = \frac{1}{2} \int_{-\infty}^{+\infty} G_{\alpha\beta}(\tau) \mathrm{e}^{\mathrm{i}\omega\tau} \mathrm{d}\tau \\ &= -\frac{1}{2} \int_{-\infty}^{+\infty} \langle \hat{T}_\tau \{ \hat{A}_\alpha(\tau) \hat{B}_\beta(0) \} \rangle \mathrm{e}^{\mathrm{i}\omega\tau} \mathrm{d}\tau, \qquad \mathrm{i}\omega_n = \mathrm{i}(2n+1)\pi T,\ n \in \mathbb{Z}. \end{aligned} \tag{2.21}$$

Here, $\hat{A}$ and $\hat{B}$ represent fermionic creation and annihilation operators in the imaginary-time Heisenberg representation $\hat{A}(\tau) = \mathrm{e}^{+H\tau} \hat{A} \mathrm{e}^{-H\tau}$ and $\mathrm{i}\omega$ are fermionic Matsubara frequencies. The Green's function can be rewritten in the Lehmann representation

$$G_{\alpha\beta}(\mathrm{i}\omega_n) = \sum_m \frac{\langle \Psi_0 | \hat{A}_\alpha | \Phi_m \rangle \langle \Phi_m | \hat{B}_\beta^\dagger | \Psi_0 \rangle}{\mathrm{i}\omega_n - (E_m - E_0)} , \tag{2.22}$$

an expansion in the overlap between the ground state $|\Psi_0\rangle$ and the excited states $|\Phi_m\rangle$, under the influence of the operators $\hat{A}_\alpha$ and $\hat{B}_\beta^\dagger$. The Dyson equation [117] (graphical represented in Fig. 2.9)

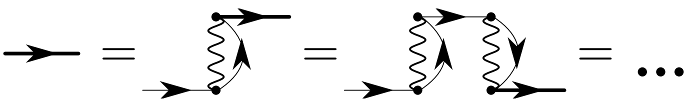

Figure 2.9: Diagrammatic representation of the Dyson equation for first-order vacuum self-energies. The bold lines indicate fully dressed Green's functions and the thin ones illustrate non-interacting Green's functions. The wiggly lines represent interactions. The figure shows the recursive nature of definition. However, in the general Dyson equation, the first-order vacuum self-energy can be replaced by any irreducible self-energy insertion, what, for simplicity, is omitted in this figure.

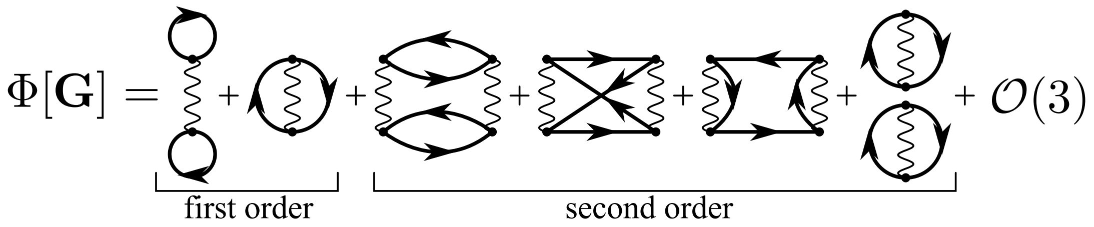

Figure 2.10: Diagrammatic representation of the Luttinger-Ward functional as an infinite series of skeleton diagrams. The bold lines indicate fully dressed Green's functions and the wiggly ones represent interactions. In this figure, only Feynman diagrams of first and second order are shown.

$$\begin{aligned} \mathbf{G}(\omega) &= \mathbf{G}_0(\omega)\,\mathbf{\Sigma}(\omega)\,\mathbf{G}(\omega) \\ \mathbf{G}^{-1}(\omega) &= \mathbf{G}_0^{-1}(\omega) - \mathbf{\Sigma}(\omega) \end{aligned} \tag{2.23}$$

describes the relation between the fully dressed Green's function of an interacting system $\mathbf{G}$ to the bare Green's function of a free system $\mathbf{G}_0(\omega) = \frac{1}{\omega+\mu-\mathbf{t}}$ and the self-energy $\mathbf{\Sigma}$, i.e. the interactions of the particles with themselves. It can be calculated by the derivation of the Luttinger-Ward functional $\Phi[\mathbf{G}]$ [118] (plotted in Fig. 2.10)

$$\mathbf{\Sigma}[\mathbf{G}] = \beta\frac{\partial\Phi[\mathbf{G}]}{\partial\mathbf{G}}\ . \tag{2.24}$$

$\Phi[\mathbf{G}]$ has no explicit dependence on one-particle parameters t. If two systems have the same two-particle parameters U, they are described by the *same* Luttinger-Ward functional [118]. By a Legendre transform, one obtains

$$\begin{aligned} F[\mathbf{\Sigma}] &= \Phi[\mathbf{G}[\mathbf{\Sigma}]] - \mathrm{Tr}(\mathbf{\Sigma}\mathbf{G}[\mathbf{\Sigma}]) \\ \Rightarrow \mathbf{G}[\mathbf{\Sigma}] &= \beta\frac{\partial F[\mathbf{\Sigma}]}{\partial\mathbf{\Sigma}}. \end{aligned} \tag{2.25}$$

On the other hand, the grand potential is given by

$$\Omega_{\mathbf{t}}[\mathbf{\Sigma}] = \mathrm{Tr}(\ln(\,-\mathbf{G})) + F[\mathbf{\Sigma}] = \mathrm{Tr}(\ln(\,-(\mathbf{G}_0^{-1} - \mathbf{\Sigma})^{-1})) + F[\mathbf{\Sigma}]\ , \tag{2.26}$$

with $\mathrm{Tr}(\mathbf{A}) = \frac{1}{\beta}\sum_{\omega,\alpha} A_{\alpha\alpha}(i\omega)$ and a fixed one-particle parameter set $\mathbf{t}$. Performing the derivative of Eq. 2.26 with respect to $\mathbf{\Sigma}$ and using Eq. 2.25,

$$\begin{aligned} \frac{\partial\Omega_{\mathbf{t}}[\mathbf{\Sigma}]}{\partial\mathbf{\Sigma}} &= \frac{\partial}{\partial\mathbf{\Sigma}}\mathrm{Tr}\left(\ln(-(\mathbf{G}_0^{-1} - \mathbf{\Sigma})^{-1})\right) + \frac{\partial}{\partial\mathbf{\Sigma}}\,F[\mathbf{\Sigma}] \\ &= -\frac{1}{\beta}(\mathbf{G}_0^{-1} - \mathbf{\Sigma})^{-1} + \frac{1}{\beta}\mathbf{G}[\mathbf{\Sigma}] \end{aligned} \tag{2.27}$$

one obtains at a stationary point:

$$\frac{\partial \Omega_{\mathbf{t}}[\mathbf{\Sigma}]}{\partial \mathbf{\Sigma}} = 0 \quad \Longleftrightarrow \quad \mathbf{G}[\mathbf{\Sigma}] = (\mathbf{G}_0^{-1} - \mathbf{\Sigma})^{-1} \tag{2.28}$$

Comparing this result with the Dyson equation (Eq. 2.23), the equality is obvious. So, only at a stationary point of $\Omega_t[\mathbf{\Sigma}]$, the Dyson equation is valid. Consequently, if $\Omega_t[\mathbf{\Sigma}]$ is completely known, the ground state can be calculated by a derivative with respect to $\mathbf{\Sigma}$.

Up to now, no approximation was used. Hence, the SFA is an exact theory. But for an arbitrary system, the exact functional $\Omega_t[\mathbf{\Sigma}]$ depends in general on an infinite number of diagrams [118], so an approximation is needed: If the phase space of $\mathbf{\Sigma}$ is reduced to a small subset, a stationary point of $\Omega_t[\mathbf{\Sigma}]$ is the closest approximation to $\mathbf{\Sigma}$ within this subset [106]. A possible reduction is to tile up the infinite lattice in small clusters which can be solved exactly, whereby $\mathbf{\Sigma}$ is limited to a small reference system. All correlation effects are exact up to the cluster-length scale but only mean-field-like beyond this point [106]. An arbitrary reference system has to feature the same two-particle operators $\mathbf{U}$ as the infinite-lattice system but may differ in one-particle operators $\mathbf{t'}$

$$\hat{H}' = \hat{H}_0(\mathbf{t'}) + \hat{H}_I(\mathbf{U}) \tag{2.29}$$

because two distinct systems must include the same two-particle operators $\mathbf{U}$ to share the same Luttinger-Ward functional. Consequently, Ω of the reference system is an implicit function of $\mathbf{t'}$:

$$\Omega_{\mathbf{t'}}[\mathbf{\Sigma}(\mathbf{t'})] = \mathrm{Tr}\left(\ln(-(\mathbf{G'}_0^{-1} - \mathbf{\Sigma}(\mathbf{t'}))^{-1})\right) + F[\mathbf{\Sigma}(\mathbf{t'})] \tag{2.30}$$

A general feature of the Luttinger-Ward functional is its independence of $\mathbf{t}$ [118]. Thus, also in the Legendre-transformed form holds $F[\mathbf{\Sigma}(\mathbf{t})] = F[\mathbf{\Sigma}(\mathbf{t'})]$. By subtracting Eq. 2.30 from Eq. 2.26

$$\Omega_{\mathbf{t}}[\mathbf{\Sigma}] - \Omega_{\mathbf{t'}}[\mathbf{\Sigma}(\mathbf{t'})] = \mathrm{Tr}\left(\ln(-(\mathbf{G}_0^{-1} - \mathbf{\Sigma})^{-1})\right) - \mathrm{Tr}\left(\ln(-(\mathbf{G'}_0^{-1} - \mathbf{\Sigma}(\mathbf{t'}))^{-1})\right) \ , \tag{2.31}$$

the unknown Luttinger-Ward functional is eliminated. Consequently, one can use the Dyson equation (Eq. 2.23) for both the infinite lattice and the reference system:

$$\boxed{\Omega_{\mathbf{t}}[\mathbf{\Sigma}] = \Omega' + \mathrm{Tr}\left(\ln(-\mathbf{G})\right) - \mathrm{Tr}\left(\ln(-\mathbf{G'})\right)} \tag{2.32}$$

Here, the abbreviation $\Omega_{\mathbf{t'}}[\mathbf{\Sigma}(\mathbf{t'})] = \Omega'$ is used for the grand potential in the reference system. By varying $\mathbf{t'}$ over a reasonable range and testing for stationary points

$$\left.\frac{\partial \Omega_{\mathbf{t}}[\mathbf{\Sigma}(\mathbf{t'})]}{\partial \mathbf{t'}}\right|_{\mathbf{t}_{\mathrm{stat}}} = 0 \quad \Longleftrightarrow \quad \mathbf{t}_{\mathrm{stat}} = \mathbf{t'} \ , \tag{2.33}$$

the best approximations of the infinite lattice can be found. This method is called variational cluster approach (VCA). It is important to stress that $\mathbf{t'}$ is not necessarily a hopping parameter but an arbitrary set of one-particle operators. This is a great advantage to other cluster approximations like the CPT [99] because it enables to include fictional

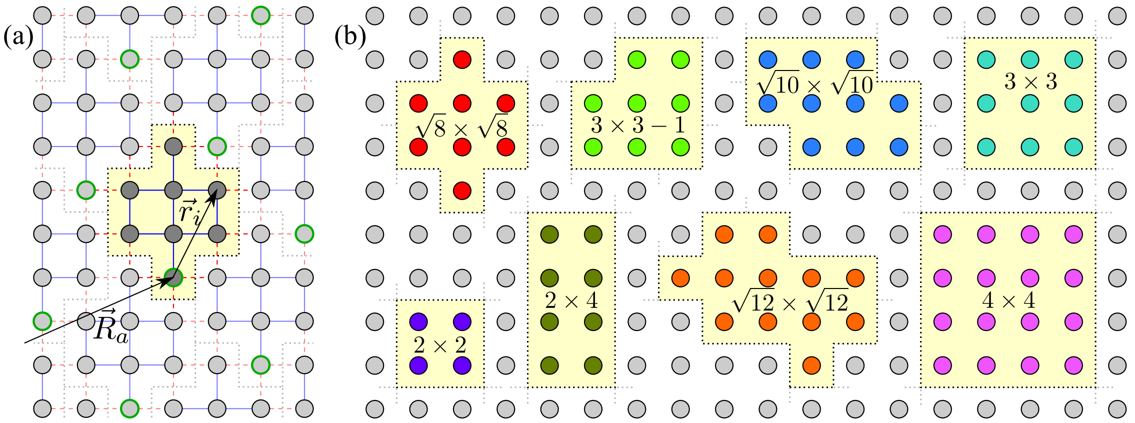

Figure 2.11: Clustering of the lattice: **(a)** Example with a $\sqrt{8}\times\sqrt{8}$ cluster. The hopping within a cluster is exactly calculated (blue solid lines), while the hopping between the clusters is perturbatively calculated (red dashed lines). A lattice site is given by the cluster vector $\vec{R}_a$ plus the vector within the cluster $\vec{r}_i$. The whole lattice is covered with clusters. The $\vec{R}_a$ (marked by sites with green borders) define a regular superlattice. **(b)** Examples for other possible clusters fragmentations.

symmetry-breaking Weiss fields, which yield a consistent description of long-range orders, e.g. antiferromagnetism and superconductivity (see also Sec. 2.4.3).

In the thermodynamical limit, the reference system fills the whole lattice and, consequently, this approach becomes exact. But by enlarging the reference cluster, the complexity and dimension of the Hamiltonian is exponentially growing, so a compromise between size and accuracy is needed.

The addends in Eq. 2.32 are calculated in App. A.2. The result is

$$\begin{aligned}\Omega_{\mathbf{t}}[\mathbf{\Sigma}] &= \Omega' + \mathrm{Tr}\left(\ln(-\mathbf{G})\right) - \mathrm{Tr}\left(\ln(-\mathbf{G'})\right)\\ \Omega_{2L_c} &= \lim_{\beta\to+\infty}\frac{\Omega_{\mathbf{t}}[\mathbf{\Sigma}]}{2L_c} = \frac{E_0}{2L_c} - \sum_m \omega_m\Theta(-\omega_m) + \sum_m \omega'_m\Theta(-\omega'_m)\end{aligned} \tag{2.34}$$

with the ground-state energy E_0, the one-particle excitation energies of the reference system ω'_m and of the infinite lattice ω_m. The Heavyside step function $\Theta(x)$ is 1 for $x > 0$ and otherwise 0. L_c is the number of sites in the reference cluster.

In the next sections, I will explain how this formalism is applied to calculate a (multiband) Hubbard model.

2.4.2 Solving the Reference Cluster

For the VCA, the reference cluster has to be solved exactly. The size of this cluster should be as large as possible to reduce the systematic errors of the VCA because only correlations within this cluster are fully considered. The upper bound of sites within the cluster is set be technical limits (see below). Some examples of possible cluster fragmentations are given in Fig. 2.11.

In this thesis, I focus on $T = 0$K (for a finite temperature implementation of the VCA, see Ref. [119]). Here, the ground state is clear without ambiguity. Starting with the basic time-independent Schrödinger equation

$$\hat{H}|\Psi_n\rangle = E_n|\Psi_n\rangle \tag{2.35}$$

with a Hamiltonian $\hat{H}$ for the reference cluster (Eq. 2.29), the lowest eigenvalue E_0 is the ground-state energy. The corresponding eigenvectors $|\Psi_0\rangle$ determine the ground-state configuration. It is reasonable to expand the eigenvectors in a base which is easy accessible. Let $|\Psi_{s,t}\rangle$ be elements of a complete orthonormal base with $\sum_s |\Phi_s\rangle\langle\Phi_s| = 1$ and $\langle\Phi_s|\Phi_t\rangle = \delta_{st}$. In this base, the energy of an arbitrary state $|\Psi_n\rangle$ reads

$$\begin{aligned} & \langle\Psi_n|\hat{H}|\Psi_n\rangle = \langle\Psi_n|E_n|\Psi_n\rangle \\ \Rightarrow \quad & E_n = \frac{\langle\Psi_n|\hat{H}|\Psi_n\rangle}{\langle\Psi_n|\Psi_n\rangle} = \frac{\sum\limits_{s,t}\langle\Psi_n|\Phi_s\rangle\langle\Phi_s|\hat{H}|\Phi_t\rangle\langle\Phi_t|\Psi_n\rangle}{\langle\Psi_n|\Psi_n\rangle} = \frac{\sum\limits_{s,t}\mathbf{U}_{ns}\langle\Phi_s|\hat{H}|\Phi_t\rangle\mathbf{U}^T_{nt}}{\langle\Psi_n|\Psi_n\rangle} \,. \end{aligned} \tag{2.36}$$

A suitable base is the electronic configuration on the lattice sites of the cluster, where an electron occupation of $\{0,\uparrow,\downarrow,\uparrow\downarrow\}$ is possible. So, the full Hilbert space has 4^{L_c} elements, with L_c being the number of sites in the cluster. Eq. 2.36 shows that the calculation of the state energies corresponds to the diagonalization of a matrix containing $\langle\Phi_s|\hat{H}|\Phi_t\rangle$ as the (s,t)-element. The transformation matrix $\mathbf{U}$ comprises the state configurations for the energies. Then, the state with the lowest energy is the ground state. The size of the Hilbert space is growing with 4^{L_c}, hence it is natural to use computers for the calculation of Eq. 2.36. After the definition of a representation for $\{0,\uparrow,\downarrow,\uparrow\downarrow\}$ and an application of the Hamiltonian $\hat{H}$, the result is a $4^{L_c}\times 4^{L_c}$ matrix with the elements $\langle\Phi_s|\hat{H}|\Phi_t\rangle$. To get the ground state and its energy, this matrix has to be diagonalized, but the use of symmetries like particle and spin conservation is impossible because the focus is on symmetry-broken phases, e.g. antiferromagnetism and superconductivity. Only for clusters with $L_c \leq 4$, a complete diagonalization is possible within an appropriate amount of CPU time. For $L_c > 4$, I used the Lanczos algorithm [120], which starts with a random state and converges to the ground state within an iterative procedure. In detail, the algorithm does not evaluate all eigenvalues but only M ones, but these are most probably the lowest ones, with no degeneracies included. I used $M = 150$, so the lowest eigenvalue, which is the ground-state energy, is certainly covered. This reduces $\mathbf{U}$ from dimension $4^{L_c}\times 4^{L_c}$ to $M\times 4^{L_c}$. Unfortunately, for $L_c > 10$ this algorithm also exceeds the resources of an ordinary personal computer and a large national computer center has to be used. For this thesis, I was awarded with CPU time at the *Leibniz-Rechenzentrum* in Garching (Germany). There, it is possible to use a reference cluster with up to 15 sites.

Beside of the ground state, the one-particle excited states are needed to calculate the Green's functions (Eq. 2.22) and the grand potential (Eq. 2.34). These states are highly degenerate, so the ordinary Lanczos algorithm is inappropriate. The solution is the modified band-Lanczos algorithm [121], which supports N (degenerate) starting vectors. This allows a two step implementation: Firstly, the ground state is calculated within the simple-Lanczos algorithm by starting with a random state. Secondly, the one-particle creation and annihilation operators are applied for all L_c sites and both spins in this ground state, resulting in $4L_c$ starting vectors for the band-Lanczos algorithm. This iterative procedure yields $4M$ excited states, with degeneracies included. Similar to the normal Lanczos algorithm, these energies are most probably the lowest ones.

Up to now, all physics are restricted to a small reference cluster. This is equal to the exact diagonalization method and has the consequence that no long-range order is possible. Also, the limited cluster size L_c in the real space is reflected in the momentum space, so only L_c momenta are accessible in the Brillouin zone and comparisons with experimental data is hard. The variational principle of the VCA opens a self-consistent route for an extrapolation to the infinite lattice.

2.4.3 Extrapolation to Lattice

The VCA formalism is a powerful tool to project the properties of the reference cluster to the infinite lattice, but the distinct Hamiltonian in Eq. 2.20 has to be considered: While the one-particle operators, e.g. hopping between sites, can differ between these two observation levels, the two-particle operators, e.g. Coulomb interaction, are forced to be identical (see the Luttinger-Ward potential, Eq. 2.24). This is a radical restriction for the Coulomb interaction because only on-site interactions can be included. For interactions which range to nearest neighbors and further away, the cluster boundaries are a drawback: In Fig. 2.11a, the clusters are put side by side, covering the whole lattice without holes, but the nearest-neighbor interactions between neighbors marked by red dashed lines are disregarded. Consequently, the reference cluster and the infinite lattice include distinct two-particle Hamiltonians, which is not permitted in the VCA. A possible fix of this problem is a mean-field decoupling of the non-local interactions in one-particle operators [109] or a generalized Luttinger-Ward functional [122].

Another ansatz is the use of periodic boundary conditions. Again, the propagated reference clusters differ from the lattice on the two-particle operator level, but, although long-range correlations between clusters are still neglected, the correlations within the cluster are considered to be more homogeneous. I will use this approximation for the non-local interaction U_{pd} in the three-band model in Sec. 3.2. In this case, the approximation is justified because the non-local interaction U_{pd} is much smaller than the on-site interactions U_{dd} and U_{pp}.

The argument that the nearest-neighbor properties of the side-by-side reference clusters and the infinite lattice are different is also valid for the hopping operators. But these are one-particle operators, so they do not have to be identical on the cluster and lattice level. The hopping operator can be divided in a part $\hat{H}_{0,\text{intra}}(a)$, which describes hoppings within a reference cluster at position $\vec{R}_a$, and $\hat{H}_{0,\text{inter}}(a,b)$, for hoppings between two reference cluster at positions $\vec{R}_a$ and $\vec{R}_b$:

$$\begin{aligned}\hat{H}_{0,\text{intra}}(a) &= \sum_{\substack{i,j\\ i\neq j}}\sum_{\sigma} t_{ij}\left(\hat{c}^{\dagger}_{ai\sigma}\hat{c}_{aj\sigma}+\text{H.c.}\right)\\ \hat{H}_{0,\text{inter}}(a,b) &= \sum_{i,j}\sum_{\sigma} V_{aibj}\left(\hat{c}^{\dagger}_{ai\sigma}\hat{c}_{bj\sigma}+\text{H.c.}\right)\ , \quad \text{with } V_{aibj}=0 \text{ if } a=b\ .\end{aligned} \tag{2.37}$$

Indeed, this distribution can be generalized to all one-particle operators, while the two-particle operators have to be restricted to the cluster. Together, the Hamiltonian reads

$$\hat{H} = \underbrace{\underbrace{\sum_{a} \left(\hat{H}_{0,\mathrm{intra}}(a) + \hat{H}_{I}(a)\right)}_{\text{reference cluster}} + \sum_{a,b} \left(\hat{H}_{0,\mathrm{inter}}(a,b)\right)}_{\text{lattice}} \ . \tag{2.38}$$

The first part of Eq. 2.38 acts only on the reference cluster, while both addends together describe the whole lattice. Hence, if the addends are applied one by one, the primary step gets the physics of the side-by-side reference clusters, while the second step adds the connections between the clusters. Without a change to Eq. 2.38, an additional operator $\hat{\Delta}(a)$ can be appended to Eq. 2.37, so that

$$\begin{aligned} \hat{H}_{0,\mathrm{intra}}(a) &= \sum_{\substack{i,j \\ i \neq j}} \sum_{\sigma} t_{ij} \left(\hat{c}^{\dagger}_{ai\sigma} \hat{c}_{aj\sigma} + \mathrm{H.c.} \right) + \hat{\Delta}(a) \\ \hat{H}_{0,\mathrm{inter}}(a,b) &= \sum_{i,j} \sum_{\sigma} V_{aibj} \left(\hat{c}^{\dagger}_{ai\sigma} \hat{c}_{bj\sigma} + \mathrm{H.c.} \right) - \delta_{a,b} \hat{\Delta}(a) \ . \end{aligned} \tag{2.39}$$

In a simple picture, this extra operator is added to the reference-cluster level, and later subtracted. Hence, it does not exist on the lattice level. Within the SFA, the operator $\hat{\Delta}(a)$ expands the test space of Eq. 2.33, so an even more suitable reference cluster can be found because $\Omega[\mathbf{\Sigma}(\Delta)]$ is optimized at a stationary point. The additional operator reads in a general form

$$\hat{\Delta}(a) = \sum_{i,j} \sum_{\sigma} \Delta_{ij} \left(\hat{c}^{(\dagger)}_{ai\sigma} \hat{c}^{(\dagger)}_{aj\sigma} + \mathrm{H.c.} \right) \ , \tag{2.40}$$

where $\hat{c}^{(\dagger)}$ indicates that also anomalous combinations of creation/annihilation operators, are allowed. However, the most important restriction is that only intracluster operators are permitted.

Indeed, more than one of this so-called variational parameters are allowed. This opens manifold possibilities for improving and verifying the reference cluster to get a more realistic picture of the lattice.

A simple example is the question of periodic or open boundary conditions on the cluster level. While other techniques like the cluster perturbation theory are not able to clarify this point, it is possible to add a periodic boundary hopping t_{pbc} as a variational parameter to the Hamiltonian within the VCA. For a quadratic lattice, the optimization process yields that the alone stationary point exists at $t_{\mathrm{pbc}} = 0$, so a reference cluster with open boundary conditions fits best to the infinite quadratic lattice [123, 124].

Within the VCA, the optimized reference cluster is the best fit to the lattice. If there are some long-range order tendencies in the lattice, a reference cluster is still to small to evolve this order. But the right choice of $\hat{\Delta}(a)$ allows to "suggest" some orders on the reference-cluster level. If this new order fits to a long-range order present on the lattice level, the VCA yields a stationary point at a non-zero field. Hence, the additional variational parameter $\hat{\Delta}(a)$ plays the role of symmetry-breaking Weiss fields [105, 106], which act only on the reference-cluster level and do not exist on the lattice level. Consequently, no additional physics are attached, but rather the test space for the variations of the reference cluster is expanded. In general, the bigger the cluster, the easier it is to break the symmetry. Thus, the optimal Weiss field tends towards zero as the cluster size goes to infinity [104]. Two examples for these Weiss fields are a staggered magnetic field for antiferromagnetism and a pairing field for superconductivity (see Sec. 3.2 for an implementation in the three-band Hubbard model). Indeed, it is impossible to detect orders that are not included in $\hat{\Delta}(a)$.

Many experiments get results in the momentum space, e.g. angle-resolved photoemission spectroscopy (ARPES), but the reference cluster is solved in real space (see the Hamiltonian in Eq. 2.38). Thus, a Fourier transform has to be applied, but in the VCA, the location of a site is given by the position of the cluster $\vec{R}_a$ plus the position of the site within this cluster $\vec{r}_i$. While the Fourier transform with respect to $\vec{R}_a$ is easy, the challenge is the second transformation from a "mixed" representation to a complete momentum-space one. In other words, the broken translational invariance of the lattice has to be restored. The solutions are a diagonalization of the Green's functions [125] or the periodization of the self-energy [126, 127].

The limited size of the reference cluster provokes a discontinuous particle density on doping. For example, the $\sqrt{8} \times \sqrt{8}$ cluster in Fig. 2.11 with 8 particles is half filled, but the next filling with 6 particles correspond to 25% doping (nothing but $S^z = 0$ configurations are considered for the ground state). If the lattice doping is set to 15%, which is close to the optimal hole doping for cuprate superconductors [12], the cluster is in a superposition of the half-filled and a 25%-doped state, which is a good approximation. A further improvement is the implementation of so-called *bath sites* [128, 129], where the interaction is neglected and only a hopping t_b between them and fully correlated sites is allowed. The bath sites act as a kind of "particle reservoir", adjusting the doping level of the reference cluster to the one of the lattice. The hopping t_b, called hybridization, and the chemical potential on the bath sites ε_b are additional variational parameters which contain only one-particle operators, so the conditions for $\hat{\Delta}(a)$ are fulfilled. Unfortunately, the two extra parameters have to be optimized together with the already included variational parameters. This enormously increases the numerical effort, so bath sites are omitted in this thesis.

Finally, there exist some cases where the VCA is exact:

- The reference-cluster size is $L_c \to \infty$: Here, the reference cluster becomes the lattice, so the self-energies are identical.

- All hoppings are prohibited: Then, all lattice sites decouple and the self-energy is local.

- No interactions are included: Both the self-energy of the reference cluster and the one of the lattice are zero.

The optimal playground for the VCA are systems with interactions which are greater than or equal to the bandwidth.

2.4.4 Two-Particle Excitations

Whereas the one-particle excitations can be easily calculated within the VCA procedure (Eq. 2.34), the two-particle excitations are a tricky problem. In his PhD-Thesis, *S. Brehm* presented a parameter-free theory for an expansion of the VCA to two-particle excitations [125]. He implemented the calculation of the transversal spin susceptibility to get the magnetic-excitation spectrum. The results for the hole-doped one-band model were published in Ref. [113]. In this section, I will follow his derivation of the theory but will include all necessary upgrades for multiband models.

The central idea is to use the two-particle equivalent of the Dyson equation (Eq. 2.23), called four-point Bethe-Salpeter equation [130], which reads

$$\begin{aligned} L(R_1,R_2,R_3,R_4) = \sum_{\vec{r}_{\text{int}},\alpha_{\text{int}}} \int \mathrm{d}\tau_{\text{int}}\, & L_0(R_1,R_2,R_3,R_4) \\ & + L_0(R_1,R_2,R_5,R_6)\; \Gamma(R_5,R_6,R_7,R_8)\; L(R_7,R_8,R_3,R_4)\ , \end{aligned} \tag{2.41}$$

with L being an arbitrary two-particle response function and Γ as an irreducible four-point vertex. L_0 represents a response function without vertex insertion, which is equivalent to two distinct fully dressed one-particle Green's functions. The indices are notated in $R_i = (\vec{r}_i, \alpha_i, \tau_i)$, which indicates site $\vec{r}_i$, orbital α_i and time τ_i. The integral has to be executed over all internal times $\mathrm{d}\tau_{\text{int}} = \mathrm{d}\tau_5 \mathrm{d}\tau_6 \mathrm{d}\tau_7 \mathrm{d}\tau_8$ and the sum is over all internal sites $\vec{r}_{\text{int}} = \{\vec{r}_5, \vec{r}_6, \vec{r}_7, \vec{r}_8\}$ and orbital degrees of freedom $\alpha_{\text{int}} = \{\alpha_5, \alpha_6, \alpha_7, \alpha_8\}$. A diagrammatic representation of the Bethe-Salpeter equation is given in Fig. 2.12a. Due to momentum end energy conservation, the equation is reduced to three internal sites and times but not orbitals. Thus, another combined index $r_i = (\vec{r}_i, \tau_i)$ is introduced, including the position vector and an imaginary time. In Chap. 3, the magnetic excitations of cuprates are considered, so the response function is specified to be the transversal spin susceptibility, which reads

$$\begin{aligned} \chi_{\alpha_i\beta_i\alpha_j\beta_j}(\vec{r}_i,\tau_i,\vec{r}_j,\tau_j) &= \langle \hat{S}^{+}_{i\alpha_i\beta_i}(\tau_i)\; \hat{S}^{-}_{j\alpha_j\beta_j}(\tau_j) \rangle \\ &= \langle \mathrm{e}^{\hat{H}\tau_1} \hat{c}^{\dagger}_{i\alpha_i\uparrow} \hat{c}_{i\beta_i\downarrow} \mathrm{e}^{-\hat{H}\tau_1}\; \mathrm{e}^{\hat{H}\tau_2} \hat{c}^{\dagger}_{j\alpha_j\downarrow} \hat{c}_{j\beta_j\uparrow} \mathrm{e}^{-\hat{H}\tau_2} \rangle \\ L(\underbrace{R_1}_{\vec{r}_1,\tau_1,\alpha_1}, \underbrace{R_2}_{\vec{r}_2,\tau_2,\alpha_2}, \underbrace{R_3}_{\vec{r}_3,\tau_3,\alpha_3}, \underbrace{R_4}_{\vec{r}_4,\tau_4,\alpha_4}) &\rightarrow \chi_{\alpha_1\beta_1\alpha_3\beta_3}(\underbrace{r_1}_{\vec{r}_1,\tau_1}, \underbrace{r_3}_{\vec{r}_3,\tau_3}) \end{aligned} \tag{2.42}$$

with the diagrammatic representation given in Fig. 2.12b. Here, the ingoing sites and times have to be identical, while the orbitals are still independent. The same holds for the outgoing parameters.

In a first approximation, the complexity of the internal integration and summation is reduced by averaging over the internal degrees of freedom [125], which was successfully applied in finite-T single-cluster quantum Monte Carlo calculations [131] as well as two-particle susceptibility calculations within the dynamical cluster approximation (DCA) [132]. The resulting response function

$$\begin{aligned} &\chi_{\alpha_1\beta_1\alpha_2\beta_2}(r_1,r_2) = \chi_{0,\alpha_1\beta_1\alpha_2\beta_2}(r_1,r_2) + \\ &\quad \sum_{\vec{r}_3\vec{r}_4} \sum_{\substack{\alpha_3\alpha_4 \\ \beta_3\beta_4}} \int \mathrm{d}\tau_3 \mathrm{d}\tau_4\; \chi_{0,\alpha_1\beta_1\alpha_3\beta_3}(r_1,r_3)\; \tilde{\Gamma}_{\alpha_3,\beta_3,\alpha_4,\beta_4}(r_3,r_4)\; \chi_{\alpha_4\beta_4\alpha_2\beta_2}(r_4,r_2) \end{aligned} \tag{2.43}$$

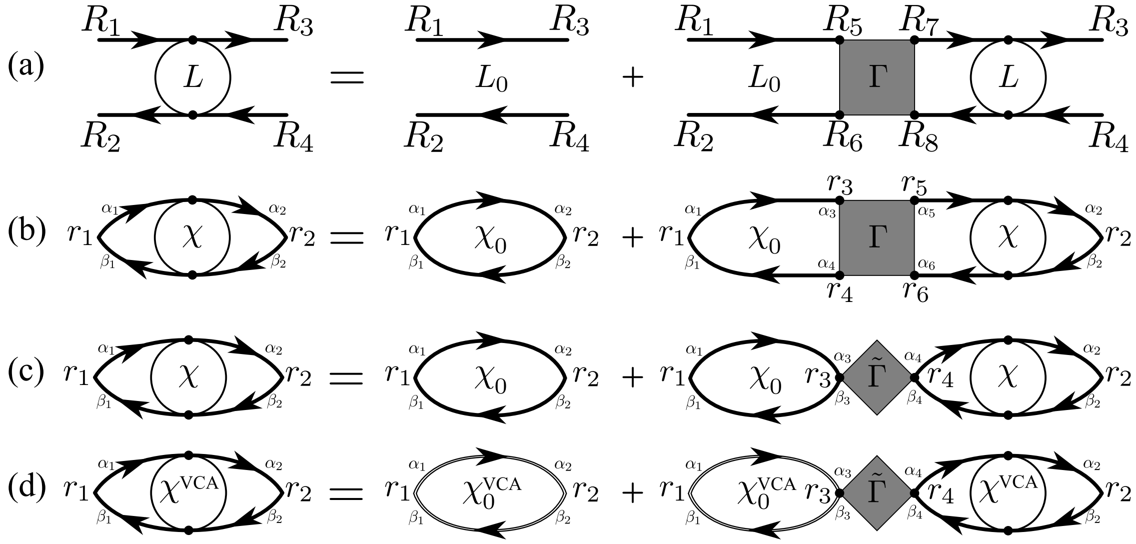

Figure 2.12: **(a)** Diagrammatic representation of the Bethe-Salpeter equation with an arbitrary response function L and the irreducible particle-hole vertex Γ. L_0 marks two distinct fully dressed Green's functions, which are indicated by bold lines. The combined indices include $R_i = (\vec{r}_i, \alpha_i, \tau_i)$ and $r_i = (\vec{r}_i, \tau_i)$, respectively. Here, the recursive nature of the general Bethe-Salpeter equation is obvious. **(b)** Special case of the spin susceptibility χ and **(c)** after the averaging over the internal degrees of freedom. **(d)** The double lines indicate fully dressed one-particle Green's functions which are obtained by the VCA.

is plotted in Fig. 2.12c. However, the orbital degrees of freedom are not affected by this approximation. For the calculation within the VCA, the clustering of the lattice has to be considered. As stated in the previous section, the position vector of an arbitrary site $\vec{r}_i$ is split into a vector of the superlattice $\vec{R}_a$ plus a vector within the cluster $\vec{r}_i'$. The translational invariance counts only for the superlattice, while it is broken in the cluster. The Fourier transform in the superlattice reads

$$\chi_{\alpha_i\beta_i\alpha_j\beta_j}(\vec{q}, \mathrm{i}\omega_m^b) = \frac{1}{N}\sum_{\vec{R}_1\vec{R}_2}\int \mathrm{d}\tau_1\mathrm{d}\tau_2\chi_{\alpha_i\beta_i\alpha_j\beta_j}(\vec{R}_1, \tau_1, \vec{R}_2, \tau_2)\cdot \mathrm{e}^{\mathrm{i}\vec{q}(\vec{R}_2-\vec{R}_1)-\mathrm{i}\omega_m^b(\tau_2-\tau_1)} . \tag{2.44}$$

The ω_m^b indicate bosonic Matsubara frequencies. This transformation can be applied to an arbitrary site and yields

$$\begin{aligned}\chi_{\alpha_i\beta_i\alpha_j\beta_j}(r_i, r_j) &\to \chi_{\alpha_i\beta_i\alpha_j\beta_j}(\vec{R}_a + \vec{r}_i', \tau_i, \vec{R}_b + \vec{r}_j', \tau_j)\\ &\to \chi_{i\alpha_i\beta_i, j\alpha_j\beta_j}(\vec{R}_a, \tau_i, \vec{R}_b, \tau_j) \mathrel{\hat{=}} \boldsymbol{\chi}(\vec{R}_a, \tau_i, \vec{R}_b, \tau_j)\\ &\overset{\text{F.T.}}{\Rightarrow} \boldsymbol{\chi}(\vec{q}, \mathrm{i}\omega_m^b),\end{aligned} \tag{2.45}$$

with the bold $\boldsymbol{\chi}$ indicating a matrix. Here, the arguments of $\boldsymbol{\chi}$ are in momentum space, while the matrix indices represent sites (and orbitals) in real space. The dimension of $\boldsymbol{\chi}$ is $\dim(\boldsymbol{\chi}) = L_c \cdot L_o^2 \times L_c \cdot L_o^2$, with L_c being the reference-cluster size and L_o the number of orbitals per site. The wave vector $\vec{q}$ is element of the reduced Brillouin zone of the superlattice. In this "mixed" representation, the Bethe-Salpeter equation (Eq. 2.43) is rewritten to

$$\boldsymbol{\chi}(\vec{q},\mathrm{i}\omega_m^b) = \boldsymbol{\chi}_0(\vec{q},\mathrm{i}\omega_m^b) + \boldsymbol{\chi}_0(\vec{q},\mathrm{i}\omega_m^b)\,\tilde{\boldsymbol{\Gamma}}(\vec{q},\mathrm{i}\omega_m^b)\,\boldsymbol{\chi}(\vec{q},\mathrm{i}\omega_m^b)\,. \tag{2.46}$$

To restore the full translational invariance, a Fourier transform with respect to the reference-cluster sites is done. Here, only diagonal elements are taken into account. For details, see Ref. [125].

In the random phase approximation (RPA), the fully dressed Green's functions are approximated by the Green's functions of the non-interacting system, hence it is restricted to the weak-coupling limit. But here, the fully dressed one-particle Green's functions are already available within the VCA technique (see last section for Details). Hence, the expectation value of the transversal spin susceptibility is rewritten to a product of Green's functions ("bubble approximation" [71, 74, 77]) and reads

$$\begin{aligned}
&\langle \mathrm{T}\,\hat{S}^{+}_{i\alpha_i\beta_i}(\tau)\,\hat{S}^{-}_{j\alpha_j\beta_j}(0)\rangle \\
&\qquad= \langle \mathrm{T}\,\hat{c}^{\dagger}_{i\alpha_i\uparrow}(\tau)\hat{c}_{i\beta_i\downarrow}(\tau)\,\hat{c}^{\dagger}_{j\alpha_j\downarrow}(0)\hat{c}_{j\beta_j\uparrow}(0)\rangle \\
&\qquad\approx \langle \mathrm{T}\,\hat{c}^{\dagger}_{i\alpha_i\uparrow}(\tau)\hat{c}_{j\beta_j\uparrow}(0)\rangle\langle \mathrm{T}\,\hat{c}_{i\beta_i\downarrow}(\tau)\hat{c}^{\dagger}_{j\alpha_j\downarrow}(0)\rangle \\
&\qquad\quad - \langle \mathrm{T}\,\hat{c}^{\dagger}_{i\alpha_i\uparrow}(\tau)\hat{c}^{\dagger}_{j\alpha_j\downarrow}(0)\rangle\langle \mathrm{T}\,\hat{c}_{i\beta_i\downarrow}(\tau)\hat{c}_{j\beta_j\uparrow}(0)\rangle \\
&\qquad= -\langle \mathrm{T}\,\hat{c}_{j\beta_j\uparrow}(0)\hat{c}^{\dagger}_{i\alpha_i\uparrow}(\tau)\rangle\langle \mathrm{T}\,\hat{c}_{i\beta_i\downarrow}(\tau)\hat{c}^{\dagger}_{j\alpha_j\downarrow}(0)\rangle \\
&\qquad\quad - \langle \mathrm{T}\,\hat{c}^{\dagger}_{i\alpha_i\uparrow}(\tau)\hat{c}^{\dagger}_{j\alpha_j\downarrow}(0)\rangle\langle \mathrm{T}\,\hat{c}_{i\beta_i\downarrow}(\tau)\hat{c}_{j\beta_j\uparrow}(0)\rangle \\
&\qquad= -G_{j\beta_j i\alpha_i\uparrow}(-\tau)\,G_{i\beta_i j\alpha_j\downarrow}(\tau) - F_{i\alpha_i j\alpha_j\uparrow\downarrow}(\tau)\,F^{*}_{j\beta_j i\beta_i\uparrow\downarrow}(-\tau)\,,
\end{aligned} \tag{2.47}$$

with the definitions

$$\begin{aligned}
G_{j\beta_j i\alpha_i\uparrow}(-\tau) &= -\langle \mathrm{T}\,\hat{c}_{j\beta_j\uparrow}(0)\hat{c}^{\dagger}_{i\alpha_i\uparrow}(\tau)\rangle \\
F_{i\alpha_i j\alpha_j\uparrow\downarrow}(\tau) &= \langle \mathrm{T}\,\hat{c}^{\dagger}_{i\alpha_i\uparrow}(\tau)\hat{c}^{\dagger}_{j\alpha_j\downarrow}(0)\rangle
\end{aligned} \tag{2.48}$$

for the normal Green's function G and the anomalous Green's function F, which can be calculated by the VCA and already include correlated physics on a one-particle level (Figs. 2.12d). If no superconducting Weiss-field is included in the Hamiltonian, the system has a particle number conservation (see Sec. 2.4.3 for details). In this case, the anomalous Green's functions are $F = 0$. After the Fourier transform

$$\begin{aligned}
\chi^{\mathrm{VCA}}_{0,i\alpha_i\beta_i j\alpha_j\beta_j}(\vec{q},\mathrm{i}\omega_m^b) = -\frac{T}{N_c}\sum_n\sum_{\vec{k}} \Big(& G^{\mathrm{VCA}}_{j\beta_j i\alpha_i\uparrow}(\vec{k},\mathrm{i}\omega_n^f)G^{\mathrm{VCA}}_{i\beta_i j\alpha_j\downarrow}(\vec{k}+\vec{q},\mathrm{i}\omega_n^f+\mathrm{i}\omega_m^b) \\
&+ F^{\mathrm{VCA}}_{i\alpha_i j\alpha_j\uparrow\downarrow}(\vec{q}-\vec{k},\mathrm{i}\omega_m^b-\mathrm{i}\omega_n^f)\,F^{*,\mathrm{VCA}}_{j\beta_j i\beta_i\uparrow\downarrow}(\vec{k},\mathrm{i}\omega_n^f)\Big)\,,
\end{aligned} \tag{2.49}$$

the susceptibility is again in a mixed representation. Here, N_c is the number of reference clusters in the lattice. This result can be included in Eq. 2.46, yielding

$$\boldsymbol{\chi}(\vec{q},\mathrm{i}\omega_m^b) = \boldsymbol{\chi}_0^{\mathrm{VCA}}(\vec{q},\mathrm{i}\omega_m^b) + \boldsymbol{\chi}_0^{\mathrm{VCA}}(\vec{q},\mathrm{i}\omega_m^b)\,\tilde{\boldsymbol{\Gamma}}(\vec{q},\mathrm{i}\omega_m^b)\,\boldsymbol{\chi}(\vec{q},\mathrm{i}\omega_m^b)\,. \tag{2.50}$$

In this equation, the vertex $\tilde{\boldsymbol{\Gamma}}$ is still unknown, hence an approximation for the four-point vertex is needed. In the RPA, it is simply approximated by the interaction U. However, in retrospect, one of the fundamental ideas of the VCA is to approximate the self-energy of the lattice by the self-energy of the reference cluster. Within the SFA framework, the optimization principle provides the best approach in the variational one-particle parameter space. By rephrasing this idea, the two-particle irreducible vertex function of the infinite lattice is approximated by the cluster equivalent, so

$$\begin{aligned}\tilde{\boldsymbol{\Gamma}}(\vec{q},\mathrm{i}\omega_m^b) &= \left(\boldsymbol{\chi}_0^{\mathrm{VCA}}(\vec{q},\mathrm{i}\omega_m^b)\right)^{-1} - \left(\boldsymbol{\chi}(\vec{q},\mathrm{i}\omega_m^b)\right)^{-1} \\ &\approx \\ \boldsymbol{\Gamma}^{\mathrm{eff}}(\vec{q},\mathrm{i}\omega_m^b) &= \left(\boldsymbol{\chi}_0^{c}(\vec{q},\mathrm{i}\omega_m^b)\right)^{-1} - \left(\boldsymbol{\chi}^{c}(\vec{q},\mathrm{i}\omega_m^b)\right)^{-1} ,\end{aligned} \tag{2.51}$$

with $\boldsymbol{\chi}_0^c$ and $\boldsymbol{\chi}^c$ being obtained on the reference-cluster level. While $\boldsymbol{\chi}_0^c$ consists of fully dressed one-particle cluster Green's functions, $\boldsymbol{\chi}^c$ is calculated by a slightly modified Lehmann representation (Eq. 2.22), where $\hat{A}$ and $\hat{B}$ are replaced by $\hat{S}^+_{i\alpha_i\beta_i}$ and $\hat{S}^-_{j\alpha_j\beta_i}$. This can be evaluated straightforwardly, comparable to the one-particle excitations. Certainly, the restriction of the vertex to the reference cluster works fine as long as the dominating two-particle correlation functions are shorter ranged than the cluster size. A possible check for the quality of the approximation provides the sum rule

$$\frac{T}{N}\sum_{\vec{q}}\sum_{m}\chi_{i\alpha_i\beta_i i\alpha_j\beta_j}(\vec{q},\mathrm{i}\omega_m^b) = \langle \hat{S}^+_{i\alpha_i\beta_i}\hat{S}^-_{i\alpha_j\beta_j}\rangle \ . \tag{2.52}$$

Both sides can be calculated independently. Consequently, if the results match together, the approximation is justified.

Furthermore, by introducing a constant prefactor α to $\boldsymbol{\Gamma}^{\mathrm{eff}}(\vec{q},\mathrm{i}\omega_m^b)$ in Eq. 2.51, the sum rule in Eq. 2.52 is forced to be fulfilled [133]. In other words, α scales $\boldsymbol{\Gamma}^{\mathrm{eff}}$, so $\tilde{\boldsymbol{\Gamma}}$ is better approximated.

It is important to stress that the additional parameter α is **not** a free parameter, but it has to be self-consistently evaluated within the VCA.

The final version of the transversal spin susceptibility equation reads

$$\begin{aligned}\boldsymbol{\chi}(\vec{q},\mathrm{i}\omega_m^b) &= \left(\mathbb{1} - \boldsymbol{\chi}_0^{\mathrm{VCA}}(\vec{q},\mathrm{i}\omega_m^b)\,\tilde{\boldsymbol{\Gamma}}(\vec{q},\mathrm{i}\omega_m^b)\right)^{-1} \boldsymbol{\chi}_0^{\mathrm{VCA}}(\vec{q},\mathrm{i}\omega_m^b) \\ \boldsymbol{\chi}(\vec{q},\mathrm{i}\omega_m^b) &= \left(\mathbb{1} - \boldsymbol{\chi}_0^{\mathrm{VCA}}(\vec{q},\mathrm{i}\omega_m^b)\,\alpha\left(\left(\boldsymbol{\chi}_0^{c}(\vec{q},\mathrm{i}\omega_m^b)\right)^{-1} - \left(\boldsymbol{\chi}^{c}(\vec{q},\mathrm{i}\omega_m^b)\right)^{-1}\right)\right)^{-1} \boldsymbol{\chi}_0^{\mathrm{VCA}}(\vec{q},\mathrm{i}\omega_m^b)\end{aligned} \tag{2.53}$$

Further details of the numerical implementation of the formalism introduced in this section are presented in Ref. [125] for the one-band Hamiltonian. In almost the same manner, the three-band equations can be modified to calculate the longitudinal spin susceptibility or the charge susceptibility. In general, this formalism is not restricted to $T = 0$, but the VCA implementation I used is limited to absolute zero (see Sec. 2.4.2 for details). In opposite, in Ref. [132], the DCA is expanded to two-particle excitations at finite temperatures with a similar approximation based on the Bethe-Salpeter equation, which enables the calculation of a temperature-dependent phase diagram.

In addition, if the self-constantly calculated constant α is close to 1, the selected reference system is a suitable choice to represent the physics in the lattice. Otherwise, the two-particle correlation functions act on a length scale larger than the cluster size. A possible fix is to increase the reference-cluster size. On the other hand, if the doping level is increased, the scattering between particles is enforced, so the correlation length of two-particle excitations is reduced. In both cases, α approaches 1 [113]. Also, a stronger coupling reduces the effective range of interactions and, consequently, the appropriate reference-cluster size. For the three-band model in Sec. 3.2, the controlling constant was calculated to $\alpha = 1.03$, so the effective vertex approximation is justified.

2.4.5 Gap Function for Superconductivity

In general, the self-energy reflects the interaction of the particles among themselves and, due to the Dyson equation (Eq. 2.23), depends on the Green's functions of electrons. If the two operators $\hat{A}$ and $\hat{B}$ in Eq. 2.21 are both creation operators $\hat{c}^\dagger$, the Green's function is anomalous. Accordingly, two annihilation operators $\hat{c}$ are also possible. Thus, the anomalous Green's functions correspond to Cooper pairs. With the Nambu representation [134], the general Green's function is rewritten to a 2×2 block-matrix which includes both normal and anomalous contributions. Consequently, the self-energy also features an anomalous part, which corresponds to the pairing strength and dynamics of the Cooper pairs. Hence, to describe the pairing dynamics of the system, the Dyson equation (Eq. 2.23) can be rewritten to

$$\begin{pmatrix} \mathbf{G}^{cc^\dagger} & \mathbf{G}^{c^\dagger c^\dagger} \\ \mathbf{G}^{cc} & \mathbf{G}^{c^\dagger c} \end{pmatrix}^{-1} = \begin{pmatrix} \mathbf{G}_0^{cc^\dagger} & 0 \\ 0 & \mathbf{G}_0^{c^\dagger c} \end{pmatrix}^{-1} - \begin{pmatrix} \boldsymbol{\Sigma}^{cc^\dagger} & \boldsymbol{\Sigma}^{c^\dagger c^\dagger} \\ \boldsymbol{\Sigma}^{cc} & \boldsymbol{\Sigma}^{c^\dagger c} \end{pmatrix} . \tag{2.54}$$

It is $\mathbf{G}_0^{c^\dagger c^\dagger} = \mathbf{G}_0^{cc} = 0$ because the interaction-free system does not include any pairing fields. After some algebra, the equation can be dissolved to the anomalous part of the self-energy:

$$\begin{aligned} \begin{pmatrix} \boldsymbol{\Sigma}^{cc^\dagger} & \boldsymbol{\Sigma}^{c^\dagger c^\dagger} \\ \boldsymbol{\Sigma}^{cc} & \boldsymbol{\Sigma}^{c^\dagger c} \end{pmatrix} &= \begin{pmatrix} \left(\mathbf{G}_0^{cc^\dagger}\right)^{-1} & 0 \\ 0 & \left(\mathbf{G}_0^{c^\dagger c}\right)^{-1} \end{pmatrix} - \begin{pmatrix} \mathbf{G}^{cc^\dagger} & \mathbf{G}^{c^\dagger c^\dagger} \\ \mathbf{G}^{cc} & \mathbf{G}^{c^\dagger c} \end{pmatrix}^{-1} \\ \boldsymbol{\Sigma}^{c^\dagger c^\dagger} &= 0 - \left(\begin{pmatrix} \mathbf{G}^{cc^\dagger} & \mathbf{G}^{c^\dagger c^\dagger} \\ \mathbf{G}^{cc} & \mathbf{G}^{c^\dagger c} \end{pmatrix}^{-1} \right)_{\begin{smallmatrix} \square & \blacksquare \\ \square & \square \end{smallmatrix}} \end{aligned} \tag{2.55}$$

Here, $\begin{smallmatrix} \square & \blacksquare \\ \square & \square \end{smallmatrix}$ indicates that only the upper right quarter of the block-matrix has to be considered. Finally, the gap function $\phi(\vec{k}, \omega)$ is defined as the anomalous part of the self-energy, after a Fourier transform to momentum space:

$$\phi(\vec{k}, \omega) = \sum_{ij} \Sigma_{ij}^{c^\dagger c^\dagger}(\omega)\ \mathrm{e}^{\mathrm{i}(\vec{r}_i - \vec{r}_j)\vec{k}} \tag{2.56}$$

This result is used in Sec. 3.6 for the interpretation of the pairing dynamics of the Hubbard model for cuprates. There, the comparison of the one-band model (Mott insulator) and the three-band model (charge-transfer insulator) yield discrepancies in the pairing dynamics. The VCA implementation of both models is suitable for the strongly correlated cuprates, but simulations of weak-coupling materials need another theoretical framework.

2.5 Analytical Renormalization Group at Infinitesimal Coupling

Over the last century, a myriad of methods to describe condensed-matter physics have been developed. Together with the rise of supercomputers, numerical simulations became more important and provided powerful tools to answer open questions. Both in the strong-coupling ansatz of the variational cluster approach (VCA, Sec. 2.4) and the weak-coupling approach of the functional renormalization group (fRG, Sec. 2.6) there are many competing phases, resulting in a colorful phase diagram. However, if the focus is just on superconductivity, elaborate techniques are redundant. In this case, the analytical renormalization group (aRG) is a suitable approximation.

This section provides the technical background of the aRG. It will be used to investigate the effects of long-range interactions to the superconducting instability in the honeycomb and the kagome lattice, respectively. The results are presented in Chap. 6.

2.5.1 Basic Concept and Formalism

The aRG is a perturbative approach to Fermi-liquid instabilities subject to an infinitesimal interaction. Hence, the main generic instability found therein is superconductivity [135]. Initiated by *W. Kohn* and *J.M. Luttinger* [136], this has become an established tool for electronically driven superconducting Fermi-surface instabilities, and has been formulated more rigorously by *S. Raghu et al.* [135, 137]. In the limit of infinitesimal interactions, this approach is identical to the functional renormalization group scheme, introduced in Sec. 2.6.

In this ansatz, only the two-particle vertex Γ is investigated. Concerning the infinitesimal-coupling limit, all self-energy effects and higher-particle vertices can be neglected (this argument is discussed in detail for the fRG in Sec. 2.6.3). At low temperatures, the pairing susceptibility in the superconducting channel is logarithmically diverging for infinitesimally interacting Fermi liquids, ignoring the shape of the Fermi surface (FS) [19]. The only instability that is generically nested for arbitrary kinetic theories conserving inversion symmetry $\vec{k} \to -\vec{k}$ is the Cooper channel, so the focus is on this instability. For this purpose, one has to consider all possible diagrams up to second order in the interaction which contribute to the Cooper channel. These are illustrated in Fig. 2.13. The notation of straight lines already suggests that the interaction vertex (dashed line) conserves spin, i.e. it is spin-rotationally invariant.

It is important to stress that this ansatz is not equivalent to RPA-type summations. To obtain the perturbative vertex $\Gamma(\vec{k}_1\sigma, -\vec{k}_1\tau, \vec{k}_2\sigma, -\vec{k}_2\tau)$, one has to sum over all six diagrams depicted in Fig. 2.13. The FS is discretized in N patches (equivalent to fRG, see Fig. 2.19), so the vertex Γ is mapped to an $N \times N$ matrix. Numerically, one momentum at

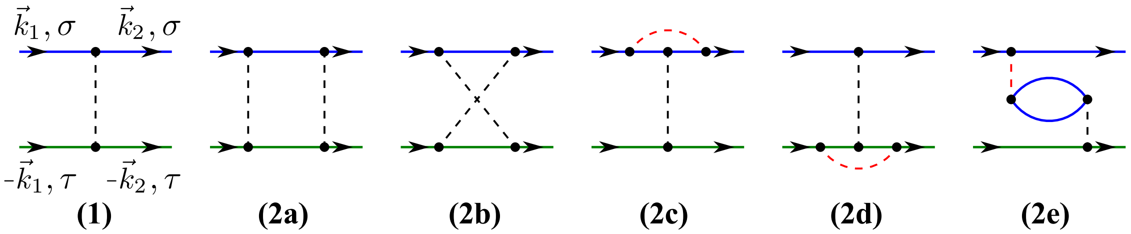

Figure 2.13: Diagrammatic expansion up to second order of plaquet diagrams in the cooper channel. Continuous propagator lines indicate conserved spin. For the $S_z = 0$ sector in spin-rotationally invariant scenarios, the spins can be set to $\sigma = \uparrow$ (blue lines) and $\tau = \downarrow$ (green lines), without loss of generality. For a strictly local interaction, the interaction vertices (dashed lines) can only connect propagators with antiparallel spins. This is violated in the diagrams **(2c)**, **(2d)** and **(2e)**, indicated by red dashed lines. Hence, these diagrams have to be omitted if the interaction is local.

the FS represents all momenta on this patch. The regularized vertex reads

$$g_{\vec{k}_1,\vec{k}_2} := \rho \frac{\bar{v}}{\sqrt{v(\vec{k}_1)\, v(\vec{k}_2)}} \Gamma(\vec{k}_1\sigma, -\vec{k}_1\tau, \vec{k}_2\sigma, -\vec{k}_2\tau) \,, \tag{2.57}$$

where ρ is the total density of states at the Fermi level, $v(\vec{k})$ is the Fermi velocity at momentum $\vec{k}$ and $\bar{v}$ is the harmonic mean-averaged Fermi velocity defined as

$$\frac{1}{\bar{v}} = \int \frac{\mathrm{d}\hat{k}}{l_F} \frac{1}{v_F(\hat{k})} \,, \tag{2.58}$$

where the integral is performed as a line integral along the FS, indicated by the $\hat{k}$ notation. l_F is the linear length of the given FS and accordingly the normalization for this line integral. The external variables for the Γ function are the values $\vec{k}_1$ and $\vec{k}_2$. In this discretized $N \times N$ representation, the eigenfunction system of g read

$$\sum_{\vec{p}} \frac{\delta l_F(\vec{p})}{l_F} g_{\vec{k},\vec{p}} \theta^n_{\vec{p}} = \lambda^n \theta^n_{\vec{k}} \,, \tag{2.59}$$

with $n = \{1, \ldots, N\}$. $\delta l_F(\vec{p})$ is the size of the line element from one patch of the Brillouin zone. This prefactor ensures that the eigenvalues λ become invariant under the discretization N. A negative eigenvalue signals an instability towards superconductivity. The lowest eigenvalue $\lambda^n_c := \min[\lambda^n]$ is the critical one with the associated superconducting form factor $\Delta(\vec{k}) = \theta^n_{c,\vec{k}}$ and

$$T_c \sim W \mathrm{e}^{-\frac{1}{|\lambda|}} \,, \tag{2.60}$$

with the bandwidth W of the kinetic theory. Formally, an infrared cutoff Ω_0 at the Fermi level is required to avoid divergences, which, at the same time, for local Hubbard U_0, should reside in the regime

$$W \mathrm{e}^{-\frac{1}{\rho U_0}} < \Omega_0 < \frac{U_0^2}{W} \tag{2.61}$$

to make the infinitesimal-coupling formulation independent of Ω_0. The bounds are derived from above constraints imposed on the perturbative diagrams [135]. The exponential IR bound of the cutoff ensures a broad regime in units of U where the aRG is formally applicable. Assuming that U is still the leading or at least jointly leading interaction energy scale, this line of reasoning does not change for long-range interactions.

The numerical effort to compute the perturbative diagrams can largely be reduced by the following assumptions, listed with decreasing generality:

1. From infinitesimal coupling, there follows the limitation to the diagrams in Fig. 2.13 and a constraint to the Cooper channel.
2. From spin-rotational invariance of the interaction, it follows that the diagrams only carry two spin indices and the propagators represent lines of conserved spin.
3. From spin-rotational invariance of the kinetic theory and (2.), one can go even further and suppress all spin dependencies of the vertex because both the triplet and the singlet channel are located in the $S_z = 0$ sector, so one can assume without loss of generality that $\sigma = \uparrow$ and $\tau = \downarrow$ and suppress the spin notation in Γ. Then, the singlet and triplet channel is simply obtained by

$$\Gamma^{s,t} = \frac{1}{2}\left(\Gamma(\vec{k}_1, -\vec{k}_1, \vec{k}_2, -\vec{k}_2) \mp \Gamma(-\vec{k}_1, \vec{k}_1, \vec{k}_2, -\vec{k}_2)\right) \ . \tag{2.62}$$

   Accordingly, the lowest eigenvalue has to be picked considering both the singlet and triplet channel.
4. The focus is on single-band physics at the Fermi level. Hence, also the band index of the propagators are suppressed, assuming the relevant electron to be located in the band that forms the FS. Otherwise the vertex would carry 4 band indices.

Furthermore, if the interaction is strictly local ($U_0 \sim \hat{n}_{i\uparrow}\hat{n}_{i\downarrow}$), there exist an additional constraint to the diagrams in Fig. 2.13 because only propagator lines with antiparallel spins can be connected, which excludes the diagrams **(2c)**, **(2d)** and **(2e)**. Hence, the range of the interaction has to be carefully considered.

2.5.2 Interaction and Long-Range Scenario

As stated in the latter section, the long-range Hubbard interaction is set to be spin-rotationally invariant (see also [2]). To distinguish the short-range from the long-range scenario, the on-site Hubbard term is separated from the long-range part:

$$V = U_0 + U_> \tag{2.63}$$

This is required because the local part of the interaction is suppressed in diagrams **(2c)**, **(2d)** and **(2e)** of Fig. 2.13 and needs a special treatment.

Physically, diagram **(1)** is the lowest order in V of this perturbative ansatz. Given that V represents energy scales constrained to the bounds in Eq. 2.61, it is also the dominant diagram as it is linear in V. Exactly as in the work by *W. Kohn* and *J.M. Luttinger* [136], diagram **(1)** effectively acts as a projector to a certain null space where the other diagrams can form superconducting instabilities. For illustration, diagram **(1)** of U_0 in an otherwise trivial single-pocket FS effectively acts like a finite energy projector on the $\vec{k}$-featureless s-wave solution of Γ. In matrix notation, diagram **(1)** would then give $\Gamma_{i,j} = U_0$ and hence assign $\lambda^N = U_0$ to the s-wave susceptibility $\Theta^N_{\vec{k}} \sim \rho$ and $\lambda^n = 0$ for $n = 1,\ldots,N-1$. This is a very intuitive way to see that any superconducting instability in infinitesimally correlated systems has to form within the susceptibility null space spanned by diagram **(1)**, which for U_0 would be the coset space of the s-wave channel. The inspection of diagram **(2a)** yields that the result is form-invariant to diagram **(1)**. In addition, if $U_> \ll U_0$, diagram **(2a)** is negligible, and also otherwise diagram **(2a)** only renormalizes diagram **(1)** by an order of V/W. Consequently, diagram **(2a)** never has to be explicitly considered. The joint effect of diagram **(1)** and diagram **(2a)** hence is to project the susceptibility onto the null space of diagram **(1)**.

The first diagram in Fig. 2.13 gives the notation of order of arguments for the vertex function: First both ingoing momenta, then both outgoing momenta, where the order is such that the first ingoing and first outgoing are linked along the same propagation line. The sign of the diagrams can be obtained by a prefactor

$$(-1)^{\#_V+\#_G+\#_L+1}\,, \tag{2.64}$$

with the number of interaction vertices $\#_V$, the number of internal Green's functions $\#_G$, the number of closed fermion loops $\#_L$ and a 1 from the action ($\int \mathrm{D}\, \mathrm{e}^{-S_0-S'}$). Altogether, this yields

$$\begin{aligned}
\mathbf{(1)} &= V(\vec{k}_1,-\vec{k}_1,\vec{k}_2,-\vec{k}_2)\\
\mathbf{(2a)} &= -\int\limits_{\vec{p}} V(\vec{k}_1,-\vec{k}_1,\vec{p},-\vec{p})\; V(\vec{p},-\vec{p},\vec{k}_2,-\vec{k}_2)\; \mathcal{G}_{\vec{p}}\; \mathcal{G}_{-\vec{p}}\\
\mathbf{(2b)} &= -\int\limits_{\vec{p}} V(\vec{p},-\vec{k}_1,\vec{k}_2,\vec{p}-\vec{k}_1-\vec{k}_2)\; V(\vec{k}_1,\vec{p}-\vec{k}_1-\vec{k}_2,\vec{p},-\vec{k}_2)\; \mathcal{G}_{\vec{p}}\; \mathcal{G}_{\vec{p}-\vec{k}_1-\vec{k}_2}\\
\mathbf{(2c)} &= -\int\limits_{\vec{p}} V(\vec{p},-\vec{k}_1,\vec{p}-\vec{k}_1+\vec{k}_2,-\vec{k}_2)\; V_>(\vec{k}_1,\vec{p}-\vec{k}_1+\vec{k}_2,\vec{p},\vec{k}_2)\; \mathcal{G}_{\vec{p}}\; \mathcal{G}_{\vec{p}-\vec{k}_1+\vec{k}_2}\\
\mathbf{(2d)} &= -\int\limits_{\vec{p}} V(\vec{k}_1,\vec{p},\vec{k}_2,\vec{p}+\vec{k}_1-\vec{k}_2)\; V_>(-\vec{k}_1,\vec{p}+\vec{k}_1-\vec{k}_2,\vec{p},-\vec{k}_2)\; \mathcal{G}_{\vec{p}}\; \mathcal{G}_{\vec{p}+\vec{k}_1-\vec{k}_2}\\
\mathbf{(2e)} &= -\int\limits_{\vec{p}} \Big(V_0(\vec{p}+\vec{k}_1-\vec{k}_2,-\vec{k}_1,\vec{p},-\vec{k}_2)\; V_>(\vec{k}_1,\vec{p},\vec{k}_2,\vec{p}+\vec{k}_1-\vec{k}_2)\; \mathcal{G}_{\vec{p}}\; \mathcal{G}_{\vec{p}+\vec{k}_1-\vec{k}_2}\\
&\qquad -2V_>(\vec{p}+\vec{k}_1-\vec{k}_2,-\vec{k}_1,\vec{p},-\vec{k}_2)\; V_>(\vec{k}_1,\vec{p},\vec{k}_2,\vec{p}+\vec{k}_1-\vec{k}_2)\; \mathcal{G}_{\vec{p}}\; \mathcal{G}_{\vec{p}+\vec{k}_1-\vec{k}_2}\Big)\,,
\end{aligned} \tag{2.65}$$

where

$$\int\limits_{\vec{p}} := \int \frac{\mathrm{d}\omega\, \mathrm{d}^2 p}{(2\pi)^3} \tag{2.66}$$

and

$$\mathcal{G}_{\vec{p}} = \frac{1}{\mathrm{i}\omega_p - \varepsilon_{\vec{p}}} \,. \tag{2.67}$$

The reason for the appearance of $V_>$ in **(2c)**, **(2d)** and **(2e)** is discussed above. Also, the fermion loop in **(2e)** is indefinite only if both interaction vertices are of long-range order, so a case differentiation is necessary. As the interactions are assumed static because of the infinitesimal coupling, the frequency integration over the two Green's functions can be easily worked out:

$$\begin{aligned} \int_{\vec{p}} F(\vec{k}_1,\vec{k}_2,\vec{p})\ \mathcal{G}_{\vec{p}}\mathcal{G}_{\vec{p}+\vec{q}} &= \int \frac{\mathrm{d}^2 p}{(2\pi)^2} F(\vec{k}_1,\vec{k}_2,\vec{p}) \frac{n_F(\varepsilon_{\vec{p}+\vec{q}}) - n_F(\varepsilon_{\vec{p}})}{\varepsilon_{\vec{p}+\vec{q}} - \varepsilon_{\vec{p}}} \\ &= \frac{1}{V} \sum_{p_x,p_y} F(\vec{k}_1,\vec{k}_2,\vec{p}) \frac{n_F(\varepsilon_{\vec{p}+\vec{q}}) - n_F(\varepsilon_{\vec{p}})}{\varepsilon_{\vec{p}+\vec{q}} - \varepsilon_{\vec{p}}} \,, \end{aligned} \tag{2.68}$$

for an arbitrary function $F(\vec{k}_1,\vec{k}_2,\vec{p})$ and momentum shift $\vec{q}$. n_F is the Fermi function, which, for $T = 0$, becomes the standard Heavyside step function $n_F(\varepsilon) \to \Theta(\varepsilon_F - \varepsilon)$, and V is the volume of the given system in units of the lattice constant $a = 1$. In a numerical implementation, this V is the number of discretized parcels into which the Brillouin zone is divided. This results in a summation over p_x and p_y, which corresponds to the number of unit cells considered, what is a consequence of the discrete-continuum relation:

$$\int \mathrm{d}x \to \sum_{x_i} a \qquad \text{and} \qquad \int \mathrm{d}k/2\pi \to \sum_{k_i} \frac{1}{L} \,. \tag{2.69}$$

The integral **(2a)** yields a divergence upon frequency integration $\sim \rho \log(W/\Omega_0)$. With Eq. 2.61, this divergence is compensated for.

2.5.3 Numerical Implementation: Short-Range versus Long-Range

As the number of relevant diagrams differs depending on the long-range character of the interactions, it is useful to set up three scenarios for the numerical evaluation of the problem:

1. $V = U_0$
   Firstly, diagram **(2a)** is absorbed in diagram **(1)**. As discussed above, the further diagrams **(2c)**, **(2d)** and **(2e)** are zero. So, only diagram **(1)** is acting as a projector and just diagram **(2b)** has to be computed. Here, the physics of the superconducting instability is to be found.

2. $V = U_0 + U_>,\, U_> \sim U_0/W$
   In the case of small long-range Coulomb interactions, as only the terms quadratic in U are considered, the assumptions of (1.) are still valid. Just the vertex of diagrams **(1)** and **(2b)** should explicitly keep the full V, while all other diagrams are still negligible. Again, diagram **(1)** acts as a projector, so both scenarios (1.) and (2.) differ only by the treatment of diagram **(2b)**.

3. $V = U_0 + U_>, U_> \sim U_0$
   Except of the absorption of diagram **(2a)** in diagram **(1)**, which is still a projector, the diagrams **(2b)**-**(2e)** have to be considered with Eq. 2.65.

With this simple numerical technique, it is possible to evaluate the influence of long-range interactions on the pairing instability.

2.6 Functional Renormalization Group

The crucial factor in condensed-matter physics is the strength of the interaction between the electrons. In addition to the bare Coulomb interaction U between the quasiparticles in the solids, i.e. electrons surrounded by a polarization cloud, also the magnetic interaction $J \sim \frac{t^2}{U}$ plays a key role. These interactions drive phenomena like metal-insulator transition, magnetic orders or unconventional superconductivity. However, while the Coulomb interaction is a few eV, the critical scale for superconductivity is down to some meV, so very different energy scales have to be considered.

An exact and generic solution of condensed-matter physics is impossible, so one has to use approaches and model systems to get an access to the physical properties which can be detected by experiments. For this purpose, the electronic system has to be mapped to a simplified model which includes all relevant degrees of freedom. “It can scarcely be denied that the supreme goal of all theory is to make the irreducible basic elements as simple and as few as possible without having to surrender the adequate representation of a single datum of experience”[1]. Also the size of U compared to the bandwidth W is limiting the practicality of physical approximation methods. An optimal principle has to include (i) a handling of different energy scales at the same time and (ii) an unbiased implementation of various orders. For example, the last statement is violated in the random phase approximation (RPA) [70, 73] because a preselection of Feynman diagrams is executed. But the functional renormalization group (fRG) provides the claimed properties.

> The method combines functional methods of quantum field theory with the intuitive renormalization group idea of *K.G. Wilson*. This technique allows to interpolate smoothly between the known microscopic laws and the complicated macroscopic phenomena in physical systems. In this sense, it bridges the transition from simplicity of microphysics to complexity of macrophysics[2].

In the fRG, Feynman diagrams in various particle channels are summed up at the same time. Hence, there is a competition of several orders and no a priori preselection for a single phase. By integrating out the high-energy degrees of freedom, the underlying low-energy long-range orders can be extracted. Furthermore, the temperature at which the fRG-flow diverges is direct proportional to the critical temperature scale of the instability.

---

[1] Albert Einstein in Philosophy of Science, Vol. 1, No. 2, p. 165 (April 1934)

[2] “Functional renormalization group”from Wikipedia. Wikimedia Foundation, Inc. page version updated on 24 February 2012 at 20:53. ⟨http://en.wikipedia.org/wiki/Functional_renormalization_group⟩

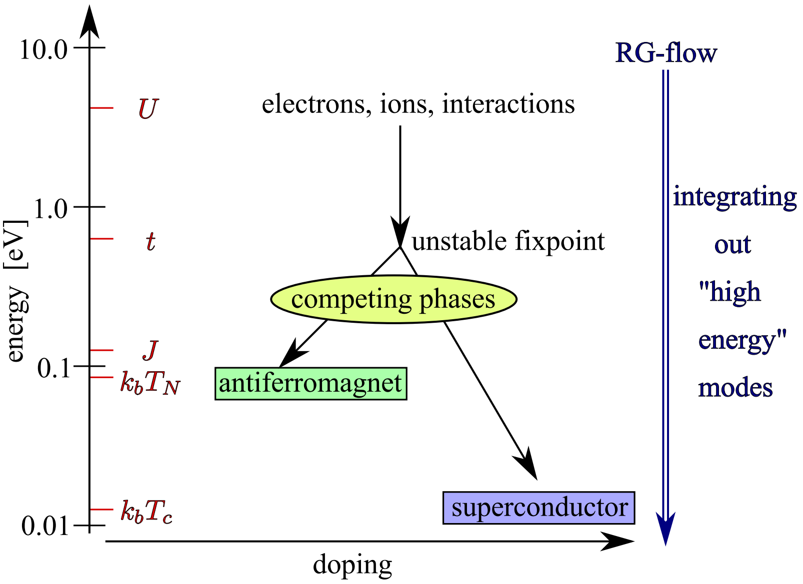

Figure 2.14: Simplified picture of the fRG-flow from high to low energies for hole-doped cuprates (Fig. 1.2). The important energy scales are the Coulomb interaction U, the kinetic energy parameter t (hopping) and the magnetic interaction J. Depending on the doping level, the fRG-flow yields either an antiferromagnetic order at the Néel temperature T_N or superconductivity at the critical temperature T_c.

The first materials studied with the fRG were cuprate superconductors [62, 138, 139]. Although their strong-coupling physics are not the optimal playground for the fRG, the results were quite suitable. But its triumphal procession started when it was applied to new weakly correlated systems. In the last decade, the fRG initially was adopted to the triangular lattice [140] and ruthenates with triplet superconductivity [141]. After the discovery of iron-based high-T_c superconductors, there were a lot of publications on the iron pnictides [46–48, 142–146]. In addition, graphene [147, 148] and an anisotropic triangular lattice [149] are accessible by fRG calculations.

For this thesis, the fRG was applied to NaCoO (three-band model in triangular lattice) in Chap. 4, to graphene (honeycomb lattice) in Chap. 5 and to a generic kagome lattice in Chap. 7. In this section, I give a short overview of the basic concepts of the fRG and the derivation of the flow equations. They define the change of an effective action, driven by the reduction of an external parameter. Here, I focus on the implementation of the "temperature-flow". After this, the handling of some technical problems is discussed. In the conclusion of this section, I give a guide how to interpret the resulting coupling functions. A more detailed review was published recently by *W. Metzner et al.* [150].

2.6.1 Basic Concept: The Flow to Low Energies

To illustrate the basic idea behind the fRG, the cuprate superconductors can serve as an example. The relevant energy scales are plotted in Fig. 2.14, with the Coulomb interaction U between the electrons as the starting point. For cuprates, the common assumption is $U \approx 4\text{eV}$. But the long-range orders form at a lower energy scale, where

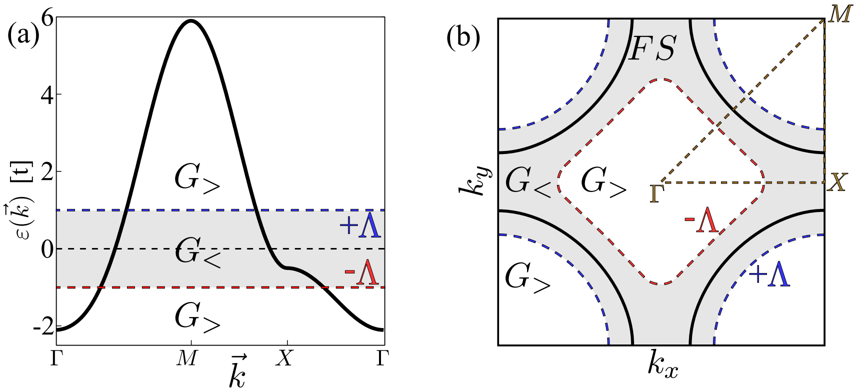

Figure 2.15: **(a)** The cutoff energy ±Λ divides the band structure in slow modes $G_<$ and fast modes $G_>$. The modes at ±Λ are integrated out and subsequently becoming fast modes. **(b)** Corresponding segmentation of the Brillouin zone (BZ).

thermal fluctuations do not disturb them. For this purpose, the high-energy effects have to be "subtracted". For example, the critical temperature below antiferromagnetic order can be formed (Néel temperature) is equivalent to $T_N \approx 0.1$eV, while the superconducting transition temperature is even lower, equivalent to $T_c \approx 0.01$eV. The fRG is a powerful tool that provides an algorithm to systematically "integrate out" the high-energy modes, resulting in a coupling function, which acts as an effective interaction. This low-energy model is appropriate to determine the underlying long-range order of the system. Here, the size and shape of the Fermi surface (FS) plays a crucial role. It is important to stress that there are many competing orders and the fRG does not include any preselection. For example, in the fRG implementation of the cuprates, the result (antiferromagnetism or superconductivity, respectively) is depending on the doping level because it alters the FS and, consequently, the nesting condition.

One implementation of the fRG is based on the division of the band structure and the corresponding Brillouin zone (BZ) into fast modes $G_>$ and slow modes $G_<$, as plotted in Fig. 2.15. The classification follows the cutoff energy Λ. By a set of differential equations ("flow equations"), a small decrease of Λ is evaluated and results in a new effective vertex, which describes the interaction at this lower energy scale. At this step, only the slow modes are fully included, while the modes at Λ are integrated out. The fast modes are neglected but indirectly considered by the coupling function. This fRG-step can be repeated iteratively, so Λ is continuously decreasing and more slow modes are integrated out and become fast modes. The effective vertex is constantly changing, resulting in the fRG-flow of the interaction. As every iterative procedure, the fRG needs a break condition. This happens if the effective vertex is partially diverging, marking the tendency to long-range order in the system. After the decoupling of the effective vertex for various channels in a mean-field treatment, the most dominating order can be extracted. Furthermore, the scale of the critical cutoff energy Λ_c is an upper limit for the critical temperature of the order.

In summary, the fRG provides a simple recipe: At the start, the total band structure is included completely in the slow modes, defining Λ_0. By an iteratively decreasing of Λ, the faster modes are integrated out subsequently, resulting in an effective vertex.

When this coupling function is diverging, the fRG-flow breaks down and the tendency to a long-range order can be extracted. In the old-style Wilson RG, momenta and fields have to be rescaled, while integrating out some degrees of freedom [151]. This is due the fact that the quartic part of the effective action has to be form-invariant under the RG-flow. The functional RG flow equations do not involve any rescaling [150]. Additionally, the complete set of source fields remains included in the ongoing flow of the generating functionals, not only low-energy ones or long wavelength behavior [150].

The division of the propagators in the BZ in slow and fast modes is only one possible implementation of the fRG ("momentum-cutoff-flow"). In general, after a modification of the flow equations, any arbitrary external parameter can be used. Another common implementation is the temperature-flow ("T-flow", see Ref. [139]), and the "frequency-cutoff-flow" [152]. Even an "interaction-flow" was considered [153].

In general, the choice of the flow-parameter depends on regularization of infrared singularities, minimization of truncation errors, respecting symmetries, and technical convenience [150]. Within this thesis, I use the T-flow. The advantages of this implementation will be revealed in the subsequent derivation of the method.

2.6.2 Functional Flow Equations

There are some basic reviews on the renormalization group for fermionic systems [150, 151, 154, 155], particularly Ref. [150] is focusing on state-of-the-art functional RG. In this section, I present the required formalism to derivate the flow equations. As a start, the grand canonical partition function $\mathcal{Z}$ can be rewritten in the functional integral formalism (for details, see Ref. [69, 75])

$$\begin{aligned} \mathcal{Z} &= \int \mathrm{D}\bar{\psi}\mathrm{D}\psi \, \mathrm{e}^{-\mathcal{S}[\bar{\psi},\psi]} \qquad \text{with} \\ \mathrm{D}\bar{\psi}\mathrm{D}\psi &= \lim_{N\to\infty} \prod_{n=1}^{N} \prod_{i} \mathrm{d}\bar{\psi}_i^n \mathrm{d}\psi_i^n \; . \end{aligned} \tag{2.70}$$

In general, the action $\mathcal{S}$ has the form

$$\begin{aligned} \mathcal{S}\left[\psi,\bar{\psi}\right] &= -T \sum\!\!\!\!\!\!\int_{xy} G_0^{-1}(x,y)\; \bar{\psi}(x)\; \psi(y) + T^3 V\left[\psi,\bar{\psi}\right] \qquad \text{with} \\ V\left[\psi,\bar{\psi}\right] &= \frac{1}{4} \sum\!\!\!\!\!\!\int_{\substack{x_1x_2\\y_1y_2}} V(y_1,y_2,x_1,x_2)\; \bar{\psi}(y_1)\; \bar{\psi}(y_2)\; \psi(x_2)\; \psi(x_1) \; , \end{aligned} \tag{2.71}$$

with G_0 being the propagator of the interaction-free system, T the temperature, ψ and $\bar{\psi}$ are Grassmann fields, while x and y are reasonable sets of quantum numbers, including imaginary time or frequency. $\sum\!\!\!\!\!\int$ indicates that an integral or a sum has to be evaluated, depending on a continuous or discrete quantum number, respectively. Furthermore, some additional prefactors like volume are omitted. For simplicity, the temperature T is only mentioned if it is important. By introducing some external source fields η and $\bar{\eta}$, a generating functional

$$\mathcal{F}^G[\eta,\bar{\eta}] = -\ln\left(\int D\psi D\bar{\psi}\; e^{-\mathcal{S}[\psi,\bar{\psi}]}\; e^{\sum\!\!\!\!\!\!\int(\bar{\eta}\psi+\bar{\psi}\eta)}\right) \qquad \text{with} \tag{2.72}$$

$$\mathcal{F}^G[0,0] = -\ln(\mathcal{Z})\ , \qquad \psi = -\frac{\partial\mathcal{F}^G}{\partial\bar{\eta}} \qquad \text{and} \qquad \bar{\psi} = \frac{\partial\mathcal{F}^G}{\partial\eta} \tag{2.73}$$

can be obtained. For the interaction-free system, the partition function of $\mathcal{Z}_0$ is connected to G_0 by

$$\int D\psi D\bar{\psi}\; e^{\sum\!\!\!\!\!\!\int G_0^{-1}\bar{\psi}\psi}\; e^{\sum\!\!\!\!\!\!\int(\bar{\eta}\psi+\bar{\psi}\eta)} = \underbrace{\int D\psi D\bar{\psi}\; e^{\sum\!\!\!\!\!\!\int G_0^{-1}\bar{\psi}\psi}}_{\mathcal{Z}_0}\; e^{-\sum\!\!\!\!\!\!\int G_0^{-1}\bar{\eta}\eta}\ . \tag{2.74}$$

Otherwise, for the interacting system, Eq. 2.73 can be rewritten in a Taylor expansion with connected Green's functions G:

$$\begin{aligned} \mathcal{F}^G[\eta,\bar{\eta}] = &-\ln\mathcal{Z} + \sum\!\!\!\!\!\!\!\int_{xy} G_2(x,y)\;\bar{\eta}(x)\;\eta(y) \\ &+ \frac{1}{(2!)^2}\sum\!\!\!\!\!\!\!\int_{\substack{x_1x_2\\y_1y_2}} G_4(x_1,x_2,y_1,y_2)\;\bar{\eta}(x_1)\;\bar{\eta}(x_2)\;\eta(y_1)\;\eta(y_2) + \ldots \end{aligned} \tag{2.75}$$

To calculate the connected n-particle Green's functions G_{2n}, one has to derivate the generating functional with respect to the source fields:

$$\begin{aligned} G_{2n}(x_1,\ldots,x_n,y_1,\ldots,y_n) &= -\langle\psi(x_1)\ldots\psi(x_n)\;\bar{\psi}(y_n)\ldots\bar{\psi}(y_1)\rangle_c \\ &= (-1)^n \left.\frac{\partial^{2n}\mathcal{F}^G[\eta,\bar{\eta}]}{\partial\bar{\eta}(x_1)\ldots\partial\bar{\eta}(x_n)\;\partial\eta(y_n)\ldots\partial\eta(y_1)}\right|_{\eta=\bar{\eta}=0} \end{aligned} \tag{2.76}$$

Here, $\langle\ldots\rangle_c$ donates the connected average of products of Grassmann variables. Starting from now, the one-particle Green's function G_2 is simply listed by G.

A Legendre transform of $\mathcal{F}^G[\eta,\bar{\eta}]$ (Eq. 2.73) yields the effective action $\mathcal{F}^\Gamma[\psi,\bar{\psi}]$:

$$\mathcal{F}^\Gamma[\psi,\bar{\psi}] = \sum\!\!\!\!\!\!\!\int(\bar{\eta}\psi+\bar{\psi}\eta) + \mathcal{F}^G[\eta,\bar{\eta}] \tag{2.77}$$

The one-particle irreducible vertex functions Γ_{2n} can be accessed by a derivation of the effective action with respect to the fields:

$$\Gamma_{2n}(y_1,\ldots,y_n,x_1,\ldots,x_n) = \left.\frac{\partial^{2n}\mathcal{F}^\Gamma[\psi,\bar{\psi}]}{\partial\bar{\psi}(y_1)\ldots\partial\bar{\psi}(y_n)\;\partial\psi(x_n)\ldots\partial\psi(x_1)}\right|_{\psi=\bar{\psi}=0} \tag{2.78}$$

For example, in an interaction-free system, it holds

$$\mathcal{F}^\Gamma[\psi,\bar{\psi}] = -\ln\mathcal{Z}_0 - \sum\!\!\!\!\!\!\!\int_{xy} G_0^{-1}(x,y)\;\bar{\psi}(x)\;\psi(y)\ . \tag{2.79}$$

The connected n-particle Green's functions G_{2n} consist of all permitted combinations of vertex functions Γ_{2m} with $m \leq n$ which are linked with free propagators. For example, the connected two-particle Green's function

$$G_4(x_1,x_2,y_1,y_2) = \sum\!\!\!\!\!\!\int_{\substack{z_1 z_2\\ z_3 z_4}} G(x_1,z_3)\; G(x_2,z_4)\; \Gamma_4(z_3,z_4,z_1,z_2)\; G(z_1,y_1)\; G(z_2,y_2) \tag{2.80}$$

is depending on the two-particle vertex function and four (one-particle) Green's functions. The functional derivatives of $\mathcal{F}^{\Gamma}$ in first and second order can be written as

$$\frac{\partial \mathcal{F}^{\Gamma}}{\partial \psi} = -\bar{\eta} \qquad \frac{\partial \mathcal{F}^{\Gamma}}{\partial \bar{\psi}} = \eta \tag{2.81}$$

$$\mathbf{F}^{\Gamma,(2)}\left[\psi,\bar{\psi}\right] = \begin{pmatrix} \frac{\partial^2 \mathcal{F}^{\Gamma}}{\partial \bar{\psi}(x)\; \partial \psi(y)} & \frac{\partial^2 \mathcal{F}^{\Gamma}}{\partial \bar{\psi}(x)\; \partial \bar{\psi}(y)} \\ \frac{\partial^2 \mathcal{F}^{\Gamma}}{\partial \psi(x)\; \partial \psi(y)} & \frac{\partial^2 \mathcal{F}^{\Gamma}}{\partial \psi(x)\; \partial \bar{\psi}(y)} \end{pmatrix} := \boldsymbol{\partial}^2 \mathcal{F}^{\Gamma}\,, \tag{2.82}$$

where the second one is abbreviated in a matrix representation. The same is possible for the second derivative of $\mathcal{F}^{G}$:

$$\mathbf{F}^{G,(2)}\left[\eta,\bar{\eta}\right] = -\begin{pmatrix} \frac{\partial^2 \mathcal{F}^{G}}{\partial \bar{\eta}(x)\; \partial \eta(y)} & -\frac{\partial^2 \mathcal{F}^{G}}{\partial \bar{\eta}(x)\; \partial \bar{\eta}(y)} \\ -\frac{\partial^2 \mathcal{F}^{G}}{\partial \eta(x)\; \partial \eta(y)} & \frac{\partial^2 \mathcal{F}^{G}}{\partial \eta(x)\; \partial \bar{\eta}(y)} \end{pmatrix} \tag{2.83}$$

$$\mathbf{F}^{G,(2)}\left[\eta,\bar{\eta}\right] = \left(\mathbf{F}^{\Gamma,(2)}\left[\psi,\bar{\psi}\right]\right)^{-1} \tag{2.84}$$

Another generating functional is the effective interaction [156]

$$\mathcal{F}^{V}\left[\chi,\bar{\chi}\right] = -\ln\left(\frac{1}{\mathcal{Z}_0}\int \mathrm{D}\bar{\psi}\mathrm{D}\psi\; \mathrm{e}^{\sum\!\!\!\!\!\int G_0^{-1}\bar{\psi}\psi}\; \mathrm{e}^{-V[\psi+\chi,\bar{\psi}+\bar{\chi}]}\right)\,, \tag{2.85}$$

with the interaction V as defined in Eq. 2.71 and new fields

$$\chi = G_0(x,y)\;\eta \qquad \text{and} \qquad \bar{\chi} = G_0(y,x)\;\bar{\eta}\;. \tag{2.86}$$

A functional derivation of $\mathcal{F}^{V}\left[\chi,\bar{\chi}\right]$ with respect to the fields χ and $\bar{\chi}$ yields Feynman diagrams without external legs and bare internal propagators [75]. The generating functionals are connected via

$$\mathcal{F}^{V}\left[\chi,\bar{\chi}\right] = \mathcal{F}^{G}\left[\eta,\bar{\eta}\right] + \ln\left(\mathcal{Z}_0\right) - \sum\!\!\!\!\!\!\int \bar{\eta} G_0 \eta\;. \tag{2.87}$$

This can be verified by inserting the substitution $\psi \rightarrow \psi - \chi$ in Eq. 2.85 and using Eq. 2.73. In an interaction-free system, the functional is $\mathcal{F}^{V}\left[\chi,\bar{\chi}\right] = 0$. For the next step, it is useful to introduce the functional Laplacian

$$\Delta_{G_0} = \sum\!\!\!\!\!\!\int_{xy} \frac{\partial}{\partial \chi(x)} G_0(x,y)\; \frac{\partial}{\partial \bar{\chi}(y)}\;. \tag{2.88}$$

With this, the effective interaction

$$\begin{aligned}
\mathrm{e}^{-\mathcal{F}^V[\chi,\bar{\chi}]} &= \frac{1}{\mathcal{Z}_0}\int \mathrm{D}\psi\mathrm{D}\bar{\psi}\; \mathrm{e}^{\sum\!\!\!\!\!\!\int G_0^{-1}\bar{\psi}\psi}\; \mathrm{e}^{-V[\psi+\chi,\bar{\psi}+\bar{\chi}]} \\
&= \frac{1}{\mathcal{Z}_0}\mathrm{e}^{-V\left[\partial_{\bar{\eta}},\partial_{\eta}\right]}\int \mathrm{D}\psi\mathrm{D}\bar{\psi}\; \mathrm{e}^{\sum\!\!\!\!\!\!\int G_0^{-1}\bar{\psi}\psi}\;\; \mathrm{e}^{\sum\!\!\!\!\!\!\int(\bar{\eta}(\psi+\chi)+\eta(\bar{\psi}+\bar{\chi}))}\Big|_{\eta=\bar{\eta}=0} \\
&= \mathrm{e}^{-V\left[\partial_{\bar{\eta}},\partial_{\eta}\right]}\;\; \mathrm{e}^{\sum\!\!\!\!\!\!\int G_0\bar{\eta}\eta}\; \mathrm{e}^{\sum\!\!\!\!\!\!\int(\bar{\eta}\chi+\eta\bar{\chi})}\Big|_{\eta=\bar{\eta}=0} \\
&= \mathrm{e}^{-V\left[\partial_{\bar{\eta}},\partial_{\eta}\right]}\;\; \mathrm{e}^{\sum\!\!\!\!\!\!\int G_0\partial_{\chi}\partial_{\bar{\chi}}}\; \mathrm{e}^{\sum\!\!\!\!\!\!\int(\bar{\eta}\chi+\eta\bar{\chi})}\Big|_{\eta=\bar{\eta}=0} \\
&= \mathrm{e}^{\Delta_{G_0}}\; \mathrm{e}^{-V[\chi,\bar{\chi}]}
\end{aligned} \tag{2.89}$$

can be rewritten into an expression with functional derivatives.

Now, the effective interaction $\mathcal{F}^V\,[\chi,\bar{\chi}]$ has to be calculated. In quantum mechanics, it is a common approach, firstly, to solve the non-interacting part of the system and, thereafter, to switch on the interaction slowly (see Ref. [76]). Here, a similar approach is possible. For that, an external parameter Λ is introduced, so the bare propagator G_0 is modified to

$$G_{0,\Lambda} = \begin{cases} G_0 & \text{for} \quad \Lambda \to 0 \\ 0 & \text{for} \quad \Lambda \to \Lambda_0 \end{cases} . \tag{2.90}$$

Here, Λ_0 is the starting condition for the external parameter. A possible implementation of the external parameter is the cutoff energy Λ_c. In this case, G_0 is modified to

$$G_0(\mathrm{i}\omega_n,\vec{k}) \to G_{0,\Lambda_c}(\mathrm{i}\omega_n,\vec{k}) = \frac{\Theta(|\varepsilon(\vec{k})-\mu|-\Lambda)}{\mathrm{i}\omega_n-(\varepsilon(\vec{k})-\mu)} \tag{2.91}$$

with $\varepsilon(\vec{k})$ being the band energy at momentum $\vec{k}$ and the Heavyside function Θ. In this approximation, the BZ is divided into slow modes and fast modes (see Fig. 2.15 for illustration). Another goal of the introduction of the modified propagator is to suppress infrared singularities and prepare a well-defined route to low energies.

In general, the derivation of the flow equations is not depending on the included external parameter. With the modified propagator $G_{0,\Lambda}$ from Eq. 2.90, Eq. 2.89 becomes

$$\mathrm{e}^{-\mathcal{F}^V_\Lambda[\chi,\bar{\chi}]} = \mathrm{e}^{\Delta_{G_{0,\Lambda}}}\; \mathrm{e}^{-V[\chi,\bar{\chi}]} . \tag{2.92}$$

For a better legibility, the functional dependencies are omitted from now if they are obvious. From Eq. 2.73 and Eq. 2.92 follows that

$$\mathcal{F}^G_\Lambda = \begin{cases} \mathcal{F}^G & \text{for} \quad \Lambda \to 0 \\ 0 & \text{for} \quad \Lambda \to \Lambda_0 \end{cases} \tag{2.93}$$

$$\mathcal{F}^\Gamma_\Lambda = \begin{cases} \mathcal{F}^\Gamma & \text{for} \quad \Lambda \to 0 \\ \mathcal{S} & \text{for} \quad \Lambda \to \Lambda_0 \end{cases} \tag{2.94}$$

$$\mathcal{F}^V_\Lambda = \begin{cases} \mathcal{F}^V & \text{for} \quad \Lambda \to 0 \\ V & \text{for} \quad \Lambda \to \Lambda_0 \end{cases} . \tag{2.95}$$

This implies that $\mathcal{F}_\Lambda^{G,\Gamma,V}$ is solvable for $\Lambda \to \Lambda_0$. By decreasing Λ, there is a smooth interpolation between the interaction V and the generating functional $\mathcal{F}^V$. Eq. 2.89 can be rewritten to

$$\mathrm{e}^{-\mathcal{F}^V} = \mathrm{e}^{\Delta_{G_0}}\,\mathrm{e}^{-V} = \mathrm{e}^{\Delta_{\bar{G}_{0,\Lambda}}+\Delta_{G_{0,\Lambda}}}\,\mathrm{e}^{-V} = \mathrm{e}^{\Delta_{\bar{G}_{0,\Lambda}}}\,\mathrm{e}^{-\mathcal{F}_\Lambda^V} \tag{2.96}$$

with Eq. 2.92 and the inverse propagator $\bar{G}_{0,\Lambda} = G_0 - G_{0,\Lambda}$. For a cutoff energy, $\bar{G}_{0,\Lambda_c}$ is restricted to slow modes. The derivation with respect to the external parameter

$$\begin{aligned}
\frac{\mathrm{d}}{\mathrm{d}\Lambda}\mathcal{F}_\Lambda^V &= -\mathrm{e}^{\mathcal{F}_\Lambda^V}\frac{\mathrm{d}}{\mathrm{d}\Lambda}\mathrm{e}^{-\mathcal{F}_\Lambda^V}\\
&\overset{\text{Eq. 2.92}}{=} -\mathrm{e}^{\mathcal{F}_\Lambda^V}\frac{\mathrm{d}}{\mathrm{d}\Lambda}\left(\mathrm{e}^{\Delta_{G_{0,\Lambda}}}\,\mathrm{e}^{-V}\right)\\
&= -\mathrm{e}^{\mathcal{F}_\Lambda^V}\mathop{\int\!\!\!\!\!\!\sum}\frac{\mathrm{d}G_{0,\Lambda}}{\mathrm{d}\Lambda}\frac{\partial}{\partial\chi}\frac{\partial}{\partial\bar{\chi}}\mathrm{e}^{-\mathcal{F}_\Lambda^V}\\
&= -\left(\mathop{\int\!\!\!\!\!\!\sum}\frac{\mathrm{d}G_{0,\Lambda}}{\mathrm{d}\Lambda}\frac{\partial\mathcal{F}_\Lambda^V}{\partial\chi}\frac{\partial\mathcal{F}_\Lambda^V}{\partial\bar{\chi}}\right) - \mathrm{Tr}\left(\frac{\mathrm{d}G_{0,\Lambda}}{\mathrm{d}\Lambda}\frac{\partial^2\mathcal{F}_\Lambda^V}{\partial\bar{\chi}\partial\chi}\right)
\end{aligned} \tag{2.97}$$

yields a renormalization group equation [156]. With the initial condition $\mathcal{F}_{\Lambda_0}^V = V$, the full "flow" of $\mathcal{F}_\Lambda^V$ is determined. Using Eq. 2.87 and Eq. 2.86, the exact flow equations for the generating functional $\mathcal{F}_\Lambda^G$ can be obtained:

$$\frac{\mathrm{d}}{\mathrm{d}\Lambda}\mathcal{F}_\Lambda^G = \left(\mathop{\int\!\!\!\!\!\!\sum}\frac{\mathrm{d}G_{0,\Lambda}^{-1}}{\mathrm{d}\Lambda}\frac{\partial\mathcal{F}_\Lambda^G}{\partial\eta}\frac{\partial\mathcal{F}_\Lambda^G}{\partial\bar{\eta}}\right) - \mathrm{Tr}\left(\frac{\mathrm{d}G_{0,\Lambda}^{-1}}{\mathrm{d}\Lambda}\frac{\partial^2\mathcal{F}_\Lambda^G}{\partial\bar{\eta}\,\partial\eta}\right) \tag{2.98}$$

Both the flow equations for $G_{2n,\Lambda}$ and $V_{2n,\Lambda}$ generate one-particle reducible terms, which are more complicated to handle [150]. This problem is solved by a Legendre transform to the effective action (Eq. 2.77),

$$\mathcal{F}_\Lambda^\Gamma[\psi,\bar{\psi}] = \mathop{\int\!\!\!\!\!\!\sum}(\bar{\eta}\psi + \bar{\psi}\eta) + \mathcal{F}_\Lambda^G[\eta,\bar{\eta}] \qquad \text{with} \tag{2.99}$$

$$\psi = -\frac{\partial\mathcal{F}_\Lambda^G}{\partial\bar{\eta}} \qquad \text{and} \qquad \bar{\psi} = \frac{\partial\mathcal{F}_\Lambda^G}{\partial\eta}\,, \tag{2.100}$$

which does not generate one-particle reducible terms [150]. The derivation yields

$$\begin{aligned}
\frac{\mathrm{d}}{\mathrm{d}\Lambda}\mathcal{F}_\Lambda^\Gamma[\psi,\bar{\psi}] &= \mathop{\int\!\!\!\!\!\!\sum}\left(\frac{\mathrm{d}\bar{\eta}}{\mathrm{d}\Lambda}\psi + \bar{\psi}\frac{\mathrm{d}\eta}{\mathrm{d}\Lambda}\right) + \frac{\mathrm{d}}{\mathrm{d}\Lambda}\mathcal{F}_\Lambda^G[\eta,\bar{\eta}]\\
&= \mathop{\int\!\!\!\!\!\!\sum}\left(\frac{\mathrm{d}\bar{\eta}}{\mathrm{d}\Lambda}\psi + \bar{\psi}\frac{\mathrm{d}\eta}{\mathrm{d}\Lambda}\right) + \left.\frac{\mathrm{d}\mathcal{F}_\Lambda^G[\eta,\bar{\eta}]}{\mathrm{d}\Lambda}\right|_{\eta,\bar{\eta}\text{ fixed}} + \mathop{\int\!\!\!\!\!\!\sum}\left(\frac{\mathrm{d}\bar{\eta}}{\mathrm{d}\Lambda}\frac{\mathcal{F}_\Lambda^G}{\bar{\eta}} + \frac{\mathrm{d}\eta}{\mathrm{d}\Lambda}\frac{\mathcal{F}_\Lambda^G}{\eta}\right)\\
&\overset{\text{Eq. 2.100}}{=} \left.\frac{\mathrm{d}\mathcal{F}_\Lambda^G[\eta,\bar{\eta}]}{\mathrm{d}\Lambda}\right|_{\eta,\bar{\eta}\text{ fixed}}\\
&\overset{\text{Eq. 2.98}}{=} \left.\mathop{\int\!\!\!\!\!\!\sum}\frac{\mathrm{d}G_{0,\Lambda}^{-1}}{\mathrm{d}\Lambda}\frac{\partial\mathcal{F}_\Lambda^G}{\partial\eta}\frac{\partial\mathcal{F}_\Lambda^G}{\partial\bar{\eta}}\right|_{\eta,\bar{\eta}\text{ fixed}} - \mathrm{Tr}\left.\left(\frac{\mathrm{d}G_{0,\Lambda}^{-1}}{\mathrm{d}\Lambda}\frac{\partial^2\mathcal{F}_\Lambda^G}{\partial\bar{\eta}\partial\eta}\right)\right|_{\eta,\bar{\eta}\text{ fixed}}\\
&\overset{\substack{\text{Eq. 2.81}\\\text{Eq. 2.84}}}{=} -\mathop{\int\!\!\!\!\!\!\sum}\left(\frac{\mathrm{d}G_{0,\Lambda}^{-1}}{\mathrm{d}\Lambda}\bar{\psi}\psi\right) - \frac{1}{2}\mathrm{Tr}\left(\left(\frac{\mathrm{d}}{\mathrm{d}\Lambda}\mathbf{G}_{0,\Lambda}^{-1}\right)\left(\mathbf{F}_\Lambda^{\Gamma,(2)}[\psi,\bar{\psi}]\right)^{-1}\right)
\end{aligned} \tag{2.101}$$

with $\mathbf{F}_{\Lambda}^{\Gamma,(2)}$ being the Λ-modified version of Eq. 2.82 and

$$\mathbf{G}_{0,\Lambda}^{-1} = \begin{pmatrix} G_{0,\Lambda}^{-1}(x,y) & 0 \\ 0 & -G_{0,\Lambda}^{-1}(y,x) \end{pmatrix} . \tag{2.102}$$

So the final result for the flow equation of the effective action is

$$\boxed{\frac{\mathrm{d}}{\mathrm{d}\Lambda}\mathcal{F}_{\Lambda}^{\Gamma}[\psi,\bar{\psi}] = -\sum\!\!\!\!\!\!\int \left(\frac{\mathrm{d}G_{0,\Lambda}^{-1}}{\mathrm{d}\Lambda}\bar{\psi}\psi\right) - \frac{1}{2}\mathrm{Tr}\left(\left(\frac{\mathrm{d}}{\mathrm{d}\Lambda}\mathbf{G}_{0,\Lambda}^{-1}\right)\left(\mathbf{F}_{\Lambda}^{\Gamma,(2)}[\psi,\bar{\psi}]\right)^{-1}\right)} \tag{2.103}$$

In contrast to the traditional renormalization group by *K.G. Wilson* [151], which is limited to momentum shell integration, Eq. 2.103 includes flow equations for an arbitrary external parameter [150], e.g. the temperature [139]. But the exact calculation is possible only for a few special models because the initial condition for $\mathcal{F}^{\Gamma}$ is the bare action S (Eq. 2.94), which includes all combinations of one-particle irreducible vertex functions,

2.6.3 Truncation of the Hierarchy in the T-flow

If an exact solution is impossible in physics, a commonly accepted ansatz is to expand the function in a power series and analyze the coefficients. Hence, the effective action is expanded in powers of the fields

$$\mathcal{F}_{\Lambda}^{\Gamma}[\psi,\bar{\psi}] = \sum_{n=0}^{\infty} \mathcal{A}_{2n,\Lambda}[\psi,\bar{\psi}] \qquad \text{with} \tag{2.104}$$

$$\mathcal{A}_{2n,\Lambda}[\psi,\bar{\psi}] = \frac{(-1)^n}{(n!)^2} \sum_{\substack{x_1\ldots x_n \\ y_1\ldots y_n}} \Gamma_{2n,\Lambda}(y_1,\ldots,y_n,x_1,\ldots,x_n)\, \bar{\psi}(y_1)\ldots\bar{\psi}(y_n)\, \psi(x_1)\ldots\psi(x_n) \tag{2.105}$$

for coefficients with $n \geq 1$. The 0-th one is

$$\mathcal{A}_{0,\Lambda}[\psi,\bar{\psi}] = \mathcal{F}_{0,\Lambda}^{\Gamma}[\psi,\bar{\psi}] \overset{\text{Eq. 2.77}}{=} \mathcal{F}_{0,\Lambda}^{G}[\eta,\bar{\eta}] \overset{\text{Eq. 2.76}}{=} -\ln\mathcal{Z} = \frac{1}{T}\Omega_{\Lambda} , \tag{2.106}$$

identical to the modified grand potential Ω, divided by the temperature T. The final flow equation (Eq. 2.103) includes the inverse of $\mathbf{F}_{\Lambda}^{\Gamma,(2)}[\psi,\bar{\psi}]$. With the full propagator

$$\mathbf{G}_{\Lambda} = \left(\mathbf{F}_{\Lambda}^{\Gamma,(2)}[\psi,\bar{\psi}]\Big|_{\psi=\bar{\psi}=0}\right)^{-1} = \begin{pmatrix} G_{\Lambda}(x,y) & 0 \\ 0 & -G_{\Lambda}(y,x) \end{pmatrix} , \tag{2.107}$$

the second derivative of the effective action can be rewritten to

$$\begin{aligned} \mathbf{F}_{\Lambda}^{\Gamma,(2)}[\psi,\bar{\psi}] &\overset{\text{Eq. 2.82}}{=} \underbrace{\partial^2\mathcal{F}_{\Lambda}^{\Gamma} - (\mathbf{G}_{\Lambda})^{-1}}_{:=\,-\tilde{\boldsymbol{\Sigma}}_{\Lambda}[\psi,\bar{\psi}]} + (\mathbf{G}_{\Lambda})^{-1} \\ &= (\mathbf{G}_{\Lambda})^{-1} - \tilde{\boldsymbol{\Sigma}}_{\Lambda}[\psi,\bar{\psi}] , \end{aligned} \tag{2.108}$$

hence the inverse yields

$$
\begin{aligned}
\left(\mathbf{F}^{\Gamma,(2)}_{\Lambda}[\psi,\bar{\psi}]\right)^{-1} &= \left((\mathbf{G}_{\Lambda})^{-1} - \tilde{\boldsymbol{\Sigma}}_{\Lambda}[\psi,\bar{\psi}]\right)^{-1} \\
&= \left(1 - \mathbf{G}_{\Lambda}\tilde{\boldsymbol{\Sigma}}_{\Lambda}[\psi,\bar{\psi}]\right)^{-1}\mathbf{G}_{\Lambda} \\
&= \left(1 + \mathbf{G}_{\Lambda}\tilde{\boldsymbol{\Sigma}}_{\Lambda}[\psi,\bar{\psi}] + \mathbf{G}_{\Lambda}\tilde{\boldsymbol{\Sigma}}_{\Lambda}[\psi,\bar{\psi}]\;\mathbf{G}_{\Lambda}\tilde{\boldsymbol{\Sigma}}_{\Lambda}[\psi,\bar{\psi}] + \dots\right)\mathbf{G}_{\Lambda}\,,
\end{aligned}
\tag{2.109}
$$

where a geometric series is used. Inserting this result in Eq. 2.103 and using the cyclic invariance of the trace, the result is:

$$
\begin{aligned}
\frac{\mathrm{d}}{\mathrm{d}\Lambda}\mathcal{F}^{\Gamma}_{\Lambda} &= -\int\!\!\!\!\!\!\sum\left(\frac{\mathrm{d}G^{-1}_{0,\Lambda}}{\mathrm{d}\Lambda}\bar{\psi}\psi\right) - \frac{1}{2}\mathrm{Tr}\left(\left(\frac{\mathrm{d}}{\mathrm{d}\Lambda}\mathbf{G}^{-1}_{0,\Lambda}\right)\left(\mathbf{F}^{\Gamma,(2)}_{\Lambda}\right)^{-1}\right) \\
&= -\int\!\!\!\!\!\!\sum\left(\frac{\mathrm{d}G^{-1}_{0,\Lambda}}{\mathrm{d}\Lambda}\bar{\psi}\psi\right) - \frac{1}{2}\mathrm{Tr}\left(\left(\frac{\mathrm{d}}{\mathrm{d}\Lambda}\mathbf{G}^{-1}_{0,\Lambda}\right)\left(1 + \mathbf{G}_{\Lambda}\tilde{\boldsymbol{\Sigma}}_{\Lambda} + \mathbf{G}_{\Lambda}\tilde{\boldsymbol{\Sigma}}_{\Lambda}\mathbf{G}_{\Lambda}\tilde{\boldsymbol{\Sigma}}_{\Lambda} + \dots\right)\mathbf{G}_{\Lambda}\right) \\
&= -\int\!\!\!\!\!\!\sum\left(\frac{\mathrm{d}G^{-1}_{0,\Lambda}}{\mathrm{d}\Lambda}\bar{\psi}\psi\right) - \mathrm{Tr}\left(\frac{\mathrm{d}G^{-1}_{0,\Lambda}}{\mathrm{d}\Lambda}G_{\Lambda}\right) \\
&\quad - \frac{1}{2}\mathrm{Tr}\left(\left[\mathbf{G}_{\Lambda}\left(\frac{\mathrm{d}}{\mathrm{d}\Lambda}\mathbf{G}^{-1}_{0,\Lambda}\right)\mathbf{G}_{\Lambda}\right]\left(\tilde{\boldsymbol{\Sigma}}_{\Lambda} + \tilde{\boldsymbol{\Sigma}}_{\Lambda}\mathbf{G}_{\Lambda}\tilde{\boldsymbol{\Sigma}}_{\Lambda} + \dots\right)\right) \\
&= -\int\!\!\!\!\!\!\sum\left(\frac{\mathrm{d}G^{-1}_{0,\Lambda}}{\mathrm{d}\Lambda}\bar{\psi}\psi\right) - \mathrm{Tr}\left(\frac{\mathrm{d}G^{-1}_{0,\Lambda}}{\mathrm{d}\Lambda}G_{\Lambda}\right) - \frac{1}{2}\mathrm{Tr}\left(\mathbf{S}_{\Lambda}\left(\tilde{\boldsymbol{\Sigma}}_{\Lambda} + \tilde{\boldsymbol{\Sigma}}_{\Lambda}\mathbf{G}_{\Lambda}\tilde{\boldsymbol{\Sigma}}_{\Lambda} + \dots\right)\right)
\end{aligned}
\tag{2.110}
$$

Here, the *single-scale propagator* $S_{\Lambda}(x,y)$ is involved, which is defined as

$$
\begin{aligned}
S_{\Lambda} &= \left.\frac{\mathrm{d}}{\mathrm{d}\Lambda}G_{\Lambda}\right|_{\Sigma_{\Lambda}\text{ fixed}} \\
&= \left.\frac{\mathrm{d}}{\mathrm{d}\Lambda}\left(G^{-1}_{0,\Lambda} - \Sigma_{\Lambda}\right)^{-1}\right|_{\Sigma_{\Lambda}\text{ fixed}} \\
&= -(G^{-1}_{0,\Lambda} - \Sigma_{\Lambda})^{-1}\left(\frac{\mathrm{d}}{\mathrm{d}\Lambda}G^{-1}_{0,\Lambda}\right)(G^{-1}_{0,\Lambda} - \Sigma_{\Lambda})^{-1} \\
&= G_{\Lambda}\left(\frac{\mathrm{d}}{\mathrm{d}\Lambda}G^{-1}_{0,\Lambda}\right)G_{\Lambda}\,,
\end{aligned}
\tag{2.111}
$$

where the Dyson equation $G_{\Lambda} = (G^{-1}_{0,\Lambda} - \Sigma_{\Lambda})^{-1}$ is used. The matrix representation is

$$
\mathbf{S}_{\Lambda} = \begin{pmatrix} S_{\Lambda}(x,y) & 0 \\ 0 & -S_{\Lambda}(y,x) \end{pmatrix} = \mathbf{G}_{\Lambda}\left(\frac{\mathrm{d}}{\mathrm{d}\Lambda}\mathbf{G}^{-1}_{0,\Lambda}\right)\mathbf{G}_{\Lambda}\,. \tag{2.112}
$$

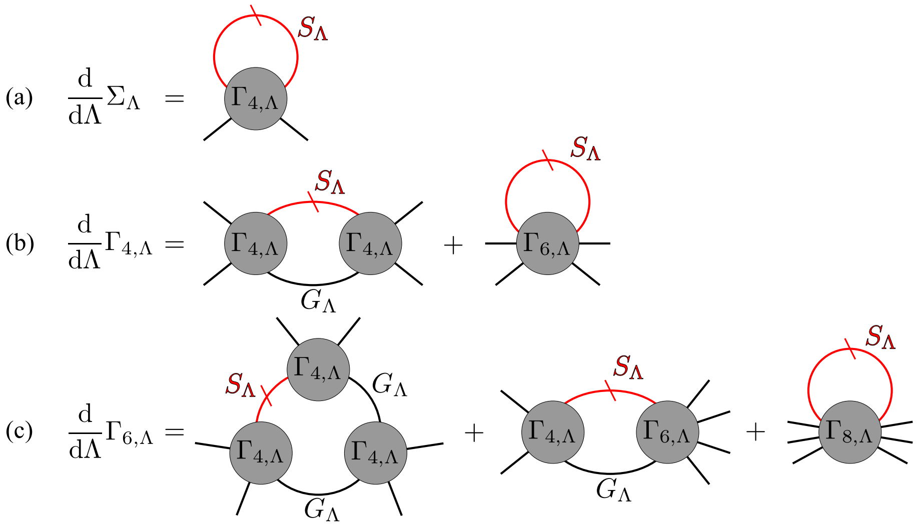

Figure 2.16: Diagrammatic representation of the flow equations of the first three orders. Red lines with a dash image the single-scale propagator S_Λ, the other intern lines the fully dressed normal propagator G_Λ. **(a)** The first order corresponds to the self-energy Σ_Λ and includes a two-particle vertex $\Gamma_{4,\Lambda}$, which flows in the second order **(b)**. That in turn includes a three-particle vertex of the third order **(c)**, and so on. Hence, this expansion does not close.

Now, one can expand both side of Eq. 2.103 in a power series and compare the coefficients. This yields a system of differential equations for $\mathcal{A}_{n,\Lambda}$:

$$\begin{aligned}
\frac{\mathrm{d}}{\mathrm{d}\Lambda}\mathcal{A}_{0,\Lambda} &= -\mathrm{Tr}\left(\frac{\mathrm{d}G_\Lambda^{-1}}{\mathrm{d}\Lambda}G_\Lambda\right)\\
\frac{\mathrm{d}}{\mathrm{d}\Lambda}\mathcal{A}_{2,\Lambda} &= -\frac{1}{2}\mathrm{Tr}\left(\mathbf{S}_\Lambda\boldsymbol{\partial}^2\mathcal{A}_{4,\Lambda}\right) - \mathop{\sum\!\!\!\!\!\!\int} G_{0,\Lambda}^{-1}\bar{\psi}\psi\\
\frac{\mathrm{d}}{\mathrm{d}\Lambda}\mathcal{A}_{4,\Lambda} &= -\frac{1}{2}\mathrm{Tr}\left(\mathbf{S}_\Lambda\boldsymbol{\partial}^2\mathcal{A}_{6,\Lambda}\right) + \frac{1}{2}\mathrm{Tr}\left(\mathbf{S}_\Lambda\boldsymbol{\partial}^2\mathcal{A}_{4,\Lambda}\boldsymbol{\partial}^2\mathcal{A}_{4,\Lambda}\right)\\
\frac{\mathrm{d}}{\mathrm{d}\Lambda}\mathcal{A}_{6,\Lambda} &= -\frac{1}{2}\mathrm{Tr}\left(\mathbf{S}_\Lambda\boldsymbol{\partial}^2\mathcal{A}_{8,\Lambda}\right) + \ldots
\end{aligned} \tag{2.113}$$

Inserting Eq. 2.105, the first two orders of the hierarchy read

$$\begin{aligned}
\frac{\mathrm{d}}{\mathrm{d}\Lambda}\Sigma_\Lambda(y,x) &= \mathop{\sum\!\!\!\!\!\!\int}_{z_1,z_2} S_\Lambda(z_1,z_2)\,\Gamma_{4,\Lambda}(y,z_2,x,z_1)\\
\frac{\mathrm{d}}{\mathrm{d}\Lambda}\Gamma_{4,\Lambda}(y_1,y_2,x_1,x_2) &= -\mathop{\sum\!\!\!\!\!\!\int}_{z_1,z_2} S_\Lambda(z_1,z_2)\,\Gamma_{6,\Lambda}(y_1,y_2,z_2,x_1,x_2,z_1)\\
&\quad + \mathop{\sum\!\!\!\!\!\!\int}_{\substack{z_1,z_2\\z_3,z_4}} G_\Lambda(z_1,z_2)\,S_\Lambda(z_3,z_4)\cdot\Big(\Gamma_{4,\Lambda}(y_1,y_2,z_1,z_3)\,\Gamma_{4,\Lambda}(z_2,z_4,x_1,x_2)\\
&\quad - \Gamma_{4,\Lambda}(y_1,z_4,x_1,z_1)\,\Gamma_{4,\Lambda}(z_2,y_2,z_3,x_2) - \Gamma_{4,\Lambda}(y_1,z_2,x_1,z_3)\,\Gamma_{4,\Lambda}(z_4,y_2,z_1,x_2)\\
&\quad + \Gamma_{4,\Lambda}(y_2,z_4,x_1,z_1)\,\Gamma_{4,\Lambda}(z_2,y_1,z_3,x_2) + \Gamma_{4,\Lambda}(y_2,z_2,x_1,z_3)\,\Gamma_{4,\Lambda}(z_4,y_1,z_1,x_2)\Big)\,.
\end{aligned} \tag{2.114}$$

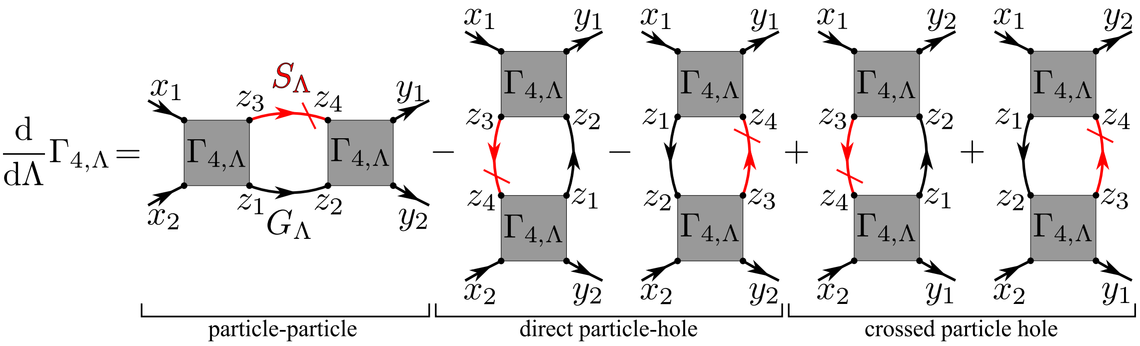

Figure 2.17: In detail diagrammatic representation of the contributions to the flow of the two-particle vertex $\Gamma_{4,\Lambda}$, with $\Gamma_{6,\Lambda}$ being cut off. The diagrams can be sorted into the particle-particle (one member), the direct particle-hole (two members) and the crossed particle-hole channel (two members).

This leads to flow equations for the self-energy Σ_Λ (Fig. 2.16a), the two-particle vertex $\Gamma_{4,\Lambda}$ (Fig. 2.16b), the three-particle vertex $\Gamma_{6,\Lambda}$ (Fig. 2.16c) and higher-order vertices like $\Gamma_{8,\Lambda}$, $\Gamma_{10,\Lambda}$, etc. The internal lines G_Λ and S_Λ are dressed by self-energy corrections. Only one-particle irreducible one-loop diagrams contribute. This yields an infinite series of diagrams because the flow of the n-th order vertex $\Gamma_{2n,\Lambda}$ depends on an $(n+1)$-th order vertex $\Gamma_{2(n+1),\Lambda}$. The diagrammatic representation of the flow equations is show in Fig. 2.16. If the contribution of $\Gamma_{6,\Lambda}$ is neglected, the flow for the two-particle vertex can be plotted in detail (Fig. 2.17). Red lines with a dash image the single-scale propagator S_Λ, the other intern lines the fully dressed normal propagator G_Λ. Here, the resulting diagrams can be sorted into one particle-particle and four particle-hole diagrams. The flow equations and the diagrams for the higher-order vertices $\Gamma_{n,\Lambda}$ with $n \geq 6$ can be calculated in a similar way.

Since the hierarchy of flow equations is an infinite series, one has to set a break condition at a well-defined order. It is accepted to cut off all flow equations for $\Gamma_{n,\Lambda}$ with $n \geq 6$ [150]. Indeed, a focus on the second-order flow equation with the neglect of three-particle vertex $\Gamma_{6,\Lambda}$ is sufficient to get the competition of different orders like superconductivity, spin-density and charge-density waves [150]. Although this low-level truncation looks similar to a Hartree-Fock approximation, it is completely dissimilar and works also in systems where Hartree-Fock fails [150].

Up to now, the exact modification of the bare propagator G_0 has been irrelevant. Only the boundary conditions were defined in Eq. 2.90, namely

$$G_{0,\Lambda} = \begin{cases} G_0 & \text{for} \quad \Lambda \to 0 \\ 0 & \text{for} \quad \Lambda \to \Lambda_0 \end{cases}, \tag{2.115}$$

with the external parameter Λ. For the calculation of the contributions in Eq. 2.114, one has the choose a reasonable Λ. Usually, a simple cutoff in the energy of the free propagator is implemented [62]. For that, G_0 is multiplied with a momentum- or frequency-dependent cutoff function (Eq. 2.91). Thus, the propagators are divided into fast and slow modes, where the latter ones are integrated out step by step (Fig. 2.15). This is similar to the old-style Wilson RG [151], where momentum modes are integrated shell by shell. Unfortunately, local conservation laws are violated, resulting in Λ-dependent Ward identities [150]. Another crucial error arises from the fact that only small shells around the finite cutoff energy are considered in an fRG step. Hence, collective modes with an ordering vector $Q = (0,0)$ (e.g. ferromagnetism) are omitted until the end of the flow, when $\Lambda \to 0$. Thus, these orders are completely underestimated compared to other competing orders which are considered for any $\Lambda < \Lambda_0$. Consequently, $Q = (0,0)$-orders are not visible in the cutoff flow. In addition, the cutoff-energy flow has to be separately executed for each relevant temperature. For details, the review of *W. Metzner et al.* [150] elaborately responds to the flow driven by a cutoff energy.

The second common external parameter is the temperature T [139], which provides several advantages: On the one hand, there is a direct temperature dependence, so the critical scale of the flow parameter T is identical to the critical temperature of the instability. On the other hand, in the T-flow the complete energy spectrum is considered at each step, so low-energy particle-hole excitations with small momentum transfer are correctly handled. Hence, orders with ordering vectors $Q = (0,0)$ are in competition. Thirdly, the local symmetries and their corresponding Ward identities are respected at least with the complete hierarchy [150].

Due to these benefits, I implemented the T-flow. Here, one starts by moving the T^3 prefactor of the interaction in Eq. 2.71 to the fields. For that, some new fermionic fields

$$\bar{\psi}_T = T^{3/4}\bar{\psi} \qquad \text{and} \qquad \psi_T = T^{3/4}\psi \tag{2.116}$$

are introduced. Thereby, only the quartic part of the action remains T-dependent. Here, a new bare propagator can be defined:

$$G_{0,T}(\mathrm{i}\omega_n,\vec{k}) = \frac{T^{1/2}}{\mathrm{i}\omega_n - \varepsilon(\vec{k})} \tag{2.117}$$

With this modifications, the effective action in the new fields $\mathcal{F}_T^\Gamma\left[\psi_T,\bar{\psi}_T\right]$ is form invariant to the basic flow equation (Eq. 2.103). In this approach, self-energy corrections are neglected. In addition to the truncation of the flow equation hierarchy, this restricts the implementation of the fRG used within this thesis to weakly correlated fermionic systems. Hence, as a rough estimate, the total strength of the interaction has to be smaller than the bandwidth of the spectral function [157]. An fRG implementation including self-energy corrections and frequency-dependence is presented in Refs. [158, 159]. These expansions only effect the critical scale of the flow but do not change the leading instability. Without self-energy corrections, the dressed one-particle propagator is identical to the propagator of the free system

$$G_T(\mathrm{i}\omega_n,\vec{k}) = \frac{T^{1/2}}{\mathrm{i}\omega_n - \varepsilon(\vec{k})}\ . \tag{2.118}$$

Thus, the single-scale propagator S_T (Eq. 2.111) in the T-flow implementation is given by

$$\begin{aligned} S_T(\mathrm{i}\omega_n,\vec{k}) &= G_T(\mathrm{i}\omega_n,\vec{k})\left(\frac{\mathrm{d}}{\mathrm{d}T}G_{0,T}^{-1}(\mathrm{i}\omega_n,\vec{k})\right)G_T(\mathrm{i}\omega_n,\vec{k}) \\ &= -\frac{T^{-1/2}}{2}\frac{\mathrm{i}\omega_n + \varepsilon(\vec{k})}{(\mathrm{i}\omega_n - \varepsilon(\vec{k}))^2}\ . \end{aligned} \tag{2.119}$$

For simplicity, a combined index

$$\begin{aligned} (\mathrm{i}\omega_n, \vec{k}_x) &:= k_x \qquad \text{as well as} \\ \varepsilon(\vec{k}_x) &:= \varepsilon_x \qquad \text{and} \qquad \omega_n := \omega_x \end{aligned} \tag{2.120}$$

are introduced. If the system's Hamiltonian consists of more than one band, this combined index may also include a band index. In general, the effective action has to preserve all symmetries of the initial action. For a spin-rotationally invariant system, this requires [150]

$$\begin{aligned} &\Gamma_{4,T}(k_1,\sigma_1,k_2,\sigma_2,k_3,\sigma_3,k_4,\sigma_4) = \\ &\qquad V_T(k_1,k_2,k_3,k_4)\ \delta_{\sigma_1\sigma_3}\delta_{\sigma_2\sigma_4} - V_T(k_2,k_1,k_3,k_4)\ \delta_{\sigma_1\sigma_4}\delta_{\sigma_2\sigma_3} \end{aligned} \tag{2.121}$$

with the four-point interaction V_T. Here, the translational invariance of the lattice and the time forces a momentum conservation at each vertex. Thus,

$$V_T(k_1,k_2,k_3,k_4) \overset{!}{=} V_T(k_1,k_2,k_3,k_1+k_2-k_3)\ . \tag{2.122}$$

If a multiorbital system is considered, the 4-th momentum has still a degree of freedom due choosing the band index. As an auxiliary construction, a product of a full propagator G_T with a single-scale propagator S_T is defined:

$$\begin{aligned} \mathcal{L}_T(k_1,k_2) &= S_T(k_1)\ G_T(k_2) + G_T(k_1)\ S_T(k_2) \\ &= -\frac{1}{2}\left(\frac{\mathrm{i}\omega_1+\varepsilon_1}{(\mathrm{i}\omega_1-\varepsilon_1)^2}\frac{1}{\mathrm{i}\omega_2-\varepsilon_2} + \frac{1}{\mathrm{i}\omega_1-\varepsilon_1}\frac{\mathrm{i}\omega_2+\varepsilon_2}{(\mathrm{i}\omega_2-\varepsilon_2)^2}\right) \\ &= \frac{\omega_1\omega_2+\varepsilon_1\varepsilon_2}{(\mathrm{i}\omega_1-\varepsilon_1)^2\ (\mathrm{i}\omega_2-\varepsilon_2)^2} \\ &= \frac{\mathrm{d}}{\mathrm{d}T}\left(T\frac{1}{\mathrm{i}\omega_1-\varepsilon_1}\frac{1}{\mathrm{i}\omega_2-\varepsilon_2}\right) \end{aligned} \tag{2.123}$$

Now, Eq. 2.114 can be rewritten to

$$\begin{aligned} \frac{\mathrm{d}}{\mathrm{d}T}\Sigma_T(k) &= -\int \mathrm{d}^4p\ \left(2V_T(k,p,k,p) - V_T(k,p,p,k)\right) S_T(p) \\ \frac{\mathrm{d}}{\mathrm{d}T}V_T(k_1,k_2,k_3,k_4) &= \mathcal{C}_{\mathrm{PP},T}(k_1,k_2,k_3,k_4) + \mathcal{C}_{\mathrm{dPH},T}(k_1,k_2,k_3,k_4) + \mathcal{C}_{\mathrm{cPH},T}(k_1,k_2,k_3,k_4) \end{aligned} \tag{2.124}$$

with

$$\begin{aligned} \mathcal{C}_{\mathrm{PP},T}(k_1,k_2,k_3,k_4) &= \int \mathrm{d}^4p\ V_T(k_1,k_2,p)\ \mathcal{L}_T(p,-p+k_1+k_2)\ V_T(p,-p+k_1+k_2,k_3) \\ \mathcal{C}_{\mathrm{dPH},T}(k_1,k_2,k_3,k_4) &= \int \mathrm{d}^4p\ \big(-2V_T(k_1,p,k_3)\ \mathcal{L}_T(k,p+k_1-k_3)\ V_T(p+k_1-k_3,k_2,p) \\ &\qquad + V_T(k_1,p,p+k_1-k_3)\ \mathcal{L}_T(p,p+k_1-k_3)\ V_T(p+k_1-k_3,k_2,p) \\ &\qquad + V_T(k_1,p,k_3)\ \mathcal{L}_T(p,p+k_1-k_3)\ V_T(k_2,p+k_1-k_3,p)\big) \\ \mathcal{C}_{\mathrm{cPH},T}(k_1,k_2,k_3,k_4) &= \int \mathrm{d}^4p\ V_T(k_1,p+k_2-k_3,p)\ \mathcal{L}_T(p,p+k_2-k_3)\ V_T(p,k_2,k_3)\ . \end{aligned} \tag{2.125}$$

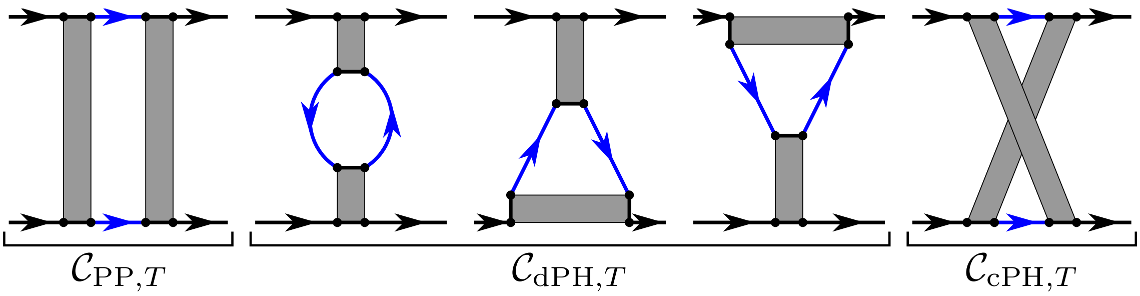

Figure 2.18: Diagrammatic representation of the contributions to the flow of the four-point vertex $V_T(k_1,k_2,k_3,k_4)$. The diagrams can be sorted into the particle-particle ($\mathcal{C}_{\mathrm{PP},T}$) as well as the direct ($\mathcal{C}_{\mathrm{dPH},T}$) and the crossed particle-hole ($\mathcal{C}_{\mathrm{cPH},T}$) channel. Each diagram has two intern lines (blue), where one of them is a single-scale propagator S_T, the other is a full propagator G_T. So, in total, ten distinct diagrams have to be summed up.

The contributions to the second-order flow are divided into a particle-particle channel $\mathcal{C}_{\mathrm{PP},T}$ and a direct and crossed particle hole channel $\mathcal{C}_{\mathrm{dPH},T}$ and $\mathcal{C}_{\mathrm{cPH},T}$, respectively (see Fig. 2.18 for a diagrammatic representation). The frequency dependence of the coupling function $V_T(k_1,k_2,k_3,k_4)$ is not considered. That is possible because its most singular part is at zero Matsubara frequency [150].

At this point, the generic derivation of the fRG-flow is completed. At the beginning of the calculation, a starting interaction $V_{T,0}$ has to be selected. After this, the derivative of the four-point vertex with respect to the temperature $\frac{\mathrm{d}}{\mathrm{d}T}V_T$ can be calculated by the evaluation of one-loop diagrams. While the flow parameter T is decreased in small steps, the effective vertex V_T develops the signature of a dominating instability.

In detail, some technical issues concerning the implementation of the fRG-flow have to be considered, which are presented in the following section.

2.6.4 Implementation

At each fRG-step, the flow equations have to be solved (see Eq. 2.125 or Fig. 2.18, respectively). For this purpose, five one-loop diagrams have to be considered, with two alternatives each. In any diagram, there is one free internal propagator. While the integration of the momentum has to be numerically solved, the summation over the Matsubara frequencies can be done analytically (see App. A.3 for an extensive calculation). The results reads

$$\begin{aligned}
\mathcal{L}_{T,\mathrm{PP}}(\vec{p}_1,\vec{k}_1+\vec{k}_2-\vec{p}_1) &= -\frac{\frac{\mathrm{d}}{\mathrm{d}T}\left(n_F(\varepsilon_{\vec{k}_1+\vec{k}_2-\vec{p}_1})\right)+\frac{\mathrm{d}}{\mathrm{d}T}\left(n_F(\varepsilon_{\vec{p}_1})\right)}{\varepsilon_{\vec{k}_1+\vec{k}_2-\vec{p}_1}+\varepsilon_{\vec{p}_1}} \\
\mathcal{L}_{T,\mathrm{PH}}(\vec{p}_1,-\vec{k}_1+\vec{k}_2+\vec{p}_1) &= -\frac{\frac{\mathrm{d}}{\mathrm{d}T}\left(n_F(\varepsilon_{-\vec{k}_1+\vec{k}_2+\vec{p}_1})\right)-\frac{\mathrm{d}}{\mathrm{d}T}\left(n_F(\varepsilon_{\vec{p}_1})\right)}{\varepsilon_{-\vec{k}_1+\vec{k}_2+\vec{p}_1}-\varepsilon_{\vec{p}_1}}
\end{aligned} \tag{2.126}$$

for the particle-particle and the particle-hole channel, respectively.

The numerical integration of $\int \mathrm{d}^3\vec{p}$ is still intricate, but the $\vec{p}_z$-dependence can be neglected and thus the integration simplifies to two dimensions because the focus of

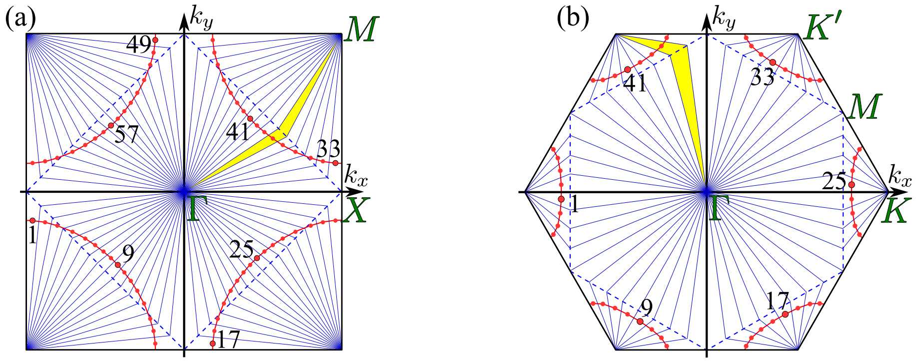

Figure 2.19: Patching scheme for the discretization of the Fermi surface (FS). The bounds of the patches are indicated with solid blue lines. The umklapp surface (dashed blue line) ensures that each patch intersects the FS (red line). All vectors within one patch, e.g. the yellow shaded area, are mapped to one point at the FS (red dots). **(a)** Quadratic BZ for the quadratic lattice (Sec. 2.2). **(b)** Hexagonal BZ for the kagome lattice (Sec. 2.2), very similar to the patching schemes for the triangular (Sec. 2.2) and honeycomb lattice (Sec. 2.2).

this thesis is on two-dimensional lattices (Sec. 2.2). To get the angular momentum dependencies very accurately, the numerical integration is performed in polar coordinates $\iint_{\mathrm{BZ}} r\ \mathrm{d}r\ \mathrm{d}\varphi$. Next, coupling function $V_T(\vec{k}_1,\vec{k}_2,\vec{k}_3)$ in Eq. 2.124 and Eq. 2.125 includes three momenta as continuous input parameters (the 4th is fixed by momentum conservation). To implement the exact flow equations in a computer program, one would need an infinite number of variables to get the complete momentum resolution in V_T. Hence, some kind of discretization is needed. Also, one has to take into consideration that with N discretization points, V_T has the dimension $N \times N \times N$. Consequently, N is limited in size. The discretization into the patching schemes displayed in Fig. 2.19 exposed to be a well-working choice [155]. Here, the BZ is divided into 48 up to 256 patches. Certainly, more patches are possible, but the dramatic increase in CPU time is confronted to a minimal improvement of accuracy (at least in the models I used). To ensure that each patch intersects the FS, an umklapp surface is implemented. The centers of the FS within the patches are the discretized momenta, so $V_T(\vec{k}_1,\vec{k}_2,\vec{k}_3) \rightarrow V_T(k_1,k_2,k_3)$. The reduction of the full momentum dependence to momenta on the FS is a reasonable approximation because excitations of particles around the Fermi energy need only a slight amount of energy, and so they are the most probable ones. Also, the life time of the quasi-particles increase when approaching the Fermi energy. All vectors have to be mapped on the patch vectors. For example, if the 4th momentum $\vec{k}_4 = \vec{k}_1 + \vec{k}_2 - \vec{k}_3$ is somewhere in the yellow shaded area in Fig. 2.19, one has to map $\vec{k}_4 \rightarrow \vec{k}_{\text{patch } 38}$. Due to the discretization and mapping of the momenta in the BZ, some symmetries are broken. For example, $V_T(k_1,k_2,k_3) = V_T(k_2,k_1,k_4)$ is generally not correct. But the angular momentum dependence around the FS is approximated very well [150]. This is sufficient to capture the correct long-range order of the system. With the previous assumptions, the implementation of a numerical fRG-flow is possible. The starting value of the flow parameter T_0 should be chosen sufficiently large, so all high-energy modes are included. This is satisfied if T_0 is in order of the bandwidth.

The next question is, when the flow has to be terminated. This is the case if one element

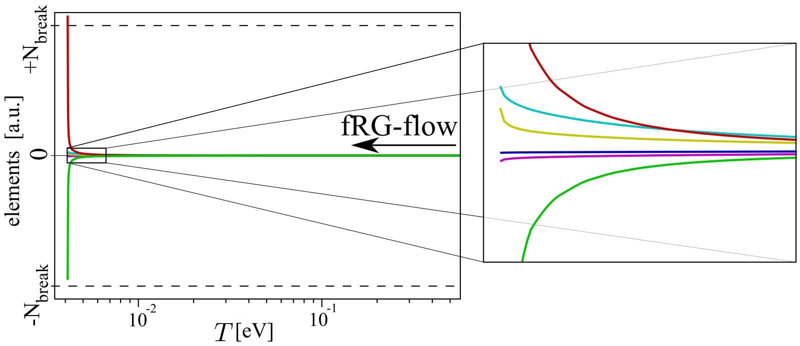

Figure 2.20: Flow of matrix elements in coupling function $V_T(k_1,k_2,k_3)$. The dimension of the matrix is $N\times N\times N$ with N being the number of patches. Here, only the larges element (red line) and the smallest one (green line) is plotted, together with some arbitrary elements (other lines). Just before the critical value of the flow T_{crit} is reached, the coupling function is quite homogeneous (see amplification). After this, some elements are diverging. This is the break point for the fRG-flow.

of the coupling function becomes significantly large and surpasses the bandwidth [62,150] (Fig. 2.20). If this happens, the truncation of the flow equation hierarchy after the second order, as described in Sec. 2.6.3, is not a well-defined approximation any more. At this point, the flow has to be terminated. But now, the renormalized coupling function includes the dominating fluctuations, so the tendency to long-range orders can be extracted.

When the fRG coupling function $V_T(k_1,k_2,k_3)$ is "flowing", controlled by the flow equations, various orders are competing with each other, until one order gets totally dominant and the flow breaks down. The fRG is a weak-coupling approximation, so long-range orders accompanying with a reorganization of the FS are out of range. But the diverging instability at the break-down of the fRG-flow demonstrates the tendency to form long-range orders at low energies. Hence, the goal of this principle is to determine which order is dominating at low energies. During the flow, various scattering processes take place with different amplitudes, depending on the changes of the coupling function

$$\hat{H}_{\text{scatt}} = V_T(\vec{k}_1,\vec{k}_2,\vec{k}_3,\vec{k}_4)\ \hat{c}^\dagger_{\vec{k}_1\alpha_1\sigma}\hat{c}^\dagger_{\vec{k}_2\alpha_2\tau}\hat{c}_{\vec{k}_3\alpha_3\tau}\hat{c}_{\vec{k}_4\alpha_4\sigma}\ . \tag{2.127}$$

Here α indicate additional degrees of freedom, e.g. a band or a sublattice index. They are omitted in the following derivation, except they are necessary. To determine the strength of an arbitrary order, a mean-field decoupling into one-particle operators $\hat{O}$ can be performed [160,161] (for details, see App. A.4). For this purpose, the Hamiltonian for scattering processes is decomposed to

$$\begin{aligned}\hat{H}_{\hat{O}} &= \sum_{\vec{k}\vec{p}} V_T(\vec{k},\vec{p})\ \hat{O}^\dagger_{\vec{k}}\hat{O}_{\vec{p}}\\ &= \sum_{\vec{k}\vec{p}}\left(\sum_i w_i(T)\ f_i(\vec{k},T)\ f_i^T(\vec{p},T)\right)\ \hat{O}^\dagger_{\vec{k}}\hat{O}_{\vec{p}}\ .\end{aligned} \tag{2.128}$$

In the second step, the decoupled vertex $V_T(\vec{k},\vec{p})$ is rewritten to a representation with eigenvalues $w_i(T)$ and eigenvectors $f_i(\vec{k},T)$. When the fRG-flow is running and T is subsequently decreased, the absolute of the most negative eigenvalue is growing. This indicates that the system is tending to develop an order within this channel. For all combinations of $\hat{O}$, a mean-field decoupling has to be performed. The system tends to the order with the (absolute) largest eigenvalue w_i. The dominating order is characterized by

$$O_i = \sum_{\vec{k}} f_i(\vec{k}) \, \langle \hat{O}^{\dagger}_{\vec{k}} \rangle \ , \tag{2.129}$$

with the order parameter O_i. The eigenvector $f_i(\vec{k})$ represents the transformation characteristics under rotation and reflection of the lattice (see Sec. 2.3 for details).

The tendencies to long-range orders can be separated in various channels by a mean-field decoupling [161]. These instabilities are accessible in each fRG step, so the flow to long-range orders can be logged. The detailed derivation is done in App. A.6. The final results for the mean-field decoupled vertex read

$$\begin{aligned}
V_{\mathrm{SDW}}(\vec{k},\vec{p},\vec{Q},T) &= -2V_T(\vec{k},\vec{p},\vec{p}-\vec{Q},\vec{k}+\vec{Q}) \\
V_{\mathrm{CDW}}(\vec{k},\vec{p},\vec{Q},T) &= V_T(\vec{k},\vec{p},\vec{k}+\vec{Q},\vec{p}-\vec{Q}) - \frac{1}{2}V_T(\vec{k},\vec{p},\vec{p}-\vec{Q},\vec{k}+\vec{Q}) \\
V_{\mathrm{FM}}(\vec{k},\vec{p},T) &= -2V_T(\vec{k},\vec{p},\vec{p},\vec{k}) \\
V_{\mathrm{PI}}(\vec{k},\vec{p},T) &= V_T(\vec{k},\vec{p},\vec{k},\vec{p}) - \frac{1}{2}V_T(\vec{k},\vec{p},\vec{p},\vec{k}) \\
V_{\mathrm{sSC}}(\vec{k},\vec{p},T) &= V_T(\vec{k},-\vec{k},\vec{p},-\vec{p}) + V_T(\vec{k},-\vec{k},-\vec{p},\vec{p}) \\
V_{\mathrm{tSC}}(\vec{k},\vec{p},T) &= V_T(\vec{k},-\vec{k},\vec{p},-\vec{p}) - V_T(\vec{k},-\vec{k},-\vec{p},\vec{p}) \ .
\end{aligned} \tag{2.130}$$

The labels of the channels are spin-density wave (SDW), charge-density wave (CDW), ferromagnetism (FM), Pomeranchuk instability (PI), singlet superconductivity (sSC) and triplet superconductivity (sSC). These labels give only a hint to the actually realized real space pattern of the long-range order. For example, in the kagome lattice, the charge bond order forms in the CDW channel (see Sec. 7.4 for details). Depending on the symmetry point group of the system, an analysis of the degeneracy of the eigenvalues and the form of the eigenvectors allows a more accurate denotation of the orders, e.g. s-wave, p-wave or d-wave superconductivity. Now, it is possible to distinguishing between the dominating orders at any step of the flow, as plotted in Fig. 2.21. At the break condition of the fRG-flow, the absolute eigenvalue of one channel is dramatically increasing, which determines the resulting long-range phase of the system.

The leading eigenvalue of the mean-field decoupled channels is a first hint to the realized long-range order of the system. A more accurate indication is the grand potential, which has to be minimized. The mean-field decoupling can also be used to determine the size of the band gaps which are triggered by long-range orders [160]. I will present the formalism for the Cooper channel with the (not yet symmetrized) pairing operators $\hat{d}^{\dagger}_{\vec{q}} = \hat{c}^{\dagger}_{\vec{q}\uparrow}\hat{c}^{\dagger}_{-\vec{q}\downarrow}$. The other channels can be handled analogously. In the Cooper channel, the

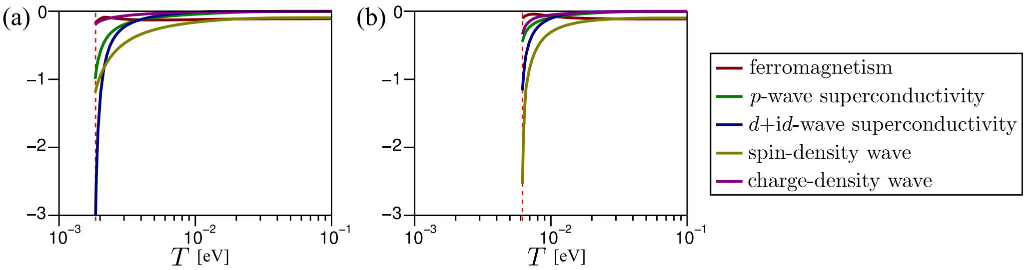

Figure 2.21: Examples for the flow of the leading (negative) eigenvalues in various channels for $\mathsf{Na}_x\mathsf{CoO}_2$ with initial interaction $U_1 = 0.24$eV, $U_2 = 0.31$eV, $J_H = 0.09$eV, and $J_P = 0.09$eV (see Chap. 4 for details). **(a)** At a doping level of $x = 0.15$, the eigenvalue in the d+id channel is diverging at 1.7meV, equivalent to 20K. **(b)** With an increased doping level of $x = 0.24$, the flow stops already at 5.8meV or 67K, respectively. Here, the SDW channel is dominating.

Hamiltonian in momentum space reads (Eq. 2.1, Eq. 2.3)

$$\begin{aligned}
\hat{H}_{\text{pair}} &= \sum_{\sigma}\sum_{\vec{k}} \varepsilon(\vec{k})\hat{c}^{\dagger}_{\vec{k}\sigma}\hat{c}_{\vec{k}\sigma} + \frac{1}{N}\sum_{\vec{k}\vec{q}} V_{\text{pair}}(\vec{k},\vec{q})\ \left(\hat{c}^{\dagger}_{\vec{k}\uparrow}\hat{c}^{\dagger}_{-\vec{k}\downarrow}\hat{c}_{-\vec{q}\downarrow}\hat{c}_{\vec{q}\uparrow}\right) \\
&\overset{\text{App. }A.4}{\approx} \sum_{\vec{k}} \varepsilon(\vec{k})\ \left(\hat{c}^{\dagger}_{\vec{k}\uparrow}\hat{c}_{\vec{k}\uparrow} + \hat{c}^{\dagger}_{\vec{k}\downarrow}\hat{c}_{\vec{k}\downarrow}\right) \\
&\quad + \frac{1}{N}\sum_{\vec{k}\vec{q}} V_{\text{pair}}(\vec{k},\vec{q})\ \left(\langle\hat{c}_{-\vec{q}\downarrow}\hat{c}_{\vec{q}\uparrow}\rangle\hat{c}^{\dagger}_{\vec{k}\uparrow}\hat{c}^{\dagger}_{-\vec{k}\downarrow} + \langle\hat{c}^{\dagger}_{\vec{k}\uparrow}\hat{c}^{\dagger}_{-\vec{k}\downarrow}\rangle\hat{c}_{-\vec{q}\downarrow}\hat{c}_{\vec{q}\uparrow} - \langle\hat{c}^{\dagger}_{\vec{k}\uparrow}\hat{c}^{\dagger}_{-\vec{k}\downarrow}\rangle\langle\hat{c}_{-\vec{q}\downarrow}\hat{c}_{\vec{q}\uparrow}\rangle\right) \\
&= \sum_{\vec{k}}[\varepsilon(\vec{k})\ \hat{c}^{\dagger}_{\vec{k}\uparrow}\hat{c}_{\vec{k}\uparrow} + \varepsilon(\vec{k})\ (1 - \underbrace{\hat{c}_{\vec{k}\downarrow}\hat{c}^{\dagger}_{\vec{k}\downarrow}}_{\vec{k}\to-\vec{k}}) - \frac{1}{N}\sum_{\vec{k}\vec{q}} V_{\text{pair}}(\vec{k},\vec{q})\ \langle\hat{c}^{\dagger}_{\vec{k}\uparrow}\hat{c}^{\dagger}_{-\vec{k}\downarrow}\rangle\langle\hat{c}_{-\vec{q}\downarrow}\hat{c}_{\vec{q}\uparrow}\rangle \\
&\quad + \underbrace{\frac{1}{N}\sum_{\vec{k}\vec{q}} V_{\text{pair}}(\vec{k},\vec{q})\ \langle\hat{c}_{-\vec{q}\downarrow}\hat{c}_{\vec{q}\uparrow}\rangle\ \hat{c}^{\dagger}_{\vec{k}\uparrow}\hat{c}^{\dagger}_{-\vec{k}\downarrow}}_{=\Delta_{\vec{k}}} + \underbrace{\frac{1}{N}\sum_{\vec{k}\vec{q}} V_{\text{pair}}(\vec{k},\vec{q})\ \langle\hat{c}^{\dagger}_{\vec{k}\uparrow}\hat{c}^{\dagger}_{-\vec{k}\downarrow}\rangle\ \hat{c}_{-\vec{q}\downarrow}\hat{c}_{\vec{q}\uparrow}}_{\overset{\vec{k}\leftrightarrow\vec{q}}{=}\Delta^{*}_{\vec{k}}}] \\
&= \sum_{\vec{k}}[\hat{c}^{\dagger}_{\vec{k}\uparrow}\varepsilon(\vec{k})\ \hat{c}_{\vec{k}\uparrow} - \hat{c}_{-\vec{k}\downarrow}\varepsilon(-\vec{k})\ \hat{c}^{\dagger}_{-\vec{k}\downarrow} + \hat{c}^{\dagger}_{\vec{k}\uparrow}\Delta_{\vec{k}}\hat{c}^{\dagger}_{-\vec{k}\downarrow} + \hat{c}_{-\vec{k}\downarrow}\Delta^{*}_{\vec{k}}\hat{c}_{\vec{k}\uparrow}] \\
&\quad + \underbrace{\sum_{\vec{k}}\varepsilon(\vec{k}) - \frac{1}{N}\sum_{\vec{k}\vec{q}} V_{\text{pair}}(\vec{k},\vec{q})\ \langle\hat{c}^{\dagger}_{\vec{k}\uparrow}\hat{c}^{\dagger}_{-\vec{k}\downarrow}\rangle\langle\hat{c}_{-\vec{q}\downarrow}\hat{c}_{\vec{q}\uparrow}\rangle}_{\mathcal{K}}
\end{aligned} \tag{2.131}$$

with the order parameter (Eq. 2.129) of the pairing field

$$\Delta_{\vec{k}} = \frac{1}{N}\sum_{\vec{q}} V_{\text{pair}}(\vec{k},\vec{q})\langle\hat{c}_{-\vec{q}\downarrow}\hat{c}_{\vec{q}\uparrow}\rangle\ . \tag{2.132}$$

Now, the Nambu formalism can be applied, and the resulting 2×2 matrix can be diagonalized

$$\begin{aligned}\hat{H}_{\text{pair}} &= \sum_{\vec{k}} \left[\begin{pmatrix} \hat{c}^{\dagger}_{\vec{k}\uparrow} & \hat{c}_{-\vec{k}\downarrow} \end{pmatrix} \begin{pmatrix} \varepsilon(\vec{k}) & \Delta_{\vec{k}} \\ \Delta^{*}_{\vec{k}} & -\varepsilon(-\vec{k}) \end{pmatrix} \begin{pmatrix} \hat{c}_{\vec{k}\uparrow} \\ \hat{c}^{\dagger}_{-\vec{k}\downarrow} \end{pmatrix} \right] \\ &= \sum_{\vec{k}} \left[\begin{pmatrix} \hat{c}^{\dagger}_{\vec{k}\uparrow} & \hat{c}_{-\vec{k}\downarrow} \end{pmatrix} \mathbf{U} \begin{pmatrix} +\sqrt{(\varepsilon(\vec{k}))^2 + |\Delta_{\vec{k}}|^2} & 0 \\ 0 & -\sqrt{(\varepsilon(\vec{k}))^2 + |\Delta_{\vec{k}}|^2} \end{pmatrix} \mathbf{U}^{T} \begin{pmatrix} \hat{c}_{\vec{k}\uparrow} \\ \hat{c}^{\dagger}_{-\vec{k}\downarrow} \end{pmatrix} \right] .\end{aligned} \tag{2.133}$$

Here, the additional constant $\mathcal{K}$ is neglected because it shifts only the ground-state energy [162]. The modified creation and annihilation operators $\begin{pmatrix} \hat{a}^{\dagger}_{\vec{k}} \\ \hat{a}_{-\vec{k}} \end{pmatrix} := \mathbf{U}^{T} \begin{pmatrix} \hat{c}_{\vec{k}\uparrow} \\ \hat{c}^{\dagger}_{-\vec{k}\downarrow} \end{pmatrix}$ are linear combinations of the bare electron creation and annihilation operators. Thus, the Bogoliubov-transform matrix $\mathbf{U}$ mix up electrons and holes, so $\hat{a}^{\dagger}_{\vec{k}}$ correspond to quasiparticles. The Hamiltonian can be written in these new creation and annihilation operators, so

$$\begin{aligned}\hat{H}_{\text{pair}} &= \sum_{\vec{k}} \mathcal{E}(\vec{k}) \left(\hat{a}^{\dagger}_{\vec{k}\uparrow} \hat{a}_{\vec{k}\uparrow} - \hat{a}_{\vec{k}\downarrow} \hat{a}^{\dagger}_{\vec{k}\downarrow} \right) + \mathcal{K} \\ &= \sum_{\sigma} \sum_{\vec{k}} \mathcal{E}(\vec{k})\, \hat{a}^{\dagger}_{\vec{k}\sigma} \hat{a}_{\vec{k}\sigma} + \underbrace{\mathcal{K} - \mathcal{E}(\vec{k})}_{\tilde{\mathcal{K}}}\end{aligned} \tag{2.134}$$

with $\mathcal{E}(\vec{k}) = \sqrt{(\varepsilon(\vec{k}))^2 + |\Delta_{\vec{k}}|^2}$ being the one-particle excitation energies of the quasi-particles. The grand potential corresponding to this Hamiltonian reads

$$\Omega = -T \sum_{\vec{k}} \ln \left(1 + \mathrm{e}^{-\frac{\mathcal{E}(\vec{k})}{T}} \right) + \sum_{\vec{k}} \varepsilon(\vec{k}) + \sum_{\vec{k}} \mathcal{E}(\vec{k}) - \sum_{\vec{k}} \langle \hat{c}^{\dagger}_{\vec{k}\uparrow} \hat{c}^{\dagger}_{-\vec{k}\downarrow} \rangle \Delta_{\vec{k}} \tag{2.135}$$

and its stationary points with respect to the pairing fields define the gap equation of the pairing state to [162]

$$\frac{\partial \Omega}{\partial \langle \hat{c}^{\dagger}_{\vec{k}\uparrow} \hat{c}^{\dagger}_{-\vec{k}\downarrow} \rangle} = 0 \quad \Leftrightarrow \quad \Delta_{\vec{k}} = -\frac{1}{N} \sum_{\sigma} \sum_{\vec{q}} V_{\text{pair}}(\vec{k}, \vec{q})\, \frac{\Delta_{\vec{q}}}{2\mathcal{E}(\vec{q})} \tanh \left(\frac{\mathcal{E}(\vec{q})}{2T} \right) . \tag{2.136}$$

The form factor of the gap can be solved iteratively because Eq. 2.136 provides a self-consistency check. At the start, one can use the form factors of Eq. 2.129. At convergence, one can calculate Ω by inserting Eq. 2.136 into Eq. 2.135:

$$\begin{aligned}\Omega_{\text{stat}} &= -T\sum_{\sigma}\sum_{\vec{k}}\ln\left(1+\mathrm{e}^{-\frac{\mathcal{E}(\vec{k})}{T}}\right)+\sum_{\vec{k}}\varepsilon(\vec{k})+\sum_{\vec{k}}\mathcal{E}(\vec{k})\\ &\quad-\sum_{\vec{k}}\langle\hat{c}^{\dagger}_{\vec{k}\uparrow}\hat{c}^{\dagger}_{-\vec{k}\downarrow}\rangle\left(-\frac{1}{N}\sum_{\vec{q}}V_{\text{pair}}(\vec{k},\vec{q})\,\frac{\Delta_{\vec{q}}}{2\mathcal{E}(\vec{q})}\tanh\left(\frac{\mathcal{E}(\vec{q})}{2T}\right)\right)\\ &= -T\sum_{\sigma}\sum_{\vec{k}}\ln\left(1+\mathrm{e}^{-\frac{\mathcal{E}(\vec{k})}{T}}\right)+\sum_{\vec{k}}\varepsilon(\vec{k})+\sum_{\vec{k}}\mathcal{E}(\vec{k})\\ &\quad+\sum_{\vec{q}}\frac{\Delta^{*}_{\vec{q}}\Delta_{\vec{q}}}{2\mathcal{E}(\vec{q})}\tanh\left(\frac{\mathcal{E}(\vec{q})}{2T}\right)\end{aligned}\tag{2.137}$$

Now, the grand potential of all decoupled orders can be calculated. The order with the lowest one is realized. Also, if more than one possible form factors are competing, e.g. if there is a degeneracy in eigenvalues, the most favorable can be determined. Also a linear combination might be realized.

2.6.5 Visualization of Competing Orders

With the theoretical background of the latter sections, it is possible to picture distinct orders. The flow of the leading eigenvalues in various channels, e.g. plotted in Fig. 2.21, gives a first hint for the competition between different orders. The final confirmation needs the iterative solution of the gap equation (Eq. 2.136) with a subsequent evaluation of the grand potential (Eq.2.137). However, in my results, the channel with the leading eigenvalue had the lowest grand potential.

When any element in the coupling function $V(k_1,k_2,k_3)$ exceeds the predefined threshold, the fRG-flow has to be aborted. Now, $V(k_1,k_2,k_3)$ is an effective vertex which is not homogeneous any more but includes dominant and suppressed scattering processes. These channels can be extracted by the mean-field decoupling described in the latter section. But the dominating channel is also visible in the final vertex, as presented in Fig. 2.22 for a simple one-band Hamiltonian in the quadratic lattice. Since $V(k_1,k_2,k_3)$ includes three independent momenta, one is fixed to get a two-dimensional density plot representation. Also, the discretization of the BZ into $N = 64$ patches has to be considered. By modifying the parameter setting, the final effective vertex develops distinct patterns, which are characteristic for various long-range orders. At phase transitions, two distinct orders are in a close competition, so the vertex cuts have patterns of both orders and the winner is not obvious. Then, the evaluation of the grand potential is required to determine the realized order. Furthermore, while the patterns in Figs. 2.22b,c are continuously positive or negative, respectively, there is a clear change of sign in Fig. 2.22a. Hence, the SDW and CDW presumably feature an s-wave form factor, while the SC one is more intricate.

This result can be verified by the mean-field decoupling of the final vertex, where the eigenvector corresponding to the leading eigenvalue determines the form factor. Thus, the s-wave form factor of the SDW and the CDW phase can be confirmed (Fig. 2.22e,f). In

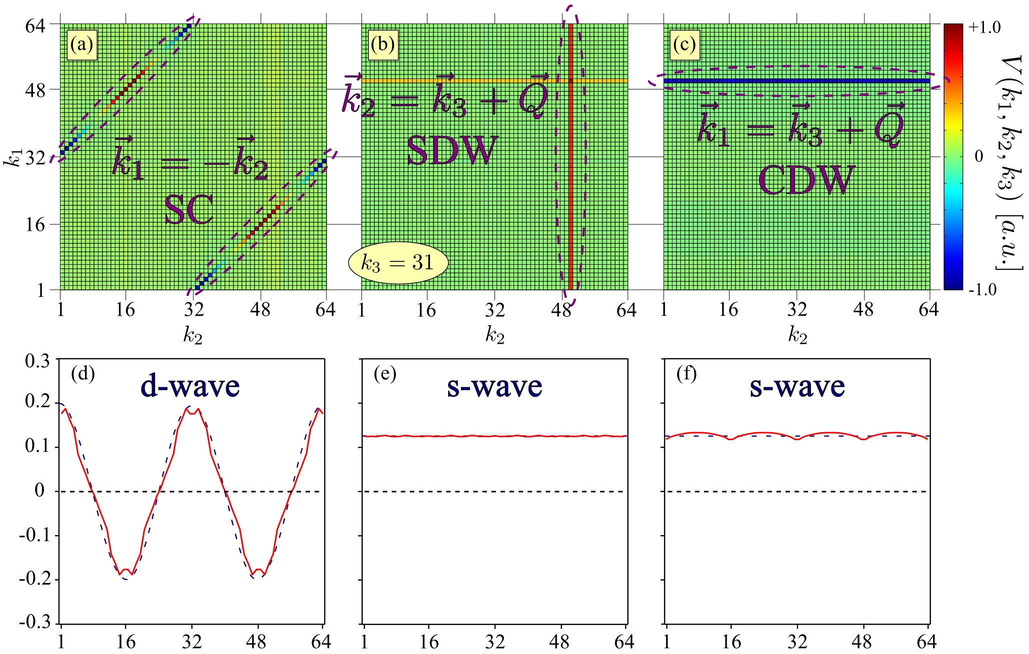

Figure 2.22: **(a-c)** Examples for cuts through the final coupling function $V(k_1,k_2,k_3)$ and **(d-f)** the corresponding form factors for a simple one-band model in the quadratic lattice (see Sec. 2.2 for details). The division of the BZ into 64 patches is plotted in Fig. 2.19a. The 3rd momentum is set to patch 31, while the 4th momentum is fixed by momentum conservation. The particle density is set to $n = 0.5$ and the other parameters are **(a)** $t' = -0.3t$ and $U_0 = 4.0t$, **(b)** $t' = 0$ and $U_0 = 0.4t$ or **(c)** $t' = 0$ and $U_1 = 0.4t$, respectively. Here, the nesting vector is $\vec{Q} = (\pi,\pi)$. For each setting, a representative pattern emerges which has to be compared to the mean-field channels in Eq. 2.130. Hence, the visible phases are superconductivity ((**a**), SC), spin-density wave ((**b**), SDW) and charge-density wave ((**c**), CDW), respectively. **(d)** The SC form factor (solid line) clearly features nodes. A fit to harmonical functions in the quadratic lattice (dashed line) yield a very good correlation to $\cos(k_x) - \cos(k_y)$, which corresponds to d-wave superconductivity with pairs on nearest neighbors. **(e,f)** In the SDW and CDW phase, the form factor does not have any nodes, hence it is of s-wave type.

opposite, the form factor for superconductivity (Fig. 2.22d) includes clear nodes. Now, the harmonical functions of the underlying quadratic lattice have to be considered (see Sec. 2.3 for details). In addition, the distance of the pairs is important. Thus, a pairing between particles on nearest neighbors, next-nearest neighbors, 3rd-nearest neighbors and so on has to be tested. In Fig. 2.22d, the best fit is $\cos(k_x) - \cos(k_y)$, which corresponds to a d-wave pairing between nearest neighbors.

These considerations are based in the momentum space. To get a real-space pattern, one has to perform a Fourier transform (Eq. 2.11). Additionally, the band representation has to be rewritten to an orbital or sublattice representation. For this purpose, the mean-field decoupling of the final vertex (Eq. 2.130) is combined with the Bogoliubov-transform matrix elements $u_{mn}(\vec{k})$. $V(\vec{k}_1,\vec{k}_2,\vec{k}_3,\vec{k}_4)$ depends on four independent momenta and the sublattice structure of the order is unknown, so all combinations of sublattice indices have to be checked. Different possible nesting vectors have also to be considered. After this, the leading eigenvalues determine the dominating phase and the corresponding eigenvectors coincide with the form factors. This reveals a possible real-space pattern. For example, the instability in the charge-density channel in the kagome lattice can clearly be transformed to an expectation value for a directed hopping between sublattices, resulting in a bond-ordered phase, as presented in Sec. 7.4. Otherwise, after the transformation of the spin-density wave channel for graphene, there is no significant sublattice structure. This suggests that the real-space pattern of this SDW phase is intricate. A detailed discussion about that order is given in Sec. 5.6.

2.7 Confrontation of Methods

To conclude this chapter, I present a confrontation of the analytical renormalization group (aRG), the functional renormalization group (fRG) and the variational cluster approach (VCA). There are similarities and distinctions in following properties, with the most important characteristics highlighted by colors:

	aRG	**fRG**	**VCA**
technique	renormalization	renormalization	embedded cluster
coupling	infinitesimal	weak	intermediate - strong
space	momentum	momentum	real
temperature	upper limit for T_c	upper limit for T_c	$T=0$
underlying lattice (Sec. 2.2)	any	any	any
discretization	BZ patching (Fig. 2.19)	BZ patching (Fig. 2.19)	reference cluster (Fig. 2.11)
hopping range	any	any	any
interaction range	any	any	local: exact long range: mean-field level
competing orders	SC only	unbiased	explicit with Weiss fields

Firstly, the appropriate interaction scales from infinitesimal to strong coupling, so the choice of a suitable method is deeply depending on the simulated system.

Furthermore, there are no competing orders in the aRG because this infinitesimal-coupling approach is sensitive only to the superconducting instability. On the other hand, the VCA is capable of including any competing order. But each possible order has to be implemented by an additional Weiss field, increasing the reference-cluster test space. Thus, the optimization of the grand potential is depending on further parameters, essentially increasing the CPU time. Hence, the limitation to a few reasonable Weiss field is recommendable. Only the fRG is totally unbiased without any preselection of competing orders. Thus, also unforeseen long-range orders are detectable. Due to the momentum-space nature of the fRG, the real-space pattern of the dominating order is revealed by a Fourier transform. For some tricky orders, this can be very complicated.

At the end of the theoretical part of my thesis, this overview summarizes the implemented numerical techniques with their fields of application and their features. In the next chapters, these techniques are applied to convenient model systems.

The models and derivations of this chapter give a small insight to the complexity of condensed-matter physics. It is fascinating what intricate systems can be simulated with a sophisticated technique and the results are in good agreement with the experimental data.

The first class of materials considered within this thesis are the high-T_c cuprates. This class includes $\mathsf{La}_{2-x}\mathsf{Ba}_x\mathsf{CuO}_4$, the first-discovered non-phonon-mediated superconductor.

Three-Band versus One-Band Hubbard Model for the high-T_c Cuprates: Pairing Dynamics, Superconductivity and the Ground-State Phase Diagram

3

One central challenge in high-T_c superconductivity is to derive a detailed understanding for the specific role of the copper $\mathrm{Cu}_{d_{x^2-y^2}}$- and oxygen $\mathrm{O}_{p_{x,y}}$-orbital degrees of freedom. In most theoretical studies, an effective one-band Hubbard or t-J model has been used. Here, the physics is that of doping into a Mott-insulator, whereas the actual high-T_c cuprates are doped charge-transfer insulators.

To shed light on the related question, where the material-dependent physics enters, I compare the competing magnetic and superconducting phases in the ground state, the single- and two-particle excitations and, in particular, the pairing interaction and its dynamics in the one- and three-band Hubbard models. The question is, which frequencies are relevant for pairing in the two models as a function of interaction strength and doping. In the three-band models, the interaction in the low- to optimal-doping regime is dominated by retarded pairing due to low-energy spin fluctuations with surprisingly little influence of interband charge fluctuations. On the other hand, in the one-band model, in addition a part comes from "high-energy" excited states (Hubbard band), which may be identified with a non-retarded contribution. These differences between a charge-transfer and a Mott insulator are renormalized away for the ground-state phase diagram of the one- or three-band models, which are in close overall agreement, i.e. are "universal".

The results of this chapter are published with *W. Hanke, M. Aichhorn, S. Brehm* and *E. Arrigoni* in Ref. [1].

3.1 One or Three Bands?

Many aspects of the physics of cuprate high-temperature superconductors remain mysterious, despite impressive progress both on the experimental and theoretical front. One key issue is, why are these composed out of CuO_2 planes and what is the specific role of Cu_d- and O_p-orbital degrees of freedom? The cuprate materials in the undoped, i.e. half-filled situation, are charge-transfer insulators [163, 164]. This fact induces an experimentally observed asymmetry between hole and electron doping: While doped holes go onto O-orbitals and may be bound to Cu spins to form *Zhang-Rice singlets*, doped electrons reside mainly on the Cu-orbitals [165–176]. This is believed to be intimately related to the more extended stability of antiferromagnetic (AF) behavior as a function of electron doping compared to that of hole doping. While introducing electrons on the Cu-sites merely produces a dilution of spins, holes on O-sites create a ferromagnetic coupling between neighboring Cu-orbitals, which is significantly more effective in destroying the AF order. Beyond magnetism, the asymmetry is also exposed in the superconducting (SC) behavior with the hole-doped materials exhibiting SC usually over wide doping regimes and with high T_c's up to 150K, whereas in the electron-doped system T_c is low and confined to a very narrow doping regime.

In much of the high-T_c theoretical studies, the starting point has not been the above three-band Hubbard model but instead the one-band Hubbard and t-J models [84, 165]. Here, the oxygen degrees of freedom are approximately eliminated via the Zhang-Rice construction [165]. The mapping has as a crucial consequence that the undoped model systems are Mott insulators and no longer governed by the charge-transfer energy Δ_{pd} between the Cu- and O-orbitals. Analytical and, in particular, numerical calculations based on these two-dimensional single-band models have demonstrated Fermi surfaces (FS), single-particle spectral weights, AF spin correlations and $d_{x^2-y^2}$ pairing correlations in qualitative agreement with experimental measurements [25,98,106,177–183]. This fact has significantly contributed to the wide-spread belief that the physics of high-T_c cuprates is that of "doping into a Mott insulator" [17]. However, how can this picture be reconciled with the charge-transfer insulator picture embedded in the three-band model? Can it be that the charge-transfer energy Δ_{pd} in the three-band model, the size of which is already decisive for the accuracy of the one-band reduction [165], plays the role of an effective on-site Hubbard U in the one-band models?

Quantifying these ideas requires solving the strongly correlated electron problem for the three- and one-band Hubbard models at very low energy (and/or temperatures). Early Quantum-Monte-Carlo (QMC) calculations for the three-band model showed that characteristic features such as the doping dependence of the electronic single-particle excitations and their interplay with magnetic excitations are in accord with experiment [166, 167]. However, the very low-T or ground-state properties including the SC state, could not be reliably resolved, due to the well-known *minus-sign problem* [184, 185]. The variational cluster approach (VCA, presented in Sec. 2.4) has been shown for the one-band model to correctly reproduce salient features of the ground-state ($T = 0$) phase diagram of the high-T_c cuprates [25, 106, 114, 179]. In particular, the AF and d-wave SC ground-states were found in doping ranges qualitatively in accord with experimental data for both electron and hole doping such as the different stability of the AF phase, in good agreement with experimental data (for a review, see Ref. [12]). It can be accounted for by a simple one-band model where the electron-hole symmetry is broken by a longer-ranged (next-nearest) hopping term [186]. Regarding the possibility of the reduction to a one-band model, there are questions concerning the direct applicability of the Zhang-Rice construction. As discussed in the literature before [171], the natural tendency of a finite oxygen band width is to delocalize and to destabilize the Zhang-Rice singlets. Secondly, the pragmatic finding that a t-t'-U one-band model with a significant value of t', captures basic physics of the cuprates and in particular their electron-hole asymmetry, cannot be accounted for in a strict Zhang-Rice picture [187]. In

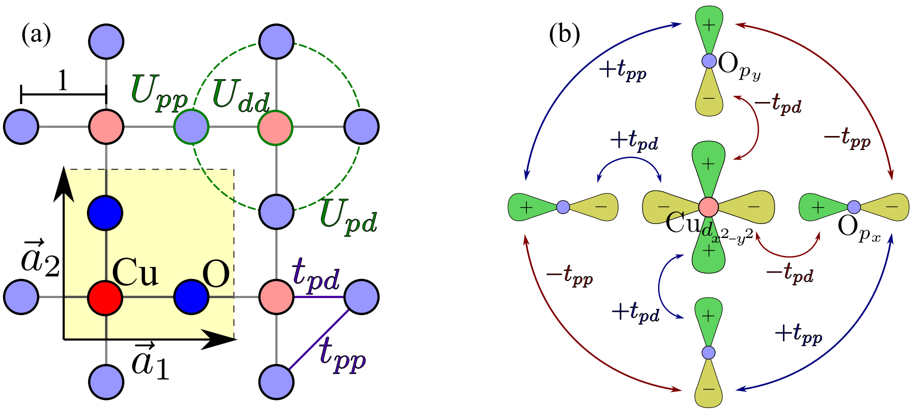

Figure 3.1: (a) Quadratic lattice with one Cu- and two-O sites per unit cell. **(b)** Orbital phase factors for Cu$_d$-O$_p$ hopping t_{pd} and direct O$_p$-O$_p$ hopping t_{pp}.

this picture, next-nearest-neighbor hoppings are very small compared to nearest neighbor terms (if again O-O hopping t_{pp} is taken into account).

What I will show in this chapter is that the three-band Hubbard model and a one-band t-t'-U Hubbard model with a significant value for t' (which may be taken as an empirical parameter adjusted to fit the Fermi-surface topology [188]) exhibit a similar low-energy (here specifically, $T = 0$) physics concerning the qualitative behavior of the ground-state phase diagram [106] and of the single-particle excitations including the asymmetry as a function of electron and hole doping.

3.2 Models and Reference Clusters

The starting point is a two-dimensional three-band Hubbard model (Sec. 2.1), with a unit cell featuring one Cu- and two O-sites. Using the Pauli exclusion principle maximal one spin-up and one spin-down electron are permitted at one site. A further approximation is that the Coulomb interaction is restricted to electrons on the same sites or on nearest neighbors. Finally, only nearest-neighbor hopping is considered:

$$\begin{aligned}\hat{H}_{3\mathrm{BHM}} = &- t_{pd}\sum_{\langle i,j\rangle}\sum_{\sigma}\left(\hat{d}^{\dagger}_{i\sigma}\hat{p}_{j\sigma}+\mathrm{H.c.}\right)+t_{pp}\sum_{\langle j,j'\rangle}\sum_{\sigma}\left(\hat{p}^{\dagger}_{j\sigma}\hat{p}_{j'\sigma}+\mathrm{H.c.}\right)\\ &+U_{dd}\sum_{i}\hat{n}^{d}_{i\uparrow}\hat{n}^{d}_{i\downarrow}+U_{pp}\sum_{j}\hat{n}^{p}_{j\uparrow}\hat{n}^{p}_{j\downarrow}+U_{pd}\sum_{\langle i,j\rangle}\sum_{\sigma,\sigma'}\hat{n}^{d}_{i\sigma}\hat{n}^{p}_{j\sigma'}\\ &-(\varepsilon_d-\mu)\sum_{i}\sum_{\sigma}\hat{n}^{d}_{i\sigma}-(\varepsilon_p-\mu)\sum_{j}\sum_{\sigma}\hat{n}^{p}_{j\sigma}\,.\end{aligned} \tag{3.1}$$

Here $\hat{d}^{\dagger}_{i\sigma}$ creates a hole with spin σ in the Cu$_{d_{x^2-y^2}}$-orbital at site i and $\hat{p}^{\dagger}_{j\sigma}$ creates a hole with spin σ in the O$_{p_{x,y}}$-orbital at site j. t_{pd} represents the Cu-O hybridization while t_{pp} stands for direct O-O-hopping. Both hoppings are restricted to nearest neighbors, indicated by $\langle i,j\rangle$ with phase factor depicted in Fig. 3.1b. The occupation numbers are $\hat{n}^{d}_{i\sigma}=\hat{d}^{\dagger}_{i\sigma}\hat{d}_{i\sigma}$ and $\hat{n}^{p}_{j\sigma}=\hat{p}^{\dagger}_{j\sigma}\hat{p}_{j\sigma}$. U_{dd} represents the Coulomb interaction between holes on Cu-sites and U_{pp} on O-sites respectively, while U_{pd} interacts between nearest-neighbor Cu- and O-sites. Additionally to chemical potential μ, local orbital levels ε_d and ε_p are introduced. This three-band Hubbard model is a charge-transfer insulator with charge-transfer energy $\Delta = \varepsilon_p - \varepsilon_d$. $t_{pd} = 1$ is set as energy unit, $t_{pp} = 0.5$, $U_{dd} = 8.0$, $U_{pp} = 3.5$, $U_{pd} = 0.5$ and $\Delta = 3.0$. The parameters are calculated within the constrained density-functional theory [189] and are consistent with earlier extensive Quantum-Monte-Carlo (QMC) [166, 167] as well as cluster [188, 190] calculations. In addition, the long-range Coulomb interaction U_{pd} between holes on Cu- and O-sites is implemented with periodic boundary conditions. The particle density of the lattice is given by

$$\langle n \rangle = -\frac{1}{\pi L_c} \sum_{\vec{k}} \sum_{\sigma} \int_{-\infty}^{0} \mathrm{d}\omega \, \mathrm{Im} \left(\sum_{ij} \sum_{\alpha\beta} G_{i\alpha j\beta\sigma}(\omega + \mathrm{i}\eta) \, \mathrm{e}^{\mathrm{i}\vec{k}(\vec{r}_i - \vec{r}_j)} \right) \qquad \text{with } \eta \to 0 \,, \quad (3.2)$$

with the sites in the reference cluster L_c and the Green's function G of the lattice. The sublattice indices α and β indicate a $\mathrm{Cu}_{d_{x^2-y^2}}$-orbital or an $\mathrm{O}_{p_{x,y}}$-orbital, respectively. Furthermore, Eq. 3.2 is equivalent to $\langle n \rangle = -\frac{\partial \Omega}{\partial \mu}$ [106].

A further simplification is the elimination of the oxygen degrees of freedom by a Zhang-Rice construction [165] to fit a one-band Hubbard model. Then, the undoped system is not a charge-transfer insulator any more but a Mott insulator [17]. Here, the Hamiltonian reads

$$\begin{aligned} \hat{H}_{\mathrm{1BHM}} = & -t \sum_{\langle i,j \rangle} \sum_{\sigma} \left(\hat{c}^{\dagger}_{i\sigma} \hat{c}_{j\sigma} + \mathrm{H.c.} \right) - t' \sum_{\ll i,j \gg} \sum_{\sigma} \left(\hat{c}^{\dagger}_{i\sigma} \hat{c}_{j\sigma} + \mathrm{H.c.} \right) \\ & + U \sum_i \hat{n}_{i\uparrow} \hat{n}_{i\downarrow} - \mu \sum_i \left(\hat{n}_{i\uparrow} + \hat{n}_{i\downarrow} \right) \end{aligned} \quad (3.3)$$

with the same notations as for the three-band model (Eq. 3.1). Additionally, $\ll i, j \gg$ indicates next-nearest-neighbor hopping and all creators are restricted to the $\mathrm{Cu}_{d_{x^2-y^2}}$-orbital. Again the energy unit is $t = 1$.

An important remark for the comparison of the two models is that one has to set $t_{pd} \cong 1.5\mathrm{eV}$ and $t \cong 0.4\mathrm{eV}$ [189] when going back to an absolute energy scale.

To test the affinity of the models to superconductivity and antiferromagnetism, some symmetry-breaking Weiss fields

$$\begin{aligned} \hat{H}_{\mathrm{AF}} &= h'_{\mathrm{AF}} \sum_i \left(\hat{n}_{i\uparrow} - \hat{n}_{i\downarrow} \right) \mathrm{e}^{\mathrm{i}\vec{Q}\vec{R}_i} \qquad \text{and} \\ \hat{H}_{\mathrm{SC}} &= h'_{\mathrm{SC}} \sum_{\langle i,j \rangle} \frac{\xi_{ij}}{2} \left(\hat{c}^{\dagger}_{i\uparrow} \hat{c}^{\dagger}_{j\downarrow} + \hat{c}_{j\downarrow} \hat{c}_{i\uparrow} \right) \,, \end{aligned} \quad (3.4)$$

are introduced [105, 106]. h'_{AF} is a quantity for the strength of a staggered magnetic field with ordering vector $\vec{Q}_{\mathrm{AF}} = (\pi/\pi)$, while h'_{SC} is the strength of a d-wave superconductivity pairing field. The d-wave symmetry is ensured by the factor

$$\xi_{ij} = \begin{cases} +1, & \text{if} \quad \vec{R}_i - \vec{R}_j \in \{\leftarrow, \rightarrow\} \\ -1, & \text{if} \quad \vec{R}_i - \vec{R}_j \in \{\uparrow, \downarrow\} \end{cases} \,. \quad (3.5)$$

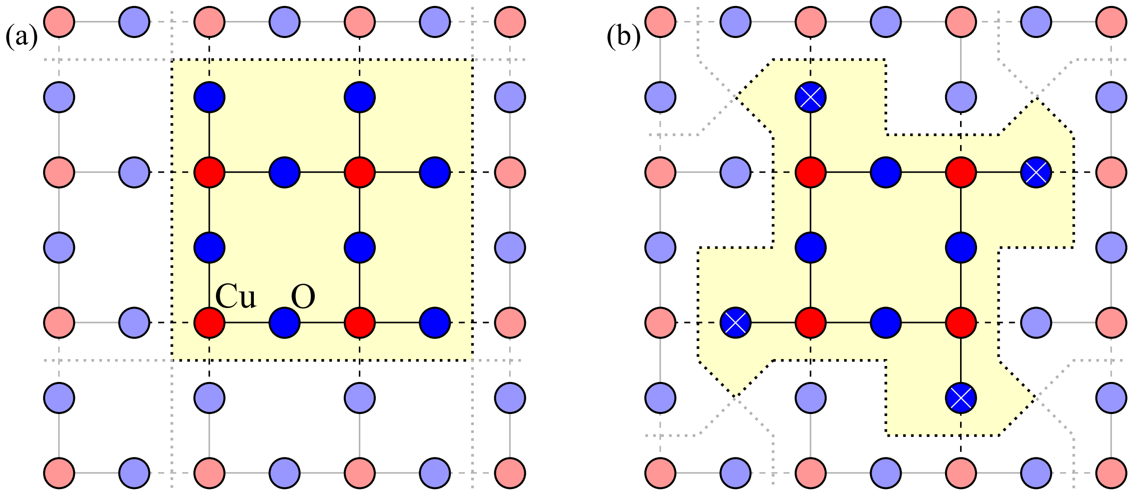

Figure 3.2: Two possible fragmentations of the lattice into clusters with 12 sites ($4 \cdot \mathrm{CuO_2}$): **(a)** straightforward fragmentation from Ref. [114]. **(b)** A more symmetric arrangement of O-sites. A third possibility has the same geometry as **(b)** but with an additional Weiss field at the "outer" O-sites of the cluster (marked with "X") (Eq. 3.7).

For the three-band model, these fields are restricted to the Cu-sites. The phases represented by these Weiss fields are characterized by order parameters which can be defined in a modification to Eq. 3.2 as

$$\begin{aligned}
\langle \mathrm{AF} \rangle &= -\frac{1}{\pi L_c}\sum_{\vec{k}}\sum_{\sigma}\int_{-\infty}^{0} \mathrm{d}\omega\, \mathrm{Im}\left(\sigma' \sum_{ij}\sum_{\alpha\beta} G_{i\alpha j\beta\sigma}(\omega+\mathrm{i}\eta)\, \mathrm{e}^{\mathrm{i}\vec{k}(\vec{r}_i-\vec{r}_j)}\, \mathrm{e}^{\mathrm{i}\vec{Q}_{\mathrm{AF}}(\vec{r}_i-\vec{r}_j)}\right) \\
\langle \mathrm{SC} \rangle &= -\frac{1}{\pi L_c}\sum_{\vec{k}}\sum_{\sigma}\int_{-\infty}^{0} \mathrm{d}\omega\, \mathrm{Im}\left(\sum_{ij}\sum_{\alpha\beta} F_{i\alpha j\beta\sigma\bar{\sigma}}(\omega+\mathrm{i}\eta)\, \mathrm{e}^{\mathrm{i}\vec{k}(\vec{r}_i-\vec{r}_j)}\, (\cos(k_x)-\cos(k_y))\right)
\end{aligned} \tag{3.6}$$

and $\eta \to 0$. F indicates the anomalous Green's function of the lattice, $\bar{\sigma}$ is identical to $-\sigma$. It is $\sigma' = 1$ for $\sigma = \uparrow$ and $\sigma' = -1$ for $\sigma = \downarrow$ [106]. But is has to be deliberated that the Weiss fields h'_{AF} and h'_{SC} are not identical with the physical fields h_{AF} and h_{SC}: The Weiss fields, as all other variational parameters, act only on the reference-cluster level. Within the VCA, these parameters are subtracted and, consequently, they are not present in the infinite lattice. In addition to these two physically motivated Weiss fields, I implemented a secondary chemical potential

$$\hat{H}_\mu = h'_\mu \sum_{\sigma} \sum_{\substack{j \\ \in \text{ outer O}}} \hat{n}^{p}_{j\sigma} \,, \tag{3.7}$$

which acts as a Weiss field at the outer O-sites of the cluster. The idea behind this expansion is to get a more uniform particle density on the O-sites of the reference cluster. The motivation for this explained later in this section. A similar variational parameter was introduced by *M. Knap et al.* for a one-dimensional chain without periodic boundary conditions [191]: They added a fictional chemical potential to the two border sites of

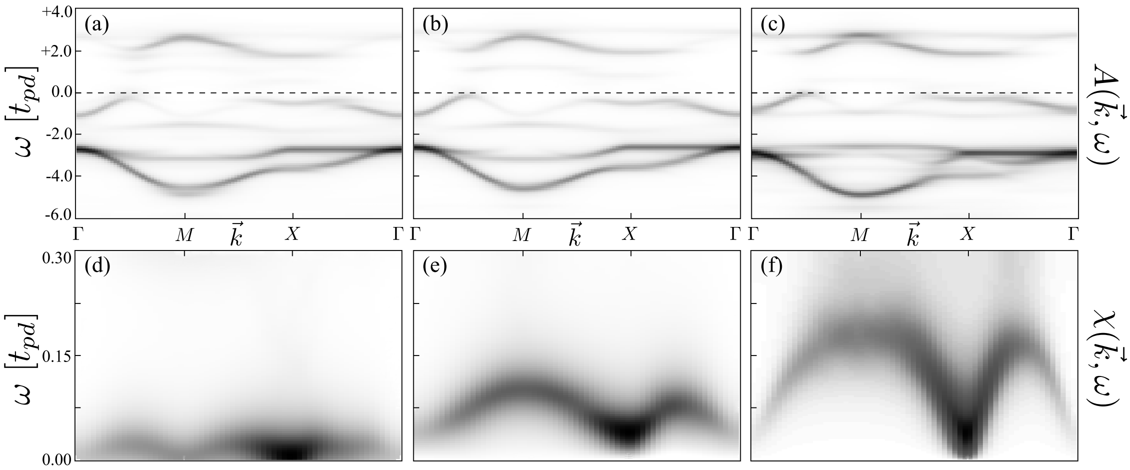

Figure 3.3: Scenario for the three-band model at 3% hole doping for various reference clusters: **(a,d)** "standard" cluster (Fig. 3.2a), **(b,e)** symmetric cluster (Fig. 3.2b), **(c,f)** symmetric cluster with additional chemical potential on the outer O-sites (Fig. 3.2b with Eq. 3.7). VCA results for these clusters are showing **(a-c)** the spectral function $A(\vec{k},\omega)$ as example for a one-particle excitation and **(d-e)** the transversal spin susceptibility $\chi(\vec{k},\omega)$ as example for a two-particle excitation.
While $A(\vec{k},\omega)$ shows only a small dependence on the reference cluster, the effects on $\chi(\vec{k},\omega)$ are very dramatic. Subfigure **(f)** has the best agreement with the one-band model in Ref. [113].

the chain to reduce the effects of the open boundary conditions. Although an additional variational parameter is always allowed in VCA, they justified this new parameter from perturbation theory to get a physically coherent picture [191].

In the end, up to three variational parameters have to be optimized, depending on the phase: μ', h'_{AF}, h'_{SC}. Furthermore, h'_{μ} has to be optimized for a homogeneous particle density on the O-sites of the reference cluster.

As stated in Sec. 2.4.2, the choice of the reference cluster of the VCA plays a crucial role: Only correlations within the cluster are exactly calculated. All long-range hoppings, correlations and orders are perturbatively treated, although the strong variational principle optimizes the results. Hence, the reference cluster has to be as large as possible. For the three-band model, a 2×2 cluster with 4 $\mathrm{CuO_2}$ unit-cells can be solved in a reasonable amount of CPU time. This is effectively a 12-site cluster, filled with 20 particles in the undoped case: At $T = 0$K, the O-sites are completely filled (16 electrons on 8 sites), while the Cu-sites are half filled (4 electrons on 4 sites). For simplicity, a particle-hole transformation is executed: In Eq. 3.1, the creation and annihilation operators act on holes, so there are 4 particles (holes) on 12 sites in the undoped ground state. At first glance, the shape of the cluster seems to have a minor influence on the results: Both, the one-particle excitations, e.q. the spectral function [109], and the two-particle excitations, e.q. the spin susceptibility [113], do not show serious discrepancies when changing the reference cluster, although some minor finite size effects occur. Indeed, the earlier results for the three-band model phase diagram and the spectral function have been in close agreement to the one-band model results [114]. There, a "standard" 2×2 layout had been used (Fig. 3.2a).

In this thesis, the two-particle excitations are added to the three-band Hubbard model

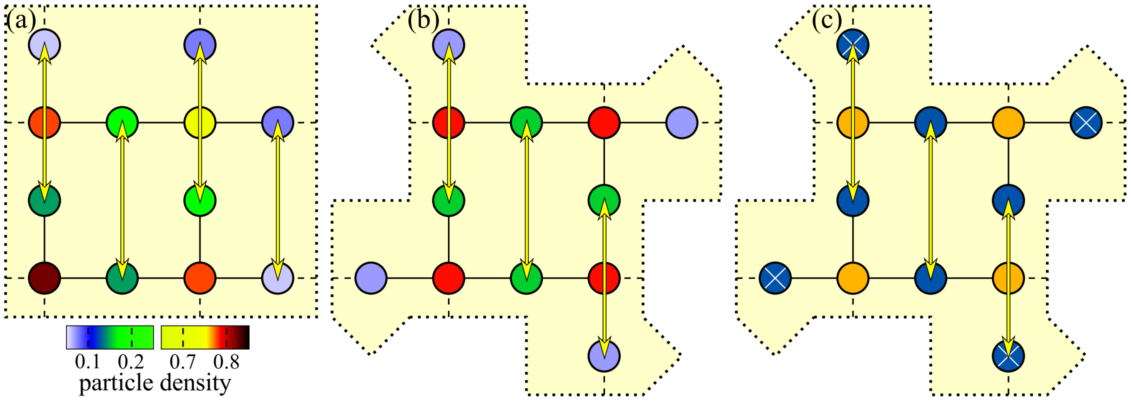

Figure 3.4: Calculated ground-state particle densities for the three-band model (3% hole doped) in various reference clusters. **(a)** "Standard" cluster, **(b)** symmetric cluster, **(c)** symmetric cluster with additional chemical potential on the outer O-sites (marked with "X"). The yellow double arrows indicate possible correlations between particles on two distinct sites within the cluster. From **(a)** to **(c)**, the particle densities on these sites are getting more uniform, so the translational symmetry of the infinite lattice is better approximated.

and calculated within the VCA (for details, read Sec. 2.4.4). When the "standard" cluster is used, the results for the transversal spin susceptibility $\chi(\vec{k},\omega)$, plotted in Fig. 3.3d, has substantial differences to both the one-band calculations in Ref. [113] and experiments in Ref. [192]: The magnon mode is very narrow. A possible solution for this artifact in the three-band model is a new arrangement of the reference cluster: If the O-site are ordered in the more symmetric composition (Fig. 3.2b), $\chi(\vec{k},\omega)$ develops a clear magnon mode, presented in Fig. 3.3e. On the other hand, it is remarkable that the spectral function $A(\vec{k},\omega)$, a one-particle excitation, undergoes only minimal changes (compare Figs. 3.3a vs. b). The crucial question is: What effect influences the two-particle excitations so drastically but neglects the one-particle ones?

A look on the particle densities of the reference cluster clarifies the discrepancies (Figs. 3.4a,b): For the two-particle excitations, the particle densities of two sites have to be considered. The red double arrows connect sites with the same vector, so the VCA spin susceptibility for these pairs should be equal (due to translational invariance of the infinite lattice). Certainly, the limited cluster has some finite size effects, but the VCA gets the "best possible approach". Obviously, the projection of the two-particle excitations to the infinite lattice is more effected by inhomogeneities than the one-particle excitations. The symmetric composition of the O-sites rearranges the particle densities on these sites, so the red arrows connect pairs with similar densities. If the homogeneous distribution of particles densities improves the approach for the two-particle excitations, a further step might be useful: By the introduction of an additional chemical potential on the "outer" O-sites (Eq. 3.7), the particles densities are rearranged again. This additional field acts at the reference cluster, but the VCA subtracts it, so it does not exist one the infinite lattice. The idea is to choose the additional potential to fix the differences of the ground-state particle densities on the O-sites. Then, the two-particle correlations will form at sites with identical particle densities, as indicated in Fig. 3.4c. The excited states may stay inhomogeneous, but the uniform ground state is dominating. The results of this symmetric cluster with enforced equability of particle densities are presented in Figs. 3.3c,f. While

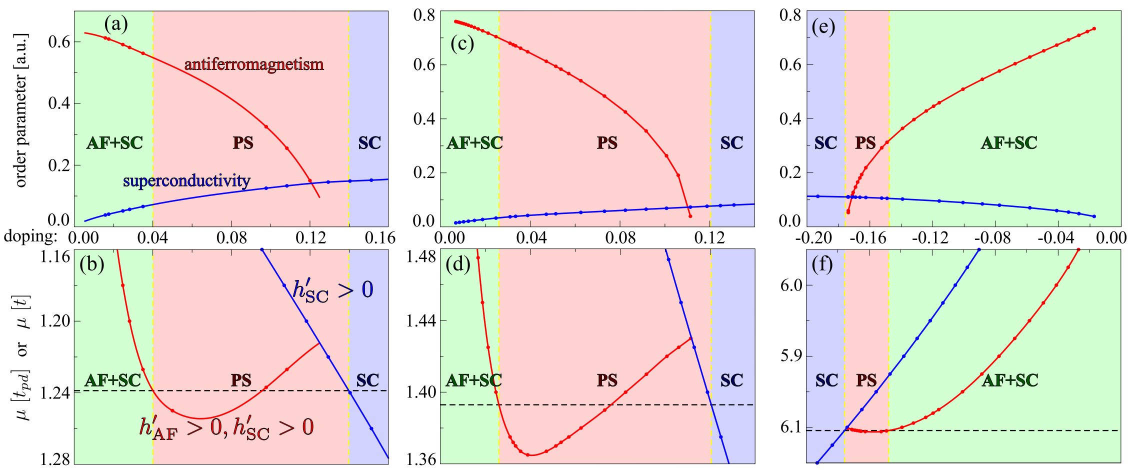

Figure 3.5: **(a,b)** Ground-state phase diagram for the three-band model, based on a 2×2 reference cluster. **(c-f)** For comparison, the one-band model based on a 4×2 reference cluster. In **(b,d,f)**, the chemical potential μ is plotted as a function of doping. The corresponding order parameters for the models are given in **(a,c,e)**. Between the mixed phase with both antiferromagnetic and superconducting order (AF+SC) and the pure superconducting phase (SC) at higher dopings, is a region of phase separation (PS), described in text. For the one-band model, both hole **(c,d)** and electron **(e,f)** doping is presented.
There is no qualitative difference between the phase diagrams of the three-band and the one-band model.

the spectral function is unaffected again, the spin susceptibility is further improved: The magnon mode is getting broader, so the bandwidth of the mode fits to the one-band model calculations in Ref. [113] (different energy units have to be considered). Therefore, in the next sections, I use the reference cluster in Fig. 3.2b with an additional chemical potential on the outer O-sites if the interest is on two-particle excitations. On the other hand, if only one-particle excitations are considered, the additional Weiss field is omitted because the additional parameter drastically increases the CPU time,

3.3 Ground-State Phase Diagram

The phase-diagram results of the three- and the one-band model presented in Figs. 3.5a,c are very similar, reproducing in both cases the overall ground-state phase diagram of the high-T_c superconductors (see also Fig. 3 of Ref. [114] or Fig. 1.2). In particular, they include salient features, such as the enhanced robustness of the AF state as a function of electron doping and the tendency towards phase separation ("PS" regime) into a mixed AF-SC phase at low doping and a pure SC phase at high (both hole and electron) doping. In the low-doping regimes, there is a homogeneous symmetry-broken state in which both the AF order parameter m and the d-wave SC order parameters Δ are nonzero. This corresponds to a phase "AF+SC", where AF and d-wave SC order microscopically coexist. A homogeneous state with pure d-wave SC ($m = 0$ and $\Delta > 0$) is obtained in the larger doping regimes. In the intermediate doping regions, a macroscopic phase separation occurs, where these two latter phases are thermodynamically unstable. *M. Aichhorn et al.* have shown for the one-band model

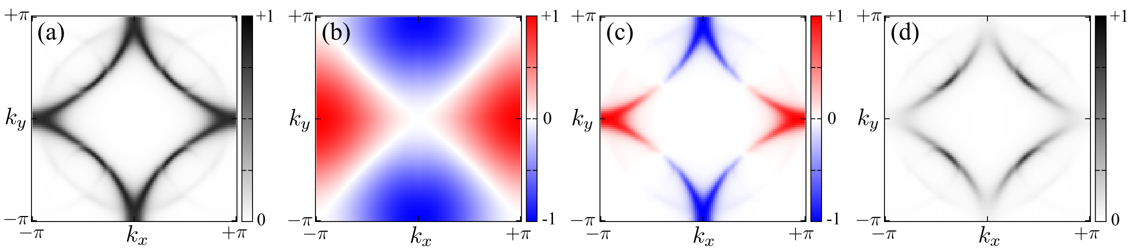

Figure 3.6: Fermi surface (FS) of the 15% hole-doped three-band model. **(a)** With the Weiss field $h'_{\mathrm{SC}} = 0$, the system is in a non-superconducting state. Hence, the one-particle excitations are gapless, resulting in a closed FS. **(b)** The d-wave form factor in the Brillouin zone. **(c)** The anomalous part of the Nambu self-energy at the FS. **(d)** Same as **(a)** but with optimized h'_{SC}. Here, the one-particle excitations are partially gaped. The FS is reduced to the nodal region of the superconducting gap ("Fermi arcs").

that larger reference clusters still yield a qualitatively similar phase diagram, with one notable exception: The larger clusters (up to 10 sites in the one-band model) results suggest that phase separation remains persistent in the hole-doped case and disappears in the electron-doped situation [106]. Based on the overall very similar phase diagrams for the 2×2 three-band model and for the 4×2 one-band model (Fig. 3.5b,d), it is obvious to expect a similar disappearance of the PS-region for electron doping also in the three-band model.

Why are the phase diagrams in Fig. 3.5 so similar despite the fact that, for example, the interband-charge fluctuations give rise to an - at higher energies $(\omega \sim \Delta_{pd})$ even qualitatively - different behavior of the dynamic pairing interaction for the three-band results when compared to the one-band data (e.g. see the gap function $I(\vec{k},\Omega)$ in Fig. 3.12 and Fig. 3.13)? The reason is that on the scale of the (maximal) d-wave gap energies, Δ_{pd} is a doping-independent "high-energy" scale ($\sim$ ten times larger than the SC gap) the role of which is taken over in the one-band model by another doping independent "high-energy" scale, namely an effective Hubbard U (see discussions, below). However, the dynamics of the pairing mechanism may be quite different. This is expected to be of importance for the "non-universality" , i.e. material-dependence of the cuprate SC.

In summary, the low-energy single-particle excitations of the three- and one-band Hubbard model are qualitatively similar, when comparing the three-band model with the empirical t-t'-U model. The corresponding nodal and anti-nodal doping regimes are directly related to the observed asymmetry in the robustness of the AF order. On closer inspection, however, there are some differences for higher energies of $O(t_{pd})$. An example is the recently much discussed "waterfall" structure or high-energy kink appearing as an abrupt change in the band dispersion, which falls vertically at binding energies below $\approx 0.4eV$ [193–195]. This "waterfall" behavior is found to be rather pronounced in the three-band model but not in the one-band model. In VCA calculations by *D. Katakiri et. al* [196], they study the relationship between charge-transfer models and the corresponding single-band Hubbard models.

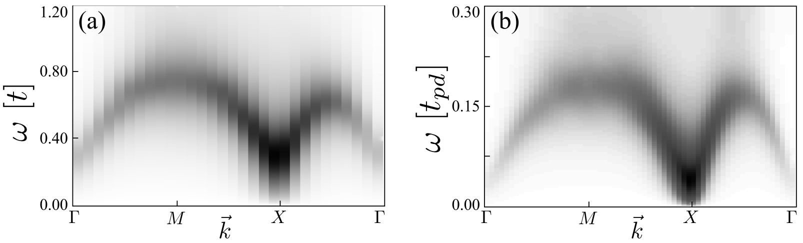

Figure 3.7: Imaginary part of the transversal spin susceptibility $\chi(\vec{k},\omega)$ for a reference system of 2×2 unit cells. **(a)** One-band Hubbard model at 4% hole doping. **(b)** three-band Hubbard model at the same doping. Different energy scales ($t \approx 0.4$eV, $t_{pd} \approx 1.5$eV) have to be considered.

3.4 Magnetic Resonance Mode

When high-T$_c$ cuprate superconductors are in the superconducting phase, inelastic neutron scattering experiments detected a resonant mode at the antiferromagnetic ordering vector $\vec{Q}_{\text{AF}} = (\pi/\pi)$ [197–199]: This collective magnetic resonance mode, which is an artifact of the magnetic parent compound of cuprate superconductors, is outshined usually by the electron-hole spin-flip continuum. However, induced by the d-wave superconducting state, a gap emerges in the continuum, opening a small window where this magnetic mode can be detected. In this sense, the resonant mode is a reminiscent "fingerprint" of the magnetic parent compound. This mode is restricted to the superconducting phase, it is absent even in the pseudogap phase [200]. The VCA is a reasonable choice for simulations because the SC phase is in the strong-coupling regime [201, 202]. The theoretical background for two-particle excitations within the VCA is given in Sec. 2.4.4. Again, the choice of the reference cluster plays a crucial role: The focus is on a weak magnetic mode within the superconducting phase. Unfortunately, the magnon mode (Fig. 3.3f) is very robust on doping: It persists far into the pure superconducting phase. That is the picture for most one-band clusters in Fig. 2.11 as well es for the three-band clusters of Fig. 3.2. A notable exception is the one-band 3×3 cluster: The advantage of this arrangement is (i) the continuation to the next clusters breaks the checkerboard order, so antiferromagnetism is completely suppressed, and (ii) the cluster filling of $8/9$ fits to the target doping of 15% on the lattice, so VCA results are improved. Unfortunately, this choice excludes the three-band clusters: $3 \times 3 \cdot 3 = 27$ sites are out of range, even with state-of-the art supercomputers.

In Ref. [114], as well as in the previous section, the qualitative similarity of the phase diagram and single-particle excitations between the three-band and the one-band Hubbard models was demonstrated. In particular, it was explicitly confirmed that the asymmetry between electron- and hole-doped cuprates, despite being of fundamentally different nature, shows very similar signatures in the single-particle spectrum of both models, provided a next-nearest-neighbor hopping t' is included in the latter one.

The question remains whether this similarity can be extended to two-particle excitations. To address this question, in Fig. 3.7 the imaginary parts of the spin susceptibility evaluated in the deeply underdoped regime ($x = 4\%$) are compared for both the one- and three-band Hubbard model. While there are some minor differences, both spectra display a dispersion which is a remnant of the spin-wave

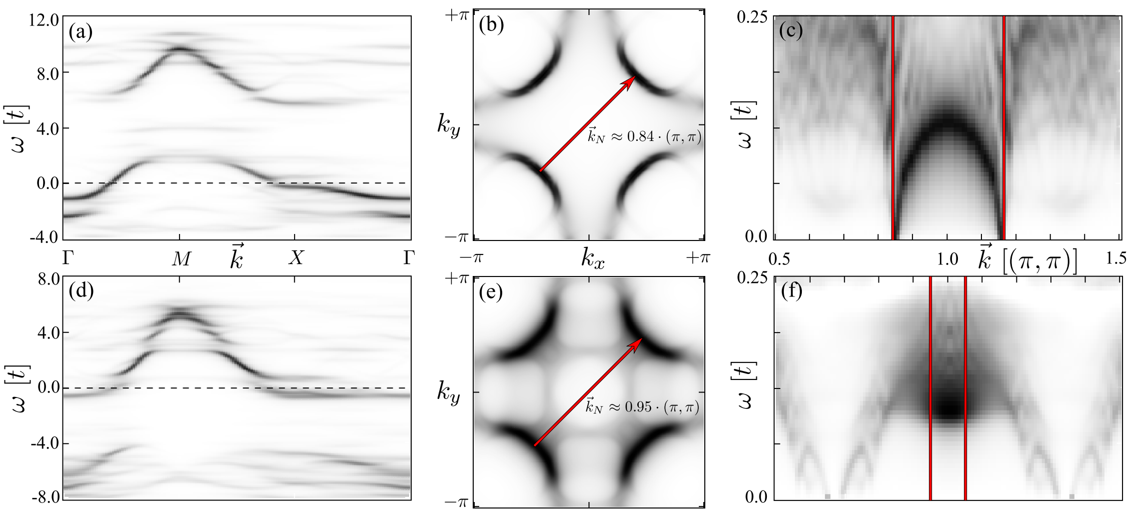

Figure 3.8: Electron vs. hole doping on a one-band 3×3 reference cluster. **(a-c)** 17% hole doped, **(d-f)** 14% electron doped. **(a,d)** The SC gap in the spectral function $A(\vec{k},\omega)$ is within the upper (lower) Hubbard band for the hole (electron) doped situation, respectively. **(b,e)** The FSs are similar, but the nodal vector $\vec{k}_N$ is slightly increased for electron doping. **(c)** For the hole-doped case, the imaginary part of the transversal spin susceptibility $\chi(\vec{k},\omega)$ shows the prominent hour-class structure [113, 198]. **(f)** $\chi(\vec{k},\omega)$ is restricted to narrow limits around $\vec{Q}_{\text{AF}}$ in the electron-doped situation (see text for further details).

band in the antiferromagnetic half-filled phase. This fact signals the presence of strong antiferromagnetic fluctuations at this doping concentration also in a doped charge-transfer insulator.

Last but not least, the VCA-extension to two-particle susceptibilities can account for the magnetic resonance in both hole- and electron-doping regimes, without any adjustable parameters (in contrast to RPA calculations in Refs. [203, 204]). Close to optimal doping, the magnetic spectrum for the hole-doped one-band Hubbard model (Fig. 3.8c) shows the famous magnetic resonance peak at energies of about $0.1t - 0.2t$ and around wave-vector $\vec{Q}_{\text{AF}} = (\pi,\pi)$ [198]. From this resonance, a downward dispersion extends down to the onset of the electron-hole continuum. In Fig. 3.8b, the vector $\vec{k}_N$ connects the FS in the nodal direction, where the d-wave gap function has nodes (Fig. 3.6). Here, electron-hole excitations can occur with $\omega \gtrapprox 0$, Landau damping all collective modes. So, the magnetic resonance mode must form within the limits given by $\vec{k}_N$ (and $(2\pi,2\pi) - \vec{k}_N$ by symmetry reasons), which is indicated by vertical red lines in Fig. 3.8c. The striking feature leading to the celebrated "hourglass" structure is, however, the additional upward dispersion, which can be seen in the spectrum of the one-band Hubbard model displayed in Fig. 3.8c. The upper branch is much weaker than the lower one because the electron-hole continuum damps this collective mode [113]. In the electron-doped case, the magnetic excitation spectrum displays a different structure. In Fig. 3.8f, the magnetic spectrum in the electron-doped case within the VCA approach for two-particle excitations is presented. As one can see, in this case the weight of the magnetic spectrum is essentially concentrated in the vicinity of (π,π) and it is mostly dispersionless, in accordance with the experimental situation [203, 204]. The downward dispersion observed in the calculation only carries very little weight, when compared with the strong peak around (π,π). Thus, this might be the reason why this dispersion is not seen in inelastic neutron scattering experiments [199]. A possible explanation is a slightly change in FS: The nodal vector $\vec{k}_N$ in Fig. 3.8e is larger than in the hole-doped case, so the resonance mode is confined to a small momentum region around $\vec{Q}_{\mathrm{AF}}$ (see red vertical lines in Fig. 3.8f). Finally, in contrast to the hole-doped case, the upward dispersion is not observed for electron doping. This is also in accordance with the experimental observations [203, 204].

In the next section, the role of two-particle excitations, especially magnetic ones, is discussed in the context of understanding the issue of the "pairing glue" in high-T_c cuprates.

3.5 The Question of the Pairing Glue

P.W. Anderson has argued that pairing in conventional "low-T_c" superconductors (SC) has a rather different microscopic origin from that in high-T_c cuprates and many other unconventional SC [205]. But in either case, the paired electrons have to avoid the strongly repulsive bare Coulomb interaction. In a low-T_c SC, this repulsion can be eliminated in favor of electron-pair binding via *"dynamic screening"*, i. e.

$$V(\vec{q},\omega) = \frac{e^2}{q^2\varepsilon(\vec{q},\omega)}, \tag{3.8}$$

where $V(\vec{q},\omega)$ is the Fourier transform of the electron-electron interaction in both space and time and $\varepsilon(\vec{q},\omega)$ is the dynamic screening due to both ions and electrons, i.e. $\varepsilon(\vec{q},\omega) = \varepsilon_{\mathrm{ion}}(\vec{q},\omega) + \varepsilon_{\mathrm{el}}(\vec{q},\omega)$. *Anderson* then gives an elegant discussion why, in his opinion, in the high-T_c SC another pairing mechanism is at work, which may be termed *"anisotropic momentum (or real-space) mechanism"*: Here, the strongly repulsive (short-range) part of the Coulomb interaction is avoided by a mechanism suggested by *L.P. Pitaevskii* [206] and *K.A. Brueckner et al.* [207] of choosing the pair state orthogonal to the repulsive core of the Coulomb interaction, i.e. putting the electron pairs in an anisotropic wave function (such as d-wave), which vanishes at the core of the Coulomb interaction.

Still following the arguments of *Anderson* for the low-T_c SC, the calculations in this chapter show an evidence that in the high-T_c materials both the anisotropic "momentum-space" mechanism and the dynamics are at work, what will be shown for two different Hubbard models (Sec. 3.2). This gives a possibility to shed light on the question to what extent both models lead to a similar pairing mechanism. The one-band Hubbard model was studied recently by *T.A. Maier et al.* [115] as well as by *B. Kyung et al.* [208], where also the pairing dynamics has been studied. The above questions are clearly of relevance for the main issue raised by *Anderson*, namely "is there glue in cuprate superconductors?", which is basically a question about the dynamics of the pairing interaction. As argued by *T.A. Maier et al.*, if the dynamics of the pairing interaction arises from virtual states, whose energies correspond to the "high-energy" Mott gap, and give rise to the exchange coupling J, the *interaction is instantaneous on the relative time scales of interest.* However, if the energies correspond to typical "low-energy" spin fluctuation (or phonon) excitations, then the *interaction is retarded.* In

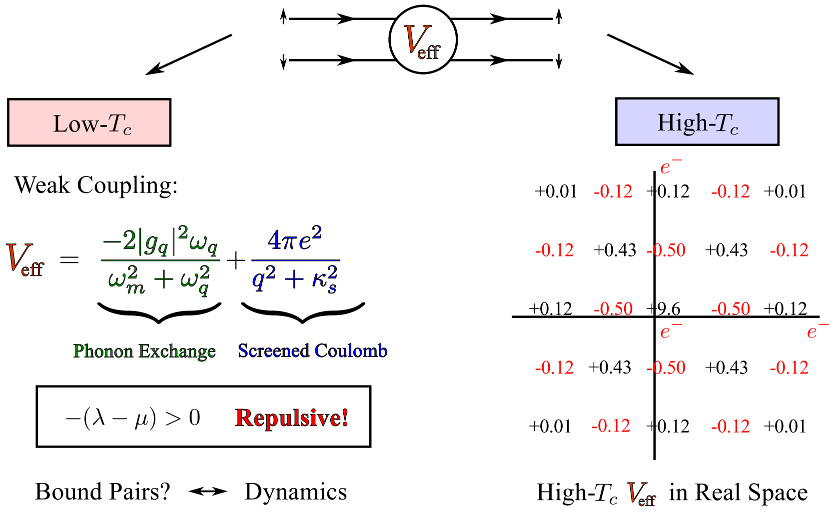

Figure 3.9: The effective pairing interaction in the weak-coupling low-T_c situation compared with high-T_c QMC simulations for the two-dimensional one-band Hubbard model by *D.J. Scalapino* and his group [209].

this case it makes sense to use the terminology "spin-fluctuation glue", which mediates the d-wave pairing.

For this question, it is useful to contrast step by step the construction of the effective electron-electron interaction for a weak-coupling low-T_c SC with the effective interaction of a high-T_c (i.e. Hubbard type) SC. In the "dynamic screening" mechanism of Eq. 3.8, one can safely replace the electronic screening by a static one (i.e. $\varepsilon_{el}(\vec{q}, \omega = 0)$). This is due to the fact that typical energies of electrons are of high energy ($\sim O(\varepsilon_{Fermi})$) compared to $k_B T_c$, i.e. the SC energy scale: The plasma of other electrons then damps away the long-range ($^1/_r$)-behavior and leaves a Thomas-Fermi screened core $e^2 \mathrm{e}^{-\kappa_S r}/r$ (κ_S: Thomas-Fermi constant). This gives rise to an essentially instantaneous interaction, which is still very repulsive, and which - when averaged over the FS - is termed μ (see below). On the other hand, for the phonon case, the screening acts anti-adiabatically, i.e. $\varepsilon_{\rm ion}(\vec{q}, \omega)$ is dynamic, since typical phonon frequencies are of the order of $k_B T_c$. In other words, the final Fourier-transformed effective interaction is

$$V_{\rm eff} = \frac{e^2}{(q^2 + x^2)\, \varepsilon(q, \omega)} \,, \tag{3.9}$$

and the effective electronic interaction is screened (anti-adiabatically) by the phonon polarizations. Fig. 3.9 summarizes this weak-coupling low-T_c situation and rewrites the effective pairing interaction as the usual sum of the dynamic phonon exchange and the Thomas-Fermi screened Coulomb part. Here, ω_q denotes phonon frequencies, g_q the electron-phonon coupling and ω_m are Matsubara frequencies. When the two terms in the sum are averaged over the FS (the brackets in Fig. 3.10 for $V_{\rm eff}$ denote an average of the momentum transfer $\vec{q}$ over ε_F), then one finds that the corresponding averaged $V_{\rm eff}$ is larger than zero, i.e. -$(\lambda - \mu) > 0$ and, thus, is still repulsive. The net interaction is thus repulsive even in the phonon case, a fact which is required to guarantee the stability of the

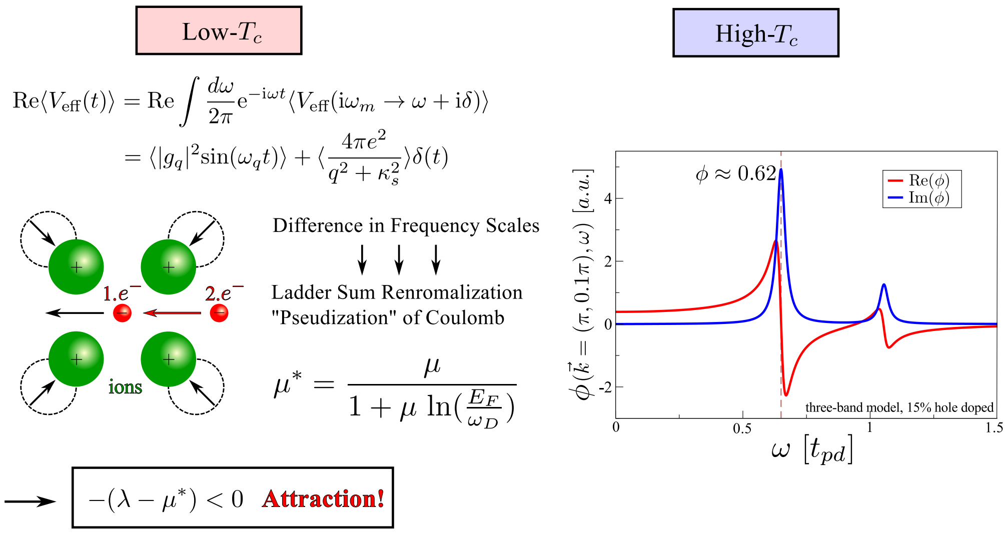

Figure 3.10: (left) Dynamics of the pairing interaction for the low-T_c case: the emergence of the difference in frequency scales, i.e. slow ionic-lattice polarization and fast Coulomb repulsion. **(right)** The SC gap function (Sec. 2.4.5) and its dynamics (both Re- and Im-parts) for the three-band model. In particular, the real part displays a certain similarity to the gap function shown for the low-T_c case in the left-hand part of Fig. 3.11. This is true for the spin-fluctuation contribution appearing around the characteristic energy $\omega_0 + \Delta_0 \cong \Phi$ (see also Figs. 3.12c,f)). At higher energies of order $\omega \cong 1$ and above additional structure appears mainly due to interband-charge fluctuations (see again Figs. 3.12c,f)).

solid.

So, how can one ever arrive at bound pairs if the interaction is never attractive? As is well-known since *L.N. Cooper's* seminal paper [6] preceding BCS theory, this is due to the difference in frequency scales or, equivalently, in time scales of the two parts of the interaction. This is pictured in Fig. 3.10: The "first" electron (anti-adiabatically) polarizes the ionic lattice and sets up a net negative charge polarization in its vicinity. This first process is "slow" and happens on the frequency scale ω_q of the ionic vibrations. A "second" electron feels this polarization, but can only profit from it and build up an effective attraction when the first electron "instantaneously" moves so as to avoid each other. Thus, the "high-energy" part of the Coulomb interaction acts only over a short time, given here by a δ-function, while the attractive electron-phonon interaction is *retarded* by the much slower lattice response. In other words, if the electrons forming the pair correlate themselves in time to avoid the short-time Coulomb repulsion, they can take advantage of the attractive electron-phonon-mediated interaction and form a Cooper pair. As is well-known, this kind of renormalization, i.e. integrating out the "high-energy" degrees of freedom in the relative pair wave function, can be done a variety of ways: By a ladder sum renormalization or a *pseudozation* of the interaction, replacing μ by μ^* [210]. Now, $-(\lambda - \mu^*) < 0$, i.e. a situation where V_{eff} can be attractive, leading in *L.N. Cooper's* sense to the pairing instability at very low energies.

In this chapter, the main focus is on the dynamics of the pairing interaction in the high-T_c cuprates and, in particular, how there the two electrons about to form a pair can avoid each other - and thus weaken their repulsion - by modifying the high-energy parts of their

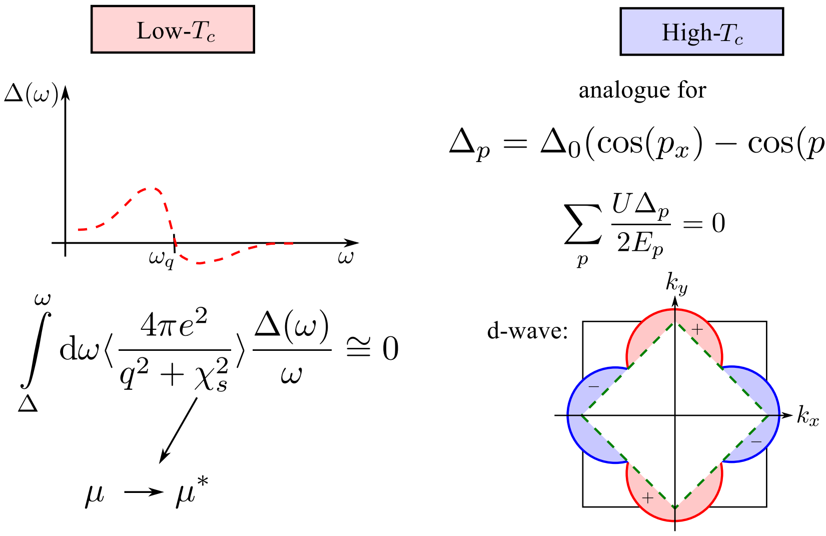

Figure 3.11: Avoiding the strongly repulsive part of the Coulomb repulsion: analogy of the gap function Δ in the low-T_c (ω-space) and high-T_c (momentum-space) situation. The figure for the momentum-space gap function in the high-T_c case is again inspired from [209]. Here, the green dashed line is the normal-state FS and the solid curve surrounding the FS gives the size of the $d_{x^2-y^2}$-gap $\Delta_{\vec{k}}$ at the momentum $\vec{k}$ on this surface.

relative wave function. For this, it is instructive to look first at the frequency dependence of the gap function of a low-T_c SC, found by solving the *Eliashberg equations* [211], following a discussion by *D.J. Scalapino* [209] (see the low-T_c case in Fig. 3.11): The real part of the corresponding gap function $\Delta(\omega)$ first increases as the typical phonon energy $\omega_{\vec{q}}$ is approached. At this characteristic "glue energy", it changes sign and remains negative out to very large values of ω. This latter observation corresponds to the instantaneous part. It just reflects the fact that the two electrons making up the pair avoid "short-time short-range encounters". This can be summarized (Fig. 3.11) in a kind of orthogonality relation, with the pair wave function $\Delta(\omega)$ being orthogonal to the "core" (i.e. the Thomas-Fermi screened short-range part) of the Coulomb interaction [209]. The essence of this orthogonality relation is that in practice $\langle 4\pi e^2/(q^2+x^2)\rangle$ can be replaced over the frequency integral Δ to several times the Debye frequency ω_D by the weak pseudo-potential μ^* [209, 210].

So then, how do the electrons in high-T_c materials act so that they are seldom or never in the same place at the same time?

Here, it is useful to first look at the effective interaction V_{eff} in real-space (or, more precisely, at the real-space Fourier transform of the singlet vertex $\Gamma(l, \omega_m = 0)$ [211] versus the separation l between the electrons in pairs). Fig. 3.9 and Fig. 3.11 plot the results for V_{eff} obtained from QMC simulations for the two-dimensional one-band Hubbard model by the Scalapino group [209]. A similar pattern for the effective interaction in the three-band model is obtained employing QMC, when again the two electrons are placed on the Cu-sites [166]. Using the BCS gap equation for illustration, i.e.

$$\Delta_p = -\sum_{p'} V_{pp'} \frac{\Delta_{p'}}{2E_{p'}} , \tag{3.10}$$

with $V_{pp'}$, the effective interaction or Fourier-transformed vertex $V_{pp'} = T(p' - p)$, one immediately sees that the two pairing electrons avoid the repulsive parts of the Coulomb interaction by arranging their pair wave-function in a $d_{x^2-y^2}$ orbit, with the simplest nearest-neighbor pairing given in momentum space by $\Delta_p = \Delta_0(\cos p_x - \cos p_y)$. This can be expressed by

$$\sum_{p'} \frac{U\Delta'_p}{2E'_p} = 0 . \tag{3.11}$$

This latter relation indeed seems to confirm *Anderson's* conjecture in that the essence of the pairing mechanism in low-T_c SC is "dynamic screening", whereas in the high-T_c cuprates it is *anisotropic momentum-space pairing*. In Fig. 3.10, however, the dynamics of the pairing interaction as reflected in the ω-dependence of the gap function $\Delta(\omega)$, what is also of relevance for the high-T_c cuprates. Here again, the real part of the gap function changes sign at a characteristic frequency Φ related to spin fluctuations and at higher energies to interband-charge fluctuations.

3.6 Dynamics of the Pairing Interaction

The question of whether one can speak of a "pairing glue" has recently been addressed by *T.A. Maier et al.* for the one-band Hubbard and *t-J* models [115, 212]. If the dynamics of the pairing interaction is due to small-energy (two-particle) excitations, such as the characteristic structures seen in the spin susceptibility, then one might speak of the interaction as being retarded on the relative time scales of interest and of a "spin-fluctuation"glue-mediating *d*-wave pairing. This clearly is reminiscent of the usual phonon-mediated pairing interaction in the low-T_c SC [115]. It is well-known that for these latter systems the gap function $\phi(\vec{k}, \omega)$ (Sec. 2.4.5) is only very weakly depending on momentum $\vec{k}$, corresponding to the local character of the pairing interaction. However, the dynamics of the gap function is important and it enters the Cauchy relations between the real and imaginary parts of $\phi(\vec{k}, \omega)$, i.e.

$$\begin{aligned} \phi(\vec{k}, \omega) &= \phi_1(\vec{k}, \omega) + \mathrm{i}\phi_2(\vec{k}, \omega) \\ \phi_1(\vec{k}, \omega) &= \frac{1}{\pi} \int \frac{\phi_2(\vec{k}, \omega')}{\omega' - \omega} \mathrm{d}\omega' \\ \phi_1(\vec{k}, \omega = 0) &= \frac{2}{\pi} \int \frac{\phi_2(\vec{k}, \omega')}{\omega'} \mathrm{d}\omega' , \end{aligned} \tag{3.12}$$

with $\omega = 0$ for the latter one. A measure for the fractional contribution to the gap function $\phi(\vec{k}, \omega = 0)$ and to pairing that comes from frequencies less than Ω can then be defined [115], i.e.

$$I(\vec{k}, \Omega) = \frac{\frac{2}{\pi} \int\limits_0^{\Omega} \frac{\phi_2(\vec{k}, \omega')}{\omega'} \mathrm{d}\omega'}{\phi_1(\vec{k}, 0)} \tag{3.13}$$

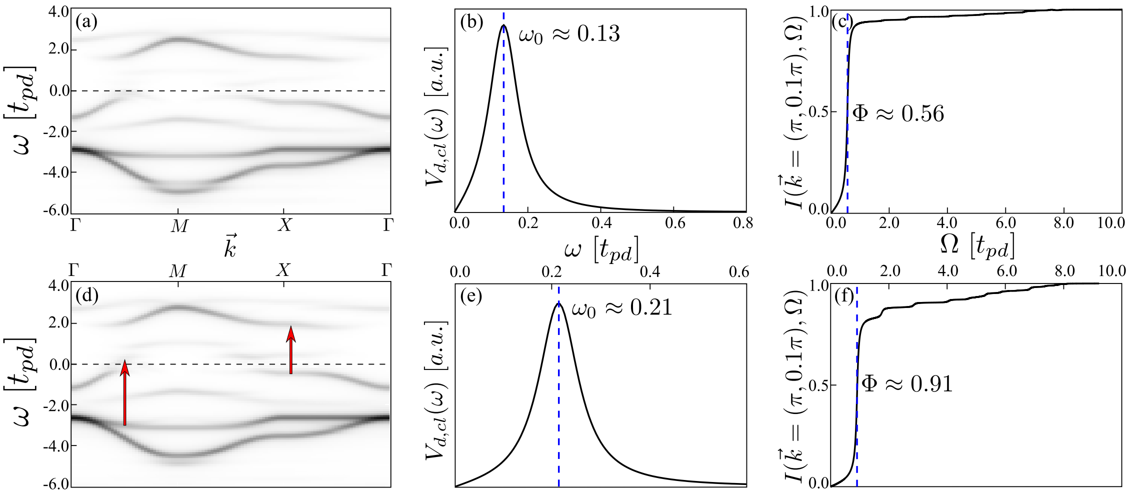

Figure 3.12: Three-band Hubbard model: **(a,d)** the single-particle spectral function $A(\vec{k},\omega)$ for a 2×2 reference cluster (as in Fig. 3.2b). **(b,e)** The cluster d-wave projection $V_{d,cl}(\omega)$ of the spin susceptibility (Eq. 3.15). **(c,f)** The integrated contribution of gap function $I(\vec{k} = (\pi, 0.1\pi), \Omega)$. For **(a-c)**, the hole doping is 4% and for **(d-f)** 15%, respectively. Each time, the system is in a pure superconducting state.

It gives the relative contribution to the pairing of the "retarded" glue part and of the non-retarded, i.e. "instantaneous" part. In Ref. [115], it has been demonstrated that $I(\vec{k},\Omega)$ is a useful diagnostic for the pairing glue (phonon contributions) in the case of Pb. $I(\vec{k},\Omega)$ increases as Ω passes through $\omega_{\text{Phonon}} + \Delta_0$, where Δ_0 denotes the SC gap and ω_0 the characteristic Pb phonon frequencies. Its asymptotic value $I(\vec{k},\Omega \gg \omega_{\text{Phonon}} + \Delta_0)$ exceeds unity reflecting the fact there exists an instantaneous Coulomb pseudo-potential. This leads to a negative, frequency-independent contribution ϕ_{NR} to $\phi(\vec{k},\omega)$. At high frequencies, $I(\vec{k},\Omega)$ exceeds 1 by the "instantaneous" contribution $-\phi_{\text{NR}}/\phi_{(0)}$. In this chapter, the question is examined if a "pairing glue" exists, which offers a way of distinguishing different pairing mechanisms for the one-band and three-band Hubbard models in the relevant strong-correlation regime for the high-T_c cuprates.

The VCA is particularly well suited for a study of the quantity $I(\vec{k},\Omega)$. This is due to the fact that the VCA allows for accurately calculating the real and imaginary parts of the anomalous self-energy and, thus, of the gap function $\phi_1(\vec{k},\omega)$. This has already been shown in a recent letter, reproducing the experimentally found gap dichotomy of the nodal and anti-nodal gaps in high-T_c cuprates as a function of doping [25]. Also the single-particle excitations (as displayed in Fig. 3.12 and Fig. 3.13 as well as earlier results by *E. Arrigoni et al.* [114]) are found qualitatively to be similar, concerning the "low-energy" physics and, in particular, the electron-hole asymmetry (Figs. 3.5c,e): Doped holes first enter around the nodal point $(\frac{\pi}{2},\frac{\pi}{2})$, where the SC gap vanishes, introducing a gapless screening which very effectively destroys long-range AF order [106]. In contrast, introducing electrons around the anti-nodal point $(\pi,0)$ fixes μ (due to the large density of states) within the SC gap, in a regime where this gap is maximal. Here, an incomplete screening cannot disrupt AF order up to significantly large electron dopings where, finally, μ enters also here the gapless $(\frac{\pi}{2},\frac{\pi}{2})$ region. So again, it is the corresponding low-energy physics embedded in the qualitatively rather similar

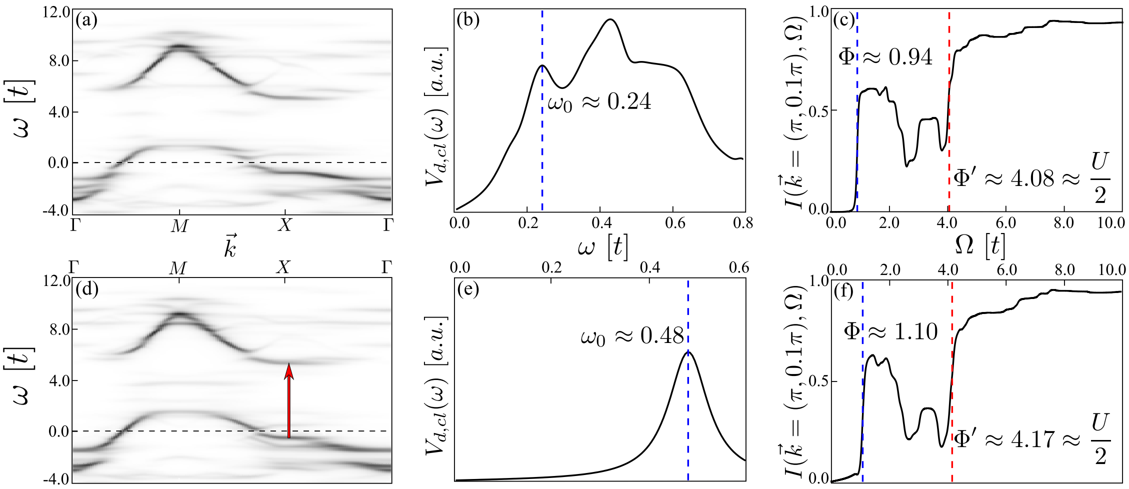

Figure 3.13: One-band Hubbard model: **(a,d)** the single-particle spectral function $A(\vec{k},\omega)$ for a 3×3 reference cluster. **(b,e)** The cluster d-wave projection $V_{d,cl}(\omega)$ of the spin susceptibility (Eq. 3.15). **(c,f)** The Integrated contribution of the gap function $I(\vec{k}=(\pi,0.2\pi),\Omega)$. For **(a-c)**, the hole doping is 5% and for **(d-f)** 15%, respectively. Each time, the system is in a pure superconducting state.

single-particle spectra plotted in Fig. 3.12 and Fig. 3.13, which determines salient (here AF) features of the phase diagram.

So, back to the question of the dynamics in the pairing interaction, the fractional contribution $I(\vec{k},\Omega)$ to the gap function in the three- as well as one-band models has to be considered. The results for $I(\vec{k},\Omega)$ for the three-band model, i.e. for the fraction of the zero-frequency gap function which arises from frequencies below Ω, are plotted in Figs. 3.12c,f. Here, two hole-doped cases with 4% and 15% doping are shown, together with the corresponding single-particle spectral function $A(\vec{k},\omega)$ and the data for the d-wave projection of the cluster spin susceptibility (Eq. 3.15). $I(\vec{k},\Omega)$ is plotted for the three-band model for a hole doping of 4% in Fig. 3.12c and for a higher doping of 15% in Fig. 3.12f. $\vec{k}=\pi(0.1,0)$, i.e. a momentum close to the anti-nodal point $(\pi,0)$ where the d-wave SC gap is maximal. For both dopings, a first steep rises at a typical energy Φ of about $\omega_0+\Delta_0$, where Δ_0 denotes the quasi-particle (SC) gap and ω_0 a characteristic spin fluctuation frequency. Close to half filling, ω_0 is roughly estimated by the strong-coupling result for the Cu-Cu exchange energy $\omega_0 \cong 2J_{\mathrm{Cu}}$, with

$$J_{\mathrm{Cu}} = \frac{4t_{pd}^4}{(\Delta_{pd}+U_{pd})^2}\left(\frac{1}{\Delta_{pd}+U_{pp}/2}+\frac{1}{U_{dd}}\right) \cong 0.1t_{pd} \,. \tag{3.14}$$

As shown by the d-wave projected result $V_{d,cl}(\omega)$ in Figs. 3.12b,e, for the imaginary part of the cluster spin susceptibility, with the definition

$$V_{d,cl}(\omega) = \frac{1}{N^2}\sum_{\vec{k},\vec{k}'}\left(\cos(k_x)-\cos(k_y)\right)\left(\cos(k'_x)-\cos(k'_y)\right)\mathrm{Im}\chi_{cl}(\vec{k}-\vec{k}',\omega) \,, \tag{3.15}$$

the first dominant peak is found at low doping, i.e. 4% at about this energy (here $\omega_0 \cong 0.13$ as always in units of the hopping t_{pd}) and, at 15% doping at a higher energy

$\omega_0 \cong 0.21$. This correlation function was extracted from an infinite-lattice calculation and not from the cluster spin susceptibility χ_s. The peaks in the $\mathrm{Im}(\chi_s(\vec{k},\omega))$ are shifted somewhat down when going from the cluster to the infinite-lattice case [113]. Furthermore, the celebrated low-energy neutron-scattering resonance, which is an $(S=1)$ magnetic exciton appearing in the SC gap, can only be obtained in the infinite-lattice case [113] (see Sec. 3.4 for details). On the other hand, the anomalous self-energy and, thus, the integrated gap function $I(\vec{k},\omega)$ in Fig. 3.12 and Fig. 3.13 is calculated from the variationally optimized self-energy of a reference cluster (and, as a result, implicitly also the underlying susceptibility). Thus, an identification of $\omega_0+\Delta_0$ with the energy of the steep first increase in $I(\vec{k},\omega)$ is only approximately possible (Fig. 3.13b), in particular, this latter figure contains also contributions from the magnetic spin resonance. However, given the generally accepted small weight of this resonance to the pairing [213] and the behavior of the first steep rise in Figs. 3.12c,f and Figs. 3.13c,f as function of the Hubbard-U, this rise can still be unambiguously identified with the dominant influence of spin fluctuations.

$I(\vec{k},\Omega)$ displays an amazingly prominent first increase at an energy Φ of about $\Delta_0+\omega_0$, where Δ_0 is the quasiparticle gap and ω_0 the first dominant peak in the d-wave projection of the dynamic spin susceptibility $\mathrm{Im}\chi(\vec{k},\omega)$. The quasiparticle gap is found to be at $\Delta_0 \cong 0.52$ (obtained from the spectral function) for 4% doping and at a similar value ($\Delta_0 \cong 0.41$) for 15% doping, thus $\Delta_0+\omega_0 \cong 0.65$. The first sharp rise in $I(\vec{k},\Omega)$ at the low-doping situation ($\sim 4\%$) is at about $\Phi \cong 0.56$. The observation is that in this low-doping case for the three-band model more than 90% of the saturation value of $I(\vec{k},\Omega)=1$ is due to the dynamic contribution of the spin fluctuations. For 15% doping, ω_0 is increasing [178], and so is $\omega_0+\Delta_0$. Fig. 3.14a further confirms the leading role of the spin fluctuations. Here, the first dominant increase in $I(\vec{k},\Omega)$ is plotted as a function of U/t at 15% h-doping. One sees that as the value of U/t increases, this dominant increase in $I(\vec{k},\Omega)$ is shifted to lower energies, scaling essentially with the exchange energy J, while Δ_0 is found to be essentially constant as function of U/t. Here, at 15% doping, the spin fluctuation contribution to the saturation value of $I(\vec{k},\Omega)=1$ slightly decreases compared to the 4%-doping situation. From there on a mild rise takes place, starting at about $\omega \cong 1$ for both dopings. In both doping cases, this corresponds to virtual electron-hole transitions involving the charge-transfer gap $\sim \Delta_{pd}/2$ (Fig. 3.13a). Fig. 3.14b illustrates the influence of the doping dependence of interband-charge fluctuations on $I(\vec{k},\Omega)$. Here, at first glance, the influence of these fluctuations on the integrated gap function $I(\vec{k},\Omega)$ appears to be very mild.

However, this picture changes significantly, when the three-band model results for $I(\vec{k},\Omega)$ in Figs. 3.12c,f are confronted with the corresponding ones for the one-band model and, thus, the doped Mott-insulator case (Figs. 3.13c,f): Again, for the latter model there is a first dominant rise in the integrated gap function. This first rise - when analyzing its (U/t)-dependence - can again be attributed to dynamic spin excitations. However, a second prominent increase in this one-band model case occurs after a rather pronounced drop at energies of order $(U/t)/2$. This has already been observed in this one-band model case in Ref. [115] and was termed a "non-retarded" contribution occurring at an energy scale set by the Mott gap and being related to excited states (see the red arrow in the corresponding $A(\vec{k},\omega)$ spectrum in Fig. 3.13a), involving the upper Hubbard band. For the t-J model, Ref. [115] finds this energy scale being pushed to

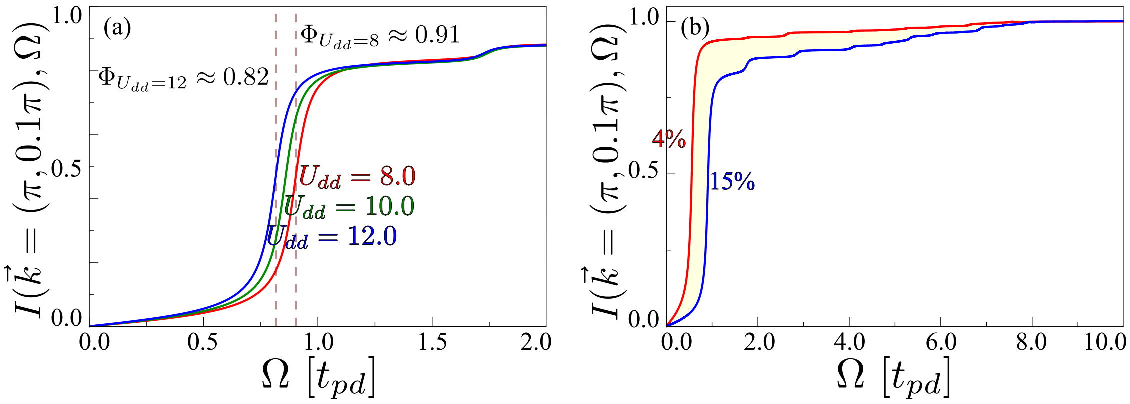

Figure 3.14: Integrated contribution of the gap function $I(\vec{k}=(\pi,0.1\pi),\Omega)$ for the three-band Hubbard model. **(a)** The first dominant increase in $I(\vec{k},\Omega)$ plotted for different values of U_{dd}/t. **(b)** The doping dependence of $I(\vec{k},\Omega)$, with the modest increase of interband-charge fluctuations as function of doping.

"infinity", with the corresponding exchange interaction being instantaneous. In contrast, the retarded (spin-fluctuation) interaction, i.e. the first steep rise in $I(\vec{k},\Omega)$, occurs at an energy scale which is small ($\omega_0 \cong 0.1t$) compared to the bare bandwidth $8t$ (and the bare U). Thus, the one-band model as well as the t-J model may be interpreted to contain both retarded and non-retarded contributions. This is qualitatively different in the three-band model: Here, in Figs. 3.12c,f and Fig. 3.14b, a rather continuous "filling in" of integrated weight is detected in the Ω regions in $I(\vec{k},\Omega)$, where in the one-band model (Figs. 3.13c,f) this weight is clearly missing. This "filling in" is due to electron-hole excitations of $O(2t_{pd})$ and, thus, due to interband-charge fluctuations (see the corresponding electron-hole transitions in Fig. 3.14d, marked with red arrows). Thus, in the sense of the interpretations used for the one-band model above (and in Ref. [115]), one may conclude that the three-band model is indeed different and contains only retarded contributions in its d-wave pairing interaction.

Then, the question whether there is a "pairing glue" in the three-band model, is a question of whether the dominant contribution to the pairing function $\phi_1(\vec{k},\omega=0)$ comes from the integral of $\phi_2(k,\omega)/\omega$ and, more specifically, a low-energy (compared to $8t$) region in this integral. Earlier results have shown that both the one-band Hubbard and t-J models exhibit spin fluctuation "pairing glue" [115, 202, 208]. For both the three- as well as for the one-band model results, with the latter displayed for a similar higher-doping case (15%) in Fig. 3.13, one can include the full range of virtual electron-hole transitions between the lower and upper Hubbard bands. As a consequence, the Cauchy relation for $\phi(\vec{k},\omega=0)$ does, strictly speaking, not contain a non-retarded contribution ϕ_{NR} and the asymptotic value of $I(\Omega)$ approaches unity. In the one-band model, there is a first steep rise, which can again be identified with a typical spin-fluctuation energy. Then, at higher energies after a drop a second steep rise occurs at energies corresponding to (virtual) electron-hole interband transition of order $\sim \frac{U}{2}$. As argued in Ref. [115], it is this part which in the t-J model for $U\rightarrow\infty$ (i.e. when the upper Hubbard band is projected out) gives rise to an instantaneous contribution ϕ_{NR}. Thus, in this sense, both one-band models also display a non-retarded interaction. The new result here is that in the three-band model only low-energy (spin-fluctuation) retarded contributions to the pairing interaction dominate, whereas in the one-band model also a significant high-energy contribution occurs. While these differences between a Mott and a charge-transfer insulator appear to be renormalized away in the very similar, i.e. universal ground-state phase diagram of these two models, one may use Eliashberg-type of arguments to form an expectation that the finite-T phase is rather different in the two models, i.e. strongly material-dependent (see also Ref. [188]).

Finally a comment about the resonating valence bond state (RVB) [84] physics in the two models: Δ_{pd} also enters in the exchange coupling J_{Cu} between spins on the Cu-sites. Thus, the role of U in the one-band model, setting the characteristic energy of the RVB-coupling J, is taken over in the three-band model by the energy of the interband-charge fluctuations (Eq. 3.14). In that sense, one may argue that the final increase in the relative pairing strength $I(\vec{k},\omega)$ to the value of $I(\vec{k},\omega) = 1$ again reflects RVB physics. However, it was showed within this section that there is quite a difference with respect to the relative weights of the spin-fluctuation and higher-energy contributions between the two models.

3.7 Summary

In this chapter, I have discussed the role of the $\mathrm{Cu}_{d_{x^2-y^2}}$- and $\mathrm{O}_{p_{x,y}}$-orbital degrees of freedom in high-T_c cuprate superconductors. The essential question if an elaborate three-band model is necessary or a simple effective one-band model is sufficient, is dissected in various model properties. This simplification had to be investigated because the physics of the one-band model is that of doping into a Mott-Hubbard insulator, but the three-band model is a doped charge-transfer insulator, just as high-T_c cuprates.

Firstly, the ground-state phase diagram is very similar in both models, including competing antiferromagnetic and superconducting orders as well as an asymmetry in electron and hole doping. Hence, the low-energy properties are successfully mapped to a one-band Hubbard model.
Secondly, the two-particle excitations were considered. The transversal spin susceptibility shows (i) a spin-wave mode, i.e. a magnon, in the antiferromagnetic phase and (ii) a magnetic resonance mode ("hour glass structure") in the superconducting phase. The latter one is a reminiscent "fingerprint" of the magnetic parent compound. Due to numerical problems and computational limits, it was only observed in the one-band model. Otherwise, for the magnon mode, the agreement of both models was showed.
Finally, the gap function, i.e. the anomalous part of the self-energy, was compared. From this quantity, an inference to the dynamic pairing interaction can be done: It is a kind of "pairing glue" for superconductivity. Here, some important differences appear: In the three-band model, there is a retarded pairing due to low-energy spin fluctuations, while in the one-band Hubbard model an additional part rises, involving excited states in the upper Hubbard band. The latter one may be associated with a "non-retarded" contribution.

In short, one may term the dynamics of the pairing interaction in the three-band Hubbard model and, thus, in a doped charge-transfer insulator as retarded and being due to a low-energy pairing glue, whereas in the one-band Hubbard model and, thus, a doped

Mott insulator both retarded and non-retarded parts contribute.

So the high-energy physics in the one-band model differ significantly from the three-band model.

After these considerations about doped Mott and charge-transfer insulators with their strongly correlated physics, the focus is switched to some systems with a weaker interaction. Thus, the relevance of Fermi-surface instabilities rises. Consequently, the SC phase in NaCoO is heavily affected by magnetic fluctuations, which is discussed in detail in the next chapter.

4 Unconventional Superconductivity and Gap Anisotropies in the Cobaltate NaCoO

The cobaltates are one of the least understood superconductors. Superconductivity (SC) appears as soon as $\mathsf{Na}_{0.3}\mathsf{CoO}_2$ is immersed with water to increase the distance between the CoO_2-layers [58]. $\mathsf{Na}_x\mathsf{CoO}_2$ without immersed water is a metal with low resistivity and extremely high thermopower, hinting strong correlations in the metal phase [214].

To begin with, standard ab initio techniques could not match the Fermi-surface structure found from angle-resolved photoemission spectroscopy (ARPES) studies [215, 216], where differences have been assigned to strong correlations [217], disorder [218], and ARPES surface effects [219]. Hence. the theoretical predictions could not be very precise and provide the whole range of s, p, and d-wave SC [220]. It is not fully settled either whether the cobaltates should be considered from a weakly coupled or strongly coupled fixed point, however, it seems such that the dominant contribution to the interaction comes from electron-electron coupling (although still some part of the literature stresses the role of phonons in the problem [221]). In addition, a topological superconducting state was proposed from first principle calculations in the surface of NaCoO_2, where the Na content of the terminating layer can be controlled by experimental conditions [222].

In this chapter, I present the results of functional renormalization-group (fRG, see Sec. 2.6 for an introduction) calculations of an effective three-band model in the triangular lattice (Sec. 2.2) that matches the band structure of bulk $\mathsf{Na}_x\mathsf{CoO}_2$ for $x \approx 0.3$. This weak-coupling approach results in a rich phase diagram, including a chiral d-wave superconducting phase.

The results of this chapter will be published with *C. Platt, W. Hanke* and *R. Thomale* in Ref. [5].

4.1 Effective Three-Band Model

The compound $\mathsf{Na}_x\mathsf{CoO}_2$ (NaCoO) features alternating Na- and CoO_2-layers, where the latter one forms a triangular lattice and the Na-layers act as an electron donor. Here, the Na-content between the CoO_2-layers can be exactly tuned. This enables a phase diagram which includes superconducting and metallic phases, together with a charge-ordered

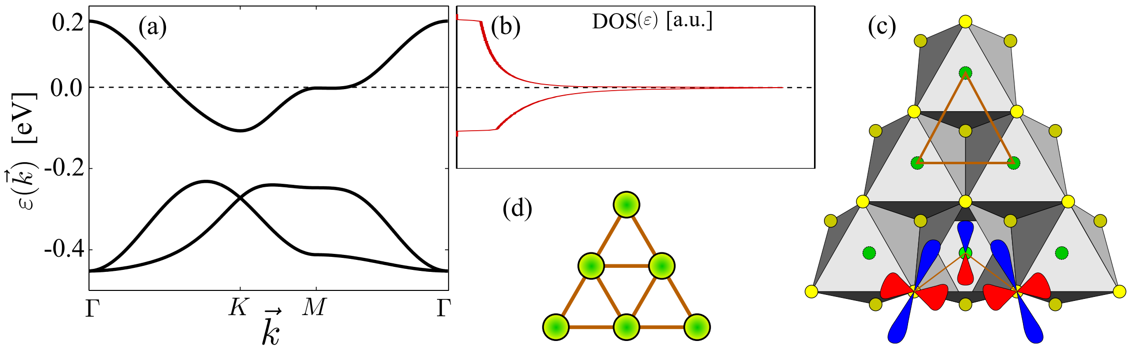

Figure 4.1: **(a)** Band structure at van Hove filling ($x = 0.09$). Only one band intersects the Fermi energy, resulting in one electron pocket at Γ. **(b)** The van Hove singularity (VHS) of this band is clearly visible in the density of states (DOS). **(c)** The crystal structure of the $\mathrm{CoO_2}$. The yellow circles indicate Co-sites with d_{xz}- and d_{yz}-orbitals, while the green circles represent O-sites with p_z-orbitals. **(d)** Simplified model of the crystal structure: A triangular lattice with three hybridized orbitals at each site.

insulator and a weak-moment magnetically ordered state in a large doping regime of $x = [0,1]$ [223–225]. SC was detected at a doping level of $x \approx 0.3$, when water is immersed [58]. Since the focus of this thesis is on superconductivity, only doping levels around the SC phase are considered. First-principles calculations, e.g. the local-density approach (LDA), failed to describe an effective low-energy Hamiltonian for NaCoO which reproduces the Fermi surface (FS) measured by angle-resolved photoemission spectra (ARPES) [226–229]: The so-called "sinking pockets" are detected below the FS, while they were predicted at the Fermi level. Dynamical mean-field theory (DMFT) studies show that the calculated heat capacity is consistent with experimental data only in models without additional pockets at the FS [230].

Here, an effective model proposed by *A. Bourgeois et al.* [231, 232] is used, which contains all relevant orbitals, i.e. Co_{3d} and O_{2p}. They started with a $\mathrm{CoO_6}$ cluster model and mapped it down to an effective three-orbital Hamiltonian. The model parameters were fitted to X-ray absorption spectroscopy (XAS) experiments. The parameter for direct Co-Co-hopping was set to fit an FS obtained by ARPES experiments. This model was subsequently solved by dynamical mean-field theory (DMFT). The bandwidth of the effective model is ~ 0.6eV, a factor of three smaller than LDA calculations predict (1.6eV [226] or 2.0eV [227]).

It is important to stress that self-energy effects are already considered in this effective Hamiltonian. But these effects are anyway neglected in the implemented fRG scheme (Sec. 2.6.3), so a double counting is excluded.

The corresponding tight-binding model includes three hybridized orbitals per site $(\tilde{d}_{xy}, \tilde{d}_{yz}, \tilde{d}_{zx})$ in a triangular superlattice (Sec. 2.2). The Hamiltonian reeds

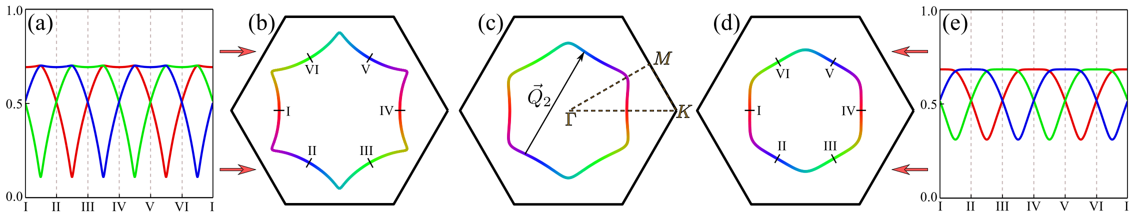

Figure 4.2: The Fermi surfaces (FS) at **(b)** $x = 0.1$, **(c)** $x = 0.2$ and **(d)** $x = 0.3$. The different colors indicate the dominant orbital weights at the FS. An explicit plot of the orbital weights at the FS is given in **(a)** for $x = 0.1$ and **(e)** for $x = 0.3$. The marks **I** to **VI** are also plotted in the corresponding FSs. The weight of one orbital is changing at the FS but never decreases to zero.

$$\begin{aligned}\hat{H} = &\sum_{\langle i,j\rangle}\sum_{\alpha\beta}\sum_{\sigma}\Big(\big(t + t'\delta_{\alpha\beta} + D\,\delta_{ij}\big)\,\hat{c}^{\dagger}_{i\alpha\sigma}\hat{c}_{j\beta\sigma} + \text{H.c.}\Big)\\ &+\mu\sum_{i}\sum_{\alpha}\sum_{\sigma}\hat{n}_{i\alpha\sigma} + U_1\sum_{i}\sum_{\alpha}\hat{n}_{i\alpha\uparrow}\hat{n}_{i\alpha\downarrow}\\ &+\frac{1}{2}\sum_{i}\sum_{\substack{\alpha\beta\\ \alpha\neq\beta}}\left(U_2\sum_{\sigma\nu}\hat{n}_{i\alpha\sigma}\hat{n}_{i\beta\sigma\nu} + J_H\sum_{\sigma\nu}\hat{c}^{\dagger}_{i\alpha\sigma}\hat{c}^{\dagger}_{i\beta\nu}\hat{c}_{i\alpha\nu}\hat{c}_{i\beta\sigma} + J_P\,\hat{c}^{\dagger}_{i\alpha\uparrow}\hat{c}^{\dagger}_{i\alpha\downarrow}\hat{c}_{i\beta\uparrow}\hat{c}_{i\beta\downarrow}\right),\end{aligned} \tag{4.1}$$

where $\hat{c}^{\dagger}_{i\alpha\sigma}$ denotes the electron creation operator with spin σ in orbital α at site i. The occupation number is defined as $\hat{n}_{i\alpha\sigma} = \hat{c}^{\dagger}_{i\alpha\sigma}\hat{c}_{i\alpha\sigma}$. Furthermore, t represents the hopping mediated by O_{p_z} and t' corresponds to a direct Co-Co-hopping while D is the crystal-field splitting. μ is the chemical potential, which fixes the doping level. These parameters are set to $t = 0.1$eV, $t' = -0.02$eV, $D = 0.105$eV [232]. The resulting dispersion relation (plotted in Fig. 4.1a) features three bands with only one band intersecting the Fermi level. There is a van Hove singularity (VHS), clearly visible in the DOS, presented in Fig. 4.1b. It is remarkable that this singularity is much more pointed than the van Hove singularities in the regular one-band models in the triangular (Fig. 2.3c), honeycomb (Fig. 2.5c) and kagome lattices (Fig. 2.6c). This also influences the local DOS at the FS.

For the weak-coupling fRG calculations, only momenta next to the FS have to be considered (as discussed in Sec. 2.6.4). Hence, the focus is on the band intersecting the FS, including the orbital contributions to this band. The FS only contains one hole pocket around the Γ-point, i.e. the center of the Brillouin zone. The evolution of this pocket is plotted in Figs. 4.2b-d for doping levels $x = \{0.1, 0.2, 0.3\}$, respectively. At $x \approx 0.28$, the nesting of the FS is optimal, with three inequivalent nesting wave vectors

$$\vec{Q}_1 = \left(-\sqrt{2}\pi, 0\right) \quad , \quad \vec{Q}_2 = \left(\frac{\pi}{\sqrt{2}}, \sqrt{\frac{3}{2}}\pi\right) \quad \text{and} \quad \vec{Q}_3 = \left(\frac{\pi}{\sqrt{2}}, -\sqrt{\frac{3}{2}}\pi\right) \ . \tag{4.2}$$

All three hybridized orbitals contribute to the FS. The orbital weights, which are the Bogoliubov-transform matrix elements of the transformation from orbital to band representation (Eq. 2.11), are presented in Fig. 4.2a (for $x = 0.1$) and Fig. 4.2e (for $x = 0.3$). Here, each orbital is represented by a red, green or blue line, respectively. The dominating regions of orbitals are also included in the FSs in Figs. 4.2b-d. Each orbital features two antipodal dominant regions, linked by the nesting vectors $\vec{Q}_1$, $\vec{Q}_2$ or $\vec{Q}_3$, respectively.

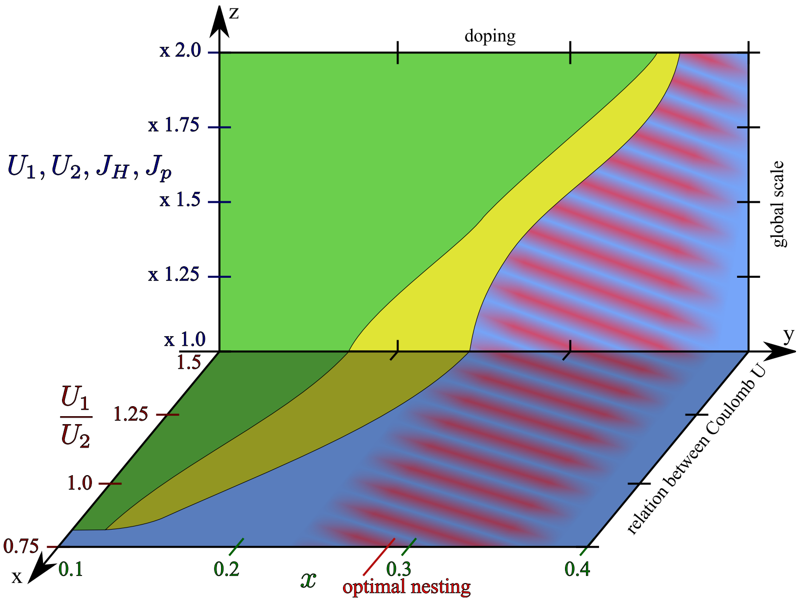

Figure 4.3: Phase diagram at electron doping. There are four phases: d+id-wave superconductivity (d+id SC, blue), weak ferromagnetism (weak FM, green), f-wave superconductivity (f SC, yellow) and a phase with competitive spin-density wave and d+id-wave superconductivity (SDW / d+id SC, purple and blue shaded). The basic interaction is $U_2 = 0.25$eV and $J_H = J_P = 0.07$eV. On the x-axis, U_1/U_2 is varied and the y-axis shows the doping dependencies. Additionally, the z-axis scales the global interaction strength (see text).

The interaction part of Eq. 4.1 features intraorbital Coulomb interaction U_1, interorbital Coulomb interaction U_2, Hund's rule coupling J_H and pair hopping J_P. In this Hamiltonian, $U_2 \lessapprox U_1$ is reasonable because hybridized orbitals are used. The parameter values ($U_1 = 0.37$eV, $U_2 = 0.25$eV, $J_H = J_P = 0.07$eV) are taken from Ref. [232], downscaled by a factor of five to satisfy the weak-coupling approach of the fRG. This is a feasible assumption because the total interaction strength is still in discussion. Hence, the global interaction scale is introduced as an additional scanning parameter.

4.2 Phase Diagram

To get a complete picture of the possible phases, the relation U_1/U_2, the doping level the and global interaction scale is changed, respectively. The results are presented in Fig. 4.3:

For large interaction strengths, the huge DOS at the VHS promote fluctuations with zero momentum transfer, resulting in weak ferromagnetism (weak FM). With a lowered interaction scale, other fluctuations become more competitive. Very recently, *G. Cao et al.* reported that additional immersed water, which raises the distance between the CoO_2-layers, increases the ferromagnetic fluctuations and hence the tendency to triplet SC [233]. In the fRG calculations of this chapter, an increased tendency to ferromagnetism and f-wave SC corresponds to an increased total interaction. A possible explanation is that the enlarged gap between layers reduces the screening of electrons and hence increases the interaction scale. In contrast, at small total interactions, the phase diagram is manifold: When the nesting of the FS is optimal, a spin-density wave (SDW) occurs. A tetrahedron magnetic order has been proposed, with four inequivalent sites in an enlarged magnetic unit cell [234]. Unfortunately, this real-space order is not accessible with fRG (the same problem is discussed in detail for the honeycomb lattice in Sec. 5.6). Within the SDW phase, singlet d+id-wave superconductivity is competitive (d+id SC). For low dopings, low interaction scale and $U_1 \lessapprox U_2$, a clear d+id SC is dominating with no SDW background. In between these three phases, in the proximity of weak ferromagnetic fluctuations, a triplet superconductivity with f-wave form factor (f SC) is dominant. The form factors of the SC phases are discussed in the next section.

This three-band model has a rich variety of phases. In contrast, the simple one-band model in the triangular lattice features the VHS and an optimal nesting at the same doping level (Sec. 2.2). There, the nesting dominates and hence neither a ferromagnetic instability nor triplet superconductivity was reported by comparable fRG calculations [140].

4.3 Form Factors and Superconducting Gap

The SC state is classified by the symmetry of the Cooper-pair wave function and the resulting band gap. In the triangular lattice (C_{6v} symmetry group), the most reasonable form factors fit to the irreducible representations (Sec. 2.3) of s-wave (spin singlet, nodeless), p+ip-wave (spin triplet, nodeless), d+id-wave (spin singlet, nodeless) and f-wave (spin triplet, with nodes) symmetry. Unfortunately, the experimental data about the symmetry of the SC state in NaCoO are still not clear: Knight shift measurements detect both singlet SC [59] and triplet SC [235], while nuclear quadrupolar resonance [60, 61], specific heat [236] and muon spin rotation [237] measurements yield evidence for an anisotropic SC gap function, featuring clear nodes. Hence, f-wave SC is a possible symmetry that fits for the triplet SC, but there is no singlet SC that features nodes. Consequently, the focus of the fRG calculations is on this ostensibly inconsistent result.

The phase diagram in Fig. 4.3 includes both a singlet and a triplet dominated SC phase. A mean-field like decoupling of the final fRG coupling function $V(\vec{k}_1,\vec{k}_2,\vec{k}_3,\vec{k}_4)$ provides the form factors associated with the different instabilities (Sec. 2.6.4). Here, the singlet SC instability is twice degenerate and corresponds to a d-wave symmetry (E_2 representation), while the triplet SC instability is non-degenerate and fulfills an f-wave symmetry (B_2 representation). The corresponding form factors for nearest-neighbor pairing are

$$\begin{aligned}
&d\text{-wave:} \quad \begin{cases} f_{E_2,1} = 2\cos(k_x) - \cos\left(\frac{k_x-\sqrt{3}k_y}{2}\right) - \cos\left(\frac{k_x+\sqrt{3}k_y}{2}\right) \\ f_{E_2,2} = \cos\left(\frac{k_x+\sqrt{3}k_y}{2}\right) - \cos\left(\frac{k_x-\sqrt{3}k_y}{2}\right) \end{cases} \\
&f\text{-wave:} \qquad f_{B_2} = \sin(k_y) - 2\cos\left(\frac{\sqrt{3}k_x}{2}\right)\sin\left(\frac{k_y}{2}\right).
\end{aligned} \tag{4.3}$$

The calculation of the gap function and the corresponding free energy of the system is explained in Sec. 2.6.4. As the degeneracy in the d+id-wave SC is protected by symmetry, the system could generically form any linear combination $d_1 + \mathrm{e}^{\mathrm{i}\theta} d_2$ of both d-wave solutions. In this fRG calculations, d+id was always the energetically preferred

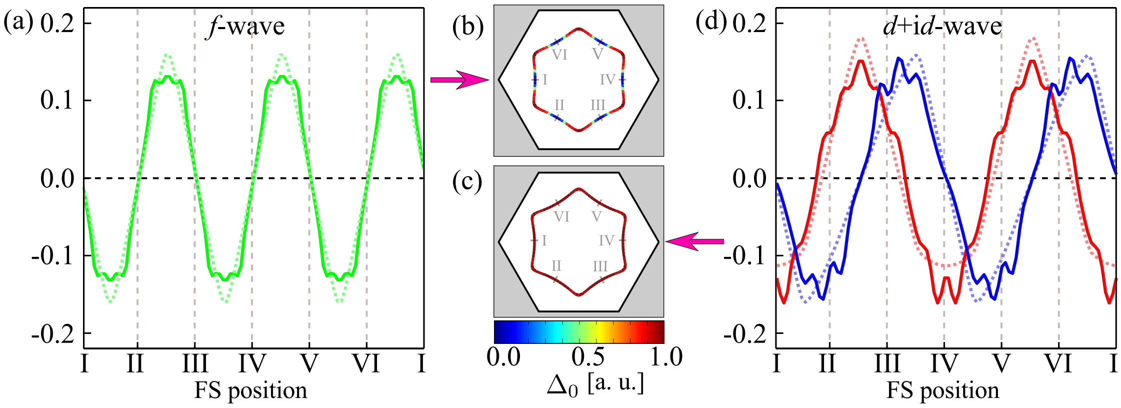

Figure 4.4: **(a)** Form factors from Eq. 4.3 (dotted lines) and the mean-field decoupled pairing channel (solid lines) for f-wave superconducting phases with $U_1 = 0.32$eV, $U_2 = 0.25$eV, $J_H = J_P = 0.07$eV, $x = 0.18$. **(b)** The corresponding gap size Δ_0 on the FS, where blue regions indicate nodes, which are absent in the d+id-wave superconducting phase, plotted in **(c)**. The corresponding form factors are presented in **(d)**. Here, the setting is $U_1 = 0.13$eV, $U_2 = 0.25$eV, $J_H = J_P = 0.07$eV $x = 0.14$.

combination. This is rather generic in a situation of degenerate nodal SC order parameters, since such a combination allows the system to avoid nodes in the gap function. In addition, a time-reversal symmetry-breaking state is always energetically favorable within a two-dimensional representation [238]. For the f-wave SC, the gap follows the absolute form factor and, consequently, features nodes. A comparison of these two phases is presented in Fig. 4.4. While there are nodes in the absolute gap of the f-wave SC (Fig. 4.4b), it is nodeless for the d+id-wave SC (Fig. 4.4c). Actually, the gap is nearly homogeneous.

The close proximity of d+id and f-wave SC can explain, why Knight shift measurements are inconsistent between singlet and triplet SC [59, 235]. But other experiments show an anisotropic gap function with nodes [60, 61, 236, 237], clearly indicating an f-wave SC. So, d+id-wave SC is disproved?

A statement of *S. Zhou and Z. Wang* invoke a d+id-pairing on next-nearest neighbors that features nodes at a doping level of $x = 0.25$, but they have no argument for preferring a next-nearest-neighbor pairing [239]. Also, the form factors in Fig. 4.4c correspond clearly to nearest-neighbor pairing, so this ansatz is questionable. In the next section, I propose that a competition between the SDW and the SC phase is the source for a strongly anisotropic d+id-wave gap.

4.4 Gap Anisotropy

Actually, the analysis of the d+id-wave gap in the previous section was within the *pure* d+id SC (blue in Fig. 4.3). But, if doping is increased, the nesting of the FS gets better and the SDW instability becomes competitive. How does this effect the d-wave instability?

The doping dependence of the two degenerate d-wave form factors and the resulting gap is plotted in Fig. 4.5. It is striking that the discrepancy between the calculated fRG

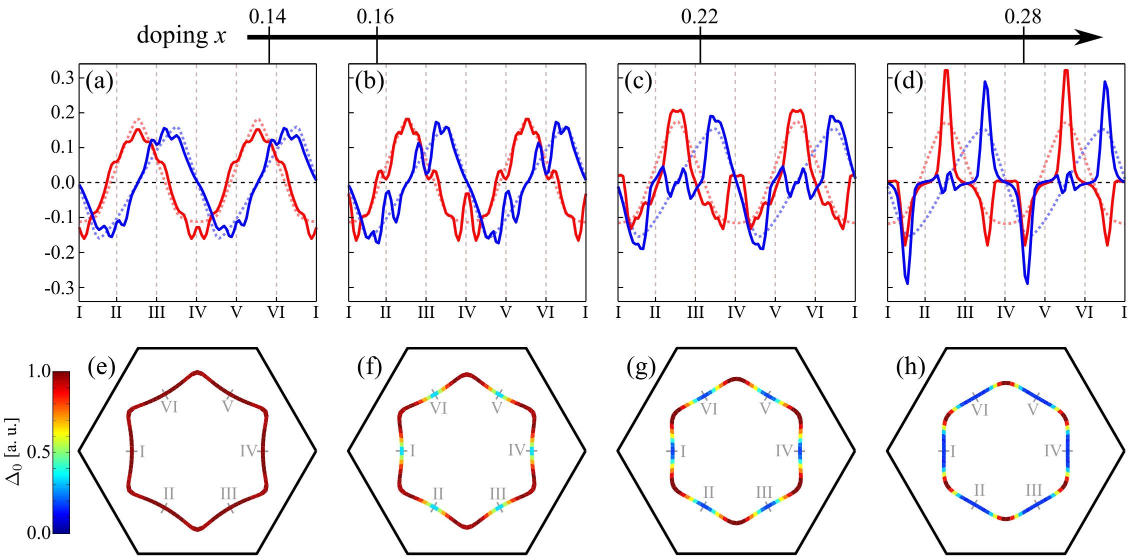

Figure 4.5: **(a-d)** Change of the d+id-wave form factor on doping. The setting is $U_1 = 0.13$eV, $U_2 = 0.25$eV, $J_H = J_P = 0.07$eV and a doping level of **(a,e)** $x = 0.14$, **(b,f)** $x = 0.16$, **(c,g)** $x = 0.22$ or **(d,h)** $x = 0.28$, respectively. While the fRG form factors (solid lines) in the pure d+id SC phase **(a)** match to Eq. 4.3 (dotted lines) pretty well, the accordance is decreasing with doping. If the SDW state is competitive **(d)**, the form factors differ significantly. **(e-h)** This influences also the SC gap of the d_1+id_2 superposition, which develops nodes on doping.

form factors and the analytical nearest-neighbor form factors of Eq. 4.3 is dramatically intensified when the doping approaches the competitive SDW / d+id SC phase. The calculation of the resulting gap reveals that the linear combination d_1+id_2 is still energetically favorable, but the structure of the gap changes. A linear combination of $|d_1\text{+i}d_2|$ has only roots if both d_1 and d_2 have roots at the same positions of the FS. Obviously, this is not the case in Fig. 4.5a, so the resulting gap is quite homogeneous (Fig. 4.5e). This changes in the competitive SDW / d+id SC phase, where d_1 and d_2 do indeed feature roots near the positions **I** to **VI** (Fig. 4.5d), hence the blue regions in Fig. 4.5h indicate a very strong reduction of the gap and possibly nodes.

Evidently, the gap anisotropy is enhanced with increased doping. To test this statement, the variance of the gap function is divided by the mean:

$$\text{gap anisotropy} := \eta = \frac{\sigma(\Delta_0)}{\overline{\Delta_0}} \tag{4.4}$$

In Fig. 4.6, η is plotted as a function of the doping x and the interaction relation $\frac{U_1}{U_2}$, corresponding to the x-y-layer in Fig. 4.3. The maximum of η is at a doping level $x \approx 0.3$, regardless of $\frac{U_1}{U_2}$. This implies that the proximity to the optimal nesting distinctly influences the d+id-wave, while the interaction scale is negligible. Thus, the FS topology and the underlying band structure play a crucial role.

Furthermore, in Chaps. 6 and 7, the mechanism for sublattice interference is discussed for the kagome lattice. There, the unfavorable distribution of the three sublattice weights to the pocket at the FS suppresses the nesting effects for a local interaction. By including long-range interactions, the suppression is reduced and, hence, the critical scale of

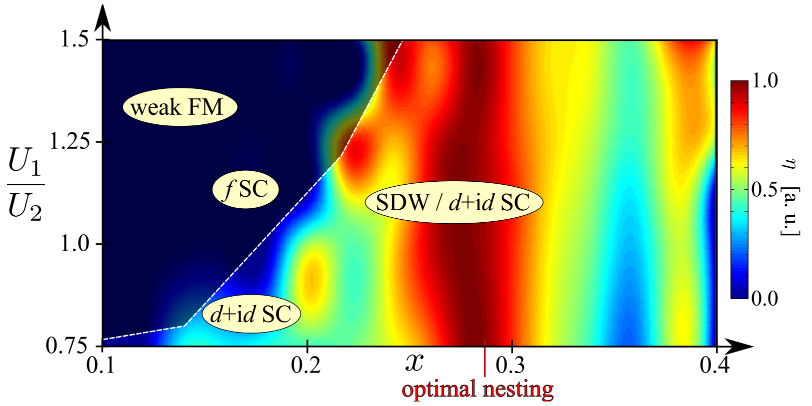

Figure 4.6: Gap anisotropy $\eta = \frac{\sigma(\Delta_0)}{\Delta_0}$ in the d+id-wave superconductivity phase. Blue regions indicate a homogeneous gap. Around the doping for the optimal nesting condition, the gap is very anisotropic, indicated by red regions.

superconductivity increased. In opposite, the orbital weights of NaCoO play a minor role because the anisotropy of the d+id-wave SC gap dramatically decreases when the doping is increased (Fig. 4.5), but the change of the orbital weights is negligible within this doping range (Fig. 4.2a vs. e). Thus, the anisotropy must have another reason.

To get a hint on the source of anisotropy, one has to compare the pure d+id SC phase with the competitive SDW / d+id SC phase. In Fig. 4.7, the FS, the DOS and the resulting gap function is confronted for both conditions. Two exemplary vectors at the FS are highlighted, one in the middle of an edge and one at a corner of the pocket. In Figs. 4.7a-c, the pure d+id phase is considered. The FS is angular and concave (Fig. 4.7a), and the optimal nesting vectors in Eq. 4.2 do not link any points. The closest vectors connect some elements (indicated by blue arrows), but there is still no nesting. So the SDW fluctuations are suppressed and an inhomogeneous local DOS (plotted in Fig. 4.7b) is insignificant. But the underlying SC fluctuations remain. This results in a homogeneous SC gap (Fig. 4.7c). In contrast, for the competitive SDW / d+id SC phase, both vectors have a good nesting condition (Fig. 4.7d), but the higher local DOS for the corner vector enforces the SDW (Fig. 4.7e) and, consequently, increasingly drives SC. At the end of the RG-flow, there is a larger gap at the corner vectors than at the edge vectors. Consequently, the gap is anisotropic (Fig. 4.7f).

This result has to be reviewed in the context of the experiments stated at the beginning of Sec. 4.3. There, an evidence for an anisotropic SC gap function with nodes was reported [60, 61, 236, 237], together with a singlet pairing state [59]. But both possible C_{6v}-symmetries with singlet configuration (s-wave and d+id-wave SC) are gapless. How does this fit together?

A possible solution is the anisotropic d+id-wave presented in this section because this SC state is twice degenerate and the corresponding form factors obey the E_2 symmetry, but they do not fit to the nearest-neighbor harmonic functions any more. Instead, they are distorted by anisotropic nesting effects. This results in a very inhomogeneous gap that is nearly closed at some vectors of the FS. This SC state is extremely unconventional. In experiments, it is hard to distinguish between this very anisotropic gap and a gap function

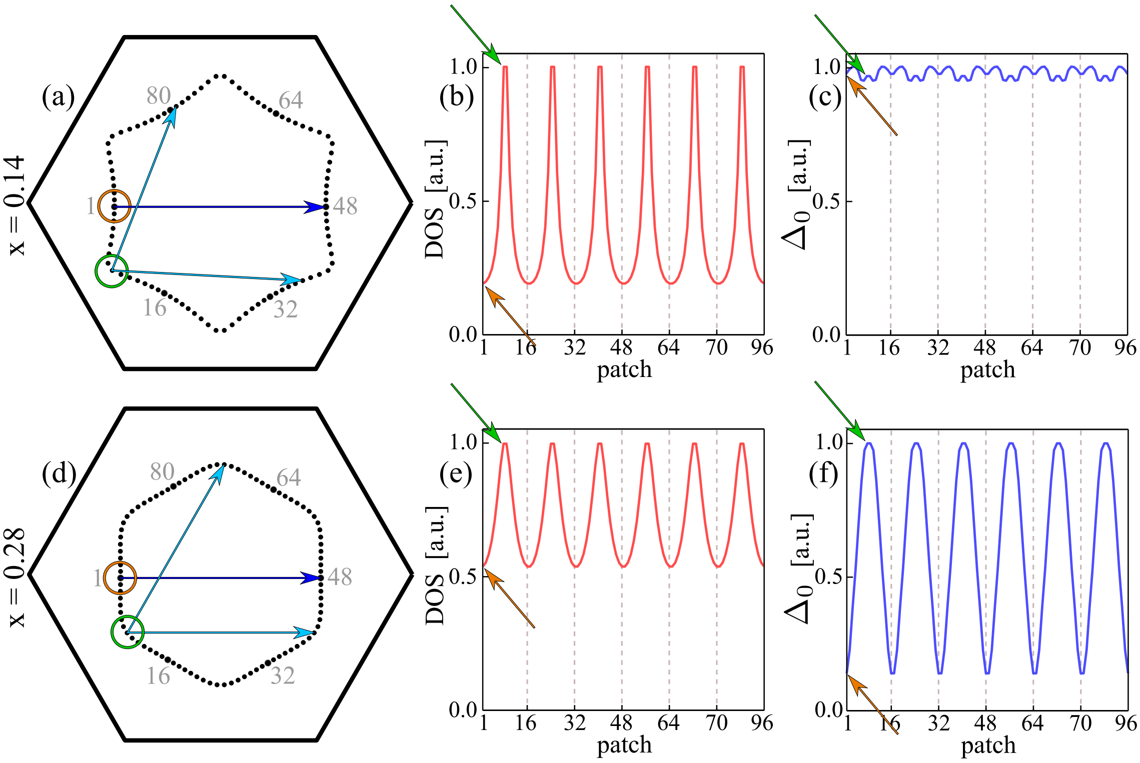

Figure 4.7: **(a-c)** A wave vector at an edge of the FS (orange marks) compared to one at a corner of the FS (green marks) for the pure d+id SC phase with $U_1 = 0.13$eV, $U_2 = 0.25$eV, $J_H = J_P = 0.07$eV, $x = 0.14$. **(a)** The vectors that are closest to the optimal nesting vectors in Eq. 4.2 do not link opposing edges, so nesting is very bad. Thus, SDW fluctuations are weak, independently of the local DOS. The SC fluctuations are homogeneous and result in an isotropic gap, plotted in **(c)**. **(d-f)** The same plots in the competitive SDW / d+id SC phase with $U_1 = 0.32$eV, $U_2 = 0.25$eV, $J_H = J_P = 0.07$eV, $x = 0.28$. Here, the perfect nesting (plotted in **(d)**) together with an anisotropic DOS (plotted in **(e)**) drive strong inhomogeneous SDW fluctuations that yield the anisotropic gap shown in **(f)**.

with real nodes.

4.5 Summary

The phase diagram of $\mathrm{Na}_x\mathrm{CoO}_2$ immersed with water is studied at a low doping regime $x \approx 0.3$, where a superconducting phase was detected. For this purpose, an effective three-band model in a triangular lattice is solved with functional-renormalization group calculations.

At doping levels around a van Hove singularity, ferromagnetic fluctuations are dominant and thus f-wave superconductivity prevails. At increased doping, the ferromagnetic fluctuations are weaker, so d+id-wave superconductivity becomes dominant. This chiral state is a candidate for topological superconductivity, which is a hot topic of condensed-matter physics (see Sec. 5.7 for an introduction).

When the distance between the CoO_2-layers is increased by additional water, a tendency to ferromagnetic fluctuations and f-wave superconductivity is experimentally observed.

In this thesis, this effect is connected with an increased interaction scale while the Fermi surface remains unchanged.

The apparent contradiction in experiments that detected a singlet pairing state together with nodes in the gap function is solved by the distortion of the d+id-wave state around the doping level for optimal nesting. Thus, the gap function is very anisotropic and is nearly partially closed, what is hard to distinguish from real nodes in experimental data.

To get a further insight into the gap anisotropy, more experimental data is needed. The superconducting state is induced by an enlargement of the layer distances by immersed water. This is hard to handle at the low temperatures needed to detect superconductivity. The substitution of water by another chemical compound might increase the stability of this material and hence facilitates the experimental analysis.

The chiral superconducting phase is an interesting new state of matter. For d-wave superconductivity, the superposition of the degenerate d_1 and d_2 solutions yield a nodeless gap function. The degeneracy of d_1 and d_2 is protected by the C_{6v} symmetry of the triangular lattice, but the competition with the spin-density phase phase induces a heavy anisotropy of the gap function. Another lattice with C_{6v} symmetry is the honeycomb lattice, which is the structure of the celebrated graphene. There, in contrast, the competition between d+id-wave superconductivity and spin-density phase does not induce a gap anisotropy, because the Fermi surface topology is distinct. This is the topic of the next chapter.

5

Competing Many-Body Instabilities and Unconventional Superconductivity in Graphene

The band structure of graphene exhibits van Hove singularities (VHS) at dopings $x = \pm 1/8$ away from the Dirac point. Near the VHS, interactions effects, enhanced due to the large density of states (DOS), can give rise to various many-body phases. The competition between different many-body instabilities in graphene are studied using the functional renormalization group (fRG, see Sec. 2.6 for technique). A rich phase diagram is predicted, which, depending on long-range hopping as well as long-range character and absolute scale of the Coulomb interaction, contains a d+id-wave superconducting (SC) phase, or a spin-density wave phase at the VHS. The d+id state is expected to exhibit quantized charge and spin Hall response, as well as Majorana modes bound to vortices. In the vicinity of the VHS, singlet d+id-wave as well as triplet f-wave SC phases are found.

The results of this chapter are published with *C. Platt, W. Hanke, D.A. Abanin* and *R. Thomale* in Ref. [2].

5.1 Graphene - New Physics in Two Dimensions

Graphene, a monolayer of carbon, hosts a two-dimensional electronic system with unique properties [57]. In particular, the Coulomb interaction plays an important role in graphene [240], giving rise to interesting many-body phenomena, including marginal Fermi-liquid behavior [241], energy-dependent renormalization of the Fermi velocity [242], as well as many-body states in the quantum-Hall regime [57]. In very high magnetic fields $B > 40$T, the quantum Hall effect is measurable even at room temperature [243]. Experimentally, graphene offers a high degree of tunability. In particular, carrier density can be controlled in a broad range. Near the Dirac point (filling level of electrons $n = 0.5$), such a control is achieved by back gates and local top gates [57]. Recently, it was demonstrated that chemical doping [244] and electrolytic gating [245] enable doping graphene far away from the Dirac point. In particular, the density can be tuned to the vicinity of the van Hove singularities (VHS) in the band structure, which occurs at fillings $n = 3/8$ and $n = 5/8$, respectively. In the case of chemical doping, the dopants form a superlattice on top of the graphene sheet. This strongly reduces the amount of disorder induced by doping [244]. Furthermore, the spacing of the superlattice is so large that hybridization in the dopant layer can be neglected and, hence, transport measurements of the graphene sample remain unaffected.

Before the strong doping of graphene has been recently accomplished experimentally, superconductivity had been predominantly studied around the Dirac point. This includes p+ip-wave predictions from electron-phonon or plasmonic [40, 246], Kekule order [247], as well as f or d+id-wave from electron-electron [248] interaction effects. Mean-field treatments [249, 250] have arrived at $T_c > 1000$K, with only slightly lower results for variational approaches [251]. Despite these predictions, SC has not been experimentally observed in this regime, due to small electronic DOS as well as weak phonon effects [252]. Near a VHS, opposite to the Dirac point regime, electronic interaction effects are expected to be strongly enhanced due to the logarithmically diverging DOS and near-nested Fermi surface (FS) [57]. In this regime, many-body states with appreciable critical temperatures may arise. Possible candidate states include charge-density wave (CDW), a spin-density wave (SDW), or an SC state. The latter has been recently considered within a perturbative three-patch renormalization group (3RG) [147] that only takes into account the saddle points of the FS. Generally, however, a subtle interplay of kinetic and interaction parameters is expected to decide which many-body instability is preferred at the VHS. For graphene, the additional complication arises that, as the band width ($\sim$ 17eV) is of the order of the interaction scale ($\sim$ 10eV), graphene cannot be suitably described from the viewpoint of strict weak-coupling approaches, and adopting a picture of intermediate coupling is necessary. Rephrased in terms of diagrammatic expansions starting from the non-interacting problem, this amounts to investigating the importance of leading *and* subleading divergent classes of diagrams. In particular, this is relevant for the competition between magnetic and SC phases in these kind of systems, one recent example of which have been the iron pnictides [46, 253].

5.2 Model and Parameter Setup

Graphene is based on a carbon monolayer which is arranged in a honeycomb structure (see Sec. 2.2 for details). With two carbon atoms per unit cell, the resulting dispersion relation features two bands. The interaction-free Hamiltonian (Eq. 2.8) includes hopping terms up to 3rd-nearest neighbors. This is the first order that shifts the VHS and the optimal nesting condition to different particle fillings.

The hopping integrals t_1, t_2 and t_3 for graphene have not yet clearly been evaluated, there are still some uncertainties about the long-range terms [57, 254]. For dominant t_1, the band structure features two van Hove singularities (VHS) at $n = 3/8$ and $n = 5/8$. Constrained to the electron-doped case, this is represented by the red line in Fig. 5.1a. As depicted, this is the regime of largely enhanced DOS which is the focus of attention in what follows. For $t_2 = t_3 = 0$, the VHS coincides with the partial nesting of different sections of the FS for

$$\vec{Q}_1 = \left(0, 2\pi/\sqrt{3}\right) \quad , \quad \vec{Q}_2 = \left(\pi, \pi/\sqrt{3}\right) \quad \text{and} \quad \vec{Q}_3 = \left(\pi, -\pi/\sqrt{3}\right) , \qquad (5.1)$$

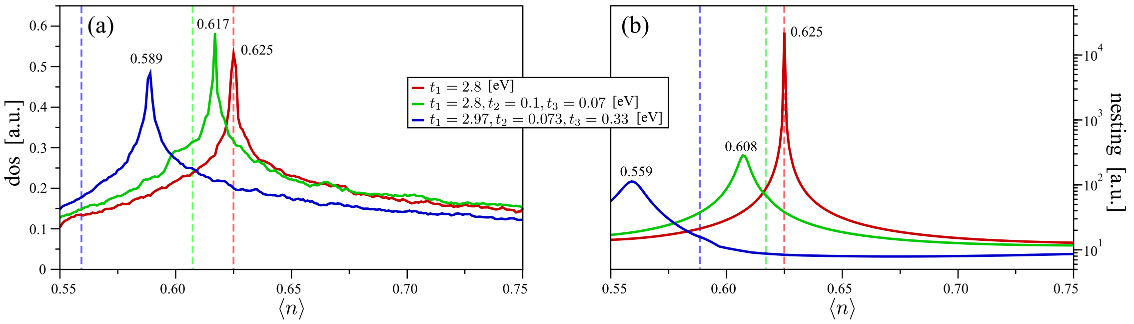

Figure 5.1: **(a)** Density of states as function of the particle density for graphene. The band structure is defined by three parameter settings. The first (red line) includes only next-nearest-neighbor hopping $t_1 = 2.8$eV. The second one (green line) extends this model with longer ranged hoppings $t_2 = 0.1$eV and $t_3 = 0.07$eV (taken from Ref. [57]). The last one (blue line) from Ref. [254] includes $t_1 = 2.97$eV, $t_2 = 0.073$eV and $t_3 = 0.33$eV. The peaks correspond to van Hove singularities. **(b)** Nesting factor as function of particle density. It tests how many (infinitesimal) elements of the Fermi surface (FS) can be connected by the same vector.
The vertical dashed lines in both plots indicate the peaks in the other plot. This clearly reveals that only in the first setting, the van hove singularity and the optimal nesting are at the same particle density $n = 5/8$. For the phase diagram obtained in the next section, I used the setting with $t_2 = 0.1$eV and $t_3 = 0.07$eV.
The FSs corresponding to this parameter settings are plotted in Fig. 5.2.

as shown in Fig. 5.1 with the red solid line. For a realistic band structure estimate with finite t_2 and t_3 [57,254], this gives a relevant shift of the perfect nesting position versus the VHS as well as DOS at the VHS (see green and blue solid lines in Fig. 5.1), and affects the many-body phase found there. The FSs for all three parameter settings are plotted in Fig. 5.2. Only in setting (a) with $t_2 = t_3 = 0$, the particle filling for VHS and optimal Nesting is identical, resulting in the same FS. For $t_2 > 0$ and $t_3 > 0$ (Figs. 5.2b,c), two different particle densities are needed to get VHS or optimal nesting, so two different FSs are plotted.

The Coulomb interactions were represented in Eq. 2.9 and included the Coulomb repulsion scale from on-site to the next-nearest-neighbor interaction. It depends on the DOS how strongly the Coulomb interaction is screened. At the VHS, perfect screening is assumed, so only the local limit U_0 is considered, while away from the VHS, the effects of U_1 and U_2 are taken into consideration. The typical scale of the effective local repulsion has been found to be $U_0 \sim 10\text{eV} < W$ [255], where $W \sim 17$eV is the kinetic bandwidth. This is in the limits of weakly correlated systems, so graphene can be calculated within the fRG framework, as described in Sec. 2.6.

To analyze all possible many-body phases and their dependence on the system parameters, the fRG provides a systematic unbiased summation of diagrams in both particle-particle channels *and* particle-hole channels as well as vertex corrections, and keeps track of the whole FS. Here, the most important low-energy physics will form at momenta near the FS. It is possible to confine the considerations to the band crossing the FS, while the contributions of the other band is negligible. So the band index of the Bogoliubov-transform matrix elements is fixed ($u_{mn}(\vec{k}) \to u_m(\vec{k})$). For the discretization of the fRG-flow, the Brillouin zone has to be divided into patches, which is shown in

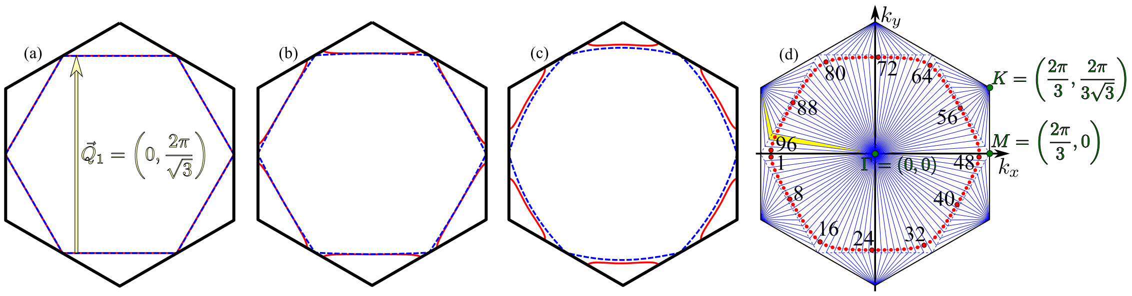

Figure 5.2: (a,b,c) FSs for graphene with three different settings for hopping parameters. The particle densities are chosen to set the FS at the van Hove singularity (dashed blue line) or at optimal nesting (solid red line), respectively (Fig. 5.1). The Parameter sets are: **(a)** $t_1 = 2.8$eV; **(b)** $t_1 = 2.8$eV, $t_2 = 0.1$eV, $t_3 = 0.07$eV [57] (used for the phase diagram), **(c)** $t_1 = 2.97$eV, $t_2 = 0.073$eV, $t_3 = 0.33$eV [254]. **(d)** The complete Brillouin zone is divided into 96 patches.

Fig. 5.2d.

5.3 Phase Diagram

The phase diagram as a function of doping, obtained for realistic microscopic kinetic and interaction parameters [57, 255] is shown in Fig. 5.3. At the same time, however, trends are investigated of how the system evolves when the parameters are tuned away from this setting.

At the VHS (orange-shaded area in Fig. 5.3), the DOS is so large that a local Hubbard description is appropriate. (The conclusions drawn here also persist as small long-range Coulomb components would be taken into account at exact van Hove filling.) For realistic $U_0 \sim 10eV$, the d+id SC instability is dominant, assuming finite hopping parameters $t_2 = 0.1$eV and $t_3 = 0.07$eV [57]. (The result is rather similar for the values of [254].) Only at scales of $U_0 > 18$ eV the SDW becomes dominant for this scenario. However, t_2 is reduced, the system gets more biased to the SDW, as the SDW fluctuations in the nesting channel get enhanced. For t_1 only, the SDW already wins for $U_0 > 8.5$eV, and can give rise to a helical magnet scenario, as discussed in Sec. 5.6.

Doped away from the VHS (blue shaded area in Fig. 5.3), details of the band structure become less relevant, and the critical instability scale T_c drops stronger towards the Dirac point than away from it, mainly as a consequence of the reduced DOS. As SDW fluctuations are weakened, SC phases become dominant. Still assuming rather local Coulomb interactions ($U_1/U_0 < 0.40$), the system still favors the d+id SC state. If the reduced screening of the Coulomb interaction does not justify the assumption of a local Hubbard model description, a longer ranged Coulomb interactions [255] can significantly change the phase diagram. Hence, allowing for more long-range Hubbard interactions, the picture changes: The CDW fluctuations are comparable to the SDW fluctuations which would bias the system towards singlet SC, and triplet f-wave pairing becomes competitive.

The results suggest that in experiment, modifications of the band structure such as imposed by pressure as well as changing the dielectric environment of the graphene

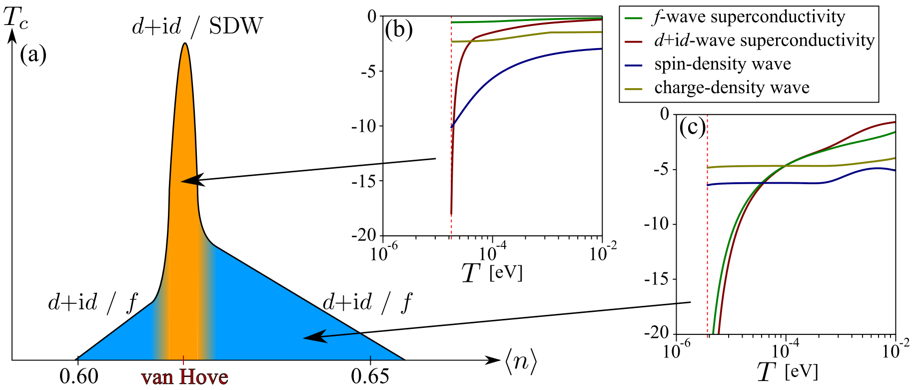

Figure 5.3: **(a)** Phase diagram for graphene around van Hove filling as obtained by fRG. T_c serves as an upper bound for the critical temperature of phase transitions as a function of doping. **(b)** Dominant d+id instability at van Hove filling for $U_0 = 10$eV and the band structure in Ref. [57]. **(c)** Away from van Hove filling (blue shaded area), T_c drops. Whether d+id or f-wave SC instability is preferred depends on the strength of long-range interactions ($U_1/U_0 = 0.45$ and $U_2/U_0 = 0.15$).

sample would enable the realization of different many-body states and possible phase transitions between them.

5.4 Singlet Superconductivity: d+id-Wave Symmetry

At the VHS and nothing but a local interaction, the dominating phase is d-wave SC. After the decomposition of the final vertex into the SC-channels (Eq. 2.130), the form factors $f(\vec{k})$ of the singlet channel can be calculated (see Sec. 2.6.5 for details). Here, the leading eigenvalue is twice degenerate, so two form factors have to be considered. The results are plotted with solid lines in Figs. 5.4c,d. From the Fourier transform of the momentum-resolved form factors along the FS it is possible to obtain the pairing amplitudes of the real-space SC pairing function [256]. Here, the form factors corresponding to nearest, next-nearest, 3rd-nearest and so on, neighbor hopping are calculated and transformed to momentum space and compared to the fRG form factors.

The honeycomb lattice is characterized by C_{6v} symmetry about the center of hexagons, and the SC order parameter transforms as one of the irreducible representations. As explained in Sec. 2.3, the $d_{x^2-y^2}$ and d_{xy}-wave follow the two-dimensional E_2 representation and are hence degenerate. Fig. 5.4b shows the character of the E_2 representation. If these are applied to the next-nearest neighbors (see yellow arrows in Fig. 5.4a, they read

$$\begin{aligned} f_{E_2,1} &= 2\cos\left(\sqrt{3}k_y\right) - \cos\left(\frac{\sqrt{3}k_y - 3k_x}{2}\right) - \cos\left(\frac{\sqrt{3}k_y + 3k_x}{2}\right) \\ f_{E_2,2} &= \cos\left(\frac{\sqrt{3}k_y - 3k_x}{2}\right) - \cos\left(\frac{\sqrt{3}k_y + 3k_x}{2}\right) . \end{aligned} \tag{5.2}$$

and (plotted with dotted lines in Figs. 5.4c,d) fit very well to the fRG ones. So one can

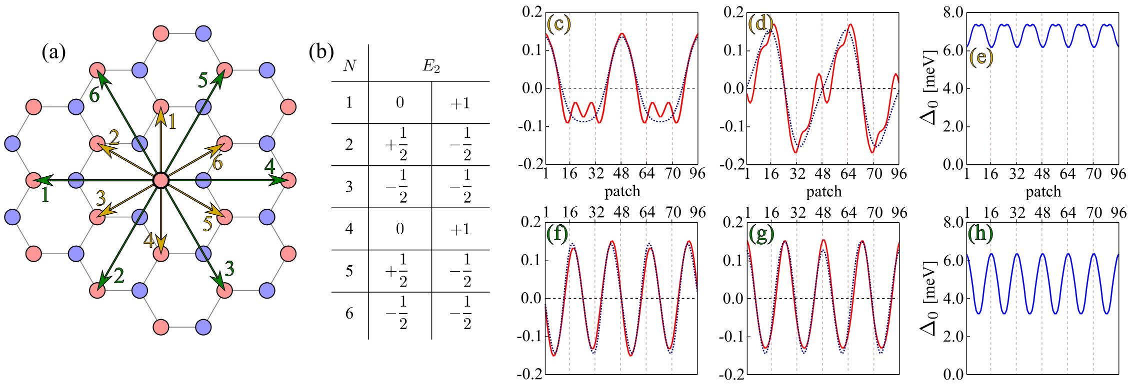

N	E_2	
1	0	$+1$
2	$+\frac{1}{2}$	$-\frac{1}{2}$
3	$-\frac{1}{2}$	$-\frac{1}{2}$
4	0	$+1$
5	$+\frac{1}{2}$	$-\frac{1}{2}$
6	$-\frac{1}{2}$	$-\frac{1}{2}$

Figure 5.4: **(a)** Real-space pattern of pairings between nearest (yellow arrows) and next nearest (green arrows) neighbors in the *same* sublattice. **(b)** Possible character table of the E_2 representation of the C_{6v} symmetry group. Combined with the positions marked in **(a)**, they yield the analytic form factors, as discussed in Sec. 2.3. $d_{x^2-y^2}$ and d_{xy}-wave solutions for **(c-e)** $U_0 = 10\text{eV}$, $U_1/U_0 = 0.45$ and $n = 5/8$ (VHS) or **(f-h)** the same parameters with additionally $U_2/U_0 = 0.15$, respectively. (c,d,f,g) show the form factors of $d_{x^2-y^2}$ and d_{xy} plotted along the FS according to patch indices defined in Fig. 5.2d. The solutions change from **(c,d)** to **(f,g)**. The analytic form factors given in the text (blue dotted lines) fit the numerical data (red solid lines). **(e)** and **(h)** show the gap profile of d+id along the FS (actual connection to experimental energy scale can still vary by a global factor). The gap anisotropy increases from **(e)** to **(h)**.

conclude that the Cooper pairing emerges on nearest neighbors of the *same* hexagonal sublattice.

In the broader vicinity of the VHS, when long-range Hubbard interaction can not be neglected, the form factors retain the d-wave E_2 representation, while the Cooper pair wave function changes as shown in Figs. 5.4f,g ($U_1/U_0 = 0.45$, $U_2/U_0 = 0.15$). There, the form factors change to

$$\begin{aligned} f_{E_2,1} &= 2\cos(3k_x) - \cos\left(\frac{3\sqrt{3}k_y - 3k_x}{2}\right) - \cos\left(\frac{3\sqrt{3}k_y + 3k_x}{2}\right) \\ f_{E_2,2} &= \cos\left(\frac{3\sqrt{3}k_y - 3k_x}{2}\right) - \cos\left(\frac{3\sqrt{3}k_y + 3k_x}{2}\right), \end{aligned} \tag{5.3}$$

corresponding to a doubled number of nodes along the FS. Here the pairing spreads out to the next-nearest neighbor of the *same* sublattice (see green arrows in Fig. 5.4a). This is a consequence of the long-range Coulomb interactions: The Cooper pair wave function seeks to develop more nodes to minimize Coulomb repulsion, and is able to do so by longer ranged Cooper pairing. This, however, is not the form of the gap function of the d-wave instability. As the degeneracy is protected by symmetry, the system could generically form any linear combination $d_{x^2-y^2} + e^{i\theta} d_{xy}$ of both d-wave solutions. The gap equation Eq. 2.136 is iteratively solved, with the form factors of d_1, d_2 and d_1+id_2 as starting conditions. After the minimization, the grand potential is evaluated (Eq. 2.137), where always d+id is the energetically preferred combination. This is rather generic in a situation of degenerate nodal SC order parameters, since such a combination allows the system to avoid nodes in the gap function. The gaps are hence nodeless and only slightly change their anisotropy as the pairing function varies (Figs. 5.4e,h).

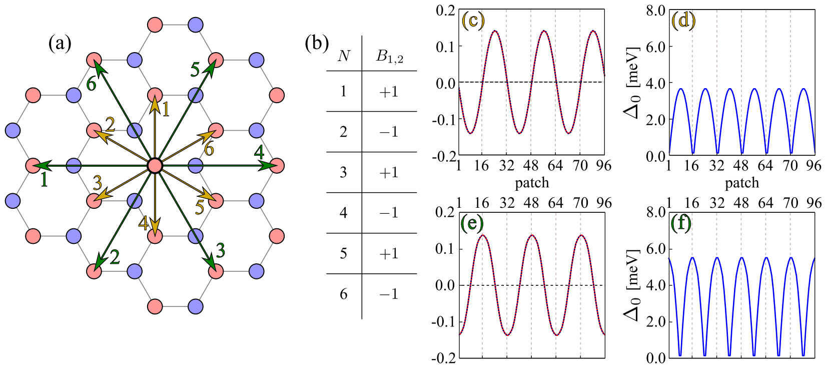

Figure 5.5: (a,b) The real-space pattern is identical to Fig. 5.4a, but the character table now describes the B_2 (nearest neighbors) or the B_1 (next-nearest neighbors) symmetry, as discussed in Sec. 2.3. **(c-f)** Pairing amplitudes, form factors, and gap profiles for the f-wave phase as defined in Fig. 5.4, representative for $n = 0.65$ (larger than the VHS) for **(a)** $U_1/U_0 = 0.6$ to **(b)** $U_1/U_0 = 0.6, U_2/U_0 = 0.2$. The gap profile is nodal and the nodal points shift from **(d)** to **(f)**.

As graphene can be tuned rather accurately to the van Hove filling, it may be a reasonably accessible experimental system to study such an SC phase. The expected experimental evidence for d+id would be a nodeless gap detectable through transport measurements and singlet pairing due to a Knight shift drop below T_c. A minor caveat is given by the role of impurities which may spoil the symmetry between the two d-wave solutions. This could give rise to a nodal gap beyond sufficient impurity concentration [257].

5.5 Triplet Superconductivity: f-Wave Symmetry

It is similarly interesting to investigate the triplet f-wave instability [135], which dominates for longer ranged Coulomb interaction (Fig. 5.5). It obeys the one-dimensional B_1 or B_2 representation, depending on the range of the Coulomb interaction. For $U_1/U_0 = 0.6$, the form factor and pairing amplitudes are plotted in Figs. 5.5c,d as well as for $U_1/U_0 = 0.6$, $U_2/U_0 = 0.2$ in Figs. 5.5e,f. Again, the Cooper pair distance increases with longer ranged interactions, which manifests itself as a change of the form factor

$$\begin{aligned} f_{B_2} &= \sin\left(\sqrt{3}k_y\right) - 2\sin\left(\frac{\sqrt{3}k_y}{2}\right)\cos\left(\frac{3k_x}{2}\right) \quad \text{in (c) to} \\ f_{B_1} &= \sin\left(3k_x\right) - 2\sin\left(\frac{3k_x}{2}\right)\cos\left(\frac{3\sqrt{3}k_y}{2}\right) \quad \text{in (e) .} \end{aligned} \tag{5.4}$$

The gap function follows the absolute value of the form factor, showing a nodal gap, where the points of the nodes change with increasing Coulomb range. In the case of f-wave, the position of the nodes would hence indicate the Cooper pairing distance associated with the long-range properties of the Coulomb interaction, and suggest experimental evidence of a nodal gap from transport and an invariant Knight shift due to triplet pairing. For filling smaller than the VHS, the FS is disconnected and it can happen that the nodes do not coincide with the FSs. This f-wave regime is probably very low in T_c, depending on whether B_1 or B_2 is preferred, and may be nodeless.

5.6 Spin-Density Wave Order

Around the van Hove filling, there is a strong competition between the spin-density wave (SDW) and a chiral d+id-wave superconductivity. Already small changes in filling, hopping ranges or interaction ranges change the dominating channel in the fRG-flow.

The discussion on the dominating order at van Hove filling is still active because some calculations predict chiral d+id superconductivity [147, 244, 258], while others get a magnetic order [148]. Indeed, results from angle-resolved photoemission spectroscopy verify the calculated band structures [244], but the real-space pattern of the magnetic order is not clear. At the moment, there are two different suggestions:
The first one was proposed by *T. Li* [259] and continued by *W.-S. Wang et al.* [148]. Here, the order is not restricted to an S_z projection but includes a full three-dimensional spin. The three equivalent nesting vectors prefer different real-space orders. To implement all three orders at once, each nesting vector is combined with an orthogonal spin direction. Hence, energetically favorable spin structure is a linear combination [259]

$$\begin{aligned}\langle \vec{S}_{\vec{R},A} \rangle &= \vec{M}_3 \mathrm{e}^{\mathrm{i}\vec{Q}_3\vec{R}} + \vec{M}_1 \mathrm{e}^{\mathrm{i}\vec{Q}_1\vec{R}} + \vec{M}_2 \mathrm{e}^{\mathrm{i}\vec{Q}_2\vec{R}} \\ \langle \vec{S}_{\vec{R},B} \rangle &= \vec{M}_3 \mathrm{e}^{\mathrm{i}\vec{Q}_3\vec{R}} - \vec{M}_1 \mathrm{e}^{\mathrm{i}\vec{Q}_1\vec{R}} - \vec{M}_2 \mathrm{e}^{\mathrm{i}\vec{Q}_2\vec{R}}\end{aligned} \tag{5.5}$$

with three mutually orthogonal and equal length vectors $\vec{M}_{1,2,3}$. This results in a real-space pattern with four different sublattices with spin

$$\begin{aligned}\text{sublattice 1}: &\ +\vec{M}_1 + \vec{M}_2 + \vec{M}_3 \\ \text{sublattice 2}: &\ -\vec{M}_1 - \vec{M}_2 + \vec{M}_3 \\ \text{sublattice 3}: &\ +\vec{M}_1 - \vec{M}_2 - \vec{M}_3 \\ \text{sublattice 4}: &\ -\vec{M}_1 + \vec{M}_2 - \vec{M}_3\ ,\end{aligned} \tag{5.6}$$

which form the vertices of a tetrahedron. A possible real-space pattern of this order is plotted in Fig. 5.6b. This chiral SDW state breaks parity and time-reversal invariance. Also, the rotational symmetry C_6 is broken and the translational symmetry is reduced to a unit cell with eight sites. This pattern yields a magnetic state with nonzero spin chirality. It is an insulator and features the anomalous quantized Hall effect [259]. An insulator with nonzero Hall conductance is called a Chern insulator.
The other magnetic order was introduced by *R. Nandkishore and G.-W. Chern et al.* [260, 261] and features a paramagnetic phase that breaks the translational invariance without changing the point-group symmetry of the lattice. It includes a new unit cell with eight sites, namely, six sites with momentum $-\Delta$ and two sites with $+3\Delta$. So, the $O(3)$ spin-rotationally symmetry is broken. There are four equivalent orders, which can not be transformed into each other by a global spin rotation [261]. The uniaxial SDW state is plotted in Fig. 5.6c. A particular feature of this state are the gapless charged excitations in just one spin branch, resulting in a half-metallic behavior [260].

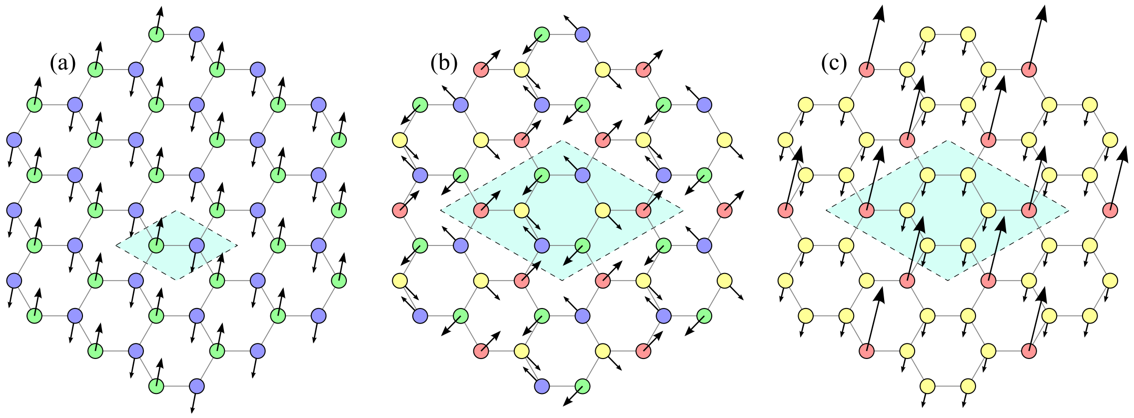

Figure 5.6: Various implementations of the real-space pattern of the SDW phase in graphene. **(a)** In the standard Heisenberg antiferromagnet, one sublattice is populated by spin-up electrons (green sites), the other one by spin-down electrons (blue sites). The magnetic unit cell is identical to the non-magnetic one and contains two sites. **(b)** Tetrahedron magnetic ordering [148, 259]. There are four different spin orientations (red/green/blue/yellow sites), which reflect the vertices of a tetrahedron. The magnetic unit cell contains eight sites. **(c)** Uniaxial SDW order [260, 261]. In a unit cell of eight sites, there are six sites with spin down (yellow sites) and two sites with a trice spin up (red sites). The rotational symmetry is still present.

Now, the task is to determine the real-space pattern of the SDW phase obtained by fRG within this thesis. As described in Sec. 2.6.5, it is possible to transform the final vertex from band to sublattice representation. After the mean-field decoupling of all possible combinations, the dominating channel (now with sublattice indices) can be determined. Indeed, there is *no* significantly dominating channel for the SDW phase. The reason is that the decoupled vertex is still in momentum space, with a real-space unit cell containing two sublattices. If the SDW order is a classical antiferromagnetic order (see Fig. 5.6a, realized in graphene at half filling [248]), electrons in one sublattice have spin up, the others spin down. Here, the mean-field channel with $\langle \hat{c}^{\dagger}_{i\alpha\uparrow} \hat{c}_{i\alpha\downarrow} \rangle$, i.e a spin flip in the *same* sublattice, is significantly larger than the channel with spin-flip hopping between *different* sublattices. But both the tetrahedron SDW and the uniaxial SDW form a new magnetic unit cell with eight sites. So there are more than one spin direction in one sublattice and the band to sublattice transformation fails. So, the fRG does not tell anything about the SDW order? Actually, one statement is clear: From the three real-space pattern in Fig. 5.6, order (a) is excluded. But it is not possible to distinguish between the other two orders.

5.7 Outlook: Topological Superconductors

The possibility of the time-reversal symmetry-breaking d+id phase in graphene is very intriguing because it has been noted early on in the context of the cuprates that such a phase would have various interesting properties such as quantized edge currents [162, 262]. Furthermore, provided Rashba spin-orbit interaction is present, d+id phase supports Majorana modes in the vortex cores obeying non-Abelian statistics [263]. This topic is very present in current discussions, so a closer look on topological phases is appropriate.

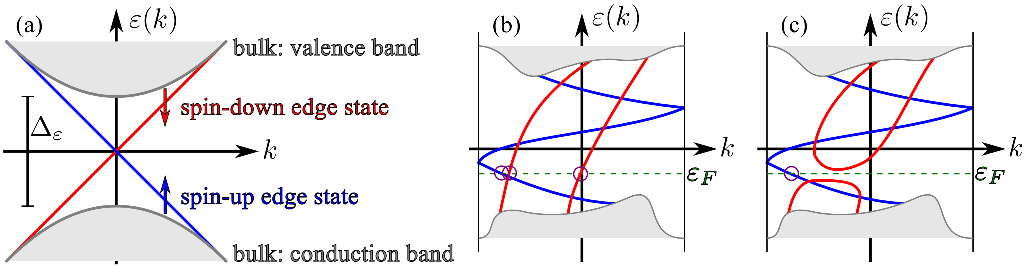

Figure 5.7: **(a)** Band structure of a two-dimensional topological insulator. The bulk is an insulator with gap size Δ_ε, while two distinguishable edge states are crossing within the energy gap. In this example, the edge states have antiparallel spin polarization. The crossing point is protected by topology because a possible back scattering is extremely improbable because of the antiparallel spins. In a three-dimensional topological insulator, the surface states are protected. **(b)** Another example with three edge states. The two distinguishable edge channels, indicated by red and blue solid lines, differ by spin polarization. There is one edge state in the blue channel and two in the red one, resulting in three zero energy modes (indicated by circles). **(c)** Slightly deformed band structure. Here, only the zero energy mode in the odd channel was protected by topology.

Firstly, the so-called *topological insulators* are band insulators in the bulk but have metallic edge states that are protected by topology (Fig. 5.7a). These materials break time-reversal symmetry and/or parity. The number of edge/surface states is odd or even, represented by a $\mathbb{Z}_2$ symmetry group. The topological invariant of an insulator can not be changed, except the band gap of the bulk is closed [264]. Only with an odd number of edge/surface states per channel, these are protected by topology (Figs. 5.7b,c). In these systems, a new state of matter can be realized, the quantum spin Hall effect [265, 266]. That effect is also present in graphene with a Rashba coupling [267, 268]. In general, the distinction between a normal and topological insulating phase is expressed by a topological number $\nu \in \mathbb{Z}_2$. A review on topological insulators is given in Refs. [264, 269, 270].

This concept can be transfered to superconductors [264, 270] because these are (at least partially) gaped within the superconducting phase. If the time-reversal symmetry as well as parity is broken, there exist surface states between the superconducting domain and the normal one [238]. These states are protected by symmetry and hence stable. The topology of these phases is characterized by the Chern number [238]. Again, to change the Chern number of a topological superconductor, the gap has to be closed.

Up to now, all discovered high-T_c superconductors are Type-II superconductors [271, 272], which, above a critical magnetic field H_{c1}, feature a lattice of vortices in the superconducting phase. Within a single vortex, there is a quantized magnetic flux, while there is no magnetic field in the remaining superconducting domain (Meissner effect). Only if the magnetic field is larger than H_{c2}, the superconducting state completely vanishes. The boundaries of the vortices are surfaces between superconducting and normal domains, so they can feature topological surface states if the requirements are fulfilled. In the superconducting state, the particle conservation is violated, but there is a particle-hole symmetry for excitations of quasiparticles. Hence, with $\hat{c}_\sigma(\varepsilon)$ being the annihilation operator of a quasiparticle with spin σ and energy ε, the particle-hole symmetry yields

$$\begin{aligned} \hat{c}_\sigma(\varepsilon) &= \hat{c}^\dagger_\sigma(-\varepsilon) \\ \lim_{\varepsilon\to 0}\left(\hat{c}_\sigma(\varepsilon)\right) &= \lim_{\varepsilon\to 0}\left(\hat{c}^\dagger_\sigma(-\varepsilon)\right) \\ \hat{c}_\sigma(0) &= \hat{c}^\dagger_\sigma(0) \\ \hat{\gamma} \ &= \hat{\gamma}^\dagger \ . \end{aligned} \tag{5.7}$$

So, creator and annihilator are equal. In other words, the (quasi)particle and its antiparticle are identical. This construction is called a Majorana fermion (MF) [273–275] at zero energy. Originally, it had been proposed for high-energy particle physics to describe elementary particles, e.g. the neutrino. There, the "classical" fermions are called Dirac fermions. In condensed-matter physics, one need the combination of two MFs to create a Dirac fermion:

$$\left.\begin{aligned} \hat{f} \ &= \tfrac{\hat{\gamma}_1+i\hat{\gamma}_2}{2} \\ \hat{f}^\dagger &= \tfrac{\hat{\gamma}_1-i\hat{\gamma}_2}{2} \end{aligned}\right\} \quad \hat{f} \ \neq \hat{f}^\dagger \tag{5.8}$$

Two separate MFs can form a Dirac fermion, so this construction is non-local. In addition, the non-local states described by $\hat{f}$ can be filled and emptied with no energy cost, resulting in a ground-state degeneracy [275]. Hence, $\hat{\gamma}$ rotates the wave function inside of the ground-state manifold in a non-commutative fashion [275].

To clarify the impact of this statement, one has to take a look on statistics: Particles with an Abelian statistic include a commutation relation $\langle\Psi_1\Psi_2\rangle = \langle\Psi_2\Psi_1\rangle e^{i\phi}$. Here, $\phi = 0$ describe bosons, $\phi = \pi$ are fermions and the others are called anyons. So, only a complex phase is multiplied, when two particles are exchanged. However, the quasi-particles created by $\hat{\gamma}$ are more complicated because an exchange of two of these non-Abelian anyons results in a complete new quantum state. So, if a vortex in a superconductor binds an MF, the exchange of two vortices also will obey non-Abelian statistics. Here, it is important to notice that only an odd number of MFs within a vortex obey non-Abelian statistics [263].

Very recently, *V. Mourik et al.* claimed the detection of MFs in hybrid superconductor-semiconductor nanowire devices [276]. If this result is verified, it would be the first experimental realization of this theoretical concept. This will boost the interest in research on MFs.

Now, one has to examine the circumstances for MFs in superconducting surface states. As Eq. 5.7 states, MFs have a fixed (quasi-) spin. Hence, systems with only one kind of fermionic constituents for Cooper pairs provide ideal platforms [275], e.g. a spin-triplet superconductor of *p*+i*p*-wave type. Another possible realization is a spin-singlet superconductor with Rashba spin-orbit coupling in a magnetic field. Here, the *s*-wave type need a Zeeman splitting larger than the superconducting gap, while for the *d*+i*d*-wave type a small magnetic field is sufficient [263]. Also, this type is more stable than *p*+i*p*-wave one [263]. One candidate is *d*+i*d*-wave superconductivity in $\mathrm{Na_{0.3}CoO_2 \cdot H_2O}$ [263] (see also Chap. 4). As shown in this chapter, also graphene has a phase with *d*+i*d*-wave superconductivity. The tunability of the Rashba interaction in graphene [277] may enable realization of the Majorana modes in vortices; owing to the two-dimensional nature of graphene and its remarkable tunability, their observation and manipulation should be easier than in other materials.

The MFs in vortices of a topological superconductor with their non-Abelian statistics are proposed to be candidates for a quantum computer device [275] because the energy of the manifold-degenerate ground state of MFs is within the band gap, so this state is robust to thermal fluctuations. In addition, the non-local origin of the MFs reduces the probability of a random change in the ground state. Hence, a defined state is very stable [275]. If this state is manipulated by an exchange of two vortices, i.e. the exchange of two MFs, the state does not gain a simple phase but is completely altered, due to the non-Abelian statistics. This corresponds to a rotation in the space of the manifold-degenerate ground state and is equivalent to the manipulation of "qubits", which are an arbitrary superposition of $|0\rangle$ and $|1\rangle$ [278], in contrast to classical computers, which save information in digital bits with the values 0 and 1. Hence, with the same number of bits and qubits, respectively, the quantum computer is able to save by far more information. But this is only correct as long as the program is running because, when the result is read, the superposition collapses. A review on quantum computers is given in Ref. [278].

The advantage of such a quantum computer is enormous: For example, *P. Shor* has published an algorithm for integer factorization that runs in polynomial time [279]. Unfortunately, nowadays the encryption of important data is based on public-key cryptography, which in turn is based on multiplication of very large integers. So the factorization of very large integers is needed to break the encryption. A classical computer needs far to long to do this task, but a quantum computer with a Shor's algorithm would break all encryptions in a reasonable short time.

Up to day, the realization of a suitable quantum computer is still science fiction. But the concepts presented in this section show a possible route to this invention.

5.8 Summary

This chapter has provided a detailed analysis of the competing many-body phases of graphene at and around van Hove filling. For realistic band structure parameters and interactions, the exotic nodeless singlet d+id-wave superconductivity phase is preferred over an extended phase-space regime around the van Hove singularity.

Variations of the kinetic parameters and effective interaction scales can drive a transition to a spin-density wave phase at the van Hove point. Away from the van Hove singularity, reduced Coulomb screening and, thus, longer ranged Coulomb interactions change the form of the d+id Cooper pair wave function, and in certain limits can favor a nodal triplet f-wave SC phase. The real-space pattern of the spin-density wave is still in discussion, but with the techniques used in this thesis it was not possible to make a statement on this topic. Here, some open questions remain.

Finally, I gave a short outlook on Majorana fermions and quantum computers and showed that the d+id phase of graphene is a possible compound for the realization of this future technology.

In summary, the chiral d+id-wave superconductivity and its properties have been discussed for $\mathsf{Na_{0.3}CoO_2} \cdot y\mathsf{H_2O}$ and graphene. These materials are based on the triangular and the honeycomb lattice, respectively, which feature the C_{6v} symmetry. Hence, it is consequent to propose a d+id-wave superconducting state also in the (C_{6v}-symmetric) kagome lattice. Especially the similarity of the low-energy band structures of the honeycomb and the kagome lattice suggest that statement. However, as discussed in the next chapters, a closer look on the properties of the FS of the kagome lattice reveals the effect of sublattice interference, which has a dramatic impact on FS instabilities and, in particular, d+id-wave superconductivity.

6

Sublattice Interference in the Kagome-Hubbard Model

Using an analytic renormalization group analysis, the electronic phases are studied in the infinitesimal-coupling limit around van Hove filling of the kagome lattice (Sec. 2.2). There exists an interference mechanism where the kagome sublattice structure affects the character of the Fermi-surface instabilities. This roots in the observation that similar to multiorbital models, where the Fermi surface (FS) can have varying orbital weights at distinct points in the Brillouin zone (BZ), the multisublattice kagome Hubbard model with local interactions exhibits reduced nesting effects due to different sublattice distributions at the nested Fermi-surface regions. This leads to major suppression of T_c for d+id superconductivity (SC) and causes an anomalous increase of T_c upon addition of longer-range Hubbard interactions. The suppression of conventional Fermi-liquid instabilities makes the kagome Hubbard model a prototype candidate for hosting unconventional electronic states of matter at intermediate coupling.

The results of this chapter are published with *R. Thomale* in Ref. [3].

6.1 Motivation

Understanding the variations of the critical scale T_c of unconventional, i.e. electronically mediated, superconductivity is a long-standing challenge in condensed matter. For the cuprates, T_c as a non-universal quantity has been found to depend on various quantities such as structural parameters [280], number of layers [281], Fermi-surface topology [282], and orbital content of electrons at the Fermi level [283]. For the latter, the d_{z^2} admixture to the dominant $d_{x^2-y^2}$ Fermi-surface character has been suggested as a substantial influence on T_c, a motif which is even more visible in the iron pnictides. There, all t_{2g} Fe_d-orbitals host large portions of electronic states in the vicinity of the FS, which generically necessitates a multiband description. As a consequence, universal trends of superconductivity both in terms of order parameter anisotropy and T_c sensitively depend on the structural features which determine this orbital composition [46, 284].

Multiband descriptions are both implied due to multiple orbitals and multiple sites associated with the unit cell of a given lattice. While previously mentioned

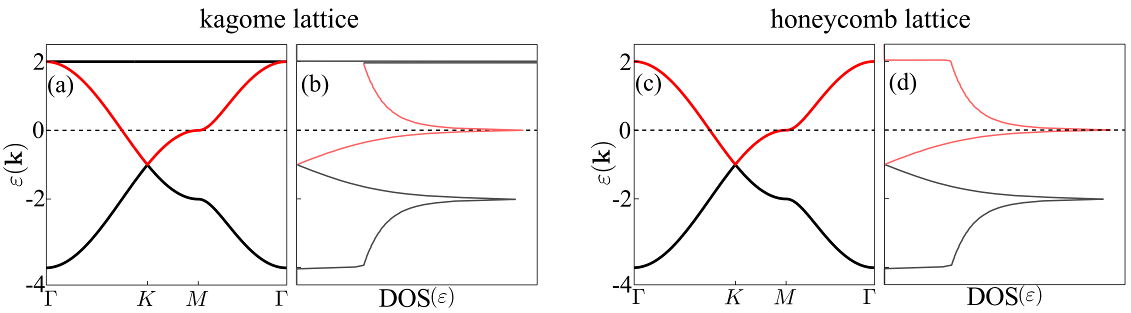

Figure 6.1: Tight-binding model in the kagome **(a,b)** and the honeycomb **(c,d)** lattice, respectively. If only nearest-neighbor hopping is included, the band structure of both lattices, plotted in **(a,c)**, is nearly equal. The kagome lattice features an additional flat band, but its valence band dispersion is identical to the honeycomb one (red colored). The valence band filling n_v is the partial filling of this bands. **(b,d)** The corresponding density of states (DOS) is consequently identical in the proximity of the Fermi surface (FS).

superconductors are all square lattices with one single site per unit cell, the kagome lattice [285] possesses a minimal three-band model due to three sites per unit cell. This lattice is presented in Sec. 2.2. For the kagome Hubbard model, the three sublattices imply fundamental problems in characterizing its preferred electronic many-body phases. In the strong-coupling limit at half filling, the kagome spin model exhibits strong quantum-disorder fluctuations and both in theory and experiment has become one of the paradigmatic models of frustrated magnetism [286–288]. While the associated Mott transition at finite coupling might still be described within dynamical mean field theory [289], the scope of collective electronic phases at intermediate Hubbard strength and general filling is particularly challenging to investigate: In the same way as electronic Bloch states at the Fermi level can involve different orbital admixtures for the multiorbital case, the electronic states in the kagome lattice can be distributed differently among the multiple sublattices. Furthermore, as the three sublattices spoil particle-hole symmetry, large scale numerical simulations of two-dimensional systems such as quantum Monte Carlo calculations cannot be employed due to the sign problem.

From a tight-binding perspective (Fig. 6.1a), it is conceivable that the filling is a sensitive parameter: In addition to two strongly dispersive bands, the kagome Hubbard model features one flat band which, for appropriate fillings, has been suggested to be particularly susceptible to ferromagnetism along Stoner's criterion [290]. While it is an ongoing challenging effort to identify kagome lattice materials at different electron fillings, a promising alternative route starts to emerge in optical kagome lattices of ultra-cold atomic gases, where the optical wavelengths can be suitably adjusted for fermionic isotopes such as $^{6}\mathrm{Li}$ and $^{40}\mathrm{K}$ [291].

In this chapter, the focus is on the response of the tight-binding kagome model to weak local and longer-range Hubbard interactions. The motivation is twofold. First, the kind of competing Fermi-surface instabilities are questioned, revealing the interplay of the sublattice structure and Fermi-surface topology. Here, the regime of the dispersive bands around van Hove filling is considered, where critical scales are enhanced due to large density of states (DOS) and nesting becomes relevant (Fig. 2.6c, Fig. 6.2a). For superconductivity, which is expected as the generically dominant instability channel

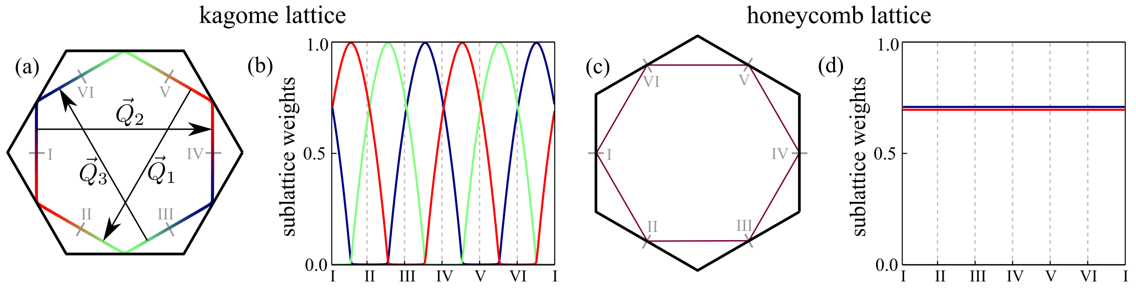

Figure 6.2: **(a)** FS of the kagome tight-binding model at $n = 5/12$ total filling. It touches the M point of the hexagonal Brillouin zone (BZ), where the DOS is maximal; its topology allows for three pairs of nesting features such as $\vec{Q}_3 = (-\pi/2, \sqrt{3}\pi/2)$. The colors blue, red, and green label the major sublattice occupation of the Fermi-surface band eigenstates. **(b)** The FS labels **I-VI** defined in **(a)** along with the color shift assist to read off the change of sublattice occupation weights $|u_s(\vec{k})|$ counterclockwise along the FS. **(c)** FS of the honeycomb tight-binding model at $n = 5/8$. Compared to **(a)**, the FS topology and DOS are approximately identical. **(d)** The sublattice occupation along the FS is homogeneous.

for weak coupling [136], the multidimensional irreducible lattice representations in the kagome lattice, i.e. C_{6v} symmetry about the center of the hexagons (see Sec. 2.3 for details), also suggests the possibility of topological chiral singlet superconducting phases [2]. Second, the infinitesimal-coupling limit provides a pivotal point of the parameter space which can be solve up to analytic precision [135, 137]. This is a valuable starting point for subsequent effective studies at intermediate coupling in Chap. 7.

An introduction to the features of the kagome lattice is presented in Sec. 2.2, including the Hamiltonian in real and momentum space. The analytical renormalization group is elaborately explained in Sec. 2.5. The core information which is relevant for investigating the interacting problem is encoded in the transformation coefficients $u_{sn}(\vec{k})$ of the Bogoliubov transformation matrix from the real-space and sublattice picture to the momentum-space and band representation, defined in Eq. 2.11:

$$\hat{c}^{\dagger}_{is\sigma} = \sum_{\vec{k}} \sum_{n} u^{*}_{sn}(\vec{k})\; \hat{c}^{\dagger}_{\vec{k}n\sigma}\, \mathrm{e}^{-\mathrm{i}\vec{k}(\vec{R}_i+\vec{r}_s)}. \tag{6.1}$$

For a given band n and momentum point in the BZ $\vec{k}$, the coefficients obey $\sum_s |u_{sn}(\vec{k})|^2 = 1$, where the band index n can be omitted because only the interaction in the band at the Fermi level plays a crucial role. In the following, these coefficients are called sublattice weights.

6.2 Local Hubbard interaction

Firstly, U_1 is set to zero, so the interaction is strictly local. The FS at van Hove filling $n = 5/12$ is depicted in Fig. 6.2a. The interaction vertex takes the simple form

$$V(\vec{k}_1, \vec{k}_2, \vec{k}_3, \vec{k}_4) = U_0 \sum_{s} u^{*}_{s}(\vec{k}_1) u^{*}_{s}(\vec{k}_2) u_s(\vec{k}_3) u_s(\vec{k}_4). \tag{6.2}$$

From Eq. 6.2, because of the locality of U_0, the only momentum dependence is given by the sublattice weights. Their evolution along the FS is depicted through color

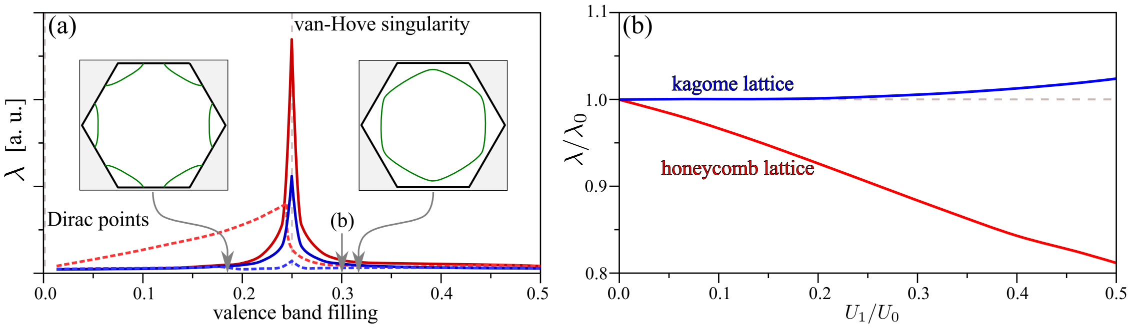

Figure 6.3: **(a)** Critical SC scale λ versus valence band filling for infinitesimal coupling with nothing but a local interaction, presented for the kagome scenario in Figs. 6.2a,b (blue) and the honeycomb scenario in Figs. 6.2c,d (red). Dashed line denotes f-wave, solid line d+id-wave. The valence band filling $n_v = 0.25$ corresponds to a van Hove point. All scales in the kagome case are largely reduced as compared to the honeycomb case. Below $n_v = 0.25$ the FS consists of disconnected pieces (left inset) and gives sizable f-wave for the honeycomb case. Above $n_v = 0.25$, d+id is preferred with a quick drop λ and always a higher scale for the honeycomb case. **(b)** Relative change of λ for finite U_1 as compared to the U_0 only case as a function of U_1/U_0 for both lattice scenarios at filling close to the van Hove regime. While λ drops for the honeycomb case, it rises for the kagome case.

coding in Figs. 6.2a,b. Eq. 6.2 looks very familiar from orbital makeup factors in multiorbital systems. In the kagome Hubbard model, this role is assigned to the sublattice weight distribution. As in the multiorbital case, the sublattice now affects the nesting enhancement of particle-hole fluctuations along the FS. A first guess from Fermi-surface topology without invoking the sublattice distribution would suggest the nesting vectors

$$\vec{Q}_1 = \pi\left(-\frac{1}{2}, -\frac{\sqrt{3}}{2}\right) \quad , \quad \vec{Q}_2 = \pi(1,0) \quad \text{and} \quad \vec{Q}_3 = \pi\left(-\frac{1}{2}, \frac{\sqrt{3}}{2}\right) . \tag{6.3}$$

As they connect FS points with mainly different sublattice occupation, however, the interaction vertex 6.2 will be small as it is diagonal in the sublattice index s. Consequently, this effect is called “sublattice interference”.

It is instructive to reconcile this scenario with the Hubbard model in the honeycomb lattice with two lattice sites per unit cell (Sec. 2.2). There, the tight-binding band structure matches the dispersive bands of the kagome lattice and allows one to similarly tune the honeycomb model to the equivalent van Hove filling. While the DOS as well as the Fermi-surface topology exactly match with the kagome case (compare Figs. 6.2a,c), the sublattice weights for the honeycomb model are homogeneous along the FS (Fig. 6.2d). This in turn suggests that sublattice interference is absent for the honeycomb case.

Fig. 6.3a summarizes the results for local Hubbard interaction both for the kagome and honeycomb tight-binding model. The doping is varied around van Hove filling. The valence band filling n_v is the fraction of the partially occupied band

$$\begin{aligned} \text{honeycomb: } n_v &= 2\left(n - \frac{1}{2}\right) \\ \text{kagome: } n_v &= 3\left(n - \frac{1}{3}\right) , \end{aligned} \tag{6.4}$$

which enables a direct comparison of both cases: The van Hove filling is located at $n_v = 1/4$, the Dirac cone filling at $n_v = 0$. For $0 < n_v < 1/4$, the FSs are disconnected (left inset Fig. 6.3a), while they form one contingent pocket for $n_v > 0.25$ (right inset Fig. 6.3a). For both lattice scenarios, triplet f-wave SC is preferred for the former (B_2 representation of C_{6v} symmetry group), while d+id-wave is preferred for the latter (E_2 representation). In detail, d+id features two degenerate SC eigenvalues $\lambda_{1,2}$ of d-wave symmetry, which then in any mean field treatment yield the preferential topological d+id chiral superconducting state in order to avoid loss of condensation energy due to nodes, which would necessarily cross with the FS [2].

The main difference between the kagome (k) and honeycomb (h) scenario is seen in the difference of λ (Fig. 6.3a). At van Hove filling, $\lambda_k \sim 1/3\lambda_h$. This illustrates at infinitesimal coupling how decisively sublattice interference affects the formation of superconductivity in the kagome lattice.

6.3 Long-Range Hubbard Interactions

In the case of finite U_1, the interaction vertex gets significantly more complicated than for the on-site interaction scenario (Eq. 6.2): The momentum dependence now originates both from the harmonics associated with the finite interaction range as well as the sublattice weights. The full interaction part of the Hamiltonian is written Eq. 2.16. In particular, however, V is not diagonal in the sublattice index anymore.

At a representative filling in the d+id wave regime at $n_v = 0.3$, the superconducting instabilities are plotted as a function of the ratio U_1/U_0 in Fig. 6.3b. In the plot, the ordinate is the ratio of the critical temperatures λ/λ_0, where λ_0 is the critical temperature at $U_1 = 0$. As elaborated on in Ref. [137], the generic case which applies to the honeycomb scenario is such that long-range interaction should frustrate the pairing and induce a drop of λ, which might be tuned via the degree of external capacitive screening of the superconducting layer [292].

The kagome Hubbard model shows a notably different behavior, as λ *increases* for longer range interactions. This phenomenon is intelligible from the perspective of sublattice interference and the vertex function. As the vertex becomes non-diagonal in the sublattice index due to longer range interactions, this yields a reduction of sublattice interference effects as particle hole fluctuations between different sublattice components become sizable and allow for reestablishing the full nesting enhancement given by Fermi-surface topology.

6.4 Summary

In the kagome Hubbard model, d+id and f-wave superconductivity is predicted around van Hove filling. f-wave is preferred at fillings where there are yet disconnected FSs whereas d+id is the leading instability as it becomes one contingent FS pocket (Fig. 6.3). The latter has also been found in variational cluster approximation calculations [95], where only local correlations are kept and no long-wavelength features of the electronic phase can be addressed. This finding alone combined with the shape of the dispersive bands naively suggests a strong similarity to the honeycomb model doped to van Hove filling, which has been recently investigated via random phase approximation, 3-patch renormalization group, analytical and functional renormalization group [2, 135, 147, 148, 248, 258].

However, the scales of the kagome model are largely suppressed as compared to the analogous honeycomb scenario: The kagome Hubbard model exhibits the new mechanism of *sublattice interference*, affecting the formation of Fermi-surface instabilities, as the inhomogeneous sublattice distribution of Fermi-level states causes reduced nesting effects. Furthermore, while the usual effect of long-range Hubbard interactions would be to reduce the critical scale of superconductivity [137, 292], it gets enhanced for the kagome Hubbard model as the long-range interaction help to relieve sublattice interference effects.

The consequent step is to extend this infinitesimal-coupling scenario to weak coupling. The functional Renormalization Group, which is used in the next chapter, considers not only the superconducting instability but also additional competing long-range orders. Especially long-range orders with an ordering vector $\vec{Q}_1$, $\vec{Q}_2$ or $\vec{Q}_3$, i.e. the nesting vector, are dramatically effected by the sublattice interference.

7

Unconventional Fermi Surface Instabilities in the Kagome Hubbard Model

At first glance, the structure of the kagome lattice, which consists of triangulars arranged around hexagons (Sec. 2.2), is very similar to the triangular lattice (Sec. 2.2). Consequently, at half filling and for large on-site interactions (Heisenberg model), the spin frustration in the triangulars (Fig. 2.2) is suppressing a long-range antiferromagnetic order [293, 294]. But in contrast to the triangular lattice, where the spin-frustrated triangulars are located close to each other and, hence, affect themselves, the triangulars are isolated in the kagome lattice, resulting in an enhanced spin frustration and a quantum spin liquid [91, 295–297] or a valence bond crystal [298]. Hence, the literature about the kagome lattice has its focus on the strong coupling regime. However, the herbertsmithites such as $\mathsf{ZnCu_3}(OH)_6\mathsf{Cl_2}$ appear as a relevant class of candidates for intermediately coupled materials [299]. In addition, a promising alternative route starts to emerge in optical kagome lattices of ultra-cold fermionic atomic gases such as for the isotopes ^{6}Li and ^{40}K [291].

Beside these considerations at half filling, the doped system has recently also attracted attention: *S.-L. Yu and J.-X. Li* implemented the variational cluster approach (VCA, Sec. 2.4) for the kagome lattice [95]. At a particle filling of $n = 5/12$, the density of states (DOS) has a logarithmic singularity (van Hove singularity, VHS) and the Fermi surface (FS) is perfectly nested. They found a phase diagram with chiral d+id-wave superconductivity (SC) at small interaction scales and a chiral spin-density wave (SDW) at large ones.

On the other hand, the results from the infinitesimal-coupling limit (Chap. 6) demonstrate that the instabilities, induced by the non-trivial FS, drive unexpected features because the extension of a strictly local to long-range interaction induces a contra-intuitive enhancement of superconducting fluctuations. Nevertheless, only the superconducting instability was considered in that chapter. Hence, it is natural to broaden the contemplations with the weak-coupling functional Renormalization Group (fRG, see Sec. 2.6 for an introduction). Thereby, many distinct FS instabilities are competing with each other, opening the route to various orders in a rich phase diagram.

In this chapter, I will show that the sublattice interference at the FS dramatically suppresses the SDW order. Furthermore, d+id SC is also lacking because it is driven by SDW fluctuations [2]. The absence of the commonly dominating phases opens the

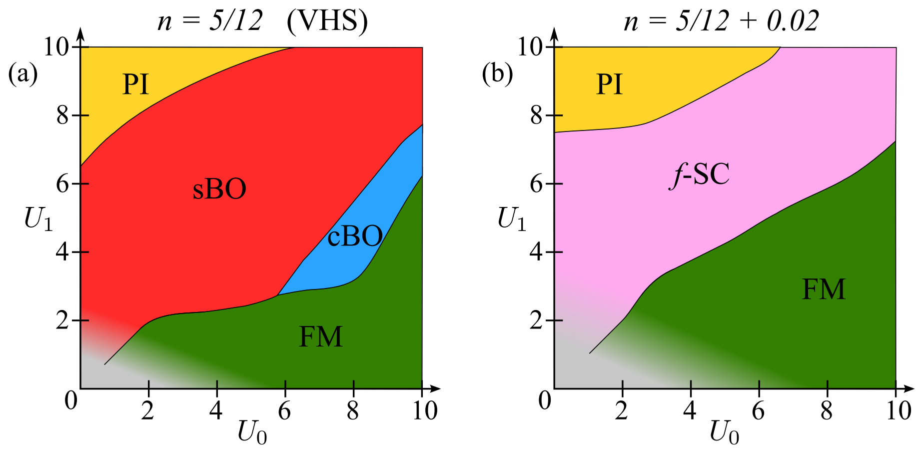

Figure 7.1: Phase diagram at and in the vicinity of the van Hove singularity (VHS). In both settings, a ferromagnetic phase (FM, green) with ordering vector $\vec{Q} = (0,0)$ is located at strong U_0, while the Pomeranchuk instability (PI, yellow) is dominant for a high U_1. For very weak interactions, the fRG combined with the patching scheme underestimates ferromagnetic fluctuations (see text for details). **(a)** At VHS, the nesting is optimal, so density-wave fluctuations are present, including a charge bond-ordered phase (cBO, blue area) and a spin bond-ordered phase (sBO, red area). **(b)** Away from van Hove filling, when the nesting is worsening, triplet f-wave superconductivity (f-SC) rises.

competition for exotic quantum states, including long-range orders with charge and spin bond-ordered phases as well as a nematic state.

The results of this chapter are available in a preprint with *C. Platt* and *R. Thomale* in Ref. [4].

7.1 Phase diagram

The Hamiltonian of the kagome Hubbard model is written in Eq. 2.10. After the Fourier transform to momentum space, the kinetic part (Eq. 2.13) and interaction part (Eq. 2.16) were implemented in the fRG formalism.

The phase diagram obtained by parameter scans is plotted in Fig. 7.1. There, two distinct fillings (at VHS and next to VHS) are confronted. It is conspicuous that only ferromagnetic (FM) fluctuations are present for a strictly local interaction ($U_0 > 0$, $U_1 = 0$). These fluctuations with $\vec{Q} = (0,0)$ are driven by the high DOS at the VHS, independently of the FS topology. The order parameter reads

$$\vec{O}_{\text{FM}} = \sum_{\vec{k},l} \sum_{\mu,\nu} \left\langle c^{\dagger}_{\vec{k}l\mu} \vec{\sigma}_{\mu\nu} c_{\vec{k}l\nu} \right\rangle , \tag{7.1}$$

with the vector of Pauli matrices $\vec{\sigma}$ (Eq. A.53). In addition, the background of ferromagnetic fluctuations at high energies provides further bias for a spin bond-ordered phase at VHS and the f-wave SC phase away from VHS. Due to numerical problems induced by the discretized patching of the BZ (Fig. 2.19), the results for small interaction scales are not stable (gray area). Especially the M-points with the highest local DOS are underrated. By altering the patching scheme, so that the patches are more concentrated at the proximity of the M-points, the numerically stable parameter space is increased. With this increased numerical effort, FM remains the dominating fluctuation even at smaller interactions. The other phases (and their borders) are only minimally effected by the alternative patching, demonstrating the stability of the technique. However, at infinitesimal coupling and away from VHS, SC has to be the leading instability [136], which is discussed in detail in Chap. 6.

Compared to the VCA phase diagram (Fig. 4 in Ref. [95]), a d+id SC and an SDW phase is completely missing. Yet, they used a different ansatz to solve the system: The VCA implements a strong-coupling approach with an exact local interaction and a self-consistently optimized hopping between small clusters. The interaction U is the essential scale. However, the fRG is a weak-coupling formalism, settled on Fermi-liquid theory. Here, the topology and shape of the FS play a crucial role. As demonstrated in the latter chapter, also the sublattice weights may be essential. But, these effects are less distinctive in the VCA, so the results of the two approaches are not directly comparable.

The absence of the SDW is further discussed in the next section, while the missing of the d+id SC is a immediate consequence of the suppressed SDW fluctuations [2] because the SDW promotes the formation of antiparallel spins and, hence, singlet SC is induced by these fluctuations. In contrast, FM fluctuations form parallel spins and consequently drive (triplet) f-wave SC. This phase is present only in Fig. 7.1b since under the perfect nesting condition at $n = 5/12$, long-range orders with an ordering vector $\vec{Q}_N$ are dominating (Fig. 7.1a). Indeed, there is no long-range order for a strictly local interaction. Only the introduction of a nearest-neighbor interaction U_1 yields fluctuations in the density wave channel. However, a closer look on these orders reveals a charge bond order (cBO) and a spin bond order (sBO), two rather exotic phases. These orders can arise as the conventional SDW is suppressed. In addition, the next-nearest-neighbor interaction acts between different sublattices, thus the momentum-dependent structure of the sublattice weights drives unconventional fluctuations. Also, there are three equivalent nesting vectors

$$\vec{Q}_1 = \pi\left(-\frac{1}{2}, -\frac{\sqrt{3}}{2}\right) \quad , \quad \vec{Q}_2 = \pi(1,0) \quad \text{and} \quad \vec{Q}_3 = \pi\left(-\frac{1}{2}, \frac{\sqrt{3}}{2}\right) . \tag{7.2}$$

One can show that $\vec{Q}_i \hat{=} -\vec{Q}_i$, where “$\hat{=}$” indicates “is equivalent modulo a reciprocal lattice vector”. Each nesting vector induces a different long-range order, seated on distinct pairs of sublattices and independent from each other. Hence, a superposition of all three orders is possible. Finally, for large U_1, the kagome lattice features a Pomeranchuk instability (PI) phase. Here, the ordering vector is $\vec{Q} = (0,0)$ and, consequently, it is independent from the nesting condition. Thus, the PI remains stable away from $n = 5/12$. Equivalent to the FM instability for finite U_0, the FS is reorganized to avoid the high DOS at the Fermi energy: While for the FM, the DOS is reduced by a spin-dependent shift of the FS, in the PI phase, a deformation of the parts of the FS with the highest DOS decreases the total DOS. This deformation reduces the rotational symmetry of the FS, while the translational symmetry of the lattice remains unaffected (“nematic phase”).

This U_0-U_1-n phase diagram features already some very exotic and interesting phases and an extension to longer ranged interactions U_2 and U_3 is dropped within this thesis.

The interesting phases are discussed in the next sections.

7.2 Suppression of the Spin-Density Wave

The first phase usually discussed is the spin-density wave (SDW), which is absent in the phase diagram. At first, the long-range interaction is disabled, and only a local interaction is considered with $U_0 > 0$. If the FS features a perfect nesting condition, both $\mathsf{Na}_x\mathsf{CoO}_2$ (NaCoO) and graphene evolve strong SDW fluctuations, as depicted in the phase diagrams of Fig. 4.3 and Fig. 5.3, respectively. In contrast, the kagome lattice shows only a weak ferromagnetic fluctuation (Fig. 7.1), which is driven by the high DOS at the Fermi level. For both NaCoO and graphene, these fluctuations are superimposed by an SDW. Only at very high interaction scales, where the weak-coupling limit of the fRG is exhausted, FM fluctuations become competitive.

In a direct comparison of the honeycomb lattice (graphene) and the kagome lattice, the FS and the DOS are identical (Figs. 7.2a,d,e,h). Hence, the source for the missing SDW fluctuations in the kagome lattice has to be connected to the different sublattice contributions to the FS (Figs. 7.2c,g). To check this assumption for the kagome lattice, the sublattice weights are set to a constant value of $1/\sqrt{3}$ for all bands and momenta, neglecting the sublattice structure. With this simplification, the SDW is the dominating instability, confirming that the sublattice weights play a key role for the understanding of the missing SDW. Although the band structure of graphene and the kagome lattice are very similar, the sublattice weights at the FS are different: For graphene, both sublattices contribute equally to all elements on the FS, while for the kagome lattice, each sublattice has distinct dominating FS parts.

Fig. 7.2 shows the differences and their consequences in detail: The first column displays the FSs of both lattices with magenta- and cyan-colored arrows representing two nested FS parts. The second column plots the sublattice contributions at this patch. These are the transformation coefficients $u_{sn}(\vec{k})$ of the Bogoliubov transformation matrix from the real-space and sublattice picture to the momentum-space and band representation, defined in Eq. 2.11:

$$\hat{c}^{\dagger}_{im\sigma} = \sum_{\vec{k}} \sum_{n} u^{*}_{mn}(\vec{k})\ \hat{c}^{\dagger}_{\vec{k}n\sigma} \mathrm{e}^{-\mathrm{i}\vec{k}(\vec{R}_i+\vec{r}_m)}. \tag{7.3}$$

Only the band intersecting the FS is considered, so the band index n is neglected. The local interaction is diagonal in the sublattice indices s:

$$V(\vec{k}_1,\vec{k}_2,\vec{k}_3,\vec{k}_4) = U_0 \sum_{s} u^{*}_{m}(\vec{k}_1) u^{*}_{m}(\vec{k}_2) u_{m}(\vec{k}_3) u_{m}(\vec{k}_4). \tag{7.4}$$

In the SDW channel, some parts of the FS are connected by a nesting vector $\vec{Q}_n$. Thus, for a strictly local interaction, the nesting condition is modified by an overlap of the sublattice weights $\sum_m u_m(\vec{k})u_m(\vec{k}+\vec{Q}_N)$, here subsequently called interaction overlap. This is plotted in the third column of Fig. 7.2. Finally, the fourth column shows the local DOS at the FS.

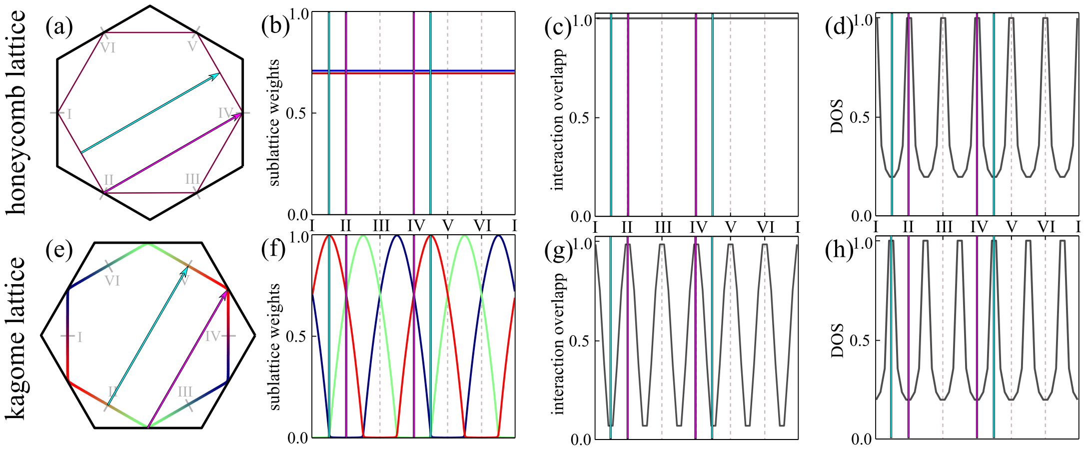

Figure 7.2: Comparison of the SDW fluctuations in the honeycomb and kagome lattice. **(a,e)** The Fermi surfaces (FS) are identical (except for a rotation of the Brillouin zone (BZ)). The magenta- and cyan-colored arrows are representatives of nesting vectors connecting corners and sides of the FS, respectively. The corresponding parts of the FS are marked by vertical lines in the other subplots. **(b,f)** Sublattice weights at the FS. **(c,g)** The corresponding local interaction overlap (IO, defined in text) is strongly anisotropic for the kagome lattice, while it is constant at 1 in the honeycomb lattice. **(d)** The local density of states (DOS) at the FS for the honeycomb lattice is anisotropic, but at least the magenta colored vector in **(a)** connects parts of the FS with high local DOS and IO. This is sufficient to drive the SDW instability. **(h)** In the kagome lattice, the local DOS and IO are anti cyclical, so the nesting condition is extremely weakened and no SDW develops.

In the last three columns, the vertical magenta- and cyan-colored lines indicate the parts of the FS marked in the first column.

For graphene, the sublattice weights are homogeneous at the FS, hence the interaction overlap is constant at 1. The local DOS is very high for the magenta-colored vectors in the FS plot, so these drive the fRG-flow to an SDW instability.

On the other side, for the kagome lattice, the nesting vectors connect parts of the FS with inappropriate sublattice contributions: At the parts connected by the magenta-colored vector, the first one is dominated by the green sublattice, while the red and blue ones are negligible, but at the second vector, the red sublattice is the main contributor. Hence, the channel indicated by the magenta-colored arrow has a tiny weight in the interaction overlap. On the other hand, the cyan-colored arrow connects two parts where both the green and the blue sublattice contribute to the FS and hence the interaction overlap is finite. But on these parts, the local DOS is very low. Thus, the nesting condition is strongly weakened and not sufficient to drive the fRG-flow to an SDW. As a consequence, the ferromagnetic fluctuations are stronger and dominate the fRG-flow.

In summary, in the kagome lattice, the inhomogeneous distribution of sublattice contributions to the FS linked with an inappropriate local DOS results in a strong suppression of the SDW fluctuations. This effect is subsequently labeled as “sublattice interference”.

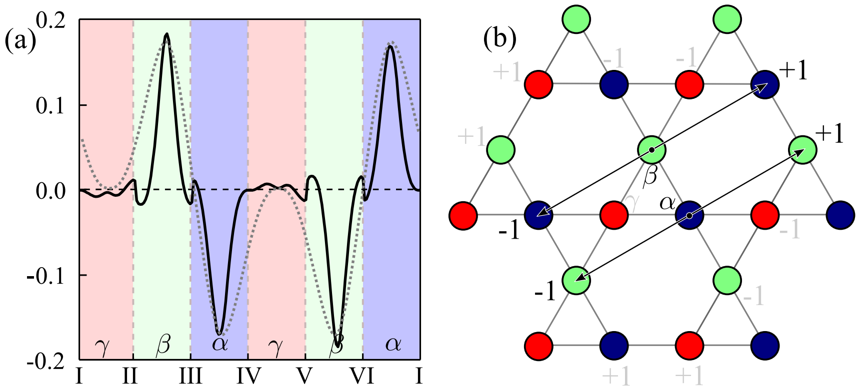

Figure 7.3: **(a)** f-wave Form factor for hopping between next-nearest neighbors on α- and β-sites. The filling is next to the VHS ($n = 5/12 + 0.02$ and $U_1 = 6$) and the labels I-VI are define in Fig. 7.2e. After the transformation to sublattice representation, the fRG form factor (solid line) fits to the analytical form factor for next-nearest-neighbor pairing (Eq. 7.5, dashed line). **(b)** The corresponding real-space pattern of the α-β-pairing. The other two combinations are hinted.

7.3 f-wave Superconductivity

A superconducting instability appears if the filling is set away from the VHS and the Coulomb interaction is long ranged (Fig. 7.1). The vertex flow diverges in the spin-triplet channel and is not degenerate. So, the form factor should have an f-wave symmetry (Sec. 2.3). The mean-field decoupled vertex in the spin-triplet channel (Eq. 2.130) yields the form factor after a transformation to sublattice representation (see Sec. 7.4 for details). This reveals that the best accordance is given for pairings between next-nearest neighbors, which are located in different sublattices.

Each pair of sublattices is separated from the other ones as they form one-dimensional chains. Within these chains, the next-nearest-neighbor hopping is transformed to momentum space, modulated with an f-wave formfactor. This results in:

$$\begin{aligned} f_{\alpha\beta}(\vec{k}) &= \sin\left(\frac{3}{2}k_x + \frac{\sqrt{3}}{2}k_y\right) \\ f_{\beta\gamma}(\vec{k}) &= \sin\left(\frac{3}{2}k_x - \frac{\sqrt{3}}{2}k_y\right) \\ f_{\alpha\gamma}(\vec{k}) &= \sin\left(\sqrt{3}k_y\right) \end{aligned} \tag{7.5}$$

with $f_{m,n} = f_{n,m}$ and $f_{m,m} = 0$. In Fig. 7.3a, the form factor of the α-β-pairing is compared to the analytical ones. It fits very well to the mean-field results (Fig. 7.3a). The pair forms between next-nearest neighbors because, due to an increased pairing distance, the (non-local) nearest-neighbor Coulomb interaction is compensated [2]. The final superposition of all three sublattice pairings restore the full f-wave symmetry (B_2 element of the C_{6v} group). Together, they form the order parameter

$$O_{\mathrm{fSC}} = \sum_{\vec{k},m,n} \left\langle c^{\dagger}_{\vec{k}m\uparrow} c^{\dagger}_{\vec{k}n\downarrow} + c^{\dagger}_{\vec{k}m\downarrow} c^{\dagger}_{\vec{k}n\uparrow} \right\rangle f_{m,n}\left(\vec{k}\right) \,, \tag{7.6}$$

which can be rotated within the spin-triplet sector to the $S_z = \pm 1$ states.

In contrast to graphene, where the pairs favor the same sublattice (Sec. 5.5), in the kagome lattice, the pairing is between different sublattices.

7.4 Charge and Spin Bond Order

The vertex flow shows also a leading instability in the density wave channels of Eq. 2.130. These instabilities are threefold degenerate, one for each nesting vector $\vec{Q}_1$, $\vec{Q}_2$ and $\vec{Q}_3$. The challenge is to determine to resulting phase: Is one $\vec{Q}_i$ selected, so the symmetry is broken? Is there a superposition of all three nesting vectors?

In the literature, there are several reports on experiments about density-wave instabilities with multiple ordering vectors in systems with C_{6v} symmetry. For example, a chiral charge-density wave was measured in triangular lattice in layers [300–302]. Here, the ordering vector changes between lattice layers, resulting in multilayer structure. For the honeycomb lattice, a spin-density wave was suggested, which contains 4 unit cells [260], or in a chiral order [148], respectively. Finally, a chiral spin-density wave was also proposed in kagome lattice [95].

In this section, I will investigate the instabilities in the density-wave channels and their resulting real-space pattern. At van Hove filling $n = 5/12$, the phase diagram in Fig. 7.1 features two density-wave phases, the spin bond order (sBO) and the charge bond order (cBO). The labels of these phases are defined by the real-space patterns revealed later in this section. Since, the fRG is executed in momentum space, a Fourier transform has to be performed to determine the correct real-space picture (Eq. 2.11). Here, the sublattice structure of the kagome lattice has to be included into the consideration: The final coupling function $V(\vec{k}_1,\vec{k}_2,\vec{k}_3,\vec{k}_4)$ at the end of the fRG flow consists of 4 creation/annihilation operators, which have to be transformed back separately. Each combination of sublattice indices m_1,m_2,m_3,m_4 with $m_x \in \{\alpha,\beta,\gamma\}$ is possible. Additionally, three equivalent ordering vectors $\vec{Q}_1$, $\vec{Q}_2$ and $\vec{Q}_3$ have to be included. For all 3^5 combinations, the mean-field decoupling in the SDW or CDW channel is performed, respectively. Again, the absolute largest eigenvalues are of interest. The result is a sixfold degeneracy for $V(\vec{r}_1,m_1,\vec{r}_2,m_2,\vec{r}_3,m_3,\vec{r}_4,m_4)$ at both the SDW and the CDW channel:

m_1	m_2	m_3	m_4	$\vec{Q}_x$
α	α	γ	γ	2
γ	γ	α	α	2
β	β	γ	γ	1
γ	γ	β	β	1
α	α	β	β	3
β	β	α	α	3

These combinations are identical for both density wave phases. A closer look on the first solution in the cBO reveals:

$$V(\vec{r}_1,\alpha,\vec{r}_2,\alpha,\vec{r}_3,\gamma,\vec{r}_4,\gamma) \sim \hat{c}^\dagger_\alpha \hat{c}^\dagger_\alpha \hat{c}_\gamma \hat{c}_\gamma \approx \langle \hat{c}^\dagger_\alpha \hat{c}_\gamma \rangle \hat{c}^\dagger_\alpha \hat{c}_\gamma \tag{7.7}$$

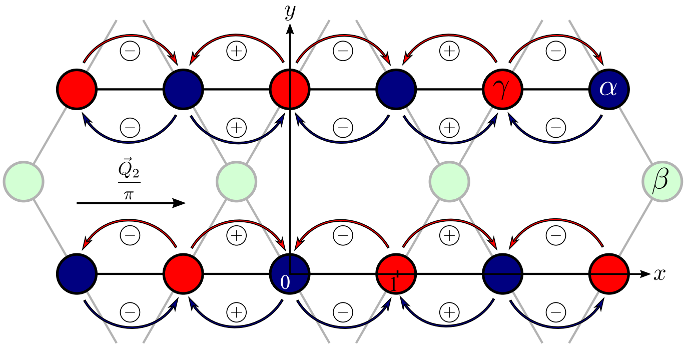

Figure 7.4: Construction of the cBO: The hopping from α- to γ-sites is modulated by Eq. 7.8 (red arrows), the hopping from γ- to α-sites by Eq. 7.9 (blue arrows). The ordering vector is parallel to the α-γ-chains, so β-sites are unaffected. Also, the ordering vector causes a minus sign between neighboring chains. In total, the hopping amplitude between some bonds is enhanced, alternating with bonds featuring reduced hopping.

with a mean-field decoupling in the last step. Indeed, there is a directed hopping expectation value $\langle \hat{c}^\dagger_\alpha \hat{c}_\gamma \rangle$, resulting in an additional hopping on bonds between sublattices α and γ. The form factor is fitted best with a $\sin(k_x)$, which corresponds to a correlation between nearest neighbors. This form factor can be rewritten to $\sin(k_x) = \sin(\vec{T}\vec{k})$ with translation vector $\vec{T} = (1,0) = \frac{\vec{Q}_2}{\pi}$, so the corresponding ordering vector is parallel to the direction of these bonds, forming quasi one-dimensional chains. The expectation value reveals the real-space order [303]:

$$\begin{gathered}
\langle \hat{c}^\dagger_{\vec{k}\gamma} \hat{c}_{\vec{k}+\vec{Q}\alpha} \rangle = \sin(\vec{T}\vec{k}) \cdot \Phi \\
\sum_{\vec{k}} \langle \hat{c}^\dagger_{\vec{k}\gamma} \hat{c}_{\vec{k}+\vec{Q}\alpha} \rangle \sin(\vec{T}\vec{k}) = \sum_{\vec{k}} \sin^2(\vec{T}\vec{k}) \cdot \Phi = \tilde{\Phi} \\
\sum_{\vec{k}} \sum_{\vec{R}_i \vec{R}_j} \langle \hat{c}^\dagger_{\vec{R}_i+\vec{r}_\gamma} \hat{c}_{\vec{R}_j+\vec{r}_\alpha} \rangle e^{i\vec{k}(\vec{R}_i+\vec{r}_\gamma)} \, e^{-i(\vec{k}+\vec{Q})(\vec{R}_j+\vec{r}_\alpha)} \, \frac{1}{2i} \left(e^{i\vec{T}\vec{k}} - e^{-i\vec{T}\vec{k}} \right) = \tilde{\Phi} \\
\sum_{\vec{k}} \sum_{\vec{R}_i \vec{R}_j} \langle \hat{c}^\dagger_{\vec{R}_i+\vec{r}_\gamma} \hat{c}_{\vec{R}_j+\vec{r}_\alpha} \rangle \frac{1}{2i} \left(e^{i((\vec{R}_i+\vec{r}_\gamma)-(\vec{R}_j+\vec{r}_\alpha)+\vec{T})\vec{k}} - e^{-i((\vec{R}_i+\vec{r}_\gamma)-(\vec{R}_j+\vec{r}_\alpha)-\vec{T})\vec{k}} \right) e^{-i\vec{Q}(\vec{R}_j+\vec{r}_\alpha)} = \tilde{\Phi} \\
\sum_{\vec{R}_j} \left(\langle \hat{c}^\dagger_{\vec{R}_j+\vec{r}_\alpha-\vec{T}} \hat{c}_{\vec{R}_j+\vec{r}_\alpha} \rangle - \langle \hat{c}^\dagger_{\vec{R}_j+\vec{r}_\alpha+\vec{T}} \hat{c}_{\vec{R}_j+\vec{r}_\alpha} \rangle \right) \frac{1}{2i} e^{-i\vec{Q}(\vec{R}_j+\vec{r}_\alpha)} = \tilde{\Phi}
\end{gathered} \tag{7.8}$$

Here, the position vector of a site is decomposed in the vector of the unit cell $\vec{R}_i$ and the vector within the unit cell $\vec{r}_x$. In addition, the square of the orbital weights is invariant under reflection, so it analogously gives

$$\begin{gathered}
\langle \hat{c}^\dagger_{\vec{k}\alpha} \hat{c}_{\vec{k}+\vec{Q}\gamma} \rangle = \sin(\vec{T}\vec{k}) \cdot \Phi \\
\sum_{\vec{R}_j} \left(\langle \hat{c}^\dagger_{\vec{R}_j+\vec{r}_\gamma-\vec{T}} \hat{c}_{\vec{R}_j+\vec{r}_\gamma} \rangle - \langle \hat{c}^\dagger_{\vec{R}_j+\vec{r}_\gamma+\vec{T}} \hat{c}_{\vec{R}_j+\vec{r}_\gamma} \rangle \right) \frac{1}{2i} e^{-i\vec{Q}(\vec{R}_j+\vec{r}_\gamma)} = \tilde{\Phi}
\end{gathered} \tag{7.9}$$

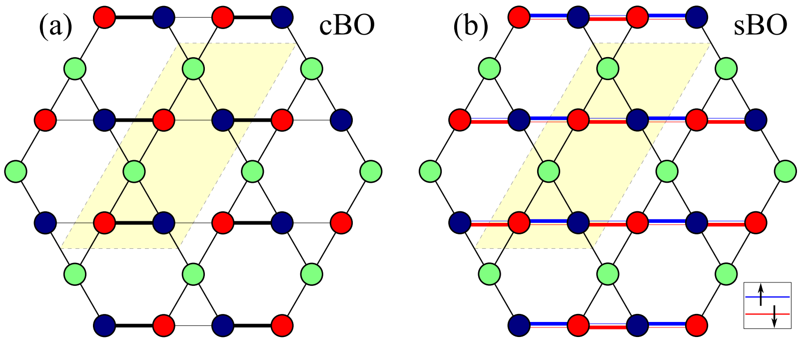

Figure 7.5: Real space pattern of the bond-ordered phases with ordering vector $\vec{Q}_2$: **(a)** cBO with the parameter setting $U_0 = 8.0$, $U_1 = 6.0$ and $n = 5/12$ (VHS). There is an alternating hopping amplitude between α- and γ-sites. The unit cell now contains 6 sites. **(b)** sBO with the parameter setting $U_1 = 6.0$ and $n = 5/12$ (VHS). The real space pattern is similar to **(a)** but the modulation depends on the spin polarization of the electrons.

Together, they form an alternating modulation of the hopping between nearest neighbors in the chains. The construction of the real-space pattern is presented in Fig. 7.4, while the final pattern is plotted in Fig. 7.5a, featuring a bond-ordered structure. Such orders have become recently accessible experimentally with sufficient tunability in dipolar fermion models [304], but the kagome lattice is the first system where these phases can be found as the natural ordered state at low energies.

For a mean-field analysis of the resulting band structure, the non-interacting Hamiltonian in Eq. 2.12 has to be adapted and expanded with a Weiss field Δ_{cBO}. Due to the broken translational symmetry, the new unit cell includes six sites and, hence, a six-band calculation is needed, which is explicitly done in App. A.5. Also, the resulting Brillouin zone (BZ), band structure and FS of this six-band model is depicted there (Fig. A.4). As a consequence of the cBO, the FS is partially gaped. The same derivation is possible for the sBO (with a spin dependence of the additional hopping term), with the resulting real-space pattern plotted in Fig. 7.5b. Furthermore, each pattern is threefold degenerate, where the other patterns are obtained by rotations by $2\pi/3$, corresponding to the ordering vectors $\vec{Q}_1$ and $\vec{Q}_3$.

It is striking that both real-space patterns of the order for $\vec{Q}_2$ (Fig. 7.5) affect only bonds between α-sites (blue) and γ-sites (red). The other bonds are included only in the orders for $\vec{Q}_1$ or $\vec{Q}_3$, respectively. Consequently, the three different orders do not interfere with each other and a simultaneous formation is possible.

Based on the assumption that a cBO order for one $\vec{Q}_m$ reduces the free energy of the system and the orders for each $\vec{Q}_i$ are independent, the simultaneous formation of all three orders should further optimize the free energy. To verify this statement, a mean-field analysis is done in App. A.5, equivalent to the six-band model but now containing 12 bands. As a result, the system linearly gains energy from forming the 3 individual mean fields, so the ordering formation along the individual bond directions is indeed independent. In addition, the new BZ is reduced to a quarter of the size and retains its hexagonal structure (Fig. 7.7a). This illustrates that the C_{6v} symmetry, which is broken if only one order with $\vec{Q}_m$ is applied, is again restored. In the reduced BZ, the spectral weight at the FS between the Γ- and M-points is shifted away from the Fermi energy

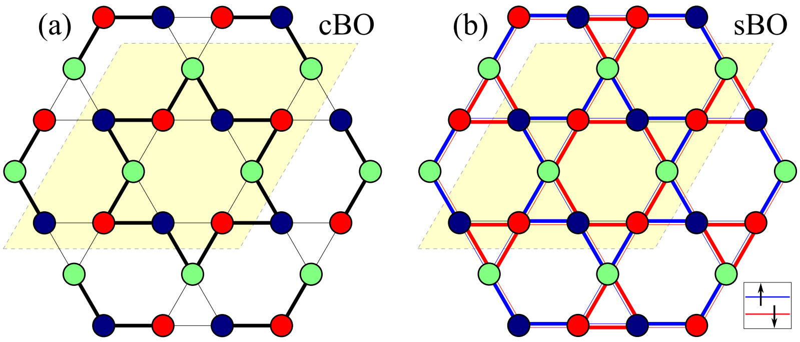

Figure 7.6: Equivalent to Fig. 7.5 but with $\vec{Q}_1$, $\vec{Q}_2$ and $\vec{Q}_3$ simultaneously applied. The unit cell contains 12 sites.

when the Weiss field Δ_{cBO} is switched on. This is clearly visible in Figs. 7.7b,c, but no gap opens at Γ- and M-points and, hence, there is no full gap in the band structure. Thus, the FS (Fig. 7.7e) is reduced to the Γ- and M-points.

The real-space patterns of the superpositions are presented in Fig. 7.6, including the enlarged unit cell with 12 sites. Their order parameters are given by

$$\begin{aligned} \vec{O}_{\mathrm{sBO}} &= \sum_{\substack{\vec{k},\mu,\nu\\ l,m,n}} \left\langle c^{\dagger}_{\vec{k}l\mu}\, \vec{\sigma}_{\mu\nu}\, c_{\vec{k}+\vec{Q}_m n\nu} \right\rangle \sin\left(\frac{\vec{Q}_m\vec{k}}{\pi}\right) |\varepsilon_{lmn}| \\ O_{\mathrm{cBO}} &= \sum_{\substack{\vec{k},\mu,\nu\\ l,m,n}} \left\langle c^{\dagger}_{\vec{k}l\mu}\, \mathbb{1}_{\mu\nu}\, c_{\vec{k}+\vec{Q}_m n\nu} \right\rangle \sin\left(\frac{\vec{Q}_m\vec{k}}{\pi}\right) |\varepsilon_{lmn}| \end{aligned} \tag{7.10}$$

with the Levi-Civita tensor ε_{lmn}.

Finally a remark on the expectation value of these bond-ordered phases: Eq. 7.8 can be rewritten and compared to Eq. 7.9, so

$$\begin{aligned} \langle \hat{c}^{\dagger}_{\vec{k}\gamma} \hat{c}_{\vec{k}+\vec{Q}_i\alpha} \rangle &= \Phi \sin(\vec{T}\vec{k}) \\ \langle (\hat{c}^{\dagger}_{\vec{k}\gamma} \hat{c}_{\vec{k}+\vec{Q}_i\alpha})\rangle^* &= (\Phi \sin(\vec{T}\vec{k}))^* \\ \langle \hat{c}^{\dagger}_{\vec{k}+\vec{Q}_i\alpha} \hat{c}_{\vec{k}\gamma} \rangle &= \Phi^* \sin(\vec{T}\vec{k}) \\ \langle \hat{c}^{\dagger}_{\vec{k}\alpha} \hat{c}_{\vec{k}-\vec{Q}_i\gamma} \rangle = \langle \hat{c}^{\dagger}_{\vec{k}\alpha} \hat{c}_{\vec{k}+\vec{Q}_i\gamma} \rangle &= \Phi^* \sin(\vec{T}(\vec{k}+\vec{Q}_i)) = \Phi^* \sin(\vec{T}\vec{k}+\pi) \\ \langle \hat{c}^{\dagger}_{\vec{k}\alpha} \hat{c}_{\vec{k}+\vec{Q}_i\gamma} \rangle = \Phi \sin(\vec{T}\vec{k}) &= -\Phi^* \sin(\vec{T}\vec{k}) \\ \Phi &= -\Phi^* \,. \end{aligned} \tag{7.11}$$

Thus, the amplitude Φ has to be imaginary, just as the current phases in Ref. [161].

7.5 Pomeranchuk Instability

For a strong nearest-neighbor interaction U_1, the phase diagram (Fig. 7.1) indicates a Pomeranchuk instability (PI). In the mean-field decoupling (Eq.2.130), it is identical to

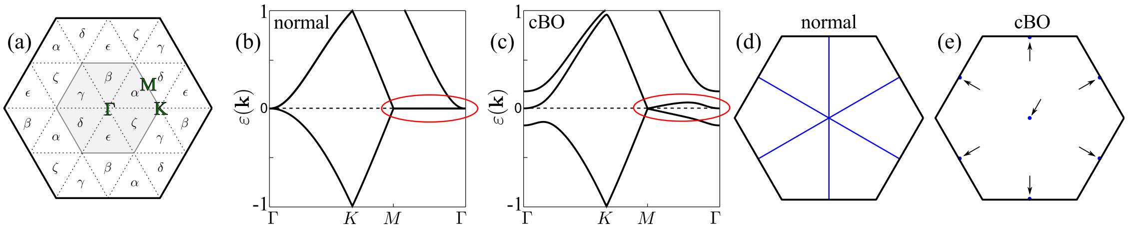

Figure 7.7: **(a)** By the simultaneous application of all three ordering vectors $\vec{Q}_i$, the size of the BZ is reduced to one fourth, but retains the hexagonal structure (shaded area). The labels α to ζ mark the back folded areas. The band structure and FS is plotted with **(b,d)** an infinitesimal Weiss field $\Delta_{\mathrm{cBO}} = 0^+$ and **(c,e)** $\Delta_{\mathrm{cBO}} = 0.1$, respectively. **(b,c)** The back folded dispersion relation results in 12 bands, but only the bands around the Fermi energy are plotted. **(d,e)** The corresponding FSs. By setting the Weiss field to $\Delta_{\mathrm{cBO}} = 0.1$, the bands are shifted, so the FS is nearly gapped. Only at the Γ- and M-points spectral weight remains at the Fermi energy.

the CDW channel with zero ordering momentum $\vec{Q} = (0,0)$. Hence, this phase does not break translational symmetry. In the comparable scenario for the cuprates (one-band model in the quadratic lattice), the PI results in a deformation of the FS, breaking its tetragonal symmetry [305]. Consequently, a similar effect can be expected for the kagome lattice.

The mean-field decoupling of the PI channel yields a twice degenerate instability. After transformation from band representation to sublattice representation (see latter section for details), the correlations between the *same* sublattice are dominating. The fRG form factors are presented in Fig. 7.8a. The analytical form factors for an E_2 representation (Sec. 2.3) on the 3rd-nearest neighbors read:

$$\begin{aligned} f_{d_{x^2-y^2}}\left(\vec{k}\right) &= \cos\left(2k_x\right) - \cos\left(k_x\right)\cos\left(\sqrt{3}k_y\right) \\ f_{d_{xy}}\left(\vec{k}\right) &= \sqrt{3}\sin\left(k_x\right)\sin\left(\sqrt{3}k_y\right) \end{aligned} \tag{7.12}$$

The accordance between analytical and calculated form factors is nearly perfect. The effective Hamiltonian reads after the mean-field decoupling:

$$\begin{aligned} \hat{H}_{\mathrm{PI}} &= \sum_{\sigma}\sum_{\vec{k}} \varepsilon(\vec{k})\hat{c}^{\dagger}_{\vec{k}\sigma}\hat{c}_{\vec{k}\sigma} + \frac{1}{N}\sum_{\sigma}\sum_{\vec{k}\vec{q}} V_{\mathrm{PI}}(\vec{k},\vec{q})\ \left(\hat{c}^{\dagger}_{\vec{k}\sigma}\hat{c}^{\dagger}_{\vec{q}\sigma}\hat{c}_{\vec{k}\sigma}\hat{c}_{\vec{q}\sigma}\right) \\ &= \sum_{\sigma}\left(\sum_{\vec{k}} \varepsilon(\vec{k})\hat{c}^{\dagger}_{\vec{k}\sigma}\hat{c}_{\vec{k}\sigma} - \frac{1}{N}\sum_{\vec{k}\vec{q}} V_{\mathrm{PI}}(\vec{k},\vec{q})\ \left(\langle\hat{c}^{\dagger}_{\vec{k}\sigma}\hat{c}_{\vec{k}\sigma}\rangle\hat{c}^{\dagger}_{\vec{q}\sigma}\hat{c}_{\vec{q}\sigma} + \hat{c}^{\dagger}_{\vec{k}\sigma}\hat{c}_{\vec{k}\sigma}\langle\hat{c}^{\dagger}_{\vec{q}\sigma}\hat{c}_{\vec{q}\sigma}\rangle - \langle\hat{c}^{\dagger}_{\vec{k}\sigma}\hat{c}_{\vec{k}\sigma}\rangle\langle\hat{c}^{\dagger}_{\vec{q}\sigma}\hat{c}_{\vec{q}\sigma}\rangle\right)\right) \\ &= \sum_{\sigma}\left(\sum_{\vec{k}} \varepsilon(\vec{k})\hat{c}^{\dagger}_{\vec{k}\sigma}\hat{c}_{\vec{k}\sigma} - \sum_{\vec{q}}\Delta_{\vec{q}}\hat{c}^{\dagger}_{\vec{q}\sigma}\hat{c}_{\vec{q}\sigma} - \sum_{\vec{k}}\Delta_{\vec{k}}\hat{c}^{\dagger}_{\vec{k}\sigma}\hat{c}_{\vec{k}\sigma} + \frac{1}{N}\sum_{\vec{k}\vec{q}} V_{\mathrm{PI}}(\vec{k},\vec{q})\langle\hat{c}^{\dagger}_{\vec{k}\sigma}\hat{c}_{\vec{k}\sigma}\rangle\langle\hat{c}^{\dagger}_{\vec{q}\sigma}\hat{c}_{\vec{q}\sigma}\rangle\right) \\ &= \sum_{\sigma}\left(\sum_{\vec{k}}\left(\underbrace{\varepsilon(\vec{k}) - 2\Delta_{\vec{k}}}_{E(\vec{k})}\right)\hat{c}^{\dagger}_{\vec{k}\sigma}\hat{c}_{\vec{k}\sigma} + \sum_{\vec{k}}\Delta_{\vec{k}}\langle\hat{c}^{\dagger}_{\vec{k}\sigma}\hat{c}_{\vec{k}\sigma}\rangle\right)\ , \end{aligned} \tag{7.13}$$

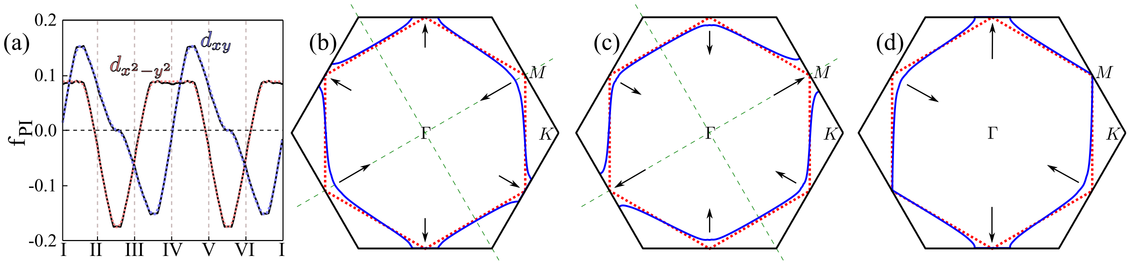

Figure 7.8: (a) Form factors of the Pomeranchuk instability. The calculated ones (solid black lines) fit very well to the analytical ones (dotted lines, Eq. 7.12). **(b)** Deformation of the FS with the PI field $\Delta_0 = 0.1$ and $\rho = -\frac{\pi}{3}$ (Eq. 7.16). At two opposite M-points, which are the points of the FS with the highest DOS, the FS is shifted towards the center of the BZ, while it is shifted away at the remaining four M-points. The symmetry group is reduced to C_{2v}. **(c)** Same as **(b)** but $\rho = \frac{2\pi}{3}$. The distortion of the FS is opposed to **(b)**. **(d)** Same as **(b)** but $\rho = \frac{\pi}{6}$. Here, the FS includes no reflection symmetries, so the symmetry group is C_2.

where the definition of the gap function

$$\Delta_{\vec{k}} := \frac{1}{N}\sum_{\vec{q}} V_{\mathrm{PI}}(\vec{k},\vec{q})\langle \hat{c}^{\dagger}_{\vec{q}\sigma}\hat{c}_{\vec{q}\sigma}\rangle \tag{7.14}$$

is used. One can further show that

$$\begin{aligned}(\Delta_{\vec{k}})^* &= (\frac{1}{N}\sum_{\vec{q}} V_{\mathrm{PI}}(\vec{k},\vec{q})\langle \hat{c}^{\dagger}_{\vec{q}\sigma}\hat{c}_{\vec{q}\sigma}\rangle)^* \\ &= \frac{1}{N}\sum_{\vec{q}} V_{\mathrm{PI}}(\vec{k},\vec{q})\langle (\hat{c}^{\dagger}_{\vec{q}\sigma}\hat{c}_{\vec{q}\sigma})^{\dagger}\rangle \\ &= \frac{1}{N}\sum_{\vec{q}} V_{\mathrm{PI}}(\vec{k},\vec{q})\langle \hat{c}^{\dagger}_{\vec{q}\sigma}\hat{c}_{\vec{q}\sigma}\rangle = \Delta_{\vec{k}} \\ &\Rightarrow \Delta_{\vec{k}} \in \mathbb{R}\,,\end{aligned} \tag{7.15}$$

so the gap function has to be real. This excludes a d+id-wave superposition of the form factors, as realized in the d+id-wave superconductivity of NaCoO (Sec. 4.3) and graphene (Sec. 5.4). Indeed, the PI adds a 3rd-nearest-neighbor hopping to the Hamiltonian, which corresponds to hoppings within the sublattice. The Hamiltonian in real space (Eq. 2.12) includes a hopping matrix (t-matrix), which is transformed to momentum space. So, the t-matrix has to be Hermitian and, consequently, the hoppings within the same sublattice have to be real. This is ensured by the superposition of the hopping and back hopping processes which annihilate any imaginary part. However, there is still a degree of freedom in the choice of the d-wave form factor because any linear combination of $d_{x^2-y^2}$ and d_{xy} is a solution. Here, the ansatz is d+id-superposition with an additional phase ρ. The imaginary part vanishes anyway, so ρ enables a smooth transition between $d_{x^2-y^2}$ and d_{xy}. After Fourier transform, the 3rd-nearest-neighbor hopping is not equivalent for all three hopping axis. The dispersion relation (Eq. 2.12) is extended to

$$\begin{aligned}\tilde{\varepsilon}_n(\vec{k}) &= \varepsilon_n(\vec{k}) + \Delta_0 \left[\mathrm{e}^{\mathrm{i}\rho} \left(d_{x^2-y^2} + \mathrm{i} d_{xy} \right) \right] + \mathrm{H.c.} \\ &= \varepsilon_n(\vec{k}) + 2\Delta_0 \mathrm{Re} \left[\mathrm{e}^{\mathrm{i}\rho} \left(\cos(2k_x) - \cos(k_x) \cos\left(\sqrt{3}k_y\right) + \mathrm{i}\sqrt{3} \sin(k_x) \sin\left(\sqrt{3}k_y\right) \right) \right]\end{aligned} \tag{7.16}$$

This results in a deformation of the FS, as presented in Figs. 7.8b-d, where the FS is shifted away from the six M points, which are the momenta of highest DOS. The order parameter is also adapted to this superposition:

$$O_{\mathrm{PI}} = \sum_{\vec{k},l,\mu} \left\langle c^{\dagger}_{\vec{k}l\mu} c_{\vec{k}l\mu} \right\rangle \mathrm{Re} \left(\mathrm{e}^{\mathrm{i}\phi} \left(f_{d_{x^2-y^2}}\left(\vec{k}\right) + \mathrm{i} f_{d_{xy}}\left(\vec{k}\right) \right) \right) \tag{7.17}$$

The phase factor ρ rotates the deformation field by $\rho/2$. In the PI phase, the symmetry of the FS is reduced to

$$\text{point group} \begin{cases} C_{2v} & \text{if } \rho = \frac{\pi}{3} z \quad \text{with } z \in \mathbb{Z} \\ C_2 & \text{else,} \end{cases} \tag{7.18}$$

while the symmetry of the lattice remains unbroken. So, the PI is a nematic phase [306, 307].

7.6 Summary

After the considerations for an infinite coupling in Chap. 6, the kagome lattice is also the topic of this chapter. Using the functional renormalization group, the weak-coupling scenario can be elaborately investigated with more details: The functional renormalization group features the flow of competing orders to Fermi surface instabilities, opening the route to a rich phase diagram. Without the necessity of a preselection of diagrams, the functional renormalization group provides an unbiased principle, so even unforeseen long-range orders are possible. For the kagome lattice, the sublattice interference suppresses the formation of a conventional spin-density wave, which is both predicted and measured in similar lattices with C_{6v} symmetry (see Secs. 4.2 and 5.3). This enables some non-conventional instabilities to form exotic long-range orders.

At van Hove filling, the phase diagram (Fig. 7.1) features two long-range orders with an ordering vector equivalent to the nesting vectors, namely the charge bond order and the spin bond order. For each ordering vector, they form an alternating pattern on the bonds in one-dimensional chains. While in the first case the charge density is modulated (charge bond order), the orientation of the spins is alternating in the second case (spin bond order). Both phases have in common that they can simultaneously coexist for all three ordering vectors, enlarging the unit cell from three to twelve sites. Thus, a gap opens at the Fermi energy, which is only closed at particular points of the Brillouin zone. Indeed, the free energy is optimized with this superposition.

Away from van Hove filling, the nesting of the Fermi surface is reduced, so long-range orders with a finite ordering vector are weakened. Here, the phase diagram indicates an f-wave superconductivity. This is unusual for a system with C_{6v} symmetry because a

d+id-wave superconductivity is completely missing, and not even present in a subleading role. This reflects the close connection between the spin-density wave and the singlet superconductivity because the suppressed spin-density wave is unable to drive the singlet superconductivity instabilities, so d+id-wave superconductivity is absent. In this sense, the f-wave superconductivity in the kagome lattice should be very stable.

Independently of the filling, there exist two instabilities with $\vec{Q} = (0,0)$: Ferromagnetism is dominating for a strictly local interaction because the sublattice interference suppresses the other competitive orders. In opposite, for a large nearest-neighbor interaction, the Pomeranchuk instability drives a deformation of the Fermi surface. Thus, the high density of states is reduced at the Fermi surface. The Pomeranchuk instability is a nematic phase, breaking the rotational symmetry, but leaving the translational symmetry unmodified.

These interesting new phases occur because the sublattice interference suppresses the instabilities for conventional orders. But the sublattice interference for a Fermi surface instability implies that the system can be approximated by the (weak-coupling) Fermi-liquid theory. Up to now, the experimental data [91–94] and some theoretical simulations [95] are in the strong-coupling regime. But the exotic phases predicted in this chapter illustrate that a closer look on weak-coupling materials would be worthwhile.

With this second chapter about the kagome lattice, I finish my overview on unconventional superconductors. In conclusion, the results of the chapters will be summarized and contrasted.

Conclusion

8

The foundation of physics is the interplay between regularities, observed in and interpolated from experiments, and theories, founded on a mathematical framework. The task of theoretical physics is to develop a theory which fits to the experimental data and reveals the essential principle behind the observations, so predictions for further experiments are possible. These confirm or disprove the theory, but it is never absolutely and completely proved: Some new measurements with a higher precision or under extreme conditions may reveal unpredicted effects and the theory has to be modified or even discarded. One famous example is the replacement of the Galilean transformation by the Lorentz transformation in the framework of the special theory of relativity.

For superconductivity in metals, the BCS theory with its phonon-mediated pairing mechanism is a complete theory. However, after the discovery of superconductivity in cuprates, it was unveiled that there is more than one mechanism to form Cooper pairs. Triggered by the revealing of additional classes of unconventional superconductors, the search for a general underlying theory was reinforced and has not yet been successfully finished.

In this thesis, I presented several distinct classes of **unconventional superconductors**. Combined with **appropriate numerical techniques**, an electronic formalism was used to reproduce the phase diagrams created by experimental data. Therein, the focus was on the superconducting phases: The symmetry of the pairing states are observable quantities (e.g. Knight shift measurements) and provide a direct comparison between theory and experiment. Thereby, **universal properties** can be highlighted.

The **source for the formation of Cooper pairs** was considered as an electronic “pairing glue” in **Chap. 3**. For the high-T_c **cuprates**, the role of Cu- and O-orbital degrees of freedom were investigated by the comparison of a **one-band and a three-band model**. This is extremely interesting because the former model is a doped **Mott insulator** while the latter one is a doped **charge-transfer insulator**. The evaluation of the gap function, i.e. the anomalous part of the self-energy, yielded that **only the Mott insulator has a non-retarded contribution to the pairing** (Sec. 3.6). In addition, in accordance with experimental data, a magnetic resonance mode (“hour glass structure”) was observed in the superconducting phase. This is a **reminiscent “fingerprint” of the magnetic parent**

compound (Sec. 3.4). Furthermore, the phase diagram presented in Sec. 3.3 features the observed asymmetry between electron and hole doping. Here, the differences between the one- and three-band model are slight, in contrast to the high-energy features.

After the cuprates, the **cobaltates** were considered (**Chap. 4**). For that, the simulation technique had to be changed from the variational cluster approach to the functional renormalization group because this implies a change from strongly correlated physics to weak-coupling physics. The model for the cobaltate $\mathrm{Na_{0.3}CoO_2 \cdot yH_2O}$ (NaCoO) features a **three-band Hamiltonian in a triangular lattice** and results in a rich phase diagram of competing phases (Sec. 4.2), including a **chiral, i.e. parity and time-reversal symmetry-breaking, *d*+i*d*-wave superconductivity**. The close correlation to the magnetic spin-density wave combined with a highly anisotropic local density of states triggers a distortion of the *d*+i*d*-wave form factors (Sec. 4.4). Thus, the **gap function becomes very anisotropic**, nearly featuring nodes, which is extremely unusual *d*+i*d*-wave superconductivity. This might explain some contradictions in experimental data.

A nodeless *d*+i*d*-wave superconductivity is present in the phase diagram of **graphene**, discussed in **Chap. 5**. If the filling is set to the van Hove singularity, **superconductivity is in heavy competition to the spin-density wave** (Sec. 5.4). Away from the van Hove singularity, the screening of the Coulomb interaction is weakened. Thus, long-range interactions were included, resulting in **enhanced charge-density wave fluctuations**. Subsequently, *f*-wave superconductivity becomes competitive (Sec. 5.5).

Finally, the focus was on the kagome lattice, where electrons at the Fermi level feature a momentum- and sublattice-dependent contribution to the Fermi surface. It is interesting that the parts of the Fermi surface which are connected by the nesting vectors are predominantly influenced by distinct sublattices. If the **interaction is strictly local**, it is diagonal in the sublattices and, hence, the **nesting condition is dramatically weakened**. Consequently, the spin-density wave fluctuations are damped and thereby *d*+i*d*-wave superconductivity. This is the new concept of **sublattice interference**. But a non-local interaction partially restores the nesting condition, so orders with finite momentum are also possible. In **Chap. 6**, a simple analytical renormalization group evaluation yielded that an addition of a **long-range interaction indeed increases the transition temperature of superconductivity** (Sec. 6.3). This evaluation was repeated with a more elaborate technique because the analytical renormalization group is limited to the superconducting instability, except at van Hove filling. In contrast, the functional renormalization group provides an unbiased flow of competing orders. The results are presented in **Chap. 7**, including a phase diagram with exotic quantum states which are usually superimposed by the spin-density wave (Sec. 7.2), namely **spin and charge bond-ordered phases** (Sec. 7.4) as well as a **Pomeranchuk instability** (Sec. 7.5), which induces a nematic long-range order. In addition, if the kagome lattice is doped away from van Hove filling, where the nesting is optimal, the bond orders are weakened and superconductivity rises. Due to the sublattice interference, the *d*+i*d*-wave form is suppressed and, hence, the ***f*-wave form is dominating without competition**. This pure triplet superconductivity is detectable by experiments, e.g. Knight shift measurements.

After the investigation of such distinct classes of superconductors, a few conclusions are possible:

Superconductivity is **connected to magnetism** because in the phase diagrams of the cuprates (Fig. 3.5), NaCoO (Fig. 4.3), graphene (Fig. 5.3) and the kagome lattice (Fig. 7.1), the superconducting phase is next to a magnetic instability. This fact resulted in the formulation of a unified theory [308], but within this theses, superconductivity and magnetism are considered as two different but affiliated phenomena. Indeed, singlet superconductivity, e.g. d+id-wave, **is driven by spin-density wave fluctuations**. This is reasonable because an inhomogeneous order of spins facilitates the formation of pairs with antiparallel spins. In contrast, triplet superconductivity, e.g. f-wave, is enhanced by ferromagnetic fluctuations. In addition, a charge-density wave equally drives both singlet and triplet superconductivity.

Furthermore, the **underlying lattice is crucial**: The formation of a chiral d+id-wave superconductivity is predicted for NaCoO and graphene because their lattices have a C_{6v}-symmetry, which **protects the degeneracy of two d-wave solutions by symmetry** (E_2 representation). This is a great advantage over the chiral s+id-wave superconductivity in pnictides, which is not protected by symmetry but has to be adjusted with extern parameters [48]. In contrast, the kagome lattice features a C_{6v}-symmetry but lacks of d+id-wave superconductivity because of the sublattice interference.

Finally, in the strongly correlated approach, the electronic mechanism for the formation of Cooper pairs is **sensitive to the parent compound**. Indeed, for the high-energy excitations, there is a difference whether the superconductor is a doped Mott insulator or a charge-transfer insulator, influencing the pairing glue of the system.

Altogether, a strictly electronic mechanism yields the phase diagrams of various superconductors, in good accordance with experimental data. A few sources for material-dependent differences are evaluated, e.g. the (sub)lattice structure. However, some universal features are existing, e.g. the connection to magnetic phases. Overall, this yields a comprehensive picture of the theory of unconventional and high-T_c superconductors.

Indeed, superconductors are not only a future technology but are already in use today:

- Electric power transmission: If a huge amount of energy has to be transported a short distance, the transport in a superconducting cable without an energy loss is less costly although the cable has to be cooled, e.g. a 1-kilometer-long cable has been installed in the inner city of Essen [309].

- Strong electromagnets: Superconductors create electric fields far beyond those of static magnets. The reduced energy costs have to be compared to high cooling costs. Two fields of application are magnetic resonance imaging and particle accelerators, e.g. the Large Hadron Collider at CERN (Geneva, Switzerland).

- Superconducting quantum interference devices (SQUID): These very sensitive magnetometers are used to measure extremely tiny magnetic fields

With the worldwide technological progress, the field of application for superconductors is also increasing. This encourages the search for materials with higher transition

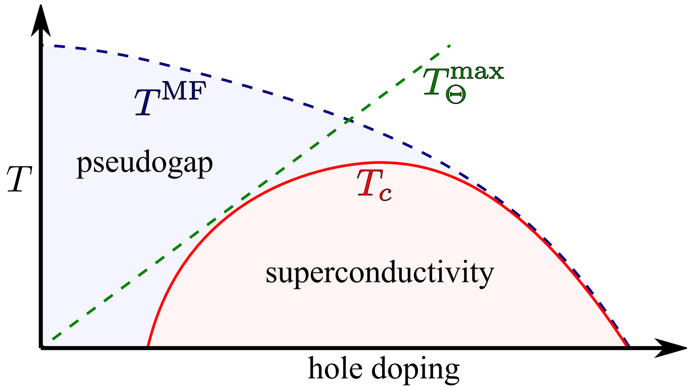

Figure 8.1: Schematic phase diagram for hole-doped cuprates as a function of temperature T and doping [22] (for a more detailed diagram, see Fig. 1.2). The superconducting transition temperature T_c is limited by both the mean-field transition temperature T^{MF}, determined by the pairing scale, and the upper bound on the phase ordering $T_\Theta^{\max}$, influenced by phase fluctuations.

temperatures.

A new idea to enhance the stability of the superconducting phase is a multilayer system composed of different materials. These heterostructures consist of a superconductor with large paring scale but low superconducting T_c due to strong phase fluctuations (Fig. 8.1), coupled to a non-interacting metallic layer. The general idea, spelled out in detail by *E. Berg et al.* in Ref. [310], is that through the coupling to the metallic layer, the phase stiffness of the low-T_c superconductor can be significantly enhanced. If this enhancement of the phase stiffness is stronger than the reduction of the pairing scale due to the coupling to the metallic layer, T_c of the composite system will be enhanced over T_c of the isolated superconducting layer.

The basic idea behind this scenario is to profit from the fact that these two layers have very different properties. The metallic layer has no pairing, but a high superfluid stiffness, while the interacting layer has a high pairing scale but negligible superfluid weight [311].

If these two layers are coupled together via electron hopping, it is interesting to study what properties this heterogeneous system has [312,313]. If this system acquires the "best of two worlds", i.e. the high superfluid stiffness with a high pairing scale (Fig. 8.1), this may result in a high transition temperature T_c [22].

Indeed, the first experimental results show an enhancement of T_c by the coupling of the superconductor to metallic layers [314] or by the coupling of underdoped and overdoped superconductors [315]. So, this is a promising route to new high-T_c superconductors.

It is undeniable that superconductivity will be one of the key technologies of the future. But as *Niels Bohr* had already mentioned:

> Prediction is very difficult, especially about the future.

Appendix

A

A.1 g-ology Model

For the functional renormalization group (fRG, see Sec. 2.6 for details), one has to set a starting value for the coupling function $V(\vec{k}_1,\vec{k}_2,\vec{k}_3,\vec{k}_4)$. The simplest ansatz is $V = U$, with U being the Coulomb interaction. This constant coupling function includes no information of the microscopic model, so its significance is minimal.

In Refs. [62, 143, 316], the so-called *g-ology model* is used. Here, only excitations near the Fermi energy are considered, resulting in band couplings in momentum space. This reduces the interaction to four independent couplings g_1,g_2,g_3 and g_4, displayed in Fig. A.1. The simplified flow equations read

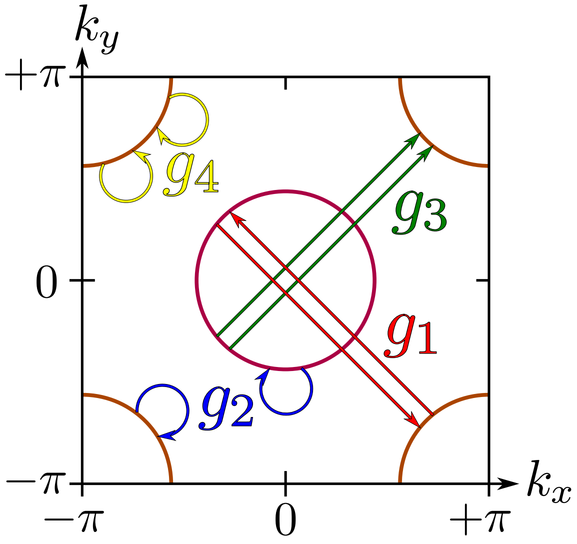

Figure A.1: The relevant scattering processes near the FS are interband (g_1), intraband (g_2 and g_4) and interband pair hopping (g_3).

$$\begin{aligned}
\dot{g}_1 &= 2g_1(g_2 - g_1) \\
\dot{g}_2 &= g_2^2 + g_3^2 \\
\dot{g}_3 &= -2g_3g_4 + 2g_3(2g_2 - g_1) \\
\dot{g}_4 &= -g_3^2 - g_4^2
\end{aligned} \tag{A.1}$$

with $\dot{g}_i = \frac{\Lambda}{\rho(0)} \frac{\mathrm{d}g_i}{\mathrm{d}\Lambda}$ and the density of states $\rho(0)$ at the Fermi energy. Λ is the flow parameter, e.g. the cutoff energy. This ansatz includes independent interactions on a band level.

In opposite, within this thesis, the interaction part of Hamiltonian is transfered to momentum space (Eq. 2.9 and Eq. 2.16) and used as starting value for the coupling function. Hence, all microscopic degrees of freedom are included.

A.2 Evaluation of the VCA-Grand Potential

In the VCA formalism, the grand potential consists of three addends (Eq. 2.32)

$$\Omega_{\mathbf{t}}[\mathbf{\Sigma}] = \Omega\text{'} + \mathrm{Tr}\,(\ln(-\mathbf{G})) - \mathrm{Tr}\,(\ln(-\mathbf{G'}))\ , \tag{A.2}$$

which are calculated one by one in the following:

Firstly, Ω’ is the grand potential of the reference system and reads

$$\Omega\text{'} = -\frac{1}{\beta}\ln\left(\mathrm{Tr}\left(\mathrm{e}^{-(\hat{H}'-\mu\hat{N}')\beta}\right)\right) = \frac{1}{\beta}\ln\left(\sum_m \mathrm{e}^{-(E'_m-\mu N'_m)\beta}\right) \tag{A.3}$$

With inverse temperature β. Performing $T \to 0$ (or equivalently $\beta \to +\infty$), the result is $\Omega\text{'} = E_0 - \mu N$.

The second addend is a little more tricky. The starting point is a general form of a fully dressed Green’s function

$$\mathbf{G}(\omega) = \frac{1}{\omega + \mu - \mathbf{t} - \mathbf{\Sigma}(\omega)} \tag{A.4}$$

and with a unitary matrix $\mathbf{U}(\omega)$ to diagonalize the fraction to $\mathbf{g}(\omega)$ with $\mathbf{G}(\omega) = \mathbf{U}(\omega)\mathbf{g}(\omega)\mathbf{U}^\dagger(\omega)$.

If $\mathbf{G}(\omega)$ conserves causality, $\mathbf{g}(\omega)$ has poles of order one at $\omega = \omega_m$ with positive residues. $\mathbf{t} + \mathbf{\Sigma}(\omega)$ is real and symmetric, so the transformation fits $\mathbf{t} + \mathbf{\Sigma}(\omega) = \mathbf{U}(\omega)\eta(\omega)\mathbf{U}^\dagger(\omega)$ with $g_\alpha(\omega) = 1/(\omega + \mu - \eta_\alpha(\omega))$. $\eta(\omega)$ features poles of order one at $\omega = \zeta_n$ with positive residue.

This results in

$$\begin{aligned}\mathrm{Tr}\,(\ln(-\mathbf{G})) &= \frac{1}{\beta}\sum_{\omega,\alpha}\mathrm{e}^{\mathrm{i}\omega 0^+}\ln\left(\frac{-1}{\mathrm{i}\omega + \mu - \mathbf{t}_{\alpha\alpha} - \mathbf{\Sigma}_{\alpha\alpha}(\mathrm{i}\omega)}\right)\\ &= -\frac{1}{\beta}\sum_{\omega,\alpha}\mathrm{e}^{\mathrm{i}\omega 0^+}\ln\left(\mathbf{U}^\dagger(\omega)\mathbf{g}(\omega)\mathbf{U}(\omega)\right)_{\alpha\alpha}\ .\end{aligned} \tag{A.5}$$

Next, a function $h(\omega) = -\beta\frac{1}{\mathrm{e}^{\omega\beta}+1}$ is introduced with poles at fermionic Matsubara frequencies $\omega_n = \frac{\pi}{\beta}(2n+1)$ and residues equal to 1. By integrating this function over a closed curve in $\mathbb{C}$ with including all poles and using the residue theorem, one obtains

$$\oint_C h(\omega)\mathrm{d}\omega = -\beta\oint_C \frac{1}{\mathrm{e}^{\omega\beta}+1}\mathrm{d}\omega = -2\pi\mathrm{i}\beta\sum_n 1\ . \tag{A.6}$$

Accordingly, a product function $h(\omega)\cdot g(\omega)$ yields

$$-\beta\oint_C \frac{1}{\mathrm{e}^{\omega\beta}+1}g(\omega)\mathrm{e}^{\omega 0^+}\mathrm{d}\omega = -2\pi\mathrm{i}\beta\sum_n g(\mathrm{i}\omega_n)\mathrm{e}^{\mathrm{i}\omega_n 0^+}\ , \tag{A.7}$$

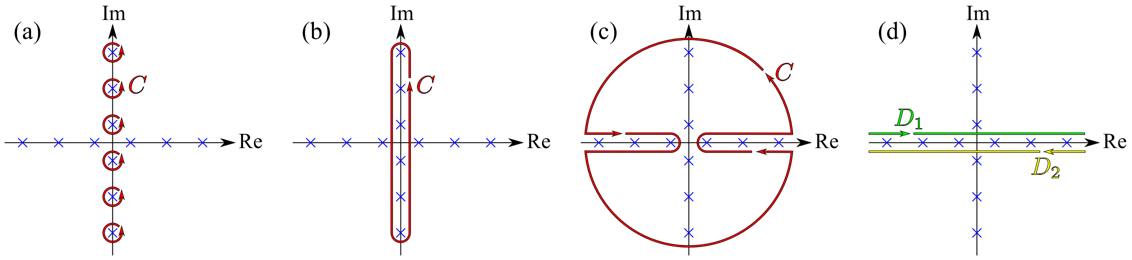

Figure A.2: Deformation of the contour of integration: All separated contours around poles at imaginary axis **(a)** are joined to a single contour **(b)**, which is enlarged as far as possible while poles only at the real axis are omitted **(c)**. Finally, the contour at infinity can be neglected and only two contributions D_1 and D_2 remain **(d)**.

with a factor $e^{\omega 0^+}$ to ensure convergence. This relation can be applied to Eq. A.5:

$$-\frac{1}{\beta}\sum_{\omega,\alpha} e^{i\omega 0^+} \ln\left(\mathbf{U}^\dagger(\omega)\mathbf{g}(\omega)\mathbf{U}(\omega)\right)_{\alpha\alpha} = \frac{-1}{2\pi i}\sum_{\alpha}\oint_C e^{\omega 0^+} h(\omega)\ln\left(-g_\alpha(\omega)\right)d\omega\,. \tag{A.8}$$

The contour of the integration can be transformed to two parallel ways next to the real axis (Fig. A.2). After some algebra,

$$\begin{aligned}\oint_C h(\omega)g(\omega)d\omega &= \int_{-\infty}^{+\infty} h(\omega+i0^+)g(\omega+i0^+)d\omega + \int_{+\infty}^{-\infty} h(\omega-i0^+)g(\omega-i0^+)d\omega\\ &\approx \int_{-\infty}^{+\infty} h(\omega)\left(g(\omega+i0^+)-g(\omega-i0^+)\right)d\omega\\ &= \int_{-\infty}^{+\infty} h(\omega)\left(g(\omega+i0^+)-\left(g(\omega+i0^+)\right)^*\right)d\omega\\ &= 2i\int_{-\infty}^{+\infty} h(\omega)\mathrm{Im}\left(g(\omega+i0^+)\right)d\omega\end{aligned} \tag{A.9}$$

this relation is applied to Eq. A.7 and yields

$$\frac{-1}{2\pi i}\sum_{\alpha}\oint_C e^{\omega 0^+} h(\omega)\ln\left(-g_\alpha(\omega)\right)d\omega = \frac{-1}{\pi}\sum_{\alpha}\int_{-\infty}^{+\infty} h(\omega)\mathrm{Im}\left(\ln\left(-g_\alpha(\omega+i0^+)\right)\right)d\omega\,. \tag{A.10}$$

If ω is expanded to $\mathbb{C}$ and an analytic continuation applied to both $g_k(\omega)$ and $\eta_k(\omega)$, this yields

$$\begin{aligned}-\frac{1}{\pi}\mathrm{Im}\left(g_k(\omega+i0^+)\right) &\geq 0\\ -\frac{1}{\pi}\mathrm{Im}\left(\eta_k(\omega+i0^+)\right) &\geq 0\,.\end{aligned} \tag{A.11}$$

After a change to polar coordinates

$$\begin{aligned} -g(\omega+\mathrm{i}0^+) &= r(\omega)\mathrm{e}^{\mathrm{i}\Phi(\omega)}, \qquad \omega\in\mathbb{R} \\ \Rightarrow \qquad \ln\left(-g(\omega+\mathrm{i}0^+)\right) &= \underbrace{\ln\left(r(\omega)\right)}_{\mathrm{Re}}+\mathrm{i}\underbrace{\Phi(\omega)}_{\mathrm{Im}} \end{aligned} \tag{A.12}$$

and a reduction to the imaginary part

$$\begin{aligned} \mathrm{Im}\left(-g(\omega+\mathrm{i}0^+)\right) &= 0^+ \\ \mathrm{Im}\left(\ln\left(-g(\omega+\mathrm{i}0^+)\right)\right) &= \Phi(\omega)\ , \end{aligned} \tag{A.13}$$

only 0 and π are possible results for the azimuth of $\Phi(\omega)$, namely

$$\begin{aligned} \Phi(\omega) &= \pi \qquad \text{if} \qquad -g(\omega)<0 \\ \Phi(\omega) &= 0 \qquad \text{if} \qquad -g(\omega)>0. \end{aligned} \tag{A.14}$$

This can be combined to a Heavyside function (step function) Θ

$$\mathrm{Im}\left(\ln\left(-g(\omega+\mathrm{i}0^+)\right)\right) = \pi\Theta\left(g(\omega)\right) = \pi\Theta\left(\frac{1}{g(\omega)}\right) \tag{A.15}$$

and inserted in Eq. A.10

$$\begin{aligned} \frac{-1}{\pi}\sum_\alpha\int_{-\infty}^{+\infty} h(\omega)\mathrm{Im}\left(\ln\left(-g_\alpha(\omega\ +\ \mathrm{i}0^+)\right)\right)\mathrm{d}\omega &= -\sum_\alpha\int_{-\infty}^{+\infty} h(\omega)\Theta\left(\frac{1}{g_\alpha(\omega+\mathrm{i}0^+)}\right)\mathrm{d}\omega \\ &= -\sum_\alpha\int_{-\infty}^{+\infty}\beta\frac{1}{\mathrm{e}^{\omega\beta}+1}\Theta\left(\omega+\mu-\eta_\alpha(\omega)\right)\mathrm{d}\omega\ , \end{aligned} \tag{A.16}$$

with $h(\omega)=-\beta\frac{1}{\mathrm{e}^{\omega\beta}+1}$ and $g_\alpha(\omega)=1/(\omega+\mu-\eta_\alpha(\omega))$ replaced. With a partial integration

$$\begin{aligned} &\sum_\alpha\int_{-\infty}^{+\infty}\beta\frac{1}{\mathrm{e}^{\omega\beta}+1}\Theta\left(\omega+\mu-\eta_\alpha(\omega)\right)\mathrm{d}\omega \\ &= \left[\frac{1}{\beta}\underbrace{\ln\left(1+\mathrm{e}^{-\omega\beta}\right)}_{0\text{ if }\omega\to+\infty}\cdot\underbrace{\Theta\left(\omega+\mu-\eta_\alpha(\omega)\right)}_{0\text{ if }\omega\to-\infty}\right]_{\omega\to-\infty}^{\omega\to+\infty} \\ &\quad -\sum_\alpha\int_{-\infty}^{+\infty}\frac{1}{\beta}\ln\left(1\ +\ \mathrm{e}^{-\omega\beta}\right)\frac{\mathrm{d}\Theta\left(\omega+\mu-\eta_\alpha(\omega)\right)}{\mathrm{d}\omega}\mathrm{d}\omega\ , \end{aligned} \tag{A.17}$$

the first addend is vanishing.

Now consider a function $f(\omega)=\omega+\mu-\eta_\alpha(\omega)$ which is analytical except at first order poles at the real axis. So, $\Theta(f(\omega))$ is constant with the same exceptions. Consequently,

$\frac{\mathrm{d}\Theta(f(\omega))}{\mathrm{d}\omega}=0$, but not at all points with $f(\omega)$ change sign, i.e the roots and poles of $f(\omega)$. The roots ω_m yield

$$f'(\omega)\delta(f(\omega)) = \sum_m \frac{f'(\omega_m)}{f'(|\omega_m|)}\delta(\omega-\omega_m) \tag{A.18}$$

with using $f'(\omega)=\frac{\partial f(\omega)}{\partial\omega}$. The roots of $f(\omega)$ correspond to poles of the diagonalized Green's function $g(\omega)$ with positive residues. So $\frac{f'(\omega_m)}{f'(|\omega_m|)}=1$.
The poles ζ_n of $f(\omega)$ can be considered analogous

$$(1/f)'(\omega)\delta((1/f)(\omega)) = \sum_n \frac{(1/f)'(\zeta_n)}{(1/f)'(|\zeta_n|)}\delta(\omega-\zeta_n)\;. \tag{A.19}$$

Accordingly the poles of $f(\omega)$ correspond to poles of the self-energy $\mathbf{\Sigma}$ with positive residues and, hence, hold $\frac{(1/f)'(\zeta_n)}{(1/f)'(|\zeta_n|)}=-1$. Together roots and poles form

$$\frac{d}{d\omega}\Theta(\omega+\mu-\eta_\alpha(\omega)) = \sum_m^{\text{roots}}\delta(\omega-\omega_m) - \sum_n^{\text{poles}}\delta(\omega-\zeta_n)\;. \tag{A.20}$$

This relation can be used in Eq. A.17, and yields

$$\begin{aligned}&\sum_\alpha\int_{-\infty}^{+\infty}\beta\frac{1}{\mathrm{e}^{\omega\beta}+1}\Theta\left(\omega+\mu-\eta_\alpha(\omega)\right)\mathrm{d}\omega = \\ &-\sum_\alpha\int_{-\infty}^{+\infty}\frac{1}{\beta}\ln\left(1+\mathrm{e}^{-\omega\beta}\right)\left(\sum_m\delta(\omega-\omega_m)-\sum_n\delta(\omega-\zeta_n)\right)\mathrm{d}\omega\;.\end{aligned} \tag{A.21}$$

Now, one can perform the ω-integration and the sum over α. The sum simply yields a factor $2L$ because $g_\alpha(\omega)$ has the same roots and poles for all α. L is the size of the reference cluster and 2 is due to spin degeneracy. One gets

$$\begin{aligned}&-\sum_\alpha\int_{-\infty}^{+\infty}\frac{1}{\beta}\ln\left(1+\mathrm{e}^{-\omega\beta}\right)\left(\sum_m\delta(\omega-\omega_m)-\sum_n\delta(\omega-\zeta_n)\right)\mathrm{d}\omega \\ &\quad=-2L\left(\sum_m\frac{1}{\beta}\ln\left(1+\mathrm{e}^{-\omega_m\beta}\right)-\sum_n\frac{1}{\beta}\ln\left(1+\mathrm{e}^{-\zeta_n\beta}\right)\right) \\ &\quad=-2L\left(\sum_m\frac{1}{\beta}\ln\left(1+\mathrm{e}^{-\omega_m\beta}\right)-R_{\mathbf{\Sigma}}\right)\end{aligned} \tag{A.22}$$

with $R_{\mathbf{\Sigma}}=\sum_n\frac{1}{\beta}\ln\left(1+\mathrm{e}^{-\zeta_n\beta}\right)$.
Finally, the limit $\beta\rightarrow+\infty$ is considered and the residues can be rewritten to

$$\lim_{\beta\rightarrow+\infty}\frac{\ln\left(1+\mathrm{e}^{-\beta\omega}\right)}{\beta}\overset{l'H}{=}\underbrace{\lim_{\beta\rightarrow+\infty}\frac{\frac{-\omega\mathrm{e}^{-\beta\omega}}{1+\mathrm{e}^{-\beta\omega}}}{1}}_{0\text{ if }\omega>0}\overset{l'H}{=}\underbrace{\lim_{\beta\rightarrow+\infty}\frac{(-\omega)^2\mathrm{e}^{-\beta\omega}}{-\omega\mathrm{e}^{-\beta\omega}}}_{-\omega\text{ if }\omega<0}\;. \tag{A.23}$$

The result for the second addend is now

$$\lim_{\beta\to+\infty} -2L\left(\sum_m \frac{1}{\beta}\ln\left(1+\mathrm{e}^{-\omega_m\beta}\right)-R_{\mathbf{\Sigma}}\right) = -2L\left(\sum_m \omega_m\Theta(-\omega_m)-R_{\mathbf{\Sigma}}\right) , \tag{A.24}$$

which is a simple summation over negative excitation energies.

The third addend in Eq. 2.32 is analog to the second one: The infinite lattice is replaced be the reference system. Consequently, one has to sum over all negative excitation energies of the reference system.

In the SFA, by definition, the self-energy of the infinite lattice and the reference system have to be equal, so $R_{\mathbf{\Sigma}}$ is also equal. If all transformations of this section are applied to Eq. 2.32, $R_{\mathbf{\Sigma}}$ is canceling out:

$$\begin{aligned} \Omega_{\mathbf{t}}[\mathbf{\Sigma}] &= \Omega\text{'} + \mathrm{Tr}\left(\ln\left(-\mathbf{G}\right)\right) - \mathrm{Tr}\left(\ln\left(-\mathbf{G'}\right)\right) \\ \Omega_{2L} = \lim_{\beta\to+\infty}\frac{\Omega_{\mathbf{t}}[\mathbf{\Sigma}]}{2L} &= \frac{E_0}{2L} - \sum_m \omega_m\Theta(-\omega_m) + \sum_m \omega\text{'}_m\Theta(-\omega\text{'}_m) \ . \end{aligned} \tag{A.25}$$

This is the final result for the VCA grand potential.

A.3 Analytical Evaluation of Loop Integrals

In the final flow equations (Eq. 2.125), the product of intern propagators $\mathcal{L}_T$ (Eq. 2.123) includes a free momentum $\vec{p}$, which has to be integrated. In detail, for a general function h

$$\int_p \mathrm{d}^4 p\, h(p) = \int_{\vec{p}} \mathrm{d}^3 \vec{p}\, \sum_n h(\mathrm{i}\omega_n, \vec{p}) \,, \tag{A.26}$$

the fourfold integration splits into a threefold integration over the momentum and a summation over the fermionic Matsubara frequencies $\mathrm{i}\omega_n = (\mathrm{i}(2n+1)\pi)T$. The latter ones can be rewritten with the residue theorem (for a textbook, see Ref. [317]) into a complex integral.

Firstly, one has to expand h to the complex numbers, so $\tilde{h}(-\mathrm{i}z)$. Now an auxiliary function

$$\begin{gathered} \tilde{g}(z) = \frac{1}{T\ \mathrm{e}^{z/T}+1} \qquad \text{with} \\ \operatorname{Res}\left[\tilde{g}(z); z = \mathrm{i}\omega_n\right] = 1 \end{gathered} \tag{A.27}$$

is defined. It has first-order poles with residue 1 at the Matsubara frequencies. If $\tilde{h}(-\mathrm{i}z)$ has isolated singularities at $\{z_k\}$, one obtains

$$\sum_n h(\mathrm{i}\omega) = \oint_{\mathcal{C}_1} \tilde{h}(-\mathrm{i}z)\, \tilde{g}(z)\, \mathrm{d}z = \oint_{\mathcal{C}_2} \tilde{h}(-\mathrm{i}z)\, \tilde{g}(z)\, \mathrm{d}z = \sum_k \operatorname{Res}\left[\tilde{h}(-\mathrm{i}z)\, \tilde{g}(z); z = z_k\right] \tag{A.28}$$

by transforming the contour $\mathcal{C}_1$ to $\mathcal{C}_2$ (“Cauchy’s integral theorem”) as plotted in Fig. A.3 and a subsequent exploit of the residue theorem. Thereby, the infinite sum $\sum_n$ is transformed into a finite sum $\sum_k$. This yields the identities

$$\begin{aligned} \sum_n \frac{T^{1/2}}{\mathrm{i}\omega_n - \varepsilon_{\vec{p}_1}} \frac{T^{1/2}}{\mathrm{i}\omega_n - \varepsilon_{\vec{p}_2}} &= \frac{T}{\varepsilon_{\vec{p}_1} - \varepsilon_{\vec{p}_2}} \tilde{g}(\varepsilon_{\vec{p}_1}) + \frac{T}{\varepsilon_{\vec{p}_2} - \varepsilon_{\vec{p}_1}} \tilde{g}(\varepsilon_{\vec{p}_2}) \\ \sum_n \frac{T^{1/2}}{\mathrm{i}\omega_n - \varepsilon_{\vec{p}_1}} \frac{T^{1/2}}{-\mathrm{i}\omega_n - \varepsilon_{\vec{p}_2}} &= \frac{T}{-\varepsilon_{\vec{p}_1} - \varepsilon_{\vec{p}_2}} \tilde{g}(\varepsilon_{\vec{p}_1}) + \frac{-T}{-\varepsilon_{\vec{p}_2} - \varepsilon_{\vec{p}_1}} \tilde{g}(-\varepsilon_{\vec{p}_2}) \,. \end{aligned} \tag{A.29}$$

To calculate the diagrams in Fig. 2.18, the translational invariance in time and space can be used: At each vertex, frequency and momentum conservation must be considered. For the particle-particle channel, it holds

$$\begin{aligned} \vec{p}_2 &= \vec{k}_1 + \vec{k}_2 - \vec{p}_1 \\ \omega_{n_2} &= \underbrace{\omega_{\mathrm{ext}_1} + \omega_{\mathrm{ext}_2}}_{0} - \omega_{n_1} \end{aligned} \tag{A.30}$$

with the external frequencies set to zero because the frequency dependencies of the vertex are neglected in this thesis. With a little bit straightforward algebra, the sum over the Matsubara frequencies in Eq. 2.123 can be evaluated:

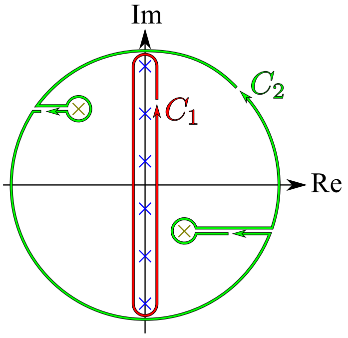

Figure A.3: Deformation of the contour of integration form $\mathcal{C}_1$ (red) to $\mathcal{C}_2$ (green): The poles of $\tilde{h}$ (blue crosses) are encircled with both contours, while the poles of $\tilde{g}$ (yellow crosses) remain outside.

$$
\begin{aligned}
\int\limits_{\vec{p}_1\vec{p}_2} \mathrm{d}^3\vec{p}_1\, \mathrm{d}^3\vec{p}_2\, \mathcal{L}_{T,\mathrm{PP}}(\vec{p}_1,\vec{p}_2) &= \frac{\mathrm{d}}{\mathrm{d}T}\left(\int\limits_{\vec{p}_1\vec{p}_2} \mathrm{d}^3\vec{p}_1\, \mathrm{d}^3\vec{p}_2 \sum_{n_1 n_2} \frac{\sqrt{T}}{\mathrm{i}\omega_{n_1}-\varepsilon_{\vec{p}_1}} \frac{\sqrt{T}}{\mathrm{i}\omega_{n_2}-\varepsilon_{\vec{p}_2}}\right) \\
&= \frac{\mathrm{d}}{\mathrm{d}T}\left(\int\limits_{\vec{p}_1\vec{p}_2} \mathrm{d}^3\vec{p}_1\, \mathrm{d}^3\vec{p}_2 \sum_{n_1} \frac{\sqrt{T}}{\mathrm{i}\omega_{n_1}-\varepsilon_{\vec{p}_1}} \frac{\sqrt{T}}{-\mathrm{i}\omega_{n_1}-\varepsilon_{\vec{k}_1+\vec{k}_2-\vec{p}_1}}\right) \\
&= \frac{\mathrm{d}}{\mathrm{d}T}\left(\int\limits_{\vec{p}_1} \mathrm{d}^3\vec{p}_1 \frac{T\,\tilde{g}(\vec{p}_1)}{-\varepsilon_{\vec{p}_1}-\varepsilon_{\vec{k}_1+\vec{k}_2-\vec{p}_1}} \frac{-T\,\tilde{g}(-\varepsilon_{\vec{k}_1+\vec{k}_2-\vec{p}_1})}{-\varepsilon_{\vec{k}_1+\vec{k}_2-\vec{p}_1}-\varepsilon_{\vec{p}_1}}\right) \\
&= -\int\limits_{\vec{p}_1} \mathrm{d}^3\vec{p}_1 \frac{\frac{\mathrm{d}}{\mathrm{d}T}\left(1+n_F(\varepsilon_{\vec{k}_1+\vec{k}_2-\vec{p}_1})+n_F(\varepsilon_{\vec{p}_1})\right)}{\varepsilon_{\vec{k}_1+\vec{k}_2-\vec{p}_1}+\varepsilon_{\vec{p}_1}} \\
&= -\int\limits_{\vec{p}_1} \mathrm{d}^3\vec{p}_1 \frac{\frac{\mathrm{d}}{\mathrm{d}T}\left(n_F(\varepsilon_{\vec{k}_1+\vec{k}_2-\vec{p}_1})\right)+\frac{\mathrm{d}}{\mathrm{d}T}\left(n_F(\varepsilon_{\vec{p}_1})\right)}{\varepsilon_{\vec{k}_1+\vec{k}_2-\vec{p}_1}+\varepsilon_{\vec{p}_1}}
\end{aligned}
\tag{A.31}
$$

Here, the Fermi-Dirac distribution $n_F(z)$ is inserted. It reads

$$
\begin{aligned}
n_F(z) &= \frac{1}{\mathrm{e}^{z/T}+1} = T\,\tilde{g}(z) \\
n_F(-z) &= 1-n_F(z) \\
\frac{\mathrm{d}}{\mathrm{d}T}\left(n_F(z)\right) &= -\frac{z\,\mathrm{e}^{z/T}}{(T^2\,\mathrm{e}^{z/T}+1)^2}
\end{aligned}
\tag{A.32}
$$

and has an inversion symmetry with respect to the inflection point. The derivative can be easily calculated. The integral over the internal propagator line still has to be numerically executed.

For the particle-hole channel, the conservation conditions read

$$\begin{aligned} \vec{p}_2 &= -\vec{k}_1 + \vec{k}_2 + \vec{p}_1 \\ \omega_{n_2} &= \underbrace{-\omega_{\text{ext}_1} + \omega_{\text{ext}_2}}_{0} + \omega_{n_1} \ , \end{aligned} \tag{A.33}$$

so the evaluation of the sum over Matsubara frequency yields:

$$\mathcal{L}_{T,\text{PH}}(\vec{p}_1, -\vec{k}_1 + \vec{k}_2 + \vec{p}_1) = -\frac{\frac{\mathrm{d}}{\mathrm{d}T}\left(n_F(\varepsilon_{-\vec{k}_1+\vec{k}_2+\vec{p}_1})\right) - \frac{\mathrm{d}}{\mathrm{d}T}\left(n_F(\varepsilon_{\vec{p}_1})\right)}{\varepsilon_{-\vec{k}_1+\vec{k}_2+\vec{p}_1} - \varepsilon_{\vec{p}_1}} \tag{A.34}$$

These results are used for the numerical evaluation of the flow equations in Sec. 2.6.4.

A.4 Mean-Field Decoupling of One-Particle Operators

This section describes the mean-field decoupling in the Cooper channel. Here, two creation operators are composed to the pairing operator. Analogously, other one-particle operators can be considered. The total interaction is equal to the sum over all these channels.

The interaction in the Cooper channel reads

$$\begin{aligned} \hat{H}_{\text{pair}} &= \frac{1}{N}\sum_{\vec{k}\vec{q}} V_{\text{pair}}(\vec{k},\vec{q})\ \hat{c}^{\dagger}_{\vec{k}\uparrow}\hat{c}^{\dagger}_{-\vec{k}\downarrow}\hat{c}_{-\vec{q}\downarrow}\hat{c}_{\vec{q}\uparrow} \\ &= \frac{1}{N}\sum_{\vec{k}\vec{q}} V_{\text{pair}}(\vec{k},\vec{q})\ \hat{d}^{\dagger}_{\vec{k}}\hat{d}_{\vec{q}} \end{aligned} \tag{A.35}$$

with the pairing operator

$$\hat{d}^{\dagger}_{\vec{q}} = \hat{c}^{\dagger}_{\vec{q}\uparrow}\hat{c}^{\dagger}_{-\vec{q}\downarrow} \qquad \text{and} \qquad \hat{d}_{\vec{q}} = \hat{c}_{-\vec{q}\downarrow}\hat{c}_{\vec{q}\uparrow}\ . \tag{A.36}$$

The product of two pairing operators can be rewritten with the expectation value $\langle\hat{d}^{\dagger}_{\vec{q}}\rangle$ and the variance $\Delta\hat{d}^{\dagger}_{\vec{q}} := \hat{d}^{\dagger}_{\vec{q}} - \langle\hat{d}^{\dagger}_{\vec{q}}\rangle$ to

$$\begin{aligned} \hat{d}^{\dagger}_{\vec{k}}\hat{d}_{\vec{q}} &= \left(\hat{d}^{\dagger}_{\vec{k}} - \langle\hat{d}^{\dagger}_{\vec{k}}\rangle + \langle\hat{d}^{\dagger}_{\vec{k}}\rangle\right)\left(\hat{d}_{\vec{q}} - \langle\hat{d}_{\vec{q}}\rangle + \langle\hat{d}_{\vec{q}}\rangle\right) \\ &= \left(\Delta\hat{d}^{\dagger}_{\vec{k}} + \langle\hat{d}^{\dagger}_{\vec{k}}\rangle\right)\left(\Delta\hat{d}_{\vec{q}} + \langle\hat{d}_{\vec{q}}\rangle\right) \\ &= \underbrace{\Delta\hat{d}^{\dagger}_{\vec{k}}\Delta\hat{d}_{\vec{q}}}_{\approx 0} + \Delta\hat{d}^{\dagger}_{\vec{k}}\langle\hat{d}_{\vec{q}}\rangle + \langle\hat{d}^{\dagger}_{\vec{k}}\rangle\Delta\hat{d}_{\vec{q}} + \langle\hat{d}^{\dagger}_{\vec{k}}\rangle\langle\hat{d}_{\vec{q}}\rangle \\ &\approx \left(\hat{d}^{\dagger}_{\vec{k}} - \langle\hat{d}^{\dagger}_{\vec{k}}\rangle\right)\langle\hat{d}_{\vec{q}}\rangle + \langle\hat{d}^{\dagger}_{\vec{k}}\rangle\left(\hat{d}_{\vec{q}} - \langle\hat{d}_{\vec{q}}\rangle\right) + \langle\hat{d}^{\dagger}_{\vec{k}}\rangle\langle\hat{d}_{\vec{q}}\rangle \\ &= \hat{d}^{\dagger}_{\vec{k}}\langle\hat{d}_{\vec{q}}\rangle - \langle\hat{d}^{\dagger}_{\vec{k}}\rangle\langle\hat{d}_{\vec{q}}\rangle + \langle\hat{d}^{\dagger}_{\vec{k}}\rangle\hat{d}_{\vec{q}} \underbrace{- \langle\hat{d}^{\dagger}_{\vec{k}}\rangle\langle\hat{d}_{\vec{q}}\rangle + \langle\hat{d}^{\dagger}_{\vec{k}}\rangle\langle\hat{d}_{\vec{q}}\rangle}_{=0}\ . \end{aligned} \tag{A.37}$$

So the final result is

$$\begin{aligned} \hat{d}^{\dagger}_{\vec{k}}\hat{d}_{\vec{q}} &\approx \langle\hat{d}_{\vec{q}}\rangle\hat{d}^{\dagger}_{\vec{k}} + \langle\hat{d}^{\dagger}_{\vec{k}}\rangle\hat{d}_{\vec{q}} - \langle\hat{d}^{\dagger}_{\vec{k}}\rangle\langle\hat{d}_{\vec{q}}\rangle \\ \hat{c}^{\dagger}_{\vec{k}\uparrow}\hat{c}^{\dagger}_{-\vec{k}\downarrow}\hat{c}_{-\vec{q}\downarrow}\hat{c}_{\vec{q}\uparrow} &\approx \langle\hat{c}_{-\vec{q}\downarrow}\hat{c}_{\vec{q}\uparrow}\rangle\hat{c}^{\dagger}_{\vec{k}\uparrow}\hat{c}^{\dagger}_{-\vec{k}\downarrow} + \langle\hat{c}^{\dagger}_{\vec{k}\uparrow}\hat{c}^{\dagger}_{-\vec{k}\downarrow}\rangle\hat{c}_{-\vec{q}\downarrow}\hat{c}_{\vec{q}\uparrow} - \langle\hat{c}^{\dagger}_{\vec{k}\uparrow}\hat{c}^{\dagger}_{-\vec{k}\downarrow}\rangle\langle\hat{c}_{-\vec{q}\downarrow}\hat{c}_{\vec{q}\uparrow}\rangle\ . \end{aligned} \tag{A.38}$$

A.5 Mean-Field Hamiltonian for Long-Range Orders in the Kagome Lattice

For long-range orders with finite ordering vector $\vec{Q} \neq (0,0)$, the translational symmetry of the system is broken. Hence, the unit cell has to be expanded. This results in a reduction of the Brillouin zone (BZ) and a back folding of the band dispersion, thus the number of bands is increased.

As an example, the charge bond order (cBO) in the kagome lattice is considered, discussed in Sec. 7.4. There are three independent ordering vectors

$$\vec{Q}_1 = \pi\left(-\frac{1}{2}, -\frac{\sqrt{3}}{2}\right) \quad , \quad \vec{Q}_2 = \pi(1,0) \quad \text{and} \quad \vec{Q}_3 = \pi\left(-\frac{1}{2}, \frac{\sqrt{3}}{2}\right) \ , \tag{A.39}$$

each corresponding to another real-space order. The expectation value $\langle \hat{c}^{\dagger}_{\vec{k}\gamma} \hat{c}_{\vec{k}+\vec{Q}\alpha} \rangle$ (Eq. 7.8) features creation and annihilation operators at distinct sublattices and momenta. Hence, the Bogoliubov transform in Eq. 2.12 is increased in dimension.

First, only $\vec{Q}_2$ is regarded, so the vector of creation operators reads

$$\hat{C}_2 = \begin{pmatrix} \hat{c}^{\dagger}_{\vec{k}\alpha} & \hat{c}^{\dagger}_{\vec{k}\beta} & \hat{c}^{\dagger}_{\vec{k}\gamma} & \hat{c}^{\dagger}_{\vec{k}+\vec{Q}_2\alpha} & \hat{c}^{\dagger}_{\vec{k}+\vec{Q}_2\beta} & \hat{c}^{\dagger}_{\vec{k}+\vec{Q}_2\gamma} \end{pmatrix} \ . \tag{A.40}$$

Consequently, the non-interacting Hamiltonian reads

$$\hat{H}_0 = \sum_{\vec{k}} \hat{C}_2 \begin{pmatrix} -\mu & A_0 & B_0 & 0 & 0 & Y_0 \\ A_0 & -\mu & C_0 & 0 & 0 & 0 \\ B_0 & C_0 & -\mu & Y_0 & 0 & 0 \\ 0 & 0 & Y_0^* & -\mu & A_{\vec{Q}_2} & B_{\vec{Q}_2} \\ 0 & 0 & 0 & A_{\vec{Q}_2} & -\mu & C_{\vec{Q}_2} \\ Y_0^* & 0 & 0 & B_{\vec{Q}_2} & C_{\vec{Q}_2} & -\mu \end{pmatrix} \hat{C}_2^{\dagger} \tag{A.41}$$

with the hopping amplitudes

$$\begin{aligned} A_{\vec{p}} &= -2t_1 \cos\left(\frac{k_x - p_x}{2} - \sqrt{3}\frac{k_y - p_y}{2}\right) \\ B_{\vec{p}} &= -2t_1 \cos\left(k_x - p_x\right) \\ C_{\vec{p}} &= -2t_1 \cos\left(\frac{k_x - p_x}{2} + \sqrt{3}\frac{k_y - p_y}{2}\right) \end{aligned} \tag{A.42}$$

and the Weiss field

$$Y_{\vec{p}} = \mathrm{i}\Delta \sin\left(k_x - p_x\right) \ . \tag{A.43}$$

The reduced BZ is plotted in Fig. A.4, together with the band dispersion and FS for $\Delta \to 0$ and $\Delta = 0.1$. The result is that a partial gap opens at the FS.

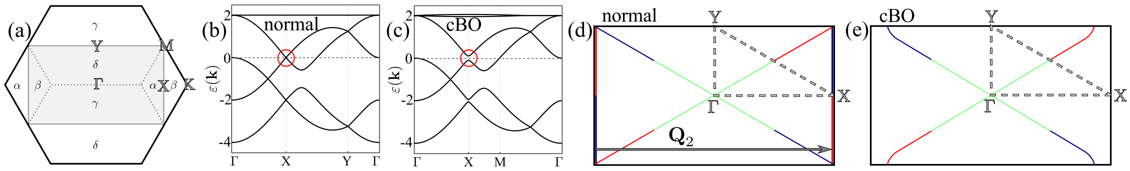

Figure A.4: **(a)** The doubling of the unit cell for the bond-ordered phases with ordering vector $\vec{Q}_2$ in Fig. 7.5 causes a halving of the BZ. The new one is rectangular (shaded area). The labels α to δ mark the back folded areas. The band structure and Fermi surface (FS) is plotted with an infinitesimal Weiss field **(b,d)** and $\Delta_{\text{cBO}} = 0.1$ **(c,e)**. The back folded dispersion relation results in 6 bands **(b,c)**. **(c)** With infinitesimal Weiss field, the FS is partially at the border of the BZ, including a perfect nesting condition. The sublattice weights of this part of the FS are dominated by α- and γ- sites. By introducing a Weiss field $\Delta_{\text{cBO}} = 0.1$, the bands are shifted near the X-point and the new FS is partially gapped, especially the parts with α and γ dominated weights.

As discussed in Sec. 7.4, it is possible to apply $\vec{Q}_1$, $\vec{Q}_2$ and $\vec{Q}_3$ simultaneously. Hence, the unit cell is expanded to 12 sites. Analogously to the above derivation, a 12-vector is defined for the creation operators:

$$\begin{aligned}\hat{C}_{12} = \Big(&\hat{c}^{\dagger}_{\vec{k}\alpha} \quad \hat{c}^{\dagger}_{\vec{k}\beta} \quad \hat{c}^{\dagger}_{\vec{k}\gamma} \quad \hat{c}^{\dagger}_{\vec{k}+\vec{Q}_1\alpha} \quad \hat{c}^{\dagger}_{\vec{k}+\vec{Q}_1\beta} \quad \hat{c}^{\dagger}_{\vec{k}+\vec{Q}_1\gamma} \cdots \\ &\cdots \hat{c}^{\dagger}_{\vec{k}+\vec{Q}_2\alpha} \quad \hat{c}^{\dagger}_{\vec{k}+\vec{Q}_2\beta} \quad \hat{c}^{\dagger}_{\vec{k}+\vec{Q}_2\gamma} \quad \hat{c}^{\dagger}_{\vec{k}+\vec{Q}_3\alpha} \quad \hat{c}^{\dagger}_{\vec{k}+\vec{Q}_3\beta} \quad \hat{c}^{\dagger}_{\vec{k}+\vec{Q}_3\gamma} \Big) \ .\end{aligned} \tag{A.44}$$

The Weiss fields corresponding to $\vec{Q}_1$ and $\vec{Q}_3$ are introduced as

$$\begin{aligned} X_{\vec{p}} &= \mathrm{i}\Delta \sin\left(-\frac{k_x - p_x}{2} - \sqrt{3}\frac{k_y - p_y}{2} \right) \\ Z_{\vec{p}} &= \mathrm{i}\Delta \sin\left(-\frac{k_x - p_x}{2} + \sqrt{3}\frac{k_y - p_y}{2} \right) \ . \end{aligned} \tag{A.45}$$

Additionally, one can show that $\vec{Q}_1 - \vec{Q}_2 \hat{=} \vec{Q}_3$. So, the complete 12×12 matrix can be built up:

$$\begin{aligned}
\hat{H}_0 = \sum_{\vec{k}} \hat{C}_{12} &\begin{pmatrix}
-\mu & A_0 & B_0 & 0 & 0 & 0 & 0 & 0 & Y_0 & 0 & Z_0 & 0 \\
A_0 & -\mu & C_0 & 0 & 0 & X_0 & 0 & 0 & 0 & Z_0 & 0 & 0 \\
B_0 & C_0 & -\mu & 0 & X_0 & 0 & Y_0 & 0 & 0 & 0 & 0 & 0 \\
0 & 0 & 0 & -\mu & A_{\vec{Q}_1} & B_{\vec{Q}_1} & 0 & Z_{\vec{Q}_1} & 0 & 0 & 0 & Y_{\vec{Q}_1} \\
0 & 0 & X_0^* & A_{\vec{Q}_1} & -\mu & C_{\vec{Q}_1} & Z_{\vec{Q}_1} & 0 & 0 & 0 & 0 & 0 \\
0 & X_0^* & 0 & B_{\vec{Q}_1} & C_{\vec{Q}_1} & -\mu & 0 & 0 & 0 & Y_{\vec{Q}_1} & 0 & 0 \\
0 & 0 & Y_0^* & 0 & Z_{\vec{Q}_1}^* & 0 & -\mu & A_{\vec{Q}_2} & B_{\vec{Q}_2} & 0 & 0 & 0 \\
0 & 0 & 0 & Z_{\vec{Q}_1}^* & 0 & 0 & A_{\vec{Q}_2} & -\mu & C_{\vec{Q}_2} & 0 & 0 & X_{\vec{Q}_2} \\
Y_0^* & 0 & 0 & 0 & 0 & 0 & B_{\vec{Q}_2} & C_{\vec{Q}_2} & -\mu & 0 & X_{\vec{Q}_2} & 0 \\
0 & Z_0^* & 0 & 0 & 0 & Y_{\vec{Q}_1}^* & 0 & 0 & 0 & -\mu & A_{\vec{Q}_3} & B_{\vec{Q}_3} \\
Z_0^* & 0 & 0 & 0 & 0 & 0 & 0 & 0 & X_{\vec{Q}_2}^* & A_{\vec{Q}_3} & -\mu & C_{\vec{Q}_3} \\
0 & 0 & 0 & Y_{\vec{Q}_1}^* & 0 & 0 & 0 & X_{\vec{Q}_2}^* & 0 & B_{\vec{Q}_3} & C_{\vec{Q}_3} & -\mu
\end{pmatrix} \hat{C}_{12}^\dagger \\
&= \sum_{\vec{k}} \sum_{n=1}^{12} \mathcal{E}_n(\vec{k})\; \hat{c}_{\vec{k}n}^\dagger \hat{c}_{\vec{k}n}
\end{aligned} \tag{A.46}$$

Again, the reduced BZ is plotted in Fig. 7.7, together with the band dispersion and FS for $\Delta \to 0$ and $\Delta = 0.1$. The result is that the FS is nearly completely gapped. Only the M- and Γ-points remain gapless.

For the calculation of the free energy, the full Hamiltonian can be rewritten with a mean-field decoupling, analogously to Eq. 2.131:

$$\begin{aligned}
\hat{H}_{\text{cCP}} &= \sum_{\vec{k}} \sum_{n=1}^{3} \varepsilon_n(\vec{k})\; \hat{c}_{\vec{k}n}^\dagger \hat{c}_{\vec{k}n} + \frac{1}{N} \sum_{\vec{k}\vec{p}} \sum_{i=1}^{3} V_{\text{cCP}}\; \hat{c}_{\vec{k}}^\dagger \hat{c}_{\vec{p}}^\dagger \hat{c}_{\vec{p}-\vec{Q}_i} \hat{c}_{\vec{k}+\vec{Q}_i} \\
&= \sum_{\vec{k}} \sum_{n=1}^{3} \varepsilon_n(\vec{k})\; \hat{c}_{\vec{k}n}^\dagger \hat{c}_{\vec{k}n} + \frac{1}{N} \sum_{\vec{k}\vec{p}} \sum_{i=1}^{3} V_{\text{cCP}} \Big(-\langle \hat{c}_{\vec{k}}^\dagger \hat{c}_{\vec{k}+\vec{Q}_i} \rangle \langle \hat{c}_{\vec{p}}^\dagger \hat{c}_{\vec{p}-\vec{Q}_i} \rangle \\
&\quad + \langle \hat{c}_{\vec{k}}^\dagger \hat{c}_{\vec{k}+\vec{Q}_i} \rangle \hat{c}_{\vec{p}}^\dagger \hat{c}_{\vec{p}-\vec{Q}_i} + \hat{c}_{\vec{k}}^\dagger \hat{c}_{\vec{k}+\vec{Q}_i} \langle \hat{c}_{\vec{p}}^\dagger \hat{c}_{\vec{p}-\vec{Q}_i} \rangle \Big) \\
&= \sum_{\vec{k}} \Big(\sum_{n=1}^{3} \varepsilon_n(\vec{k})\; \hat{c}_{\vec{k}n}^\dagger \hat{c}_{\vec{k}n} + \sum_{i=1}^{3} K_i \\
&\quad + \sum_{i=1}^{3} \underbrace{\frac{1}{N} \sum_{\vec{p}} V_{\text{cCP}}\; \langle \hat{c}_{\vec{k}}^\dagger \hat{c}_{\vec{k}+\vec{Q}_i} \rangle}_{\vec{p} \leftrightarrow \vec{k},\ \vec{Q} \leftrightarrow -\vec{Q},\ \Rightarrow \Delta_{\vec{k}i}^{\text{cCP}}} \hat{c}_{\vec{p}}^\dagger \hat{c}_{\vec{p}-\vec{Q}_i} + \sum_{i=1}^{3} \underbrace{\frac{1}{N} \sum_{\vec{p}} V_{\text{cCP}}\; \langle \hat{c}_{\vec{p}}^\dagger \hat{c}_{\vec{p}-\vec{Q}_i} \rangle}_{\Delta_{\vec{k}i}^{\text{cCP}}} \hat{c}_{\vec{k}}^\dagger \hat{c}_{\vec{k}+\vec{Q}_i} \Big) \\
&= \sum_{\vec{k}} \Big(\sum_{n=1}^{3} \varepsilon_n(\vec{k})\; \hat{c}_{\vec{k}n}^\dagger \hat{c}_{\vec{k}n} + \sum_{i=1}^{3} (2\Delta_{\vec{k}i}^{\text{cCP}} \hat{c}_{\vec{k}}^\dagger \hat{c}_{\vec{k}+\vec{Q}_i} + K_i) \Big)
\end{aligned} \tag{A.47}$$

Here, an analytic Bogoliubov transformation fails due to the effective 12-band structure. But within the mean-field approximation, the one-particle excitation energies can be calculated numerically ($\mathcal{E}(\vec{k})$ in Eq.A.46), so the total free energy reads

$$\Omega = -T \underbrace{\sum_{\vec{k}} \sum_{n=1}^{12} \ln\left(1 + \mathrm{e}^{-\frac{\mathcal{E}_n(\vec{k})}{T}}\right)}_{A} \underbrace{-2 \sum_{i=1}^{3} \sum_{\vec{k}} \langle \hat{c}^{\dagger}_{\vec{k}} \hat{c}_{\vec{k}+\vec{Q}_i} \rangle \Delta^{\mathrm{cCP}}_{\vec{k}i}}_{B} \ . \tag{A.48}$$

The second addend B is a sum over three mean fields, each corresponding to a quasi one-dimensional bond order (e.q. Fig. 7.5). Under a rotation by $\frac{\pi}{3}$, these real space patters can be transformed into each other, hence the energy cost for the creation of each mean field is identical. In other words, it is linear in the application of the individual mean fields. For addend A, this statement is not trivial, but a straightforward numerical evaluation yields the linear relation. Consequently, the ordering formation along the individual bond directions is indeed independent.

A.6 Instabilities in the Coupling Function

During the flow of the functional renormalization group (fRG), the coupling function, maps the development of instabilities for tendencies to long-range orders. A mean-field decoupling into several channels enables to analyze and compare these competing instabilities during the flow and, especially, at the break of the iterations.

As an example, a scattering processes which includes a momentum transfer identical to the nesting vector $\vec{Q}$ is considered. There are two possible processes:

$$\begin{array}{llclcl} P_1: & \vec{k} := \vec{k}_1 = \vec{k}_3 - \vec{Q} & \text{and} & \vec{p} := \vec{k}_2 = \vec{k}_4 + \vec{Q} & \text{as well as} \\ P_2: & \vec{k} := \vec{k}_1 = \vec{k}_4 - \vec{Q} & \text{and} & \vec{p} := \vec{k}_2 = \vec{k}_3 + \vec{Q} & \end{array} \tag{A.49}$$

The system can include more than one nesting vector. In this case, the mean-field decoupling has to be separately done for each $\vec{Q}$. In this channel, the two possible scattering processes are represented in the coupling function by

$$\begin{aligned} &V_{T,\vec{Q}} = \\ &= V_T(\vec{k},\vec{p},\vec{k}+\vec{Q},\vec{p}-\vec{Q})\,\hat{c}^\dagger_{\vec{k}\sigma}\hat{c}^\dagger_{\vec{p}\tau}\hat{c}_{\vec{p}-\vec{Q}\tau}\hat{c}_{\vec{k}+\vec{Q}\sigma} \\ &\quad + V_T(\vec{k},\vec{p},\vec{p}-\vec{Q},\vec{k}+\vec{Q})\,\hat{c}^\dagger_{\vec{k}\sigma}\hat{c}^\dagger_{\vec{p}\tau}\hat{c}_{\vec{k}+\vec{Q}\tau}\hat{c}_{\vec{p}-\vec{Q}\sigma} \\ &= V_T(\vec{k},\vec{p},\vec{k}+\vec{Q},\vec{p}-\vec{Q})\,\hat{c}^\dagger_{\vec{k}\sigma}\hat{c}^\dagger_{\vec{p}\tau}\hat{c}_{\vec{p}-\vec{Q}\tau}\hat{c}_{\vec{k}+\vec{Q}\sigma} - \frac{1}{2}V_T(\vec{k},\vec{p},\vec{p}-\vec{Q},\vec{k}+\vec{Q})\,\hat{c}^\dagger_{\vec{k}\sigma}\hat{c}^\dagger_{\vec{p}\tau}\hat{c}_{\vec{p}-\vec{Q}\tau}\hat{c}_{\vec{k}+\vec{Q}\sigma} \\ &\quad + V_T(\vec{k},\vec{p},\vec{p}-\vec{Q},\vec{k}+\vec{Q})\,\hat{c}^\dagger_{\vec{k}\sigma}\hat{c}^\dagger_{\vec{p}\tau}\hat{c}_{\vec{k}+\vec{Q}\tau}\hat{c}_{\vec{p}-\vec{Q}\sigma} + \frac{1}{2}V_T(\vec{k},\vec{p},\vec{p}-\vec{Q},\vec{k}+\vec{Q})\,\hat{c}^\dagger_{\vec{k}\sigma}\hat{c}^\dagger_{\vec{p}\tau}\hat{c}_{\vec{p}-\vec{Q}\tau}\hat{c}_{\vec{k}+\vec{Q}\sigma} \\ &= \underbrace{\left(V_T(\vec{k},\vec{p},\vec{k}+\vec{Q},\vec{p}-\vec{Q}) - \frac{1}{2}V_T(\vec{k},\vec{p},\vec{p}-\vec{Q},\vec{k}+\vec{Q})\right)}_{A}\underbrace{\hat{c}^\dagger_{\vec{k}\sigma}\hat{c}^\dagger_{\vec{p}\tau}\hat{c}_{\vec{p}-\vec{Q}\tau}\hat{c}_{\vec{k}+\vec{Q}\sigma}}_{B} \\ &\quad \underbrace{-2V_T(\vec{k},\vec{p},\vec{p}-\vec{Q},\vec{k}+\vec{Q})}_{C}\underbrace{\left(-\frac{1}{2}\hat{c}^\dagger_{\vec{k}\sigma}\hat{c}^\dagger_{\vec{p}\tau}\hat{c}_{\vec{k}+\vec{Q}\tau}\hat{c}_{\vec{p}-\vec{Q}\sigma} - \frac{1}{4}\hat{c}^\dagger_{\vec{k}\sigma}\hat{c}^\dagger_{\vec{p}\tau}\hat{c}_{\vec{p}-\vec{Q}\tau}\hat{c}_{\vec{k}+\vec{Q}\sigma}\right)}_{D} \end{aligned} \tag{A.50}$$

at any step of the fRG-flow, corresponding to the temperature T. Here, the two terms were expanded, so the coupling function can be reorganized. After this, the term marked with B contains two one-particle operators:

$$\begin{aligned} B: \quad \hat{c}^\dagger_{\vec{k}\sigma}\hat{c}_{\vec{k}+\vec{Q}\sigma}\hat{c}^\dagger_{\vec{p}\tau}\hat{c}_{\vec{p}-\vec{Q}\tau} &= \hat{n}_{\vec{k},\vec{Q}}\hat{n}_{\vec{p},\vec{Q}}\Big|_{\sigma\neq\tau} \qquad \text{with} \\ \hat{n}_{\vec{k},\vec{Q}} &:= \sum_\sigma \hat{c}^\dagger_{\vec{k}+\vec{Q}\sigma}\hat{c}_{\vec{k}\sigma} \end{aligned} \tag{A.51}$$

Hence, the particle-density operators are a possible implementation of the arbitrary one-particle operators in Eq. 2.128. This role is cast with spin-density operators for term

D:

$$
\begin{aligned}
D:\quad & \frac{1}{2}\hat{c}^{\dagger}_{\vec{k}\sigma}\hat{c}_{\vec{k}+\vec{Q}\tau}\hat{c}^{\dagger}_{\vec{p}\tau}\hat{c}_{\vec{p}-\vec{Q}\sigma} - \frac{1}{4}\hat{c}^{\dagger}_{\vec{k}\sigma}\hat{c}_{\vec{k}+\vec{Q}\sigma}\hat{c}^{\dagger}_{\vec{p}\tau}\hat{c}_{\vec{p}-\vec{Q}\tau} \\
&= \frac{1}{4}\sum_{\substack{\sigma\tau\\ \mu\nu}}(\hat{c}^{\dagger}_{\vec{k}\sigma}\hat{c}_{\vec{k}+\vec{Q}\tau}\hat{c}^{\dagger}_{\vec{p}\mu}\hat{c}_{\vec{p}-\vec{Q}\nu})\underbrace{(2\delta_{\sigma\nu}\delta_{\tau\mu}-\delta_{\sigma\tau}\delta_{\mu\nu})}_{=\vec{\sigma}^P_{\sigma\tau}\cdot\vec{\sigma}^P_{\mu\nu}} \\
&= \left(\frac{1}{2}\sum_{\sigma\tau}\hat{c}^{\dagger}_{\vec{k}\sigma}\vec{\sigma}^P_{\sigma\tau}\hat{c}_{\vec{k}+\vec{Q}\tau}\right)\left(\frac{1}{2}\sum_{\mu\nu}\hat{c}^{\dagger}_{\vec{p}\mu}\vec{\sigma}^P_{\mu\nu}\hat{c}_{\vec{p}-\vec{Q}\nu}\right) \\
&= \vec{S}_{\vec{k},\vec{Q}}\vec{S}_{\vec{p},\vec{Q}} \qquad \text{with} \\
& \quad \vec{S}_{\vec{k},\vec{Q}} := \frac{1}{2}\sum_{\sigma\tau}\hat{c}^{\dagger}_{\vec{k}\sigma}\vec{\sigma}^P_{\sigma\tau}\hat{c}_{\vec{k}+\vec{Q}\tau}
\end{aligned}
\tag{A.52}
$$

At this step, $\vec{\sigma}^P$ is the vector of Pauli matrices and reads

$$
\vec{\sigma}^P = \begin{pmatrix}\sigma^P_x\\ \sigma^P_y\\ \sigma^P_z\end{pmatrix} = \begin{pmatrix}\begin{pmatrix}0 & 1\\ 1 & 0\end{pmatrix}\\ \begin{pmatrix}0 & -\mathrm{i}\\ \mathrm{i} & 0\end{pmatrix}\\ \begin{pmatrix}1 & 0\\ 0 & -1\end{pmatrix}\end{pmatrix}. \tag{A.53}
$$

Now, the term A and C can be identified with the mean-field decoupled matrices in the charge-density (CDW) and the spin-density wave (SDW) channel, respectively. They read

$$
\begin{aligned}
A:\quad & V_{\mathrm{CDW}}(\vec{k},\vec{p},T) := V_T(\vec{k},\vec{p},\vec{k}+\vec{Q},\vec{p}-\vec{Q}) - \frac{1}{2}V_T(\vec{k},\vec{p},\vec{p}-\vec{Q},\vec{k}+\vec{Q}) \\
C:\quad & V_{\mathrm{SDW}}(\vec{k},\vec{p},T) := -2V_T(\vec{k},\vec{p},\vec{p}-\vec{Q},\vec{k}+\vec{Q})
\end{aligned}
\tag{A.54}
$$

This decoupling can be analogously repeated in other scattering channels. Two special cases have to be considered for an infinitesimal momentum transfer $\vec{Q}=(\varepsilon,\varepsilon)$ with $\varepsilon\to 0$. In the SDW channel, this corresponds to an order with all spins aligned in the same direction, i.e. ferromagnetism (FM). Otherwise, in the CDW channel, it maps to the Pomeranchuk instability (PI). For superconductivity, one has to regard $\vec{k}=\vec{k}_1=-\vec{k}_2$ and $\vec{p}=\vec{k}_3=-\vec{k}_4$ with the pairing operators

$$
\begin{aligned}
\Delta^{\dagger}_{s,\vec{k}} &= \frac{1}{\sqrt{2}}\left(\hat{c}^{\dagger}_{\vec{k},\sigma}\hat{c}^{\dagger}_{-\vec{k},-\sigma} + \hat{c}^{\dagger}_{-\vec{k},\sigma}\hat{c}^{\dagger}_{\vec{k},-\sigma}\right) \\
\Delta^{\dagger}_{t,\vec{k}} &= \frac{1}{\sqrt{2}}\left(\hat{c}^{\dagger}_{\vec{k},\sigma}\hat{c}^{\dagger}_{-\vec{k},-\sigma} - \hat{c}^{\dagger}_{-\vec{k},\sigma}\hat{c}^{\dagger}_{\vec{k},-\sigma}\right)
\end{aligned}
\tag{A.55}
$$

for singlet and triplet pairing, respectively. Now, the coupling function in this channel can be decomposed:

$$\begin{aligned}
V_{T,\mathrm{pair}} = {} & V_T(\vec{k},-\vec{k},\vec{p},-\vec{p})\ \underbrace{\hat{c}^\dagger_{\vec{k},\sigma}\hat{c}^\dagger_{-\vec{k},-\sigma}\hat{c}_{\vec{p},-\sigma}\hat{c}_{-\vec{p},\sigma}}_{A} + V_T(\vec{k},-\vec{k},-\vec{p},\vec{p})\ \underbrace{\hat{c}^\dagger_{\vec{k},\sigma}\hat{c}^\dagger_{-\vec{k},-\sigma}\hat{c}_{-\vec{p},-\sigma}\hat{c}_{\vec{p},\sigma}}_{B} \\
& + V_T(-\vec{k},\vec{k},\vec{p},-\vec{p})\ \underbrace{\hat{c}^\dagger_{-\vec{k},\sigma}\hat{c}^\dagger_{\vec{k},-\sigma}\hat{c}_{\vec{p},-\sigma}\hat{c}_{-\vec{p},\sigma}}_{C} + V_T(-\vec{k},\vec{k},-\vec{p},\vec{p})\ \underbrace{\hat{c}^\dagger_{-\vec{k},\sigma}\hat{c}^\dagger_{\vec{k},-\sigma}\hat{c}_{-\vec{p},-\sigma}\hat{c}_{\vec{p},\sigma}}_{D} \\
& \overset{!}{=} V_{\mathrm{sSC}}(\vec{k},\vec{p},T)\ \Delta^\dagger_{s,\vec{k}}\Delta_{s,\vec{p}} + V_{\mathrm{tSC}}(\vec{k},\vec{p},T)\ \Delta^\dagger_{t,\vec{k}}\Delta_{t,\vec{p}} \\
& = V_{\mathrm{sSC}}(\vec{k},\vec{p},T)\ \frac{1}{\sqrt{2}}\left(\hat{c}^\dagger_{\vec{k},\sigma}\hat{c}^\dagger_{-\vec{k},-\sigma} + \hat{c}^\dagger_{-\vec{k},\sigma}\hat{c}^\dagger_{\vec{k},-\sigma}\right)\ \frac{1}{\sqrt{2}}\left(\hat{c}_{-\vec{p},-\sigma}\hat{c}_{\vec{p},\sigma} + \hat{c}_{\vec{p},-\sigma}\hat{c}_{-\vec{p},\sigma}\right) \\
& \quad + V_{\mathrm{tSC}}(\vec{k},\vec{p},T)\ \frac{1}{\sqrt{2}}\left(\hat{c}^\dagger_{\vec{k},\sigma}\hat{c}^\dagger_{-\vec{k},-\sigma} - \hat{c}^\dagger_{-\vec{k},\sigma}\hat{c}^\dagger_{\vec{k},-\sigma}\right)\ \frac{1}{\sqrt{2}}\left(\hat{c}_{-\vec{p},-\sigma}\hat{c}_{\vec{p},\sigma} - \hat{c}_{\vec{p},-\sigma}\hat{c}_{-\vec{p},\sigma}\right) \\
& = \frac{1}{2}V_{\mathrm{sSC}}(\vec{k},\vec{p},T)\ (\underbrace{\hat{c}^\dagger_{\vec{k},\sigma}\hat{c}^\dagger_{-\vec{k},-\sigma}\hat{c}_{-\vec{p},-\sigma}\hat{c}_{\vec{p},\sigma}}_{B}\underbrace{+\hat{c}^\dagger_{\vec{k},\sigma}\hat{c}^\dagger_{-\vec{k},-\sigma}\hat{c}_{\vec{p},-\sigma}\hat{c}_{-\vec{p},\sigma}}_{A} \\
& \qquad \underbrace{+\hat{c}^\dagger_{-\vec{k},\sigma}\hat{c}^\dagger_{\vec{k},-\sigma}\hat{c}_{-\vec{p},-\sigma}\hat{c}_{\vec{p},\sigma}}_{D}\underbrace{+\hat{c}^\dagger_{-\vec{k},\sigma}\hat{c}^\dagger_{\vec{k},-\sigma}\hat{c}_{\vec{p},-\sigma}\hat{c}_{-\vec{p},\sigma})}_{C} \\
& \quad + \frac{1}{2}V_{\mathrm{tSC}}(\vec{k},\vec{p},T)\ (\underbrace{\hat{c}^\dagger_{\vec{k},\sigma}\hat{c}^\dagger_{-\vec{k},-\sigma}\hat{c}_{-\vec{p},-\sigma}\hat{c}_{\vec{p},\sigma}}_{B}\underbrace{-\hat{c}^\dagger_{\vec{k},\sigma}\hat{c}^\dagger_{-\vec{k},-\sigma}\hat{c}_{\vec{p},-\sigma}\hat{c}_{-\vec{p},\sigma}}_{A} \\
& \qquad \underbrace{-\hat{c}^\dagger_{-\vec{k},\sigma}\hat{c}^\dagger_{\vec{k},-\sigma}\hat{c}_{-\vec{p},-\sigma}\hat{c}_{\vec{p},\sigma}}_{D}\underbrace{+\hat{c}^\dagger_{-\vec{k},\sigma}\hat{c}^\dagger_{\vec{k},-\sigma}\hat{c}_{\vec{p},-\sigma}\hat{c}_{-\vec{p},\sigma})}_{C}
\end{aligned} \tag{A.56}$$

Due to a comparison of the prefactors of the terms marked with $\{A,B,C,D\}$, one yields a system of linear equations

$$\begin{aligned}
A: \quad V_T(\vec{k},-\vec{k},\vec{p},-\vec{p}) &= \frac{1}{2}V_{\mathrm{sSC}}(\vec{k},\vec{p},T) - \frac{1}{2}V_{\mathrm{tSC}}(\vec{k},\vec{p},T) \\
B: \quad V_T(\vec{k},-\vec{k},-\vec{p},\vec{p}) &= \frac{1}{2}V_{\mathrm{sSC}}(\vec{k},\vec{p},T) + \frac{1}{2}V_{\mathrm{tSC}}(\vec{k},\vec{p},T) \\
C: \quad V_T(-\vec{k},\vec{k},\vec{p},-\vec{p}) &= \frac{1}{2}V_{\mathrm{sSC}}(\vec{k},\vec{p},T) + \frac{1}{2}V_{\mathrm{tSC}}(\vec{k},\vec{p},T) \\
D: \quad V_T(-\vec{k},\vec{k},-\vec{p},\vec{p}) &= \frac{1}{2}V_{\mathrm{sSC}}(\vec{k},\vec{p},T) - \frac{1}{2}V_{\mathrm{tSC}}(\vec{k},\vec{p},T)\ ,
\end{aligned} \tag{A.57}$$

which can be easily solved:

$$\begin{aligned}
A+B+C+D: \quad V_{\mathrm{sSC}}(\vec{k},\vec{p},T) &= \frac{1}{2}\Big(V_T(\vec{k},-\vec{k},\vec{p},-\vec{p}) + V_T(\vec{k},-\vec{k},-\vec{p},\vec{p}) \\
&\qquad + V_T(-\vec{k},\vec{k},\vec{p},-\vec{p}) + V_T(-\vec{k},\vec{k},-\vec{p},\vec{p})\Big) \\
A-B-C+D: \quad V_{\mathrm{tSC}}(\vec{k},\vec{p},T) &= \frac{1}{2}\Big(V_T(\vec{k},-\vec{k},\vec{p},-\vec{p}) - V_T(\vec{k},-\vec{k},-\vec{p},\vec{p}) \\
&\qquad - V_T(-\vec{k},\vec{k},\vec{p},-\vec{p}) + V_T(-\vec{k},\vec{k},-\vec{p},\vec{p})\Big)\ .
\end{aligned} \tag{A.58}$$

Moreover, rotational symmetry is used, so

$$\begin{aligned} V_T(\vec{k},-\vec{k},\vec{p},-\vec{p}) &= V_T(-\vec{k},\vec{k},-\vec{p},\vec{p}) \\ V_T(\vec{k},-\vec{k},-\vec{p},\vec{p}) &= V_T(-\vec{k},\vec{k},\vec{p},-\vec{p}) \ . \end{aligned} \tag{A.59}$$

The final results for the mean-field decoupled vertex read

$$\begin{aligned} V_{\mathrm{SDW}}(\vec{k},\vec{p},\vec{Q},T) &= -2V_T(\vec{k},\vec{p},\vec{p}-\vec{Q},\vec{k}+\vec{Q}) \\ V_{\mathrm{CDW}}(\vec{k},\vec{p},\vec{Q},T) &= V_T(\vec{k},\vec{p},\vec{k}+\vec{Q},\vec{p}-\vec{Q}) - \frac{1}{2}V_T(\vec{k},\vec{p},\vec{p}-\vec{Q},\vec{k}+\vec{Q}) \\ V_{\mathrm{FM}}(\vec{k},\vec{p},T) &= -2V_T(\vec{k},\vec{p},\vec{p},\vec{k}) \\ V_{\mathrm{PI}}(\vec{k},\vec{p},T) &= V_T(\vec{k},\vec{p},\vec{k},\vec{p}) - \frac{1}{2}V_T(\vec{k},\vec{p},\vec{p},\vec{k}) \\ V_{\mathrm{sSC}}(\vec{k},\vec{p},T) &= V_T(\vec{k},-\vec{k},\vec{p},-\vec{p}) + V_T(\vec{k},-\vec{k},-\vec{p},\vec{p}) \\ V_{\mathrm{tSC}}(\vec{k},\vec{p},T) &= V_T(\vec{k},-\vec{k},\vec{p},-\vec{p}) - V_T(\vec{k},-\vec{k},-\vec{p},\vec{p}) \ . \end{aligned} \tag{A.60}$$

Bibliography

B

[1] W. Hanke, M.L. Kiesel, M. Aichhorn, S. Brehm and E. Arrigoni, *The 3-Band Hubbard-Model versus the 1-Band Model for the high-T_c Cuprates: Pairing Dynamics, Superconductivity and the Ground-State Phase Diagram*, Eur. Phys. J. Special Topics **188**, 15 (2010).

[2] M.L. Kiesel, C. Platt, W. Hanke, D.A. Abanin and R. Thomale, *Competing many-body instabilities and unconventional superconductivity in graphene*, Phys. Rev. B **86**, 020507 (2012).

[3] M.L. Kiesel and R. Thomale, *Sublattice Interference in the Kagome Hubbard Model*, Phys. Rev. B **86**, 121105 (2012).

[4] M.L. Kiesel, C. Platt and R. Thomale, *Unconventional Fermi surface instabilities in the Kagome Hubbard Model*, arXiv:1209.3398 (unpublished).

[5] M.L. Kiesel, C. Platt, W. Hanke and R. Thomale, *Anisotropic chiral $d + id$ superconductivity in* $\mathrm{Na}_x\mathrm{CoO}_2 \cdot \mathrm{H}_2\mathrm{O}$, arXiv:1301.5662 (unpublished).

[6] L.N. Cooper, *Bound Electron Pairs in a Degenerate Fermi Gas*, Phys. Rev. **104**, 1189 (1956).

[7] J. Bardeen, L.N. Cooper and J.R. Schrieffer, *Theory of Superconductivity*, Phys. Rev. **108**, 1175 (1957).

[8] J.G. Bednorz and K.A. Müller, *Possible high T_c superconductivity in the* Ba-La-Cu-O *system*, Z. Phys. B **64**, 189 (1986).

[9] C.W. Chu, L. Gao, F. Chen, Z.J. Huang, R.L. Meng and Y.Y. Xue, *Superconductivity above 150 K in* $\mathrm{HgBa}_2\mathrm{Ca}_2\mathrm{Cu}_3\mathrm{O}_{8+\delta}$ *at high pressures*, Nature **365**, 323 (1993).

[10] D.R. Harshman, A.T. Fiory and J.D. Dow, *Theory of high-T_c superconductivity: transition temperature*, J. Phys.: Condens. Matter **23**, 295701 (2011).

[11] X.J. Zhou, Z. Hussain and Z.-X. Shen, *High resolution angle-resolved photoemission study of high temperature superconductors: charge-ordering, bilayer splitting and electron-phonon coupling*, J. Electron Spectrosc. Relat. Phenom. **126**, 145 (2002).

[12] A. Damascelli, Z. Hussain and Z.-X. Shen, *Angle-resolved photoemission studies of the cuprate superconductors*, Rev. Mod. Phys. **75**, 473 (2003).

[13] T.P. Devereaux, D. Einzel, B. Stadlober, R. Hackl, D.H. Leach and J.J. Neumeier, *Electronic Raman scattering in high-T_c superconductors: A probe of $d_{x^2-y^2}$ pairing*, Phys. Rev. Lett. **72**, 396 (1994).

[14] T.P. Devereaux and R. Hackl, *Inelastic light scattering from correlated electrons*, Rev. Mod. Phys. **79**, 175 (2007).

[15] D.A. Wollman, D.J. Van Harlingen, W.C. Lee, D.M. Ginsberg and A.J. Leggett, *Experimental determination of the superconducting pairing state in* YBCO *from the phase coherence of* YBCO-Pb *dc SQUIDs*, Phys. Rev. Lett. **71**, 2134 (1993).

[16] R.J. Birgeneau, C. Stock1, J.M. Tranquada and K. Yamada, *Magnetic Neutron Scattering in Hole-Doped Cuprate Superconductors*, J. Phys. Soc. Jpn. **75**, 111003 (2006).

[17] P.A. Lee, N. Nagaosa and X.-G. Wen, *Doping a Mott insulator: Physics of high-temperature superconductivity*, Rev. Mod. Phys. **78**, 17 (2006).

[18] C.C. Tsuei and J.R. Kirtley, *Pairing symmetry in cuprate superconductors*, Rev. Mod. Phys. **72**, 969 (2000).

[19] Takami Tohyama, *Recent Progress in Physics of High-Temperature Superconductors*, Jpn. J. Appl. Phys. **51**, 010004 (2012).

[20] B. Kyung, V. Hankevych, A.-M. Daré and A.-M.S. Tremblay, *Pseudogap and Spin Fluctuations in the Normal State of the Electron-Doped Cuprates*, Phys. Rev. Lett. **93**, 147004 (2004).

[21] N.P. Armitage, P. Fournier and R.L. Greene, *Progress and perspectives on electron-doped cuprates*, Rev. Mod. Phys. **82**, 2421 (2010).

[22] V.J. Emery and S.A. Kivelson, *Importance of phase fluctuations in superconductors with small superfluid density*, Nature **374**, 434 (1995).

[23] M. Franz, *Superconductivity: Importance of fluctuations*, Nat. Phys. **3**, 686 (2007).

[24] R.-H. He, M. Hashimoto, H. Karapetyan, J.D. Koralek, J.P. Hinton, J.P. Testaud, V. Nathan, Y. Yoshida, H. Yao, K. Tanaka, W. Meevasana, R.G. Moore, D.H. Lu, S.-K. Mo, M. Ishikado, H. Eisaki, Z. Hussain, T.P. Devereaux, S.A. Kivelson, J. Orenstein, A. Kapitulnik and Z.-X. Shen, *From a Single-Band Metal to a High-Temperature Superconductor via Two Thermal Phase Transitions*, Science **331**, 1579 (2011).

[25] M. Aichhorn, E. Arrigoni, Z. B. Huang and W. Hanke, *Superconducting Gap in the Hubbard Model and the Two-Gap Energy Scales of High-T_c Cuprate Superconductors*, Phys. Rev. Lett. **99**, 257002 (2007).

[26] T. Kondo, Y. Hamaya, A.D. Palczewski, T. Takeuchi, J.S. Wen, Z.J. Xu, G. Gu, J. Schmalian and A. Kaminski, *Disentangling Cooper-pair formation above the transition temperature from the pseudogap state in the cuprates*, Nat. Phys. **7**, 21 (2011).

[27] C. Renner, B. Revaz, J.-Y. Genoud, K. Kadowaki and Ø. Fischer, *Pseudogap Precursor of the Superconducting Gap in Under- and Overdoped* $Bi_2Sr_2CaCu_2O_{8+\delta}$, Phys. Rev. Lett. **80**, 149 (1998).

[28] T. Timusk and B. Statt, *The pseudogap in high-temperature superconductors: an experimental survey*, Rep. Prog. Phys. **62**, 61 (1999).

[29] S. Chakravarty, R.B. Laughlin, D.K. Morr and C. Nayak, *Hidden order in the cuprates*, Phys. Rev. B **63**, 094503 (2001).

[30] C.-H. Hsu, S. Raghu and S. Chakravarty, *Topological density wave states of nonzero angular momentum*, Phys. Rev. B **84**, 155111 (2011).

[31] R. Khasanov, D.G. Eshchenko, H. Luetkens, E. Morenzoni, T. Prokscha, A. Suter, N. Garifianov, M. Mali, J. Roos, K. Conder and H. Keller, *Direct Observation of the Oxygen Isotope Effect on the In-Plane Magnetic Field Penetration Depth in Optimally Doped* $YBa_2Cu_3O_{7-\delta}$, Phys. Rev. Lett. **92**, 057602 (2004).

[32] R. Khasanov, A. Shengelaya, D. Di Castro, E. Morenzoni, A. Maisuradze, I.M. Savić, K. Conder, E. Pomjakushina, A. Bussmann-Holder and H. Keller, *Oxygen Isotope Effects on the Superconducting Transition and Magnetic States Within the Phase Diagram of* $Y_{1-x}Pr_xBa_2Cu_3O_{7-\delta}$, Phys. Rev. Lett. **101**, 077001 (2008).

[33] M. Serbyn and P.A. Lee, *Isotope effect on the superfluid density in conventional and high-temperature superconductors*, Phys. Rev. B **83**, 024506 (2011).

[34] G. Sangiovanni and O. Gunnarsson, *Isotope effect in the pseudogap state of high-temperature copper oxide superconductors*, Phys. Rev. B **84**, 100505 (2011).

[35] Y. Kamihara, H. Hiramatsu, M. Hirano, R. Kawamura, H. Yanagi, T. Kamiya and H. Hosono, *Iron-Based Layered Superconductor:* LaOFeP, J. Am. Chem. Soc. **128**, 10012 (2006).

[36] Z. Tesanovic, *Are iron pnictides new cuprates?*, Physics **2**, 60 (2009).

[37] K. Takada, H. Sakurai, E. Takayama-Muromachi, F. Izumi, R.A. Dilanian and T. Sasaki, *Superconductivity in two-dimensional* CoO_2 *layers*, Nature **422**, 53 (2003).

[38] A.U.B. Wolter, R. Feyerherm, E. Dudzik, S. Süllow, C. Strack, M. Lang and D. Schweitzer, *Determining ethylene group disorder levels in* $\kappa\text{-}(BEDT\text{-}TTF)_2Cu[N(CN)_2]Br$, Phys. Rev. B **75**, 104512 (2007).

[39] A.P. Mackenzie and Y. Maeno, *The superconductivity of* Sr_2RuO_4 *and the physics of spin-triplet pairing*, Rev. Mod. Phys. **75**, 657 (2003).

[40] B. Uchoa and A.H. Castro Neto, *Superconducting States of Pure and Doped Graphene*, Phys. Rev. Lett. **98**, 146801 (2007).

[41] G.R. Stewart, *Superconductivity in iron compounds*, Rev. Mod. Phys. **83**, 1589 (2011).

[42] C. de la Cruz, Q. Huang, J.W. Lynn, L. Jiying, W. Ratcliff II., J.L. Zarestky, H.A. Mook, G.F. Chen, J.L. Luo, N.L. Wang and D. Pengcheng, *Magnetic order close to superconductivity in the iron-based layered* $LaO_{1-x}F_xFeAs$ *systems*, Nature **453**, 899 (2008).

[43] K. Haule, J.H. Shim and G. Kotliar, *Correlated Electronic Structure of* $LaO_{1-x}F_xFeAs$, Phys. Rev. Lett. **100**, 226402 (2008).

[44] S. Graser, T.A. Maier, P. J. Hirschfeld and D.J. Scalapino, *Near-degeneracy of several pairing channels in multiorbital models for the* Fe *pnictides*, New J. Phys. **11**, 025016 (2009).

[45] S. Lebègue, *Electronic structure and properties of the Fermi surface of the superconductor* LaOFeP, Phys. Rev. B **75**, 035110 (2007).

[46] R. Thomale, C. Platt, W. Hanke and B.A. Bernevig, *Mechanism for Explaining Differences in the Order Parameters of* FeAs*-Based and* FeP*-Based Pnictide Superconductors*, Phys. Rev. Lett. **106**, 187003 (2011).

[47] C. Platt, R. Thomale and W. Hanke, *Superconducting state of the iron pnictide* LiFeAs*: A combined density-functional and functional-renormalization-group study*, Phys. Rev. B **84**, 235121 (2011).

[48] C. Platt, R. Thomale, C. Honerkamp, S.-C. Zhang and W. Hanke, *Mechanism for a pairing state with time-reversal symmetry breaking in iron-based superconductors*, Phys. Rev. B **85**, 180502 (2012).

[49] K.S. Novoselov, A.K. Geim, S.V. Morozov, D. Jiang, Y. Zhang, S.V. Dubonos, I.V. Grigorieva and A.A. Firsov, *Electric Field Effect in Atomically Thin Carbon Films*, Science **306**, 666 (2004).

[50] K.S. Novoselov, D. Jiang, F. Schedin, T.J. Booth, V.V. Khotkevich, S.V. Morozov and A.K. Geim, *Two-dimensional atomic crystals*, Pro. Natl. Acad. Sci. USA **102**, 10451 (2005).

[51] N.D. Mermin and H. Wagner, *Absence of Ferromagnetism or Antiferromagnetism in One- or Two-Dimensional Isotropic Heisenberg Models*, Phys. Rev. Lett. **17**, 1133 (1966).

[52] A.K. Geim and K.S. Novoselov, *The rise of graphene*, Nat. Mater. **6**, 183 (2007).

[53] A. Fasolino, J.H. Los and M.I. Katsnelson, *Intrinsic ripples in graphene*, Nat. Mater. **6**, 858 (2007).

[54] J.M. Carlsson, *Graphene: Buckle or break*, Nat. Mater. **6**, 801 (2007).

[55] K.S. Novoselov, A.K. Geim, S.V. Morozov, D. Jiang, M.I. Katsnelson, I.V. Grigorieva, S.V. Dubonos and A.A. Firsov, *Two-dimensional gas of massless Dirac fermions in graphene*, Nature **438**, 197 (2005).

[56] M.I. Katsnelson, K.S. Novoselov and A.K. Geim, *Chiral tunnelling and the Klein paradox in graphene*, Nat. Phys. **2**, 620 (2006).

[57] A.H. Castro Neto, F. Guinea, N.M.R. Peres, K.S. Novoselov and A.K. Geim, *The electronic properties of graphene*, Rev. Mod. Phys. **81**, 109 (2009).

[58] K. Takada, H. Sakurai, E. Takayama-Muromachi, F. Izumi, R.A. Dilanian and T. Sasaki, *Superconductivity in two-dimensional* $\mathsf{CoO_2}$ *layers*, Nature **434**, 53 (2004).

[59] G.-Q. Zheng, K. Matano, D.P. Chen and C.T. Lin, *Spin singlet pairing in the superconducting state of* $\mathsf{Na}_x\mathsf{CoO_2}\cdot 1.3\mathsf{H_2O}$*: Evidence from a* $^{59}\mathsf{Co}$ *Knight shift in a single crystal*, Phys. Rev. B **73**, 180503 (2006).

[60] T. Fujimoto, G.-Q. Zheng, Y. Kitaoka, R.L. Meng, J. Cmaidalka and C.W. Chu, *Unconventional Superconductivity and Electron Correlations in the Cobalt Oxyhydrate* $\mathsf{Na_{0.35}CoO_2}\cdot y\mathsf{H_2O}$ *from Nuclear Quadrupole Resonance*, Phys. Rev. Lett. **92**, 047004 (2004).

[61] G.-Q. Zheng, K. Matano, R.L. Meng, J. Cmaidalka and C.W. Chu, Na *content dependence of superconductivity and the spin correlations in* $\mathsf{Na}_x\mathsf{CoO_2}\cdot 1.3\mathsf{H_2O}$, J. Phys.: Condens. Matter **18**, L63 (2006).

[62] C. Honerkamp, M. Salmhofer, N. Furukawa and T.M. Rice, *Breakdown of the Landau-Fermi liquid in two dimensions due to umklapp scattering*, Phys. Rev. B **63**, 035109 (2001).

[63] M. Ossadnik, C. Honerkamp, T.M. Rice and M. Sigrist, *Breakdown of Landau Theory in Overdoped Cuprates near the Onset of Superconductivity*, Phys. Rev. Lett. **101**, 256405 (2008).

[64] J. Reuther, R. Thomale and S. Trebst, *Finite-temperature phase diagram of the Heisenberg-Kitaev model*, Phys. Rev. B **84**, 100406 (2011).

[65] J. Reuther, R. Thomale and S. Rachel, *Magnetic ordering phenomena of interacting quantum spin Hall models*, Phys. Rev. B **86**, 155127 (2012).

[66] P. Dai, B.C. Chakoumakos, G.F. Sun, K.W. Wong, Y. Xin and D.F. Lu, *Synthesis and neutron powder diffraction study of the superconductor* $\mathsf{HgBa_2Ca_2Cu_3O_{8+\delta}}$ *by* Tl *substitution*, Physica C **243**, 201 (1995).

[67] A.J. Leggett, *What DO we know about high Tc?*, Nat Phys **2**, 134 (2006).

[68] D.J. Scalapino, *A common thread: The pairing interaction for unconventional superconductors*, Rev. Mod. Phys. **84**, 1383 (2012).

[69] A. Altland and B. Simons, *Condensed Matter Field Theory*, Cambridge University Press, (2006).

[70] N.W. Ashcroft and N.D. Mermin, *Solid State Physics*, Thomson Learning (Toronto).

[71] A. Fetter and J. Walecka, *Quantum Theory Of Many-Particle Systems*, McGraw-Hill, (1971).

[72] J. Kakalios, *The Physics of Superheroes*, Gotham Books, (2009).

[73] G.D. Mahan, *Many-Particle Physics*, Springer, (2000).

[74] R.D. Mattuck, *A Guide to Feynman Diagrams in the Many-Body Problem*, Dover Publications, (1992).

[75] J.W. Negele and H. Orland, *Quantum Many-Particle Systems*, Westview Press, (1998).

[76] W. Nolting, *Grundkurs Theoretische Physik 7: Viel-Teilchen-Physik*, Springer (Berlin), (2005).

[77] D. Pines, *Elementary Excitations In Solids*, Perseus Books, (1999).

[78] J.J. Sakurai, *Modern Quantum Mechanics*, Benjamin/Cummings Pub., (1985).

[79] R. Shankar, *Principles Of Quantum Mechanics*, Springer, (1994).

[80] J. Hubbard, *Electron Correlations in Narrow Bands*, Proc. R. Soc. London **A 276**, 238 (1963).

[81] M. Casula, P. Werner, L. Vaugier, F. Aryasetiawan, T. Miyake, A.J. Millis and S. Biermann, *Low-Energy Models for Correlated Materials: Bandwidth Renormalization from Coulombic Screening*, Phys. Rev. Lett. **109**, 126408 (2012).

[82] P. Höpfner, J. Schäfer, A. Fleszar, S. Meyer, C. Blumenstein, T. Schramm, M. Heßmann, X. Cui, L. Patthey, W. Hanke and R. Claessen, *Electronic band structure of the two-dimensional metallic electron system* Au/Ge*(111)*, Phys. Rev. B **83**, 235435 (2011).

[83] G. Li, P. Höpfner, J. Schäfer, C. Blumenstein, S. Meyer, A. Bostwick, E. Rotenberg, R. Claessen and W. Hanke, *Magnetic-Order Induced Spectral-Weight Redistribution in a Triangular Surface System*, arXiv:1112.5062 (unpublished).

[84] P.W. Anderson, *The Resonating Valence Bond State in* La_2CuO_4 *and Superconductivity*, Science **235**, 1196 (1987).

[85] I.I. Mazin and J. Schmalian, *Pairing symmetry and pairing state in ferropnictides: Theoretical overview*, Physica C **469**, 614 (2009).

[86] G.J. Chen, R. Joynt, F.C. Zhang and C. Gros, *Phases of the t-J model from variational Monte Carlo studies: Occurrence of time-reversal symmetry breaking*, Phys. Rev. B **42**, 2662 (1990).

[87] P. Sahebsara and D. Sénéchal, *Hubbard Model on the Triangular Lattice: Spiral Order and Spin Liquid*, Phys. Rev. Lett. **100**, 136402 (2008).

[88] P.R. Wallace, *The Band Theory of Graphite*, Phys. Rev. **71**, 622 (1947).

[89] N. Furukawa, T.M. Rice and M. Salmhofer, *Truncation of a Two-Dimensional Fermi Surface due to Quasiparticle Gap Formation at the Saddle Points*, Phys. Rev. Lett. **81**, 3195 (1998).

[90] H.J. Schulz, *Superconductivity and Antiferromagnetism in the Two-Dimensional Hubbard Model: Scaling Theory*, EPL **4**, 609 (1987).

[91] J.S. Helton, K. Matan, M.P. Shores, E.A. Nytko, B.M. Bartlett, Y. Qiu, D.G. Nocera and Y.S. Lee, *Dynamic Scaling in the Susceptibility of the Spin-*$\frac{1}{2}$ *Kagome Lattice Antiferromagnet Herbertsmithite*, Phys. Rev. Lett. **104**, 147201 (2010).

[92] C. Broholm, G. Aeppli, G.P. Espinosa and A.S. Cooper, *Antiferromagnetic fluctuations and short-range order in a Kagomé lattice*, Phys. Rev. Lett. **65**, 3173 (1990).

[93] H.D. Zhou, C.R. Wiebe, Y.J. Jo, L. Balicas, R.R. Urbano, L.L. Lumata, J.S. Brooks, P.L. Kuhns, A.P. Reyes, Y. Qiu, J.R.D. Copley and J.S. Gardner, *Chemical Pressure Induced Spin Freezing Phase Transition in Kagome* Pr *Langasites*, Phys. Rev. Lett. **102**, 067203 (2009).

[94] D.E. Freedman, R. Chisnell, T.M. McQueen, Y.S. Lee, C. Payen and D.G. Nocera, *Frustrated magnetism in the* $S = 1$ *kagome lattice* $BaNi_3(OH)_2(VO_4)_2$, Chem. Commun. **48**, 64 (2012).

[95] S.-L. Yu and J.-X. Li, *Chiral superconducting phase and chiral spin-density-wave phase in a Hubbard model on the kagome lattice*, Phys. Rev. B **85**, 144402 (2012).

[96] G.E. Moore, *Cramming more components onto integrated circuits*, Electronics **38**, 4 (1965).

[97] S. Pairault, D. Sénéchal and A.-M.S. Tremblay, *Strong-Coupling Expansion for the Hubbard Model*, Phys. Rev. Lett. **80**, 5389 (1998).

[98] D.J. Scalapino, *Chapter 13: Numerical Studies of the 2D Hubbard Model*, in “Handbook of High Temperature Superconductivity”, edited by J.R. Schrieffer, Springer, Berlin / Heidelberg (2006).

[99] D. Sénéchal, D. Perez and M. Pioro-Ladrière, *Spectral Weight of the Hubbard Model through Cluster Perturbation Theory*, Phys. Rev. Lett. **84**, 522 (2000).

[100] D. Sénéchal, D. Perez and D. Plouffe, *Cluster perturbation theory for Hubbard models*, Phys. Rev. B **66**, 075129 (2002).

[101] M. Potthoff, *Self-energy-functional approach to systems of correlated electrons*, The Eur. Phy. J. B **32**, 429 (2003).

[102] T. Maier, M. Jarrell, T. Pruschke and M.H. Hettler, *Quantum cluster theories*, Rev. Mod. Phys. **77**, 1027 (2005).

[103] M. Potthoff, *Dynamical variational principles for strongly correlated electron systems*, Adv. Solid State Phys. **45**, 135 (2005).

[104] D. Sénéchal, *An introduction to quantum cluster methods*, Lectures given at the CIFAR - PITP International Summer School on Numerical Methods for Correlated Systems in Condensed Matter, Sherbrooke, Canada, May 26 - June 6 2008, arXiv:0806.2690 (unpublished).

[105] C. Dahnken, M. Aichhorn, W. Hanke, E. Arrigoni and M. Potthoff, *Variational cluster approach to spontaneous symmetry breaking: The itinerant antiferromagnet in two dimensions*, Phys. Rev. B **70**, 245110 (2004).

[106] M. Aichhorn, E. Arrigoni, M. Potthoff and W. Hanke, *Antiferromagnetic to superconducting phase transition in the hole- and electron-doped Hubbard model at zero temperature*, Phys. Rev. B **74**, 024508 (2006).

[107] M. Aichhorn and E. Arrigoni, *Weak phase separation and the pseudogap in the electron-doped cuprates*, EPL **72**, 117 (2005).

[108] P. Sahebsara and D. Sénéchal, *Antiferromagnetism and Superconductivity in Layered Organic Conductors: Variational Cluster Approach*, Phys. Rev. Lett. **97**, 257004 (2006).

[109] M. Aichhorn, H.G. Evertz, W. von der Linden and M. Potthoff, *Charge ordering in extended Hubbard models: Variational cluster approach*, Phys. Rev. B **70**, 235107 (2004).

[110] M. Nuss, E. Arrigoni, M. Aichhorn and W. von der Linden, *Variational cluster approach to the single-impurity Anderson model*, Phys. Rev. B **85**, 235107 (2012).

[111] J.C. Budich, R. Thomale, G. Li, M. Laubach and S.-C. Zhang, *Magnetic-Order Induced Spectral-Weight Redistribution in a Triangular Surface System*, arXiv:1112.5062 (unpublished).

[112] X. Lu, L. Chioncel and E. Arrigoni, *Time-reversal symmetry breaking phase in the Hubbard model: a VCA study*, Phys. Rev. B **85**, 125117 (2012).

[113] S. Brehm, E. Arrigoni, M. Aichhorn and W. Hanke, *Theory of two-particle excitations and the magnetic susceptibility in high-T_c cuprate superconductors*, EPL **89**, 27005 (2010).

[114] E. Arrigoni, M. Aichhorn, M. Daghofer and W. Hanke, *Phase diagram and single-particle spectrum of* $\mathsf{CuO_2}$ *high-T_c layers: variational cluster approach to the three-band Hubbard model*, New Journal of Physics **11**, 055066 (2009).

[115] T.A. Maier, D. Poilblanc and D.J. Scalapino, *Dynamics of the Pairing Interaction in the Hubbard and t-J Models of High-Temperature Superconductors*, Phys. Rev. Lett. **100**, 237001 (2008).

[116] M. Potthoff, *Self-energy-functional theory*, in “Springer Series in Solid-State Sciences: Theoretical Methods for Strongly Correlated Systems”, edited by A. Avella and F. Mancini, volume 171, Springer, Berlin / Heidelberg (2011).

[117] F.J. Dyson, *The S Matrix in Quantum Electrodynamics*, Phys. Rev. **75**, 1736 (1949).

[118] J.M. Luttinger and J.C. Ward, *Ground-State Energy of a Many-Fermion System. II*, Phys. Rev. **118**, 1417 (1960).

[119] G. Li, W. Hanke, A.N. Rubtsov, S. Bäse and M. Potthoff, *Accessing thermodynamics from dynamical cluster-embedding approaches*, Phys. Rev. B **80**, 195118 (2009).

[120] C. Lanczos, *An Iteration Method for the Solution of the Eigenvalue Problem of Linear Differential and Integral Operators*, J. Res. Natl. Bur. Stand **45**, 255 (1951).

[121] R.W. Freund, *Chapter 4.6*, in "Templates for the Solution of Algebraic Eigenvalue Problems: A Practical Guide", edited by Z. Bai, J. Demmel, J. Dongarra, A. Ruhe and H. van der Vorst, Society for Industrial and Applied Mathematics, Philadelphia (2000).

[122] N.-H. Tong, *Extended variational cluster approximation for correlated systems*, Phys. Rev. B **72**, 115104 (2005).

[123] M. Potthoff, M. Aichhorn and C. Dahnken, *Variational Cluster Approach to Correlated Electron Systems in Low Dimensions*, Phys. Rev. Lett. **91**, 206402 (2003).

[124] M. Aichhorn, *Ordering phenomena in strongly-correlated systems: Cluster perturbation theory approaches*, PhD-Thesis, Library of the Technische Universität Graz, (2004).

[125] S. Brehm, *Two-Particle Excitations in the Hubbard Model for High-Temperature Superconductors: A Quantum Cluster Study*, PhD-Thesis, Library of the Julius-Maximilians-Universität Würzburg, (2009).

[126] M. Potthoff, *Static and dynamic variational principles for strongly correlated electron systems*, AIP Conf. Proc. **1419**, 199 (2011).

[127] W. Koller and N. Dupuis, *Variational cluster perturbation theory for Bose-Hubbard models*, J. Phys.: Condens. Matter **18**, 9525 (2006).

[128] M. Potthoff and M. Balzer, *Self-energy-functional theory for systems of interacting electrons with disorder*, Phys. Rev. B **75**, 125112 (2007).

[129] M. Balzer, W. Hanke and M. Potthoff, *Importance of local correlations for the order parameter of high-T_c superconductors*, Phys. Rev. B **81**, 144516 (2010).

[130] E.E. Salpeter and H.A. Bethe, *A Relativistic Equation for Bound-State Problems*, Phys. Rev. **84**, 1232 (1951).

[131] N. Bulut, D.J. Scalapino and S.R. White, *Spin-fluctuation mediated interaction in the two-dimensional Hubbard model*, Physica C **246**, 85 (1995).

[132] S. Hochkeppel, F.F. Assaad and W. Hanke, *Dynamical-quantum-cluster approach to two-particle correlation functions in the Hubbard model*, Phys. Rev. B **77**, 205103 (2008).

[133] Y.M. Vilk and A.-M.S. Tremblay, *Non-Perturbative Many-Body Approach to the Hubbard Model and Single-Particle Pseudogap*, J. Phys. I France **7**, 1309 (1997).

[134] Y. Nambu, *Quasi-Particles and Gauge Invariance in the Theory of Superconductivity*, Phys. Rev. **117**, 648 (1960).

[135] S. Raghu, S.A. Kivelson and D.J. Scalapino, *Superconductivity in the repulsive Hubbard model: An asymptotically exact weak-coupling solution*, Phys. Rev. B **81**, 224505 (2010).

[136] W. Kohn and J.M. Luttinger, *New Mechanism for Superconductivity*, Phys. Rev. Lett. **15**, 524 (1965).

[137] S. Raghu, E. Berg, A.V. Chubukov and S.A. Kivelson, *Effects of longer-range interactions on unconventional superconductivity*, Phys. Rev. B **85**, 024516 (2012).

[138] C.J. Halboth and W. Metzner, *Renormalization-group analysis of the two-dimensional Hubbard model*, Phys. Rev. B **61**, 7364 (2000).

[139] C. Honerkamp and M. Salmhofer, *Temperature-flow renormalization group and the competition between superconductivity and ferromagnetism*, Phys. Rev. B **64**, 184516 (2001).

[140] C. Honerkamp, *Instabilities of interacting electrons on the triangular lattice*, Phys. Rev. B **68**, 104510 (2003).

[141] C. Honerkamp and M. Salmhofer, *Ferromagnetism and triplet superconductivity in the two-dimensional Hubbard model*, Physica C **408-410**, 302 (2004).

[142] F. Wang, H. Zhai and D.-H. Lee, *Antiferromagnetic correlation and the pairing mechanism of the cuprates and iron pnictides: A view from the functional renormalization group studies*, EPL **85**, 37005 (2009).

[143] C. Platt, C. Honerkamp and W. Hanke, *Pairing in the iron arsenides: a functional RG treatment*, New J. Phys. **11**, 055058 (2009).

[144] R. Thomale, C. Platt, J. Hu, C. Honerkamp and B.A. Bernevig, *Functional renormalization-group study of the doping dependence of pairing symmetry in the iron pnictide superconductors*, Phys. Rev. B **80**, 180505 (2009).

[145] W. Hanke, C. Platt and R. Thomale, *Order-parameter anisotropies in the pnictides - An optimization principle for multi-band superconductivity*, Ann. Phys. **523**, 638 (2011).

[146] R. Thomale, C. Platt, W. Hanke, J. Hu and B.A. Bernevig, *Exotic d-wave superconductivity in strongly hole doped* $\mathsf{K}_x\mathsf{Ba}_{1-x}\mathsf{Fe}_2\mathsf{As}_2$, Phys. Rev. Lett. **107**, 117001 (2011).

[147] R. Nandkishore, L.S. Levitov and A.V. Chubukov, *Chiral superconductivity from repulsive interactions in doped graphene*, Nat. Phys. **8**, 158 (2012).

[148] W.-S. Wang, Y.-Y. Xiang, Q.-H. Wang, F. Wang, F. Yang and D.-H. Lee, *Functional renormalization group and variational Monte Carlo studies of the electronic instabilities in graphene near* $\frac{1}{4}$ *doping*, Phys. Rev. B **85**, 035414 (2012).

[149] J. Reuther and R. Thomale, *Functional renormalization group for the anisotropic triangular antiferromagnet*, Phys. Rev. B **83**, 024402 (2011).

[150] W. Metzner, M. Salmhofer, C. Honerkamp, V. Meden and K. Schönhammer, *Functional renormalization group approach to correlated fermion systems*, Rev. Mod. Phys. **84**, 299 (2012).

[151] K.G. Wilson and J. Kogut, *The renormalization group and the* ε *expansion*, Phys. Rep. **12**, 75 (1974).

[152] S. Andergassen, T. Enss, V. Meden, W. Metzner, U. Schollwöck and K. Schönhammer, *Functional renormalization group for Luttinger liquids with impurities*, Phys. Rev. B **70**, 075102 (2004).

[153] C. Honerkamp, D. Rohe, S. Andergassen and T. Enss, *Interaction flow method for many-fermion systems*, Phys. Rev. B **70**, 235115 (2004).

[154] R. Shankar, *Renormalization-group approach to interacting fermions*, Rev. Mod. Phys. **66**, 129 (1994).

[155] D. Zanchi and H.J. Schulz, *Weakly correlated electrons on a square lattice: Renormalization-group theory*, Phys. Rev. B **61**, 13609 (2000).

[156] M. Salmhofer, *Renormalization: An Introduction*, Springer, (1999).

[157] C. Honerkamp, *Electron-doping versus hole-doping in the 2D t-t' Hubbard model*, Eur. Phys. J. B **21**, 81 (2001).

[158] K.-U. Giering and M. Salmhofer, *Self-energy flows in the two-dimensional repulsive Hubbard model*, arXiv:1208.6131 (unpublished).

[159] S. Uebelacker and C. Honerkamp, *Self-energy feedback and frequency-dependent interactions in the functional renormalization group flow for the two-dimensional Hubbard model*, arXiv:1209.3947 (unpublished).

[160] J. Reiss, D. Rohe and W. Metzner, *Renormalized mean-field analysis of antiferromagnetism and d-wave superconductivity in the two-dimensional Hubbard model*, Phys. Rev. B **75**, 075110 (2007).

[161] H. Zhai, F. Wang and D.-H. Lee, *Antiferromagnetically driven electronic correlations in iron pnictides and cuprates*, Phys. Rev. B **80**, 064517 (2009).

[162] M. Sigrist and K. Ueda, *Phenomenological theory of unconventional superconductivity*, Rev. Mod. Phys. **63**, 239 (1991).

[163] J. Zaanen, G.A. Sawatzky and J.W. Allen, *Band gaps and electronic structure of transition-metal compounds*, Phys. Rev. Lett. **55**, 418 (1985).

[164] V.J. Emery, *Theory of high-T_c superconductivity in oxides*, Phys. Rev. Lett. **58**, 2794 (1987).

[165] F.C. Zhang and T.M. Rice, *Effective Hamiltonian for the superconducting* Cu *oxides*, Phys. Rev. B **37**, 3759 (1988).

[166] G. Dopf, A. Muramatsu and W. Hanke, *Three-Band Hubbard-Model: A Monte-Carlo Study*, Phys. Rev. B **41**, 9264 (1990).

[167] G. Dopf, A. Muramatsu and W. Hanke, *Consistent description of high-T_c superconductors with the three-band Hubbard model*, Phys. Rev. Lett. **68**, 353 (1992).

[168] P. Horsch, W.H. Stephan, K. v. Szczepanski, M. Ziegler and W. von der Linden, *Quasiparticles and photoemission spectra in correlated fermion systems*, Physica C **162-164**, 783 (1989).

[169] R.T. Scalettar, D.J. Scalapino, R.L. Sugar and S.R. White, *Antiferromagnetic, charge-transfer, and pairing correlations in the three-band Hubbard model*, Phys. Rev. B **44**, 770 (1991).

[170] P. Unger and P. Fulde, *Spectral function of holes in the Emery model*, Phys. Rev. B **48**, 16607 (1993).

[171] A. Macridin, M. Jarrell, T. Maier and G.A. Sawatzky, *Physics of cuprates with the two-band Hubbard model: The validity of the one-band Hubbard model*, Phys. Rev. B **71**, 134527 (2005).

[172] C. Weber, K. Haule and G. Kotliar, *Optical weights and waterfalls in doped charge-transfer insulators: A local density approximation and dynamical mean-field theory study of* $\mathrm{La}_{2-x}\mathrm{Sr}_x\mathrm{CuO}_4$, Phys. Rev. B **78**, 134519 (2008).

[173] L. de Medici, X. Wang, M. Capone and A.J. Millis, *Correlation strength, gaps, and particle-hole asymmetry in high-T_c cuprates: A dynamical mean field study of the three-band copper-oxide model*, Phys. Rev. B **80**, 054501 (2009).

[174] C. Weber, K. Haule and G. Kotliar, *Apical oxygens and correlation strength in electron- and hole-doped copper oxides*, Phys. Rev. B **82**, 125107 (2010).

[175] X. Wang, L. de Medici and A.J. Millis, *Role of oxygen-oxygen hopping in the three-band copper-oxide model: Quasiparticle weight, metal insulator and magnetic phase boundaries, gap values, and optical conductivity*, Phys. Rev. B **83**, 094501 (2011).

[176] X. Wang, H.T. Dang and A.J. Millis, *$d_{3z^2-r^2}$ orbital in high-T_c cuprates: Excitonic spectrum, metal-insulator phase diagram, optical conductivity, and orbital character of doped holes*, Phys. Rev. B **84**, 014530 (2011).

[177] M. Imada, A. Fujimori and Y. Tokura, *Metal-insulator transitions*, Rev. Mod. Phys. **70**, 1039 (1998).

[178] R. Preuss, W. Hanke, C. Gröber and H.G. Evertz, *Pseudogaps and their Interplay with Magnetic Excitations in the doped 2D Hubbard Model*, Phys. Rev. Lett. **79**, 1122 (1997).

[179] D. Sénéchal, P.-L. Lavertu, M.-A. Marois and A.-M.S. Tremblay, *Competition between Antiferromagnetism and Superconductivity in High-T_c Cuprates*, Phys. Rev. Lett. **94**, 156404 (2005).

[180] T.A. Maier, M. Jarrell, T.C. Schulthess, P.R.C. Kent and J.B. White, *Systematic Study of d-Wave Superconductivity in the 2D Repulsive Hubbard Model*, Phys. Rev. Lett. **95**, 237001 (2005).

[181] A. Macridin, M. Jarrell, T. Maier, P.R.C. Kent and E. D'Azevedo, *Pseudogap and Antiferromagnetic Correlations in the Hubbard Model*, Phys. Rev. Lett. **97**, 036401 (2006).

[182] T.A. Maier, A. Macridin, M. Jarrell and D.J. Scalapino, *Systematic analysis of a spin-susceptibility representation of the pairing interaction in the two-dimensional Hubbard model*, Phys. Rev. B **76**, 144516 (2007).

[183] A.F. Kemper, D.G.S.P. Doluweera, T.A. Maier, M. Jarrell, P.J. Hirschfeld and H.-P. Cheng, *Insensitivity of d-wave pairing to disorder in the high-temperature cuprate superconductors*, Phys. Rev. B **79**, 104502 (2009).

[184] F.F. Assaad, W. Hanke and D.J. Scalapino, *Flux quantization in the two-dimensional repulsive and attractive Hubbard models*, Phys. Rev. Lett. **71**, 1915 (1993).

[185] F.F. Assaad, W. Hanke and D.J. Scalapino, *Temperature derivative of the superfluid density and flux quantization as criteria for superconductivity in two-dimensional Hubbard models*, Phys. Rev. B **50**, 12835 (1994).

[186] O.K. Andersen, A.I. Liechtenstein, O. Jepsen and F. Paulsen, *LDA energy bands, low-energy hamiltonians, t', t'', $t_\perp(k)$, and $J_\perp$*, J. Phys. Chem. Solids **56**, 1573 (1995).

[187] H. Eskes, G.A. Sawatzky and L.F. Feiner, *Effective transfer for singlets formed by hole doping in the high-T_c superconductors*, Physica C **160**, 424 (1989).

[188] P.R.C. Kent, T. Saha-Dasgupta, O. Jepsen, O.K. Andersen, A. Macridin, T.A. Maier, M. Jarrell and T.C. Schulthess, *Combined density functional and dynamical cluster quantum Monte Carlo calculations of the three-band Hubbard model for hole-doped cuprate superconductors*, Phys. Rev. B **78**, 035132 (2008).

[189] M.S. Hybertsen, M. Schlüter and N.E. Christensen, *Calculation of Coulomb-interaction parameters for* La_2CuO_4 *using a constrained-density-functional approach*, Phys. Rev. B **39**, 9028 (1989).

[190] F. Mila, *Parameters of a Hubbard Hamiltonian to describe superconducting* Cu *oxides*, Phys. Rev. B **38**, 11358 (1988).

[191] M. Knap, E. Arrigoni and W. von der Linden, *Benchmarking the variational cluster approach by means of the one-dimensional Bose-Hubbard model*, Phys. Rev. B **81**, 235122 (2010).

[192] H.F. Fong, P. Bourges, Y. Sidis, L.P. Regnault, J. Bossy, A. Ivanov, D.L. Milius, I.A. Aksay and B. Keimer, *Spin susceptibility in underdoped* $YBa_2Cu_3O_{6+x}$, Phys. Rev. B **61**, 14773 (2000).

[193] T. Valla, T.E. Kidd, W.-G. Yin, G.D. Gu, P.D. Johnson, Z.-H. Pan and A.V. Fedorov, *High-Energy Kink Observed in the Electron Dispersion of High-Temperature Cuprate Superconductors*, Phys. Rev. Lett. **98**, 167003 (2007).

[194] D.S. Inosov, J. Fink, A.A. Kordyuk, S.V. Borisenko, V.B. Zabolotnyy, R. Schuster, M. Knupfer, B. Büchner, R. Follath, H.A. Dürr, W. Eberhardt, V. Hinkov, B. Keimer and H. Berger, *Momentum and Energy Dependence of the Anomalous High-Energy Dispersion in the Electronic Structure of High Temperature Superconductors*, Phys. Rev. Lett. **99**, 237002 (2007).

[195] C. Raas, P. Grete and G.S. Uhrig, *Emergent Collective Modes and Kinks in Electronic Dispersions*, Phys. Rev. Lett. **102**, 076406 (2009).

[196] D. Katagiri, K. Seki, R. Eder and Y. Ohta, *Theory of the waterfall phenomenon in cuprate superconductors*, Phys. Rev. B **83**, 165124 (2011).

[197] J. Rossat-Mignod, L.P. Regnault, C. Vettier, P. Bourges, P. Burlet, J. Bossy, J.Y. Henry and G. Lapertot, *Neutron scattering study of the* $\mathsf{YBa_2Cu_3O_{6+x}}$ *system*, Physica C **185–189**, 86 (1991).

[198] S. Pailhès, Y. Sidis, P. Bourges, V. Hinkov, A. Ivanov, C. Ulrich, L.P. Regnault and B. Keimer, *Resonant Magnetic Excitations at High Energy in Superconducting* $\mathsf{YBa_2Cu_3O_{6.85}}$, Phys. Rev. Lett. **93**, 167001 (2004).

[199] S.D. Wilson, P. Dai, S. Li, S. Chi, H.J. Kang and J.W. Lynn, *Resonance in the electron-doped high-transition-temperature superconductor* $\mathsf{Pr_{0.88}LaCe_{0.12}CuO_{4-\delta}}$, Nature **442**, 59 (2006).

[200] V. Hinkov, P. Bourges, S. Pailhes, Y. Sidis, A. Ivanov, C.D. Frost, T.G. Perring, C.T. Lin, D.P. Chen and B. Keimer, *Spin dynamics in the pseudogap state of a high-temperature superconductor*, Nat. Phys. **3**, 780 (2007).

[201] S.V. Borisenko, A.A. Kordyuk, T.K. Kim, A. Koitzsch, M. Knupfer, J. Fink, M.S. Golden, M. Eschrig, H. Berger and R. Follath, *Anomalous Enhancement of the Coupling to the Magnetic Resonance Mode in Underdoped* Pb-Bi*2212*, Phys. Rev. Lett. **90**, 207001 (2003).

[202] O. Ahmadi, L. Coffey, J.F. Zasadzinski, N. Miyakawa and L. Ozyuzer, *Eliashberg Analysis of Tunneling Experiments: Support for the Pairing Glue Hypothesis in Cuprate Superconductors*, Phys. Rev. Lett. **106**, 167005 (2011).

[203] I. Eremin, D.K. Morr, A.V. Chubukov, K.H. Bennemann and M.R. Norman, *Novel neutron resonance mode in* $d_{x^2-y^2}$*-wave superconductors*, Phys. Rev. Lett. **94**, 147001 (2005).

[204] J.-P. Ismer, I. Eremin, E. Rossi and D.K. Morr, *Magnetic Resonance in the Spin Excitation Spectrum of Electron-Doped Cuprate Superconductors*, Phys. Rev. Lett. **99**, 047005 (2007).

[205] P.W. Anderson, *Is There Glue in Cuprate Superconductors?*, Science **316**, 1705 (2007).

[206] L.P. Pitaevskii, Sov. Phys. JETP **10**, 1267 (1960).

[207] K.A. Brueckner, T. Soda, P.W. Anderson and P. Morel, *Level Structure of Nuclear Matter and Liquid* ^{3}He, Phys. Rev. **118**, 1442 (1960).

[208] B. Kyung, D. Sénéchal and A.-M.S. Tremblay, *Pairing dynamics in strongly correlated superconductivity*, Phys. Rev. B **80**, 205109 (2009).

[209] D.J. Scalapino, *The case for* $d_{x^2-y^2}$ *pairing in the cuprate superconductors*, Physics Reports **250**, 329 (1995).

[210] P. Morel and P.W. Anderson, *Calculation of the Superconducting State Parameters with Retarded Electron-Phonon Interaction*, Phys. Rev. **125**, 1263 (1962).

[211] G.M. Eliashberg, Sov. Phys. JETP **11**, 696 (1960).

[212] D. Poilblanc and D.J. Scalapino, *Gap function* $\phi(k,\omega)$ *for a two-leg t-J ladder and the pairing interaction*, Phys. Rev. B **71**, 174403 (2005).

[213] T. Dahm, V. Hinkov, S.V. Borisenko, A.A. Kordyuk, V.B. Zabolotnyy, J. Fink, B. Büchner, D.J. Scalapino, W. Hanke and B. Keimer, *Strength of the Spin-Fluctuation-Mediated Pairing Interaction in a High-Temperature Superconductor*, Nat. Phys. **5**, 217 (2009).

[214] G. Garbarino, F. Morales, M. Núñez Regueiro, M. Armand and P. Lejay, *Transport and pressure properties of* $\mathrm{Na_{0.5-\delta}CoO_2}$ *single crystals with metallic ground state*, Eur. Phys. Lett. **81**, 47005 (2008).

[215] H.-B. Yang, S.-C. Wang, A.K.P. Sekharan, H. Matsui, S. Souma, T. Sato, T. Takahashi, T. Takeuchi, J.C. Campuzano, R. Jin, B.C. Sales, D. Mandrus, Z. Wang and H. Ding, *ARPES on* $\mathrm{Na_{0.6}CoO_2}$*: Fermi Surface and Unusual Band Dispersion*, Phys. Rev. Lett. **92**, 246403 (2004).

[216] M.Z. Hasan, Y.-D. Chuang, D. Qian, Y.M. Li, Y. Kong, A. Kuprin, A.V. Fedorov, R. Kimmerling, E. Rotenberg, K. Rossnagel, Z. Hussain, H. Koh, N.S. Rogado, M.L. Foo and R.J. Cava, *Fermi Surface and Quasiparticle Dynamics of* $\mathrm{Na_{0.7}CoO_2}$ *Investigated by Angle-Resolved Photoemission Spectroscopy*, Phys. Rev. Lett. **92**, 246402 (2004).

[217] S. Zhou, M. Gao, H. Ding, P.A. Lee and Z. Wang, *Electron Correlation and Fermi Surface Topology of* $\mathrm{Na}_x\mathrm{CoO_2}$, Phys. Rev. Lett. **94**, 206401 (2005).

[218] D.J. Singh and D. Kasinathan, *Destruction of the Small Fermi Surfaces in* $\mathrm{Na}_x\mathrm{CoO_2}$ *by Disorder*, Phys. Rev. Lett. **97**, 016404 (2006).

[219] D. Pillay, M.D. Johannes and I.I. Mazin, *Electronic Structure of the* $\mathrm{Na}_x\mathrm{CoO_2}$ *Surface*, Phys. Rev. Lett. **101**, 246808 (2008).

[220] G. Baskaran, *Electronic Model for* $\mathrm{CoO_2}$ *Layer Based Systems: Chiral Resonating Valence Bond Metal and Superconductivity*, Phys. Rev. Lett. **91**, 097003 (2003).

[221] A. Foussats, A. Greco, M. Bejas and A. Muramatsu, *Cooperative effect of phonons and electronic correlations for superconductivity in cobaltates*, Phys. Rev. B **72**, 020504 (2005).

[222] H. Weng, G. Xu, H. Zhang, S.-C. Zhang, X. Dai and Z. Fang, *Half-metallic surface states and topological superconductivity in* $\mathrm{NaCoO_2}$ *from first principles*, Phys. Rev. B **84**, 060408 (2011).

[223] M.L. Foo, Y. Wang, S. Watauchi, H.W. Zandbergen, T. He, R.J. Cava and N.P. Ong, *Charge Ordering, Commensurability, and Metallicity in the Phase Diagram of the Layered* $\mathrm{Na}_x\mathrm{CoO_2}$, Phys. Rev. Lett. **92**, 247001 (2004).

[224] G. Lang, J. Bobroff, H. Alloul, G. Collin and N. Blanchard, *Spin correlations and cobalt charge states: Phase diagram of sodium cobaltates*, Phys. Rev. B **78**, 155116 (2008).

[225] L. Boehnke and F. Lechermann, *Competing orders in* $\mathrm{Na}_x\mathrm{CoO_2}$ *from strong correlations on a two-particle level*, Phys. Rev. B **85**, 115128 (2012).

[226] D.J. Singh, *Electronic structure of* $\mathrm{NaCo_2O_4}$, Phys. Rev. B **61**, 13397 (2000).

[227] K.-W. Lee, J. Kuneš and W. E. Pickett, *Charge disproportionation and spin ordering tendencies in* $\mathrm{Na}_x\mathrm{CoO_2}$, Phys. Rev. B **70**, 045104 (2004).

[228] H.-B. Yang, Z.-H. Pan, A.K.P. Sekharan, T. Sato, S. Souma, T. Takahashi, R. Jin, B.C. Sales, D. Mandrus, A.V. Fedorov, Z. Wang and H. Ding, *Fermi Surface Evolution and Luttinger Theorem in* $\mathrm{Na}_x\mathrm{CoO_2}$*: A Systematic Photoemission Study*, Phys. Rev. Lett. **95**, 146401 (2005).

[229] D. Qian, L. Wray, D. Hsieh, L. Viciu, R.J. Cava, J.L. Luo, D. Wu, N.L. Wang and M.Z. Hasan, *Complete d-Band Dispersion Relation in Sodium Cobaltates*, Phys. Rev. Lett. **97**, 186405 (2006).

[230] C.A. Marianetti, K. Haule and O. Parcollet, *Quasiparticle dispersion and heat capacity of* $\mathrm{Na_{0.3}CoO_2}$*: A dynamical mean-field theory study*, Phys. Rev. Lett. **99**, 246404 (2007).

[231] A. Bourgeois, A.A. Aligia, T. Kroll and M.D. Núñez-Regueiro, *Electronic structure and Fermi-surface topology of* $\mathrm{Na}_x\mathrm{CoO_2}$, Phys. Rev. B **75**, 174518 (2007).

[232] A. Bourgeois, A.A. Aligia and M.J. Rozenberg, *Dynamical Mean Field Theory of an Effective Three-Band Model for* $\mathrm{Na}_x\mathrm{CoO}_2$, Phys. Rev. Lett. **102**, 066402 (2009).

[233] G. Cao, M.M. Korshunov, Y. Gao, M. Le Tacon, D.J. Singh and C. Lin, *Anomalous In-Plane Electronic Scattering in Charge Ordered* $\mathrm{Na}_{0.41}\mathrm{CoO}_2\cdot 0.6\mathrm{H}_2\mathrm{O}$, Phys. Rev. Lett. **108**, 236401 (2012).

[234] I. Martin and C.D. Batista, *Itinerant Electron-Driven Chiral Magnetic Ordering and Spontaneous Quantum Hall Effect in Triangular Lattice Models*, Phys. Rev. Lett. **101**, 156402 (2008).

[235] M. Kato, C. Michioka, T. Waki, Y. Itoh, K. Yoshimura, K. Ishida, H. Sakurai, E. Takayama-Muromachi, K. Takada and T. Sasaki, *Possible spin triplet superconductivity in* $\mathrm{Na}_x\mathrm{CoO}_2\cdot y\mathrm{H}_2\mathrm{O}$ $^{59}\mathrm{Co}$ *NMR studies*, J. Phys.: Condens. Matter **18**, 669 (2006).

[236] H.D. Yang, J.-Y. Lin, C.P. Sun, Y.C. Kang, C.L. Huang, K. Takada, T. Sasaki, H. Sakurai and E. Takayama-Muromachi, *Evidence of nodal superconductivity in* $\mathrm{Na}_{0.35}\mathrm{CoO}_2\cdot 1.3\mathrm{H}_2\mathrm{O}$*: A specific-heat study*, Phys. Rev. B **71**, 020504 (2005).

[237] A. Kanigel, A. Keren, L. Patlagan, K.B. Chashka, P. King and A. Amato, *Muon Spin Relaxation Measurements of* $\mathrm{Na}_x\mathrm{CoO}_2\cdot y\mathrm{H}_2\mathrm{O}$, Phys. Rev. Lett. **92**, 257007 (2004).

[238] M. Cheng, K. Sun, V. Galitski and S. Das Sarma, *Stable topological superconductivity in a family of two-dimensional fermion models*, Phys. Rev. B **81**, 024504 (2010).

[239] S. Zhou and Z. Wang, *Nodal d+id Pairing and Topological Phases on the Triangular Lattice of* $\mathrm{Na}_x\mathrm{CoO}_2\cdot y\mathrm{H}_2\mathrm{O}$*: Evidence for an Unconventional Superconducting State*, Phys. Rev. Lett. **100**, 217002 (2008).

[240] V.N. Kotov, B. Uchoa, V.M. Pereira, A.H. Castro Neto and F. Guinea, *Electron-Electron Interactions in Graphene: Current Status and Perspectives*, Rev. Mod. Phys. **84**, 1067 (2012).

[241] J. González, F. Guinea and M.A.H. Vozmediano, *Marginal-Fermi-liquid behavior from two-dimensional Coulomb interaction*, Phys. Rev. B **59**, R2474 (1999).

[242] J. González, F. Guinea and M.A.H. Vozmediano, *Non-Fermi liquid behavior of electrons in the half-filled honeycomb lattice (A renormalization group approach)*, Nucl. Phys. B **424**, 595 (1994).

[243] K.S. Novoselov, Z. Jiang, Y. Zhang, S.V. Morozov, H.L. Stormer, U. Zeitler, J.C. Maan, G.S. Boebinger, P. Kim and A.K. Geim, *Room-Temperature Quantum Hall Effect in Graphene*, Science **315**, 1379 (2007).

[244] J.L. McChesney, A. Bostwick, T. Ohta, T. Seyller, K. Horn, J. González and E. Rotenberg, *Extended van Hove Singularity and Superconducting Instability in Doped Graphene*, Phys. Rev. Lett. **104**, 136803 (2010).

[245] D.K. Efetov and P. Kim, *Controlling Electron-Phonon Interactions in Graphene at Ultrahigh Carrier Densities*, Phys. Rev. Lett. **105**, 256805 (2010).

[246] M. Einenkel and K.B. Efetov, *Possibility of superconductivity due to electron-phonon interaction in graphene*, Phys. Rev. B **84**, 214508 (2011).

[247] B. Roy and I.F. Herbut, *Unconventional superconductivity on honeycomb lattice: Theory of Kekule order parameter*, Phys. Rev. B **82**, 035429 (2010).

[248] C. Honerkamp, *Density Waves and Cooper Pairing on the Honeycomb Lattice*, Phys. Rev. Lett. **100**, 146404 (2008).

[249] G. Baskaran, *Resonating-valence-bond contribution to superconductivity in* MgB_2, Phys. Rev. B **65**, 212505 (2002).

[250] A.M. Black-Schaffer and S. Doniach, *Resonating valence bonds and mean-field d-wave superconductivity in graphite*, Phys. Rev. B **75**, 134512 (2007).

[251] S. Pathak, V.B. Shenoy and G. Baskaran, *Possible high-temperature superconducting state with a d+id pairing symmetry in doped graphene*, Phys. Rev. B **81**, 085431 (2010).

[252] M. Calandra and F. Mauri, *Theoretical Explanation of Superconductivity in* $\mathsf{C_6Ca}$, Phys. Rev. Lett. **95**, 237002 (2005).

[253] S. Maiti and A.V. Chubukov, *Renormalization group flow, competing phases, and the structure of superconducting gap in multiband models of iron-based superconductors*, Phys. Rev. B **82**, 214515 (2010).

[254] S. Reich, J. Maultzsch, C. Thomsen and P. Ordejón, *Tight-binding description of graphene*, Phys. Rev. B **66**, 035412 (2002).

[255] T.O. Wehling, E. Şaşıoğlu, C. Friedrich, A.I. Lichtenstein, M.I. Katsnelson and S. Blügel, *Strength of Effective Coulomb Interactions in Graphene and Graphite*, Phys. Rev. Lett. **106**, 236805 (2011).

[256] P. Sahebsara and D. Sénéchal, *Correlation-induced triplet superconductivity on the graphene lattice*, arXiv:0908.0474 (unpublished).

[257] S. Florens and M. Vojta, *Impact of disorder on unconventional superconductors with competing ground states*, Phys. Rev. B **71**, 094516 (2005).

[258] J. González, *Kohn-Luttinger superconductivity in graphene*, Phys. Rev. B **78**, 205431 (2008).

[259] T. Li, *Spontaneous quantum Hall effect in quarter-doped Hubbard model on honeycomb lattice and its possible realization in doped graphene system*, EPL **97**, 37001 (2012).

[260] R. Nandkishore, G.-W. Chern and A.V. Chubukov, *Itinerant Half-Metal Spin-Density-Wave State on the Hexagonal Lattice*, Phys. Rev. Lett. **108**, 227204 (2012).

[261] G.-W. Chern, R.M. Fernandes, R. Nandkishore and A.V. Chubukov, *Broken translational symmetry in an emergent paramagnetic phase of graphene*, Phys. Rev. B **86**, 115443 (2012).

[262] R.B. Laughlin, *Magnetic Induction of* $d_{x^2-y^2}+id_{xy}$ *Order in High-*T_c *Superconductors*, Phys. Rev. Lett. **80**, 5188 (1998).

[263] M. Sato, Y. Takahashi and S. Fujimoto, *Non-Abelian topological orders and Majorana fermions in spin-singlet superconductors*, Phys. Rev. B **82**, 134521 (2010).

[264] M.Z. Hasan and C.L. Kane, *Colloquium: Topological insulators*, Rev. Mod. Phys. **82**, 3045 (2010).

[265] B.A. Bernevig, T.L. Hughes and S.-C. Zhang, *Quantum Spin Hall Effect and Topological Phase Transition in* HgTe *Quantum Wells*, Science **314**, 1757 (2006).

[266] M. König, S. Wiedmann, C. Brüne, A. Roth, H. Buhmann, L.W. Molenkamp, X.-L. Qi and S.-C. Zhang, *Quantum Spin Hall Insulator State in* HgTe *Quantum Wells*, Science **318**, 766 (2007).

[267] C.L. Kane and E.J. Mele, $\mathbb{Z}_2$ *Topological Order and the Quantum Spin Hall Effect*, Phys. Rev. Lett. **95**, 146802 (2005).

[268] C.L. Kane and E.J. Mele, *Quantum Spin Hall Effect in Graphene*, Phys. Rev. Lett. **95**, 226801 (2005).

[269] X.-L. Qi and S.-C. Zhang, *The quantum spin Hall effect and topological insulators*, Phys. Today **63**, 33 (2010).

[270] X.-L. Qi and S.-C. Zhang, *Topological insulators and superconductors*, Rev. Mod. Phys. **83**, 1057 (2011).

[271] A.A. Abrikosov, *Nobel Lecture: Type-II superconductors and the vortex lattice*, Rev. Mod. Phys. **76**, 975 (2004).

[272] R. Prozorov, M.A. Tanatar, B. Shen, P. Cheng, H.-H. Wen, S.L. Bud'ko and P.C. Canfield, *Anomalous Meissner effect in pnictide superconductors*, Phys. Rev. B **82**, 180513 (2010).

[273] E. Majorana, *Teoria simmetrica dell'elettrone e del positrone*, Nuovo Cimento **14**, 171 (1937).

[274] L. Fu and C.L. Kane, *Superconducting Proximity Effect and Majorana Fermions at the Surface of a Topological Insulator*, Phys. Rev. Lett. **100**, 096407 (2008).

[275] J. Alicea, *New directions in the pursuit of Majorana fermions in solid state systems*, Rep. Prog. Phys. **75**, 076501 (2012).

[276] V. Mourik, K. Zuo, S.M. Frolov, S.R. Plissard, E.P.A.M. Bakkers and L.P. Kouwenhoven, *Signatures of Majorana Fermions in Hybrid Superconductor-Semiconductor Nanowire Devices*, Science **336**, 1003 (2012).

[277] H. Min, J.E. Hill, N.A. Sinitsyn, B.R. Sahu, L. Kleinman and A.H. MacDonald, *Intrinsic and Rashba spin-orbit interactions in graphene sheets*, Phys. Rev. B **74**, 165310 (2006).

[278] C. Nayak, S.H. Simon, A. Stern, M. Freedman and S. Das Sarma, *Non-Abelian anyons and topological quantum computation*, Rev. Mod. Phys. **80**, 1083 (2008).

[279] P. Shor, *Polynomial-Time Algorithms for Prime Factorization and Discrete Logarithms on a Quantum Computer*, Soc. Ind. Appl. Math. (SIAM) Review **41**, 303 (1999).

[280] J. Jorgensen, D. Hinks, O. Chmaissem, D. Argyriou, J. Mitchell and B. Dabrowski, *Structural features that optimize high temperature superconductivity*, in "Recent Developments in High Temperature Superconductivity", edited by J. Klamut, B. Veal, B. Dabrowski and P. Klamut, volume 475 of *Lect. Notes in Phys.*, Springer Berlin / Heidelberg (1996).

[281] A. Iyo, Y. Tanaka, H. Kito, Y. Kodama, P.M. Shirage, D.D. Shivagan, H. Matsuhata, K. Tokiwa and T. Watanabe, *T_c vs n Relationship for Multilayered High-T_c Superconductors*, J. Phys. Soc. Jpn. **76**, 094711 (2007).

[282] E. Pavarini, I. Dasgupta, T. Saha-Dasgupta, O. Jepsen and O.K. Andersen, *Band-Structure Trend in Hole-Doped Cuprates and Correlation with $T_{c,max}$*, Phys. Rev. Lett. **87**, 047003 (2001).

[283] H. Sakakibara, H. Usui, K. Kuroki, R. Arita and H. Aoki, *Origin of the material dependence of T_c in the single-layered cuprates*, Phys. Rev. B **85**, 064501 (2012).

[284] K. Kuroki, H. Usui, S. Onari, R. Arita and H. Aoki, *Pnictogen height as a possible switch between high-T_c nodeless and low-T_c nodal pairings in the iron-based superconductors*, Phys. Rev. B **79**, 224511 (2009).

[285] V. Elser, *Nuclear antiferromagnetism in a registered $^3\mathrm{He}$ solid*, Phys. Rev. Lett. **62**, 2405 (1989).

[286] A.P. Ramirez, *Strongly Geometrically Frustrated Magnets*, Annu. Rev. Mate. Sci. **24**, 453 (1994).

[287] G. Misguich and C. Lhuillier, *Two-dimensional quantum antiferromagnets*, in "Frustrated Spin Systems", edited by H.T. Diep, World Scientific, Singapore (2004).

[288] P. Mendels and F. Bert, *Quantum Kagome Antiferromagnet* $\mathrm{ZnCu_3(OH)_6Cl_2}$, J. Phys. Soc. Jpn. **79**, 011001 (2010).

[289] T. Ohashi, T. Momoi, H. Tsunetsugu and N. Kawakami, *Finite-Temperature Mott Transition in Two-Dimensional Frustrated Hubbard Models*, Prog. Theor. Phys. Supp. **176**, 97 (2008).

[290] A. Tanaka and H. Ueda, *Stability of Ferromagnetism in the Hubbard Model on the Kagome Lattice*, Phys. Rev. Lett. **90**, 067204 (2003).

[291] G.-B. Jo, J. Guzman, C.K. Thomas, P. Hosur, A. Vishwanath and D.M. Stamper-Kurn, *Ultracold Atoms in a Tunable Optical Kagome Lattice*, Phys. Rev. Lett. **108**, 045305 (2012).

[292] S. Raghu, R. Thomale and T.H. Geballe, *Optimal T_c of cuprates: role of screening and reservoir layers*, Phys. Rev. B **86**, 094506 (2012).

[293] M. Nishiyama, S. Maegawa, T. Inami and Y. Oka, *Magnetic ordering and spin dynamics in potassium jarosite: A Heisenberg kagome lattice antiferromagnet*, Phys. Rev. B **67**, 224435 (2003).

[294] J.R. Stewart, G. Ehlers, H. Mutka, P. Fouquet, C. Payen and R. Lortz, *Spin dynamics, short-range order, and spin freezing in* $Y_{0.5}Ca_{0.5}BaCo_4O_7$, Phys. Rev. B **83**, 024405 (2011).

[295] Y. Ran, M. Hermele, P.A. Lee and X.-G. Wen, *Projected-Wave-Function Study of the Spin-*$1/2$ *Heisenberg Model on the Kagome Lattice*, Phys. Rev. Lett. **98**, 117205 (2007).

[296] L. Balents, *Spin liquids in frustrated magnets*, Nature **464**, 199 (2010).

[297] S. Yan, D.A. Huse and S.R. White, *Spin-Liquid Ground State of the* $S = 1/2$ *Kagome Heisenberg Antiferromagnet*, Science **332**, 1173 (2011).

[298] R.R.P. Singh and D.A. Huse, *Ground state of the spin-*$1/2$ *kagome-lattice Heisenberg antiferromagnet*, Phys. Rev. B **76**, 180407 (2007).

[299] T. Han, S. Chu and Y.S. Lee, *Refining the Spin Hamiltonian in the Spin-*$\frac{1}{2}$ *Kagome Lattice Antiferromagnet* $ZnCu_3(OH)_6Cl_2$ *Using Single Crystals*, Phys. Rev. Lett. **108**, 157202 (2012).

[300] J. Ishioka, Y.H. Liu, K. Shimatake, T. Kurosawa, K. Ichimura, Y. Toda, M. Oda and S. Tanda, *Chiral Charge-Density Waves*, Phys. Rev. Lett. **105**, 176401 (2010).

[301] I. Guillamón, H. Suderow, J.G. Rodrigo, S. Vieira, P. Rodière, L. Cario, E. Navarro-Moratalla, C. Martí-Gastaldo and E. Coronado, *Chiral charge order in the superconductor* 2H-TaS_2, New J. Phys. **13**, 103020 (2011).

[302] J. Ishioka, T. Fujii, T. Katono, K. Ichimura, T. Kurosawa, M. Oda and S. Tanda, *Charge-parity symmetry observed through Friedel oscillations in chiral charge-density waves*, Phys. Rev. B **84**, 245125 (2011).

[303] C. Nayak, *Density-wave states of nonzero angular momentum*, Phys. Rev. B **62**, 4880 (2000).

[304] S.G. Bhongale, L. Mathey, S.-W. Tsai, C.W. Clark and E. Zhao, *Bond Order Solid of Two-Dimensional Dipolar Fermions*, Phys. Rev. Lett. **108**, 145301 (2012).

[305] C.J. Halboth and W. Metzner, *d-Wave Superconductivity and Pomeranchuk Instability in the Two-Dimensional Hubbard Model*, Phys. Rev. Lett. **85**, 5162 (2000).

[306] S.A. Kivelson, E. Fradkin and V.J. Emery, *Electronic liquid-crystal phases of a doped Mott insulator*, Nature **393**, 550 (1998).

[307] T.-M. Chuang, M.P. Allan, J. Lee, Y. Xie, N. Ni, S.L. Bud'ko, G.S. Boebinger, P.C. Canfield and J.C. Davis, *Nematic Electronic Structure in the "Parent " State of the Iron-Based Superconductor* $Ca(Fe_{1-x}Co_x)_2As_2$, Science **327**, 181 (2010).

[308] E. Demler, W. Hanke and S.C. Zhang, *The SO(5) Theory of antiferromagnetism and superconductivity*, Rev. Mod. Phys. **76**, 909 (2004).

[309] *World's Longest Superconductor Cable*, Karlsruhe Institute of Technology, Press Release 012/2012 (2012).

[310] E. Berg, D. Orgad and S.A. Kivelson, *Route to high-temperature superconductivity in composite systems*, Phys. Rev. B **78**, 094509 (2008).

[311] C. Honerkamp, W. Hanke and O.K. Andersen, *Superconductivity in novel surface and interface electronic systems*, Proposal for DFG research unit 1162 (2009).

[312] S. Okamoto and T.A. Maier, *Enhanced Superconductivity in Superlattices of High-T_c Cuprates*, Phys. Rev. Lett. **101**, 156401 (2008).

[313] L. Goren and E. Altman, *Enhancement of the superconducting transition temperature in cuprate heterostructures*, Phys. Rev. B **79**, 174509 (2009).

[314] E. Katzir, S. Yochelis, F. Zeides, N. Katz, Y. Kalcheim, O. Millo, G. Leitus, Y. Myasodeyov, B.Y. Shapiro, R. Naaman and Y. Paltiel, *Increased Superconducting Transition Temperature of a Niobium Thin Film Proximity Coupled to Gold Nanoparticles Using Linking Organic Molecules*, Phys. Rev. Lett. **108**, 107004 (2012).

[315] K. Jin, P. Bach, X.H. Zhang, U. Grupel, E. Zohar, I. Diamant, Y. Dagan, S. Smadici, P. Abbamonte and R.L. Greene, *Anomalous enhancement of the superconducting transition temperature of electron-doped* $\mathsf{La}_{2-x}\mathsf{Ce}_x\mathsf{CuO}_4$ *and* $\mathsf{Pr}_{2-x}\mathsf{Ce}_x\mathsf{CuO}_4$ *cuprate heterostructures*, Phys. Rev. B **83**, 060511 (2011).

[316] A.V. Chubukov, D.V. Efremov and I. Eremin, *Magnetism, superconductivity, and pairing symmetry in iron-based superconductors*, Phys. Rev. B **78**, 134512 (2008).

[317] L.V. Ahlfors, *Complex analysis: an introduction to the theory of analytic functions of one complex variable*, McGraw-Hill, (1979).